

Fundamentals and Applications of Particle Focusing Within Non-Newtonian Fluids Using Inertial Microfluidic Systems

Mohammad Amin Raoufi

A thesis submitted in partial fulfillment of the requirements for the degree of
Doctor of Philosophy (Ph.D.)
Department of Science and Engineering



MACQUARIE
University
SYDNEY · AUSTRALIA

Supervised by

Principal supervisors: Dr. Mohsen Asadnia and
Prof. Hamid Niazmand

Co-supervisor: Associate prof. Majid Warkiani

September 2019

To my parents

Hamid Reza Raoufi

Zarrin Rasekhi

Research outputs

Publications related to this thesis are as follow:

Journals

Note that papers will be referred to by their roman numerals throughout this dissertation.

- I. **Raoufi M.A.**, Mashhadian A., Niazmand H., Asadnia M., and Warkiani M.E., Experimental and numerical study of elasto-inertial focusing in straight channels. *Biomicrofluidics*, 2019, (Doi:10.1063/1.5093345), (CHAPTER 4).
- II. **Raoufi M.A.**, Razavi Bazaz S., Niazmand H., Asadnia M., Razmjou A., Roohi M., and Warkiani M.E., Wax 3D printing of inertial microfluidic channels with complex geometries. *Soft matter* (under review) 2019, (CHAPTER 5).
- III. Razavi Bazaz S., Rouhi O., **Raoufi M.A.**, Najafi F., Asadnia M., and Warkiani M.E., 3D direct printing of inertial microfluidic devices. *Scientific reports* (Under review), 2019, (CHAPTER 6).
- IV. Razavi Bazaz S., **Raoufi M.A.**, Hesari Z. A., Mehrizi A. A., Asadnia M., and Warkiani M.E., A novel microfluidic device for extraction of plasma by considering the non-Newtonian characteristics of human blood. *Micromachines* (Under review), 2019, (CHAPTER 7).

Conference

1. **Raoufi M.A.**, Razavi B.S., Rouh O., Asadnia M., and Warkiani M.E., Inertial separation of microcarriers from mesenchymal stem cells using wax 3D printed complex channel. *ANZNMF Conference*, 2019.
2. Razavi B.S., Rouh O., **Raoufi M.A.**, and Warkiani M.E., Inertial Focusing in straight complex microchannels. *ANZNMF Conference*, 2019.
3. **Raoufi M.A.**, Asadnia M., Niazmand H., and Warkiani M.E., Effects of viscoelasticity on particle sorting through a straight microchannel with trapezoidal cross-section. *ANZNMF Conference*, 2018.
4. **Raoufi M.A.**, Mashhadian A., Asadnia M., and Warkiani M.E., Experimental and numerical study of viscoelasticity effects on particle focusing within a straight trapezoidal channel. *MicroTas Conference*, 2018.

Awards

1. International Cotutelle Macquarie University Research Training Program (CTiMRTP) Scholarship 2018.
2. Awarded Macquarie University WiMED Student Prize (2018).

3. Awarded for achieving the 3rd position for oral presentation at HDR conference (20th Jun 2019).

Seminars and workshops

1. Speaker at IEE IMS NSW chapter 2rd Annual workshop (28, July 2018).
2. Speaker at IEE IMS NSW chapter 3rd Annual workshop (25, July 2019).

Other publications with Macquarie collaboration

1. **Raoufi M.A.**, Moshizi S. A., Razmjou A., Wu s., Warkiani M. E., Asadnia M., Development of a Biomimetic semicircular canal with MEMS sensors to restore balance, *IEEE Sensors Journal*, 2019.
2. Moshizi S. A., **Raoufi M.A.**, Ahmadi H., Wu s., Belford A., Asadnia M., Development of a bio-inspired vestibular system using MEMS sensors and 3D printing technology, ICST2019 Conference, 2019.

Work distributions in Co-Authored Articles

Each chapter of the current research has been performed with different collaborators and are published or prepared for publishing in different journals. Table 1 shows each collaborator contribution to each work.

List of Authors are: Mohammad Amin Raoufi (MAR), Sajad Razavi Bazaz (SRB), Ali Mashhadian (AM), Omid Rouhi (OR), Alireza Zabihi Hesari (AZH), Hamid Niazmand (HN), Mohsen Asadnia (MA), Amir Razmjou (AR), Majid Ebrahimi Warkiani (MEW), Steven Vasilescu (SV), Ali Abouei (AA), Fatemeh Ezheian.

Table 1: Authors' contribution

Chapter	4th Paper I	5th Paper II	6th Paper III	7th Paper IV
Conception and design	MAR	MAR	SRB, MAR, OR	SRB, AZH, MAR
Planning and implementation	MAR	MAR	SRB, MAR	SRB, MAR, AZH
Data collection	MAR	MAR	OR, MAR, FE	MAR
Analysis and interpretation	MAR, AM	MAR, SRB, OR	SRB, FE, MAR	MAR, SRB
Writing the article	MAR, AM	MAR	SRB, MAR	SRB, MAR
Revision	HN, AR	HN, AR	MAR	MA, SV
Overall responsibility	MA, MEW	MA, MEW	MA, MEW	MEW, AA

* All papers and figures are presented with the permission of the corresponding publishers.

Contents

Research outputs	IV
Work distributions in Co-Authored Articles.....	V
Abstract.....	X
Acknowledgments	XII
List of Figures.....	XIII
List of Tables	XVII
Chapter One: Introduction	1
1.1 What is Microfluidic	2
1.2 Types of Microfluidic Devices.....	2
1.3 Motivation	4
1.4 Objectives.....	4
1.5 Research Contributions	5
1.6 Thesis Outline	6
Chapter Two: Literature Review	8
2.1 Introduction	9
2.2 Physics of particle migration in viscoelastic flows	13
2.2.1 Elastic lift force.....	13
2.2.2 Inertial lift force	15
2.2.3 Drag Force	16
2.2.4 Shear-thinning effect	17
2.2.5 Brownian motion	19
2.2.6 Centrifugal force.....	20
2.2.7 Deformability-induced force	20
2.3 Direct Numerical Simulation	21
2.4 Geometrical classification of elasto-inertial systems	23
2.4.1 Sheathless flow	24
2.4.2 Sheath flow	45
2.5 Mold development of inertial microfluidic devices	53
2.5.1 Photolithography.....	54
2.5.2 Laser cutting:	55
2.5.3 Mechanical machining.....	56
2.5.4 Etching:.....	57

2.5.5	Embedding micro-wire	58
2.5.6	Hot embossing:	58
2.5.7	3D printing:.....	59
2.6	Applications of non-Newtonian systems.....	61
2.6.1	Particle focusing	62
2.6.2	Particle separation.....	62
2.6.3	Fluid exchange and cell washing	63
2.6.4	Cell stretching measurement.....	64
2.6.5	Mixing.....	65
2.7	Conclusion.....	65

Chapter Three: Methodology of sample preparation, device fabrication and experimental setup.....67

3.1	Introduction:	67
3.2	Characterization of the PEO solution.....	68
3.3	Sample preparation.....	71
3.4	Device fabrication	71
3.5	Experimental setup and Image processing	73

Chapter Four: Experimental and numerical study of Elasto-Inertial focusing in straight channels74

4.1	Introduction	77
4.2	Numerical Simulation	79
4.2.1	Background.....	79
4.2.2	Direct numerical simulation method (DNS).....	81
4.3	Experimental setup	84
4.3.1	Device structures and fabrication	85
4.4	Results and discussion:.....	86
4.4.1	Physics of elasto-inertial focusing	86
4.4.2	Particle trajectories in a viscoelastic fluid	89
4.4.3	Effect of velocity gradient on focusing pattern	90
4.4.4	Effect of Geometry on focusing	92
4.4.5	Designing the complex channel.....	94
4.5	Conclusion.....	96
4.6	Supplementary material.....	97
4.7	Acknowledgment	97

Chapter Five:Wax 3D printing of inertial microfluidic channels with complex geometries.....	98
5.1 Introduction	101
5.2 Materials and methods	104
5.2.1 Design and fabrication process	104
5.2.2 Experimental setup	107
5.2.3 Surface characterization.....	108
5.3 Results and discussion:.....	108
5.3.1 Wax 3D printer	108
5.3.2 Characterization of microfluidic devices	109
5.3.3 Numerical Simulation Results	111
5.4 Experimental Results.....	113
5.4.1 Curved Channels.....	113
5.4.2 Straight Channels.....	115
5.4.3 Separation of microcarriers from Mesenchymal Stem Cell	117
5.5 Conclusion.....	119
5.6 Acknowledgment	121
Chapter Six:3D-Direct-Printing of Inertial Microfluidic Devices.....	122
6.1 Introduction	125
6.2 Materials and method	128
6.2.1 Fabrication Method.....	128
6.2.2 Preparation of Bead Suspension	129
6.2.3 Bonding quality test.....	130
6.2.4 Surface characterization.....	130
6.2.5 Cell culture conditions	131
6.2.6 Morphological analysis and cell viability assay	131
6.2.7 Real-time PCR analysis	132
6.3 Results and discussion.....	132
6.3.1 fabrication and characterization of the 3D printed channels	132
6.3.2 Straight microchannel	138
6.3.3 Spiral Microchannel.....	140
6.3.4 Sinusoidal Microchannel	143
6.3.5 Serpentine	145
6.3.6 Contraction-expansion array.....	146

6.3.7	Cell activity assessment	147
6.4	Conclusion.....	149
6.5	Acknowledgment	150
Chapter Seven:A novel microfluidic device for extraction of plasma by considering the non-Newtonian characteristics of human blood		151
7.1	Introduction	154
7.2	Methodology for simulations and Experiments	157
7.2.1	Geometry design	157
7.2.2	Numerical simulation.....	158
7.2.3	Non-Newtonian model.....	161
7.2.4	Separation and purity efficiencies	162
7.2.5	Separation principles	163
7.2.6	Experimental Setup:.....	163
7.3	Results and Discussions	164
7.3.1	Grid study	164
7.3.2	Separation and purity efficiency	165
7.3.3	New conceptual design of the microchannel	166
7.3.4	Experimental results for the new conceptual design	170
7.4	Conclusion.....	171
Chapter Eight:Conclusions and Future work		173
8.1	Conclusions	174
8.1.1	Fundamentals of elasto inertial focusing in straight channels (Paper I, Chapter 4)	174
8.1.2	Elasto-inertial particle migration in non-conventional channels fabricated by wax 3D printing (Paper II, Chapter 5)	175
8.1.3	3D-Direct printing of inertial microfluidic devices (Paper III, Chapter 6)..	176
8.1.4	Blood-plasma separation using Dean-flow coupled elasto-inertial systems (Paper IV, Chapter 7).....	177
8.2	Future works.....	178
References		180
Appendix.....		194

Abstract

Over the last decades, inertial microfluidics has gained substantial attention due to its capability to control and manipulate particles accurately. However, these inertial forces in Newtonian fluids are not sufficient to efficiently focus small microparticles which limits their applications to larger bioparticles including stem cells, circulating tumor cells and blood cells. To address this inadequacy, recently elasto-inertial microfluidic systems have been introduced as a powerful method to sort smaller microparticles more effectively. These systems can break the restrictions of low-throughput, additional external components, and complex channel designs in Newtonian systems for submicron particle sorting.

So far, there have been several studies on the applications and fundamentals of particle migration in non-Newtonian fluids. However, most of them are limited to simple rectangular straight channels, due to the difficulty of fabrication and modeling of particle migration in non-Newtonian fluids within channels with nonlinear cross-sections. Therefore, the main purpose of this research is to study the fundamentals of particle migration in elasto-inertial microfluidic systems as well as introducing new workflows for the fabrication of non-conventional microchannels to not only explore new physics in elasto-inertial systems but to increase the efficiency and effectiveness of the current elasto-inertial devices.

To this end, in chapter two, basics and applications of particle migration in non-Newtonian fluids are reviewed and categorized based on the channel structure and design. In chapter four, the physics of elasto-inertial focusing in straight channels of different cross-sections are numerically and experimentally investigated. Then, in chapter five and six, two different Wax and DLP 3D printers for the first time are used to create novel non-conventional straight and curved microchannels suitable for inertial microfluidic applications. We propose new fabrication workflows to easily construct complex channels that are almost impossible or extremely difficult to fabricate with previous microfabrication methods. Finally, in chapter seven, a new design for blood-plasma separation is proposed based on the non-Newtonian property of the blood, Zweifach-Fung effect, and plasma skimming phenomenon. We numerically model several microchannels with different daughter branches and bifurcations to obtain the best combination of flow rate and geometry for plasma extraction. We believe that our proposed fabrication methods and presented fundamentals can pave the way for further research on elasto-inertial systems in more complex channels.

Statement of candidate

This thesis is being submitted to Macquarie University and Ferdowsi University of Mashhad in accordance with the Cotutelle agreement dated 01/07/2017.

I certify that the work in this thesis has not previously been submitted for a degree nor has it been submitted as part of the requirements for a degree to any other university or institution other than Macquarie University. I also certify that the thesis is an original piece of research, and it has been written by me. Any help and assistance that I have received In my research work and the preparation of the thesis itself have been appropriately acknowledged.

.....
Mohammad Amin Raoufi

Acknowledgments

First, I would like to express my deepest and sincerest gratitude to my supervisors, ***Dr. Mohsen Asadnia, Professor Hamid Niazmand and Dr. Majid Ebrahimi Warkiani*** for their excellent support, advice, and encouragement through my research. This work would not have been possible without their great knowledge and patient guidance.

I am grateful to all of those with whom I have had the pleasure to work during this project at Macquarie University and University of Technology Sydney (UTS). I would especially like to thank Shahin Hosseinzade and Shilun Feng, who helped me to understand and progress with my project during the initial months of my Ph.D. candidature. I would also like to thank Sajad Razavi Bazaz and Omid Rouhi for their technical assistance.

I am also thankful to the technical and administrative staff from the School of Engineering, Macquarie University, for their great support during my research period.

Words cannot express my gratitude and appreciation to my parents and siblings- Elham and Behnam- for the constant motivation and support they have provided throughout my life.

Last but not least, I would like to thank my friends and colleagues, Amanj Kheradmand, Sajad A. Moshizi, who have always stood beside me and helped me in times of need.

List of Figures

Figure 2-1. Classification of elasto-inertial microfluidic systems based on design and geometry .13	13
Figure 2-2: schematic illustration of different forces particles undergo in elasto-inertial microfluidic systems.18	18
Figure 2-3: the flowchart for the calculation of inertial lift force.23	23
Figure 2-4: graphical demonstration of the particles' alignments in a sheathless straight channel [55].25	25
Figure 2-5: mechanisms of focusing for deformable particles [76].26	26
Figure 2-6: focusing positions of beads and DNA in Newtonian and non-newtonian solutions [29].27	27
Figure 2-7: focusing of the PEG particles and WBCs based on deformability, shape and solution elasticity [57].28	28
Figure 2-8: effects of solution property on the focusing positions [77].29	29
Figure 2-9: focusing positions of deformable cells and rigid particles at 7.5 cm from the channel inlet [79].30	30
Figure 2-10: particle equilibrium positions for a) PEO (2000 ppm), b) PVP (8 wt. %) and c) DI water under different flow rates for a rectangular channel with AR of 1/3 [58].31	31
Figure 2-11: schematic of the focusing mechanisms in non-newtonian fluids [83].35	35
Figure 2-12: focusing and separation of beads and E.coli [86].36	36
Figure 2-13: separation of the candida and WBCs sample at flow rate of 100 $\mu\text{l}/\text{min}$. Fluorescent images of WBCs and bright-field microscopic images of candida were stacked to demonstrate the distinctly separated cells at the channel outlet [89].37	37
Figure 2-14: schematic of a two-stage straight channel for sheathless particle separation [90].38	38
Figure 2-15: sheathless elasto-inertial focusing and separation of rigid polystyrene particles through a multistage bifurcation straight channel [90].39	39
Figure 2-16: particle focusing phenomenon in a straight channel with side wells [94].40	40
Figure 2-17: demonstration of the different elasto-inertial focusing stages in a spiral channel [97].42	42
Figure 2-18: a) graphic demonstration of particle focusing in a serpentine channel for PEO solution. B) focusing behaviors at different zigzag turns and low rates [59].43	43
Figure 2-19: transverse movement of particles from non-newtonian sample fluid to the newtonian sheath flow [103].46	46
Figure 2-20: a) schematic illustration of sheath flow elasto-inertial particle separation using viscoelastic fluid flow in a straight microchannel. b) separation of particles at the outlet, showing while 1 μm particles remained untouched and collected from side outlets, 5 μm particles moved to the center and harvested from the middle outlet [105].47	47
Figure 2-21: comparison of particle lateral migration in different viscoelastic fluids within a rectangular microchannel (AR=2) for two conditions of side and central sheath flow [106].48	48

Figure 2-22: elasto-inertial pinched flow in a T-shaped microchannel [87].	49
Figure 2-23: separation of a mixture of 2 μm (red) and 1 μm (green) particles for different sample/sheath flow conditions. [104].	50
Figure 2-24: a) schematic illustration of the microfluidic device for exosome isolation. b) experimental and numerical results, showing the trajectories and separation of the 500 nm (red) and 100 nm (green) fluorescent particles. It also demonstrates the recovery rate for each particle as well as normalized distribution at each outlet [112].	51
Figure 2-25: flow instabilities in a 90° curved microchannel [113].	52
Figure 2-26: schematic illustration of the mask fabrication by photolithography [115].	55
Figure 2-27: schematic illustration of the mold fabrication by a) femtosecond laser ablation [114], and b) mechanical machining [121].	56
Figure 2-28: schematic illustration of the mold fabrication by a) isotropic etching, and b) anisotropic etching.	58
Figure 2-29: schematic illustration of the mold fabrication by hot embossing method.	59
Figure 2-30: schematic illustration of a) sla, and b) dlp 3d printers [134].	61
Figure 2-31: a) schematic illustration of sheathless microflow cytometer and assembled components including chip, pressure pump, oscilloscope, laser diode and laser driver [138]. b) pre-alignment of the particles using non-newtonian fluid [91].	62
Figure 2-32: schematic illustration of the non-newtonian microfluidic device for cell washing [31].	64
Figure 2-33: a) schematic illustration of the device used for measuring the cell deformation. b) focusing results for newtonian and viscoelastic solutions, showing the enhanced particle focusing in viscoelastic solution, which increases the sensitivity of the measurements [28].	65
Figure 2-34: microchannel used for the elasto-inertial mixing experiments [101].	65
Figure 3-1: focusing positions in a straight square channel for PEO solution with molecular weight of $M_w=2\text{MD}$ at different concentrations.	69
Figure 3-2: equilibrium positions for 13 μm particles in a straight square channel which shows that the tightest focusing band for PEO solution with $M_w=2\text{MDa}$ occurs at 1500 ppm.	70
Figure 3-3: equilibrium position for 13 μm particles in a straight square channel which shows the tightest focusing band occurs at 1500 ppm for PEO ($M_w=2\text{MDa}$) solution.	71
Figure 3-4: inspection results for the aluminum mold. It shows approximately 6% errors in dimensions.	72
Figure 4-1: a) different equilibrium positions and their corresponding forces for newtonian and viscoelastic solutions in a straight rectangular channel. b) schematic of the particle modeled in a portion of a rectangular channel for dns. c) mesh configuration for the portion of the channel with a length of 20a, and boundary mesh on the surface of the particle.	81
Figure 4-2: schematic of the channels with corresponding dimensions and cross-sectional optical micrograph of the pdms microfluidic chips.	85

Figure 4-3: the mechanism of elasto-inertial focusing in the square channel.	87
Figure 4-4: a) contour of first normal stress difference (N1) and pressure in the cross-section of the channel and over the particle, respectively, for flow rate of 25 $\mu\text{l}/\text{min}$. b) streamlines around the particle in x-z symmetry plane. c) distribution of inertial stress on the surface of the particle. d) distribution of total elastic stress tensor.	89
Figure 4-5: particle trajectories of newtonian a) and viscoelastic fluid b) in various cross-sections of the straight channel. The black dash lines in the newtonian fluid are minimum lift force line and in the viscoelastic fluid are the minimum shear line.	90
Figure 4-6: elasto-inertial focusing in rectangular channel.	91
Figure 4-7: a) top views of the particle trajectories in trapezoidal, square and rectangular channels. The transition from one to two focusing bands occurs at a higher flow rate in square channel under the same conditions. b) first normal stress difference contours in the corresponding channels. c) effects of corner angle on normalized gradient of n_1 as an indicator of elastic force. Corners a and b have angles of 50° and 90° respectively. A circular channel is assumed to have the corner angle of 180° . d) direction of elastic force in the first quarter of square cross-section. The direction of elastic force in the blue region is always towards the center while in the orange region is in the opposite direction.	93
Figure 4-8: focusing positions in square, rectangular and complex channels.	96
Figure 5-1: microchannel fabrication process by the wax printing approach.	106
Figure 5-2: a) top view images of the pdms devices used for particle sorting. b) characterization of the wax printed channels using a profilometer device. It shows the printed channels from different angles, and surface roughness ($1.75 \mu\text{m}$). c) cross-sectional optical micrograph of the pdms microfluidic chips.	110
Figure 5-3: velocity and helicity contours for circular, rectangular and triangular single curved channels for the flow rate of 1.1 ml/min.	112
Figure 5-4: focusing of $50 \mu\text{m}$ particles through circular, rectangular, and triangular curved channels under different flow rates at $\theta = 180^\circ$	115
Figure 5-5: focusing of $50 \mu\text{m}$ particles within straight trapezoidal and complex channels under different flow rates.	117
Figure 5-6: microcarrier separation from stem cell suspensions.	119
Figure 6-1: schematic illustration of the proposed workflow for fabrication of inertial microfluidic devices.	134
Figure 6-2: analyzing the Saffman-Taylor finger criteria for the bonding test in a microchannel versus the applied pressure.	136
Figure 6-3: a) surface topography of the double adhesive tape. Results show that the tape has homogenous roughness which does not impose any interference on the channel performance. The amount of absorbance of b) double adhesive tape and c) PMMA sheet. Results show that these two materials are transparent for visible spectra range.	137

Figure 6-4: inertial focusing in a rectangular and triangular straight microchannel.	139
Figure 6-5: illustration of a spiral microchannel with triangular cross-section where the fluid direction is from outside to inside.	142
Figure 6-6: focusing of the 7, 15 and 20 μm particles within a sheath flow trapezoidal spiral channel for PBMC separation.....	143
Figure 6-7: inertial microfluidics in a curvilinear microchannel.....	144
Figure 6-8: inertial microfluidics in a serpentine microchannel. The number of lateral positions depends on the flow rate apply at the entrance of the channel.	145
Figure 6-9: inertial focusing in a contraction-expansion arrays microchannel.	147
Figure 6-10: characterization of DU145 cells after passing the channel.....	148
Figure 7-1: geometrical parameters of the proposed plasma extraction device	157
Figure 7-2: a) grid study with different mesh element b) mesh distribution in the different regions of the microchannel	164
Figure 7-3: hydrodynamic parameters throughout the channel.....	165
Figure 7-4: the schematic illustration of pe of nth bifurcation.	167
Figure 7-5: the PE of each daughter channel as well as the ratio of plasma of each bifurcation to the inlet flow rate	168
Figure 7-6: particle trajectory along the microchannel in a) previous designed device b) new conceptual design.	169
Figure 7-7: the comparison of pe of each bifurcation and the comparison of overall PE and SE between the previous geometry and the new conceptual design.	170
Figure 7-8: fluorescent and bright-field images, showing the effect of channel design on the particle trajectories.	171

List of Tables

Table 1: authors' contribution	v
Table 2: studies performed on the elasto-inertial microfluidics within sheath-less microchannels.....	44
Table 3: studies performed on the sheath flow elasto-inertial microfluidic systems.	53
Table 4: boundary conditions of the system	83
Table 5: parameters that used for non-newtonian model.....	162

1

Chapter One: Introduction

1.1 What is Microfluidic

Microfluidics refers to the engineering and precise control of flows that are spatially confined to the channels with microscale dimensions. It is a multidisciplinary field between chemistry, physics, engineering, nanotechnology, biochemistry, and biotechnology with a myriad of practical and industrial applications [1]. Microfluidic studies commenced from the 1980s and have been employed in the development of DNA chips, inkjet printheads, micro-propulsion, lab-on-a-chip technology, and micro-thermal technologies [2-5]. This outstanding technology has many superior advantages over conventional macro-scale techniques (e.g., centrifuge) such as fast sample processing, low cost, reduced sample volumes, improved portability, high sensitivity and the potential to be highly automated and integrated to decrease human errors [6]. In microfluidic systems, accurate control and manipulation of flow and particles are essential for most of the applications such as bio-particle/cell focusing, washing, fractionation, and separation. For instance, precise focusing and isolation of microparticles allow single-cell detection, which is vital for flow cytometry [7]. Also, separation of bioparticles based on their features such as shape, size, deformability, and density makes these systems a suitable option for many applications such as preparation of biological sample, isolation, enrichment and purification of targeted cells [8-10].

1.2 Types of Microfluidic Devices

Microfluidic systems can be classified in different ways according to the source of exerted force, property of the working fluid and type of inlet. According to the source of applied force, this fascinating technology can be primarily grouped as passive and active [11]. In active devices such as magnetophoresis (MP) [12], dielectrophoresis (DEP) [13], acoustophoresis (AP) [14], particle sorting depends on external force fields, while in passive devices such as inertial microfluidics and deterministic lateral displacement (DLD), particle manipulation relies completely on the channel shape and intrinsic hydrodynamic forces [15, 16]. While controlling the particles in active devices is highly accurate, lower flow rates in these systems hinder their

use for high-throughput applications. This stems from the fact that the external force field needs a relatively long time to overcome the hydrodynamic drag force for efficient particle sorting [11]. On the other hand, passive microfluidic devices are simple, easy-to-run, and work at higher flow rates. Generally, inertial systems work at intermediate flow rates ($1 \sim < Re < \sim 100$), where both viscosity of the fluid and inertia are finite [17]. Fluid inertia triggers several fascinating inertial effects, forming the basis of inertial microfluidics, including secondary flow and inertial migration. Secondary flows or Dean vortices are two counter-rotating flows formed in curved channels due to the pressure gradient and centrifugal forces. Dean flows have proven to be beneficial for particle sorting applications and mixing phenomenon in microchannels [17].

Inertial migration is an intriguing phenomenon in which suspended particles in an internal flow gradually migrate towards some specific positions, which was discovered around 60 years ago [18]. After this observation, many experimental and theoretical investigations have been performed to explore the fundamentals of particle migration. However, this phenomenon remained impractical until the advent of advanced microfabrication technologies, which enables investigators to construct channels with dimensions comparable to those of microparticles. The lateral migration of particles in Newtonian fluids are mainly recognized by the two opposing inertial forces: 1) the wall induced lift force originated by the flow field between wall and its adjacent particles, which drives the particles toward the channel centerline, and 2) shear gradient lift force, as a result of flow velocity profile curvature and its interaction with particles, causing particles to move towards the walls [19].

According to the property and elasticity of the working fluid, inertial microfluidic systems can also be categorized into inertial and elasto-inertial systems [20]. Conventionally, all inertial systems worked with Newtonian fluids, and particle sorting happened only due to the Dean and inertial forces. However, since inertial systems are unable to sort microparticles smaller than three μm effectively, elasto-inertial systems were introduced and became suddenly widespread due to their enhanced capabilities in controlling submicron particles [21]. Inertial and elasto-

inertial systems can also be categorized to sheath or sheathless flow systems if the channel has multiple inlets with different fluids or just a single inlet, respectively. Recently, sheath flow systems have attracted significant interest due to its higher capability for submicron particle separation than sheathless systems [21].

1.3 Motivation

Elasto-inertial microfluidic systems have recently demonstrated great promise for particle sorting and have been widely used for a myriad of biological and biomedical applications. So far, there have been many efforts to increase the efficiency of these systems by altering the channel geometry, solution property, and flow rate. However, these efforts were mainly limited to the simple geometries (i.e., square and rectangular) and structures due to the complexity of the microfabrication, especially for non-conventional channels [22]. Based on our best knowledge, there is no study about the elasto-inertial particle migration in triangular or circular curved channels. In terms of sheath flow systems, all the previous studies focused on the straight channels; thereby, sheath flow elasto-inertial in spiral channels need to be carefully studied.

In addition, there are only a few numerical investigations on the fundamentals of elasto-inertial focusing in simple straight channels [23, 24]. This originates by the fact that simulation of elasto-inertial systems is extremely complicated due to the non-Newtonian property of the fluid and presence of extra elastic force. Therefore, in this research, we aim to study the fundamentals of elasto-inertial microfluidic systems in more complex channels both numerically and experimentally to shed a better light on the physics of particle migration in non-rectangular channels and increase the efficiency of currently available devices by optimizing the cross-sectional geometry.

1.4 Objectives

The objective of this research is to study the fundamentals and applications of elasto-inertial microfluidic systems in non-conventional microchannels to explore new physics and improve the efficiency of the particle sorting. Once channels and solutions are characterized by

fluorescent particles, they are tested with biological samples to showcase their accuracy for practical purposes. To this end, the following steps were planned:

- Designing different straight and curved channels based on the criteria for particle focusing.
- Fabricating these channels with new 3D printing methods, as most conventional techniques are unable to construct them.
- Tailoring the wax 3D printing and DLP 3D printing techniques for fabrication of channels suitable for inertial microfluidic applications.
- Characterizing the PEO solution (concentration and molecular weight) to achieve the tightest particle/cell focusing.
- Simulating the particle-flow interactions using direct numerical simulation (DNS) method to study the fundamentals of particle focusing in straight channels.
- Testing particle focusing in rectangular, square, trapezoidal, and complex straight channels to study the effects of geometry, flow rate, and blockage ratio on the elasto-inertial focusing.
- Testing particle/cell focusing and separation within the wax printed microchannels (i.e., rectangular, circular and triangular), to showcase the ability of wax printing method for fabrication of functionalized microchannels and to study the fundamentals of focusing in non-conventional curved channels.
- Testing particle focusing inside hard channels fabricated by DLP 3D printer to showcase the ability of direct printing for channel fabrication suitable for inertial microfluidic applications.
- Extracting plasma from blood using Zweifach-Fung effect and non-Newtonian property of the blood, by introducing new conceptual design to increase the separation efficiency.

1.5 Research Contributions

The main contribution of this work is explaining the fundamentals of elasto-inertial microfluidics in non-conventional channels as well as introducing new workflows for the

fabrication of these channels with wax and DLP 3D printers. Also, various bioparticles were separated and focused with these devices which can be further used for different biological applications. Besides, we proposed a new design for plasma extraction with high purity and efficiency.

The major contributions of this research can be summarised as follows:

1. Explaining the fundamentals of elasto-inertial focusing in straight channels, and proposing a two-stage focusing phenomenon in these systems.
2. Presenting a novel workflow to easily fabricate non-conventional microchannels suitable for inertial applications using wax 3D printing method.
3. Proposing a new workflow for easy fabrication of complex microchannels suitable for inertial applications using DLP 3D printer.
4. Exploring new physics in triangular and circular curved channels for both Newtonian and viscoelastic fluids.
5. Studying the basics of elasto-inertial microfluidics in spiral channels and separating microcarriers from Mesenchymal stem cells for cell therapy applications.
6. Blood-plasma separation via a novel straight channel with side branch using the combined effect of Zweifach-Fung and non-Newtonian property of the blood.

1.6 Thesis Outline

This dissertation is divided into eight chapters, as follows:

Chapter 1

This chapter is an introduction to microfluidic systems, their applications, and types of microfluidic devices. It gives brief information about inertial and elasto-inertial microfluidics. It also includes the objectives, motivations, and the outline of this thesis.

Chapter 2

This chapter provides a literature overview on the previous elasto-inertial microfluidic systems, physics of particle migration in non-Newtonian fluids, direct numerical simulation method, and available microfabrication methods for constructing inertial microfluidic channels.

Chapter 3

In this chapter, the methodology of sample preparation, channel fabrication, and solution preparation is comprehensively explained. To achieve accurate results in inertial microfluidics, the mentioned criteria should be carefully selected. Here, we thoroughly explained how each item is prepared and optimized before the experiments.

Chapter 4

In this chapter, particle migration in straight channels is experimentally and numerically observed to understand the combined effects of elasticity, geometry, flow rate, particle size, and inertia on the focusing positions. A new complex design then proposed, which improves the focusing of the smaller particles. Finally, Yeast cells are focused at the channel center, for flow cytometry application, to showcase the capability of the proposed design for high-throughput focusing applications.

Chapter 5

This chapter introduces wax 3D printing for the fabrication of microchannel molds, suitable for inertial microfluidic applications. For the first time, we tailored this technology to fabricate straight and curved microchannels of arbitrary shapes to study the physics of particle migration in non-conventional elasto-inertial microfluidic systems. Also, microcarriers (MCs) are separated from human mesenchymal stem cells (hMSCs) using a new complex channel to showcase the viability of the wax-printed channels for biological applications.

Chapter 6

In this chapter, DLP 3D printing technology for the first time is used to fabricate non-conventional hard chips for inertial microfluidic applications. Several channels with different geometries were readily fabricated and tested to evaluate the credibility of this method for inertial microfluidic applications. Finally, stem cells are focused in a 3D-printed serpentine channel to assess the toxicity of the resin material on cell viability, which is proven to be negligible.

Chapter 7

In this chapter, a novel microfluidic device for extraction of plasma by considering the non-Newtonian characteristics of human blood and Zweifach-Fung effect are presented. We optimized the designs numerically to achieve the highest purity and separation efficiencies. The modified design was experimentally tested with non-Newtonian PEO solution (plasma) and seven μm particles (mimicking RBCs) to evaluate the validity of the numerical results and ability of the device for blood-plasma separation.

Chapter 8

This chapter provides a general conclusion and prospects of this research work in the future.

2

Chapter Two: Literature Review

2.1 Introduction

Microfluidics refers to the flows that are spatially restricted to the channels with micrometer dimensions and has been broadly used for various biomedical applications during the last decades. Within these applications, sorting and separation of the mixture of suspended cell/particles warrant significant attention due to their huge impact on the development of therapeutic and diagnostic tools. According to the source of applied forces on the particles, microfluidic systems can be classified into the passive and active groups [11]. While in active systems particle sorting happens due to the presence of external forces like acoustic, magnetic, and electric, in passive systems particles are aligned only by the interactions between particles and their surrounding flow. Among all the passive methods for particle sorting, inertial microfluidics has proved to have the highest throughput and efficiency. According to the property of the used solution (*i.e.*, Newtonian or non-Newtonian), inertial systems can be further divided into pure inertial or elasto-inertial systems [22]. In elasto-inertial systems, extra elastic forces arising from solution viscoelasticity enhance the particle sorting even at low flow rates. Investigation of elasto-inertial systems is of great importance since inertial systems have failed to function effectively for small-size particle sorting, and many of the ubiquitous fluids in real-world issues are non-Newtonian (*i.e.*, blood, saliva, and many other body fluids) [20].

The extra viscoelasticity-induced particle displacement initiates many intriguing applications for submicron particles in microfluidic systems including bioparticles separation, cell/bacteria separation [25], particle solution exchange [26], cell washing [27], and cell deformability measurements [28]. DNA and exosomes are valuable biological particles and carry vital information which can be used for early detection of various illnesses and many therapeutic applications. Although it is almost impossible to sort these nanoscale bioparticles in Newtonian systems, researchers have been able to focus and separate them using non-Newtonian systems [29, 30]. Non-Newtonian fluids also allow isolation of bacteria and viruses from blood which is essential for early treatment of bloodstream infections (BSI) [25]. Due to

the limitation of Newtonian systems in controlling of small-size particles, conventional inertial systems were unable to sort these microorganisms effectively. Apart from separation, non-Newtonian microfluidic systems can be used for measuring the cell deformability. Cell deformation can be an indicator of different diseases such as malaria, cancer, diabetes. Recently, Cha et al. [28] measured the cell deformability using viscoelasticity-induced particle focusing, which showed a higher detection efficiency compared to its Newtonian counterpart. Cell washing and particle solution exchange have many applications in biomedical researches to wash previously labeled and conjugated cells and separate them from their media [26, 27]. Using a non-Newtonian sheath flow system, Yuan et al. [31] managed to wash and separate Jurkat cells from its culture medium.

Viscoelastic fluids are either real biological samples such as blood, plasma, HA (hyaluronic acid)) and DNA solutions or chemical solutions like PVP (poly (vinyl pyrrolidone)), PAA (polyacrylamide), PEO (poly (ethylene oxide)), and PAM (polyacrylamide) solutions. Between these viscoelastic solutions, PVP, PEO, and PAA are the most common ones in microfluidic researches due to their biocompatibility and cost-effectiveness. Among these three chemical solutions, PVP polymer has relatively the lowest molecular weight (e.g., 0.36 MDa), and its solution has a shear-rate independent viscosity, which can be considered as a Boger fluid [32]. PEO polymer possesses a moderate molecular weight ranging from 1 to 4 MDa, whose solution demonstrates a mild shear-thinning behavior especially for larger molecular weights and concentrated solutions (*e.g.*, PEO solution with $M_w=2$ MDa and concentration above 3000 ppm, or PEO solution with $M_w=4$ MDa). PAA is the heaviest polymer (e.g., 18 MDa) whose solution possesses the strongest shear-thinning property and viscoelasticity even at very low concentrations.

The phenomenon of inertial-induced migration of suspended particles in Newtonian fluids has become a hot topic since the classical observations by Segré & Silberberg [18], which showed that initially dispersed particles in a tube gradually focus into an annulus centered at a

position around 0.6 of the tube radius from the tube center-line. Following this observation, several experimental and theoretical studies have been reported by considering different particle properties and bulk flow configurations to explain the underlying mechanisms involved in this phenomenon [33-38]. This phenomenon was later confirmed in different numerical [39, 40] and analytical studies [41, 42]. It has been proven that the cross-stream migration of particles in these channels originates by two opposing shear gradient and wall induced lift forces, and the focusing positions are where these forces balance each other [43-46].

The particle lateral displacement in non-Newtonian fluids was first investigated by Mason and co-workers in 1966 [47]. They showed that the direction and magnitude of inertia-less migration strongly depend on the rheological properties of the suspending solution. In fully viscoelastic fluids, rigid spherical particles migrate in the direction of minimum shear rate, which is towards the outer cylinder wall and center-line for couette and poiseuille flows, respectively. Following that, similar studies have been performed on particle movements within viscoelastic laminar flow confined to two moving parallel plates (couette flow) [48, 49]. In 1996, Tehrani [50] showed that in a viscoelastic Boger fluid, particles shift to the channel centerline and outer wall in the case of poiseuille and couette flows. Later on, Ho and Leal [38] theoretically studied the focusing phenomenon in a second-order fluid and showed that particles migrate towards the lowest-shear region due to the normal stress differences. This behavior was further verified by other simulations and experiments where neutrally suspended particles migrate to the centerline and corners of rectangular channels [51] and the centerline of a circular pipe [52]. Using direct numerical simulation (DNS) method, Huang et al. [53, 54] investigated the effects of elasticity, inertia, blockage ratio and shear-thinning on the focusing positions of solid particles flowing in a Poiseuille and Couette flows of a viscoelastic solution. Results showed that in shear-thinning viscoelastic fluids, while elasticity pushes the particles towards the channel center, shear-thinning effect causes particles to move away from the centerline. All

the early efforts on focusing mechanisms in non-Newtonian solutions were conducted at low flow rates ($Re \rightarrow 0$) where inertial effects can be considered negligible.

Further studies for viscoelastic flows at moderate to high Re numbers showed that even weak inertial effects can significantly alter the particles' equilibrium positions [55, 56]. Lim et al. [57] interestingly found that particles can be aligned at the centerline of the channel in a weak viscoelastic flow at very high flow rates ($Re \sim 2000$). Besides, at moderate flow rates where inertial forces are comparable to elastic forces (elasto-inertial systems), by tuning the solution property and flow rate several intriguing focusing phenomena can be observed. Xiang et al. [58] reported one, two, and three different focusing positions by controlling the combined effects of elasticity and inertia in a straight channel.

Recently, due to the noticeable progress of microfabrication technologies, investigators started to study elasto-inertial systems in more complex structures such as spiral, serpentine, and expansion-contraction to not only enhance the efficiency of the conventional microfluidic systems but also explore new physics in more complex structures. For example, Yuan et al. [59] focused Jurkat cells at a flow rate of $10 \mu\text{l}/\text{min}$, benefitting from synergetic effects of Dean drags and elasto-inertial forces in a serpentine channel. More recently, Raoufi et al. investigated the fundamentals of elasto-inertial focusing and introduced a new geometry which showed a tighter focusing-band over the traditional rectangular and square channels [60].

Due to the variety of elasto-inertial systems and complexity of particle migration in these systems, it is vital to investigate the mechanisms of focusing in each one fundamentally. Therefore, In the following sections, first, the physics of particle migration in elasto-inertial systems is explained. Following this step, direct numerical simulation (DNS) method is described as a powerful approach to model the particle fluid interactions in elasto-inertial microfluidic systems. Then, all these systems are explained and classified based on the channel design to realize how geometry and flow condition affect the focusing phenomenon. Finally, different methods of microchannel fabrication suitable for inertial microfluidic applications are

introduced, and their advantages and disadvantages are explained. This is of great importance, as most conventional fabrication methods are limited to the planar geometries and finding new approaches for easy fabrication of non-planar structures is a crucial need. Figure 2-1 demonstrates different channels with their cross-sections used in elasto-inertial microfluidic systems. As can be seen, sheath flow in spiral and serpentine channels has never been studied. In addition, all the non-rectangular geometries only employed in straight channels, and their effect on particle migration in curved channels have remained unexplored.

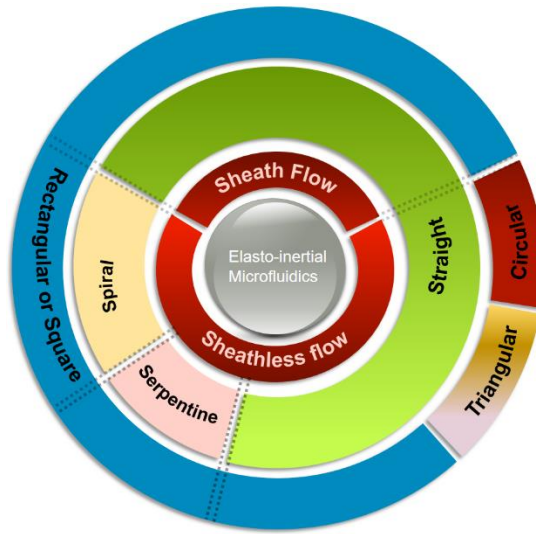


Figure 2-1. Classification of elasto-inertial microfluidic systems based on design and geometry

2.2 Physics of particle migration in viscoelastic flows

In passive non-Newtonian microfluidic systems, several forces interact with particles; each is dominant in a specific condition. These forces act at different directions and particles' final equilibrium positions are where these forces balance each other. Therefore, understanding of these forces is extremely important for proper designing and accurate functioning of microfluidic systems. In this section, we will systematically explain each force and the conditions in which they should take into account.

2.2.1 Elastic lift force

As mentioned earlier, viscosity of the fluid in Newtonian or viscous fluids is constant while it alters with shear gradient in non-Newtonian and viscoelastic solutions. Viscous fluids strain

linearly under shear forces, whereas viscoelastic solutions display time-dependent strain in response to shear stresses. In non-Newtonian solutions, the elastic force (F_E), originated by the asymmetric normal stress differences on the particles' surface, directs particles towards the lowest shear stress regions [54]. Generally, higher viscosity of the viscoelastic solutions compared to the Newtonian solutions and the presence of additional elastic force causing particles to align more effectively in non-Newtonian fluids. In these fluids the first normal stress difference ($N_1 = \tau_{11} - \tau_{22}$) causes a cross-stream migration, while the second normal stress difference ($N_2 = \tau_{22} - \tau_{33}$) tends to create secondary flows perpendicular to the main flow [61, 62], where τ_{11} , τ_{22} and τ_{33} are in the flow, velocity gradient and vorticity directions, respectively. The elastic force in dilute polymer solutions and Boger fluids can be calculated by the Oldroyd-B constitutive equation as the magnitude of N_2 is negligible compared to N_1 [61, 63]. Bird et al. [61] have measured the shear stress and N_1 for the Oldroyd-B solution as follows:

$$\tau = \tau_{21} = -\eta\dot{\gamma} \quad (2-1)$$

$$N_1 = \tau_{11} - \tau_{22} = -2\eta\lambda_d\dot{\gamma}^2 \quad (2-2)$$

where $\tau = \tau_s + \tau_p$ is the sum of solvent and polymer stress tensors, and $\eta = \eta_s + \eta_p$ is the sum of solvent and polymer viscosities. The terms λ_d and $\dot{\gamma}$ are dumbbell relaxation time and rate of the strain tensor, respectively. The lateral elastic lift force (F_E) in an Oldroyd-B solution, where N_2 values are much smaller than that of N_1 , is proportional to the gradient of N_1 and the size of particles (d) which is described as below:

$$F_E = C_l d^3 \nabla N_1 = -2C_l d^3 \eta \lambda_d \nabla \dot{\gamma}^2 \quad (2-3)$$

where C_l is a non-dimensional lift coefficient. As mentioned earlier, F_E pushes particles towards the lowest shear rate areas which are center and corners in a square channel (Figure 2-2 aIII). Typically, in elasto-inertial systems, instead of calculating the elastic force (F_E), non-dimensional Weissenberge number (Wi) is measured as an indicator of elasticity as follows:

$$Wi = \lambda_d \dot{\gamma} = \lambda_d \frac{2V}{D_h} \quad (2-4)$$

with V being the mean velocity and D_h the channel hydraulic diameter. In addition to the Wi number, elasticity number (El) compares the role of elastic and inertial forces on particle migration and can be measured by dividing the elastic force to inertial force:

$$El = \frac{Wi}{Re} = \frac{2\eta\lambda_d}{\rho D_h^2} \quad (2-5)$$

where $Re = \rho V D_h / \eta$ shows the inertial force. Previous studies demonstrated that in an inertia-less viscoelastic flow in a square channel, a closed separatrix exists which determines the final focusing positions. Particles located inside the separatrix focus at the channel center and those outside this region migrate towards the four corners [62].

2.2.2 Inertial lift force

Inertial lift forces arise in all microchannels when the blockage ratio (a/D_H) and Re number of the channel are higher than ~ 0.06 and ~ 1 , respectively. Among all the inertial lift forces act on a neutrally buoyant particle, the two opposing shear gradient (F_s) and wall induced (F_w) lift forces have been proven to be the most effective ones. The shear gradient force, which originates from the flow velocity profile curvature, directs particles away from the channel center (Figure 2-2 aII). It has zero value at the channel center, and the highest values close to the wall since the slope of velocity profile is zero at center and maximum next to the walls. The wall-induced force, caused by the local increase in pressure between the particles and its adjacent wall, pushes the particles towards the channel center (Figure 2-2 aII). This force declines by increasing the distance from the wall and vanishes around the channel center. While previous analytical studies [64, 65] using matched asymptotic expansions concluded the net inertial force ($F_w + F_s$) on a particle scales as $F_L = f_L \rho U_m^2 a^4 / H^2$, Di Carlo et al. [66] proved that the net inertial lift force near the center and wall of a confined straight rectangular channel is $F_{LS} = f_L \rho U_m^2 a^3 / H$ and $F_{LW} = f_L \rho U_m^2 a^6 / H^4$, respectively, where f_L is a non-dimensional lift coefficient, ρ is the fluid density, U_m is the mean velocity, and a is the diameter of the

particle. Inertial forces strengthen by reducing the channel size as well as increasing the flow velocity and particle diameter.

Compared to the sheath-less elasto-inertial microfluidic systems, co-flow systems have proven to possess higher efficiency and purity in the separation of submicron/Nano particles (Figure 2-2 b). In these systems, particle migration at the fluids' interface can be controlled by tuning the viscoelastic solution properties, and the velocity difference between the sample and sheath flows. In elasto-inertial sheath flows, particles laterally migrate from the sample fluid to the sheath flow due to the combined effects of inertial and elastic forces. It should be noted that elastic and inertial forces oppose each other at the fluids interface (Figure 2-2 bI). Therefore, optimizing the concentration of non-Newtonian fluid is extremely important, as high or low concentration might prevent larger particles to migrate to the sheath flow and trap them at the interface, or let all the particles penetrate to the sheath flow, respectively.

2.2.3 Drag Force

Drag force is induced by the velocity difference between particles and their surrounding flows which can be categorized into cross-stream and main-stream drag forces. The main-stream drag force causes particles to move along the channel with the main flow and can be calculated for a spherical particle as below [11]:

$$F_D = S \times f_{Drag} = \pi a^2 f_{Drag} / 4 \quad (2-6)$$

with S , f_{Drag} and a being the cross-sectional area of the particle, viscous drag coefficient, and particle diameter, respectively. Generally, viscous drag coefficient is determined by the particle Reynolds number ($Re_p = \rho v_t a / \mu$, v_t is the relative velocity of the fluid to particle). Based on the range of the particle Reynolds number, f_{Drag} can be divided into three regimes. For the case of $10^{-4} < Re_p < 0.2$ viscous drag coefficient can be expressed by the following equation:

$$f_{Drag} = 12 \mu_f (v_f - v_p) / a \quad (2-7)$$

which leads to the well-known Stokes drag equation:

$$F_D = 3\pi\mu_f a(v_f - v_p) \quad (2-8)$$

Where v_p and v_f indicate the velocities of particles and the flow around them. For the case of $0.2 < Re_p < \sim 1000$, f_{drag} can be calculated by:

$$f_{\text{Drag}} = \frac{12\mu_f(v_f - v_p)}{a} (1 + 0.15Re_p^{0.687}) \quad (2-9)$$

And for the condition of $1000 < Re_p < 2 \times 10^5$:

$$f_{\text{Drag}} = 0.22\rho_f v_t^2 \quad (2-10)$$

The cross-stream drag, originated by the secondary flows (Dean flows), can be induced by either the second normal stress difference of a viscoelastic fluid or the curvature of flow streamlines due to the channel's nonlinearity (Figure 2-2 cI). The former situation happens in strong viscoelastic fluids (e.g., highly concentrated PEO or PAA solution) where rotational secondary flows form even in straight channels, while the lateral case occurs in channels with curved boundaries (e.g., spiral or serpentine) and straight channels with side wells. The strength of these Dean flows is generally characterized by the Dean number as below:

$$Dn = Re \sqrt{D_h/2R} \quad (2-11)$$

with R being the channel curvature radius. In both conditions, the generated Dean flow is weaker than the main flow. The Dean drag can be estimated by the following equation [67]:

$$F_D = C_D \frac{\rho U_m^2 a D_h^2}{R} \quad (2-12)$$

with C_D being the non-dimensional Dean drag coefficient.

2.2.4 Shear-thinning effect

In elasto-inertial microfluidic systems, most of the solutions have either constant or shear-thinning viscosities. These properties significantly affect the focusing phenomenon as particles in the constant-viscosity regions tend to focus at the centerline of a square channel while

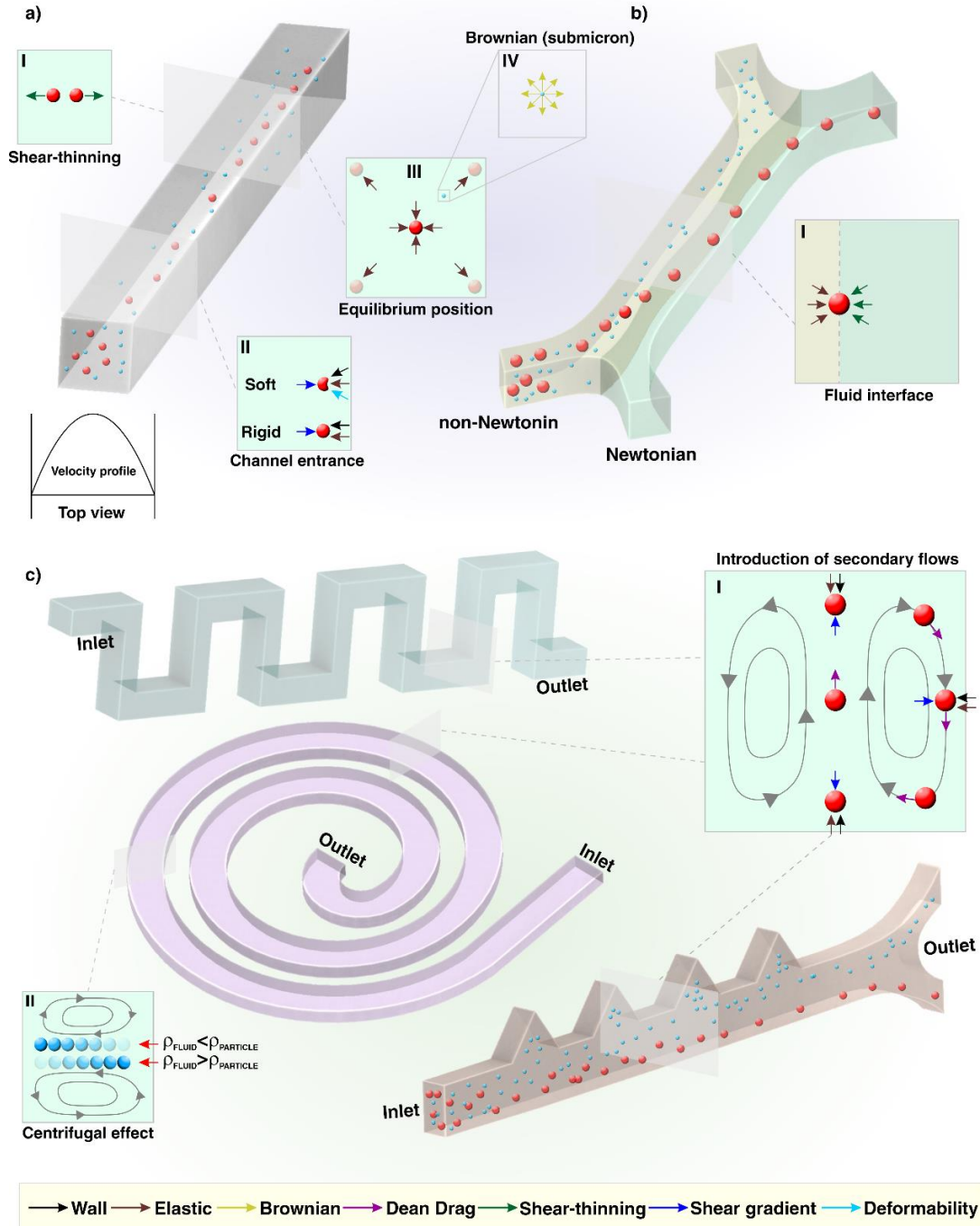


Figure 2-2: Schematic illustration of different forces particles undergo in elasto-inertial microfluidic systems. a) Focusing mechanisms in straight channels, I) Effect of shear-thinning forcing the particles towards the walls, II) Inertial, elastic and deformability force directions close to the walls, III) Focusing position in a viscoelastic solution and direction of elastic force applied on the particle, IV) Brownian motion causing the submicron particles to migrate haphazardly. b) mechanisms of separation in sheath flows, I) elasto-inertial force distribution on the particle at the interface of the Newtonian and non-Newtonian fluids. c) Effect of Dean and centrifugal forces on particle migration in Non-straight channels (i.e., serpentine, spiral and straight channels with side-wells), I) Secondary flows apply an external drag force on particles perpendicular to the main flow, causing particles to trap at regions with lowest Dean forces at moderate Re number. It makes particles to rotate with Dean vortices and mix particles at high flow rates. II) Effect of centrifugal force on non-buoyant particles, in a way that directs the particles with density higher than the surrounding fluids towards the outer wall while pushing them to the inner wall when their density is lower than the fluid one.

migrating towards the corners in shear-thinning regions [68, 69]. The shear-thinning property influences particle movement in two ways, including increasing the inertial force due to the flow rate growth and decreasing the elastic force by reduction of shear viscosity. In both cases, shear-thinning effects cause particles to move towards the channel walls (Figure 2-2 aI) [70]. Numerical simulations also showed that shear-thinning has negligible effects when the elasticity or inertia is small but noticeable effects when they are large. In Poiseuille flow of neutrally buoyant particles, the curvature of velocity profile and shear-thinning effects induce large slip velocities and shear stresses which cause particles to shift towards the channel walls. This behavior intensifies with increasing shear-thinning property [53].

2.2.5 Brownian motion

Brownian motion is the arbitrary movement of suspending submicron particles in a flow due to their frequent collision with molecules or atoms of the liquid (Figure 2-2 aIV). Generally, Brownian motion is negligible for particles with microscale dimensions. However, since many of the elasto-inertial microfluidic applications are to separate and focus sub-micron particles, this phenomenon needs to be accurately controlled. Based on the Einstein–Smoluchowski theory, the mean square distance that a dispersed particle in a fluid can diffuse in time t can be expressed as:

$$r^2 = 6DT \quad (2-13)$$

with $D = KT/3\pi\mu a$ being the diffusion coefficient. T and K are the absolute temperature and the Boltzmann's constant ($1.3806488 \times 10^{-23} \text{ J K}^{-1}$). This equation shows that decreasing the fluid temperature and increasing the viscosity reduces the particle diffusion and Brownian motion. Therefore, viscoelastic solutions are a better option for focusing of the submicron particles due to their higher viscosity and extra elastic force towards the channel center compare to the frequently used Newtonian solution. However, a high level of viscosity is undesirable for particle separation as it increases the pressure drop throughout the channel and also increases the focusing positions.

2.2.6 Centrifugal force

For non-neutrally buoyant particles, the centrifugal force at the curved parts can affect particles' movement and change the focusing patterns compared to those of buoyant particles.

For the simplest condition where the pressure gradient is constant across the particles and they are traveling in a circular path the centrifugal force can be described as [71]:

$$F_{cent} = (\rho_p - \rho_f)\pi a^3 v_{pt}^2 / 6r \quad (2-14)$$

with ρ_p , ρ_f , v_{pt} , and r being the density of particles, the density of the fluid, tangential velocity of particles, and radius of particles' orbit, respectively. The direction of the centrifugal force depends on the sign of $(\rho_p - \rho_f)$ as presented in Figure 2-2 cII. As can be seen, when $\rho_p > \rho_f$ particles migrate towards the outer wall, but for the reverse case, they move to the inner wall.

2.2.7 Deformability-induced force

In microfluidic studies, rigid spherical particles are typically used to observe the focusing phenomenon, while in clinical and practical applications these particles (*i.e.* biological organisms such as microvesicles and cells) are mostly deformable. This deformability induces extra lift force on the particles perpendicular to the main flow streamline towards the channel center, which is proven to be originated by the particle shape change and nonlinearities caused by the matching of stresses and velocities at the deformed interface (Figure 2-2 aII) [19]. Deformation of a droplet can be relatively determined by three dimensionless parameters including Weber number ($We = \rho_f V^2 a / \sigma$) with σ being the surface tension, viscosity ratio ($\lambda_d = \mu_d / \mu$), and capillary number ($Ca = \mu V a / \sigma h$) where V and μ_d are the mean velocity and viscosity of the fluid inside the droplet, respectively [19]. Chan and Leal proposed an equation to calculate the deformability induced force when the droplet is not too close to the walls and $\lambda_d < 1$ or $\lambda_d > 10$ as follow [72, 73]:

$$F_{L,deformation} = \mu V a f(\lambda_d) \frac{da^3}{H^3} \quad (2-15)$$

whit d being the distance between the channel center and the droplet. This force causes the equilibrium position of deformable particles to slightly shift towards the channel center compared to the solid particles of the same size.

All the previously mentioned forces and their corresponding equations were derived based on the analytical and experimental investigations to explain the underlying mechanisms of particle migration under different conditions. However, particles flowing through a channel only experience shear forces, pressure gradient, and body forces, which are difficult to measure based on analytical studies. Therefore, numerical simulations have been widely used to address this inadequacy and to model the particles' trajectories accurately for more complex conditions. For non-Newtonian fluids, direct numerical simulation (DNS) method is the most suitable approach to model the flow-particle interactions, which is thoroughly described in the next section.

2.3 Direct Numerical Simulation

Direct numerical simulation method (DNS) is the most widely used approach to model and calculate the particles' trajectories and lift forces in elasto-inertial microfluidic systems. In this method, first, continuity and momentum equations (Eq. (2-16) and, (2-17)) are numerically solved around a particle in the desired domain by allowing the particle to have only rotational movements. To model this condition, generally, slip velocity and moving wall boundary conditions are employed for the particle's surface and the channel walls, respectively. Continuity and momentum (Navier-Stokes) equations can be described as follows:

$$\nabla \cdot \mathbf{u} = 0 \quad (2-16)$$

$$\rho \left(\frac{\partial \mathbf{u}}{\partial t} + (\mathbf{u} \cdot \nabla) \mathbf{u} \right) = -\nabla p + \eta_s \nabla^2 \mathbf{u} + \nabla \cdot \boldsymbol{\tau} \quad (2-17)$$

where η_s , p and $\boldsymbol{\tau}$ are the Newtonian viscosity of the fluid, pressure and the polymeric part of the extra stress tensor, respectively. It has been proven that for low molecular weight PEO polymers ($\leq 1\text{MDa}$) and PEO solution with 2MDa molecular weight and concentration lower

then 2500ppm, the shear-thinning effects can be considered negligible and the extra stress can be calculated by Oldroyd-B equation [23, 24].

$$\tau + \lambda \left(\frac{\delta \tau}{\delta t} + u \cdot \nabla \tau - \nabla u^T \cdot \tau - \tau \cdot \nabla u \right) = \eta_p (\nabla u + \nabla u^T) \quad (2-18)$$

where η_p and λ indicate the polymeric viscosity and relaxation time, respectively [74]. When the flow field is obtained, the particle's linear and angular acceleration can be measured using Newtown's second law (Eq. (2-19), and (2-20)).

$$m \frac{du_p}{dt} = \oint_{\partial V_p} \left[\underbrace{-PI + \eta_s (\nabla u + \nabla u^T)}_{\text{Inertial part}} + \underbrace{\tau}_{\text{Elastic part}} \right] \cdot n \, dS \quad (2-19)$$

$$I \frac{d\Omega_p}{dt} = \oint_{\partial V_p} r \times \left\{ \left[\underbrace{-PI + \eta_s (\nabla u + \nabla u^T)}_{\text{Inertial part}} + \underbrace{\tau}_{\text{Elastic part}} \right] \cdot n \right\} dS \quad (2-20)$$

Particle's boundary conditions are updated based on the measured linear and angular velocities. After the renewal of the boundary conditions, at the next step, Navier stokes equations inside the channel are again solved to update the flow field. This procedure is repeated until the solution converges to a finite pre-defined value. When flow field around particle is solved, lift forces in all directions can be calculated and the particle's trajectory will be modeled using momentum equation as follow:

$$m_p \vec{a}_p = \vec{F}_{Elasti} + \vec{F}_D + \vec{F}_{Inertial} \quad (2-21)$$

for simplicity the main flow drag force (\vec{F}_D) can be calculated using Eq. (2-7). Inertial and elastic forces are also measured by interpolating these forces across each cross-section.

Figure 2-3 demonstrates the algorithm used for measuring the lift forces applied on a specific particle positioned at (x_1, y_1, z_1) coordinate. As mentioned before, the particle is initially at rest, without any movement. Then, using these boundary conditions and a predefined inlet velocity, continuity and Navier Stokes equations (Eq. (2-16) and, (2-17)) are solved to obtain the flow field in the domain.

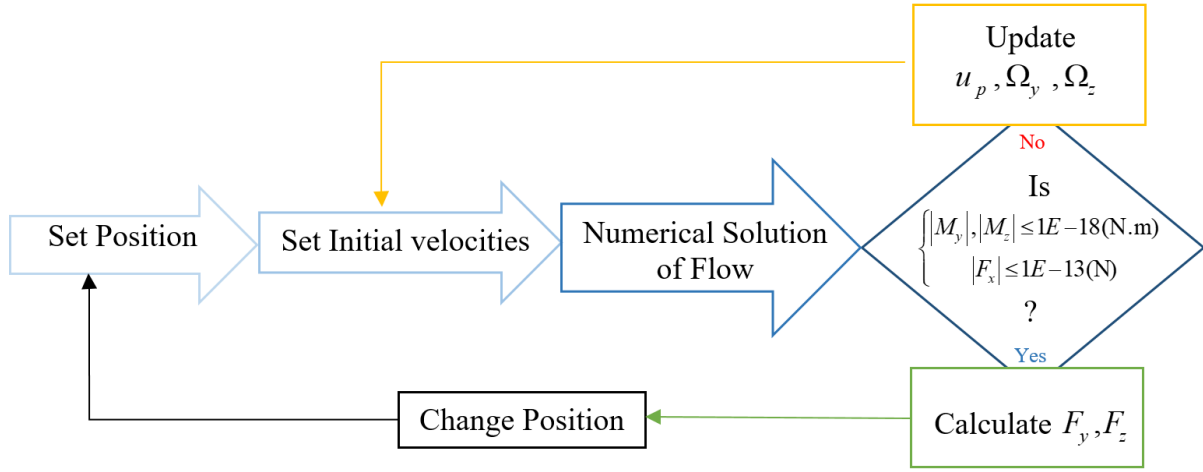


Figure 2-3: The flowchart for the calculation of inertial lift force.

Then, all drag and lift forces applied on the particle are calculated in three X, Y and Z directions. Following this, based on the Newtown's second law, particles' linear and angular accelerations are obtained by integrating the total stress on the particle's surface (Eq. (2-19), and (2-20)). At the next time step, previously obtained velocities are used to update the wall boundary conditions, and the Navier stokes equations are solved again. This algorithm terminates when the momentum values become less than the defined threshold (Figure 2-3). The surface vector plot of the elasto-inertial forces is obtained by repeating this algorithm for other points of that cross-section.

2.4 Geometrical classification of elasto-inertial systems

So far, several microchannels with different structures and cross-sections have been used to study the applications and fundamentals of elasto-inertial microfluidics. Due to the diversity of these channels and strong effects of geometry on focusing phenomenon, in this section, all these efforts are classified and explained based on their design and applications. Overall, elasto-inertial microfluidic systems can be categorized into the sheath (co-flow at the inlet) and sheathless flows based on the number and types of inlets. These channels can be further grouped as straight, spiral and serpentine based on their structure. Each of these systems has specific focusing mechanism and condition which will be described thoroughly in the following

sections. In addition, each system has its own advantage and disadvantage which is thoroughly described in its section.

2.4.1 Sheathless flow

Microfluidic systems can be grouped as sheath and sheathless flows based on the number of flow inlets. Generally, particle control and channel design are simpler in sheathless systems as the whole device works with only one fluid and one pump. However, sheath flow systems function with two or more fluids and inlets which makes the use of extra pumps and more complex designs an indispensable part of these systems. Typically, sheathless microchannels can be classified to straight, serpentine, and circular channels which are thoroughly explained in the following sections.

2.4.1.1 Straight channels

2.4.1.1.1 Simple straight

Sheathless flow in a simple straight channel (without any nonlinearity in geometry (e.g. side well, pillar)) is the most commonly used device in elasto-inertial systems to analyze the fundamentals of particle migration, and focusing phenomenon [22, 55, 68, 75]. In these systems wall induced, shear gradient and elastic lift forces are dominant and determine the particles' final equilibrium positions. As mentioned earlier, while elastic and wall induced lift forces push the particles towards the center, shear gradient lift force direct the particles towards the wall. Besides, shear-thinning effects can cause particles to migrate towards the walls and slightly changes the focusing positions.

The earliest research on elasto-inertial focusing was carried out in a simple straight channel by Yang et al. [55]. Using different concentrations of PVP and PEO solutions, they showed that one line focusing at the channel center occurs when inertia and elasticity are of the same order ($El \approx O(1 \sim 10)$) and used this condition for size-dependent separation of 6 and 2.4 μm particles. As Figure 2-4 a demonstrates for the case of Newtonian solution ($Wi=0$) and moderate flow rates, particles equilibrate at four positions due to the pure inertial forces. They also observed

that particles flowing in a 0.05 wt. % PEO solution (with elasticity behavior similar to the Newtonian solution) equilibrate at five positions around the center and corners for flow rates up to 0.16 ml/h (Figure 2-4 b), while for non-negligible inertia regime at higher flow rates and the same level of elasticity, particles focus at the centerline without applying any external force (Figure 2-4 c). This group named this phenomenon elasto-inertial focusing as it cannot happen without the synergetic effects of inertia and elasticity.

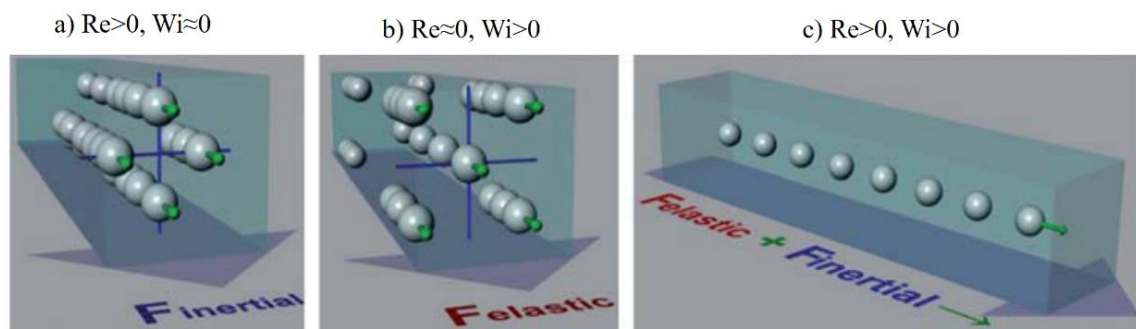


Figure 2-4: Graphical demonstration of the particles' alignments in a sheathless straight channel. a) Particles equilibrate at four positions within a square channel for Newtonian flow. b) Focusing positions for the case of negligible inertia and strong elasticity. c) one line focusing when both inertia and elasticity are of the same order. Adapted with permission from Royal Society of Chemistry [55].

They used the probability distribution function (PDF) to illustrate the strong correlation between focusing efficiency and the level of elasticity. By increasing the concentration of PEO solution, particles migrate towards the centerline more effectively. Both inertial and elastic forces intensify with the flow rate increase, which consequently narrower focusing position band. Results showed that if elasticity dominates the inertial forces, one line focusing cannot be achieved, and if the inertial forces dominate elasticity effects particles remain dispersed. In 2012, the same group [76] separated rigid particles from deformable cells in a square straight channel by synergetic effects of deformability and elasticity. Results showed that when particles are subjected to inertia-less viscoelastic flows, they tend to focus at the lowest first normal stress regions (Figure 2-5 a). Figure 2-5 b illustrates the particles' lateral migration velocity profiles in a viscoelastic flow which shows 5 focusing positions where flow vectors are approximately zero. However, focusing positions for deformable particles are closer to the channel center due to the additional deformability force towards the channel center (Figure 2-5

c and d). They found that the inertial force deteriorates the efficiency of the separation since the wall induced lift force repels the particles away from the wall regardless of their deformability. It can be concluded that in elasto-inertial systems where Re number is normally higher than 1, deformability forces can be considered negligible.

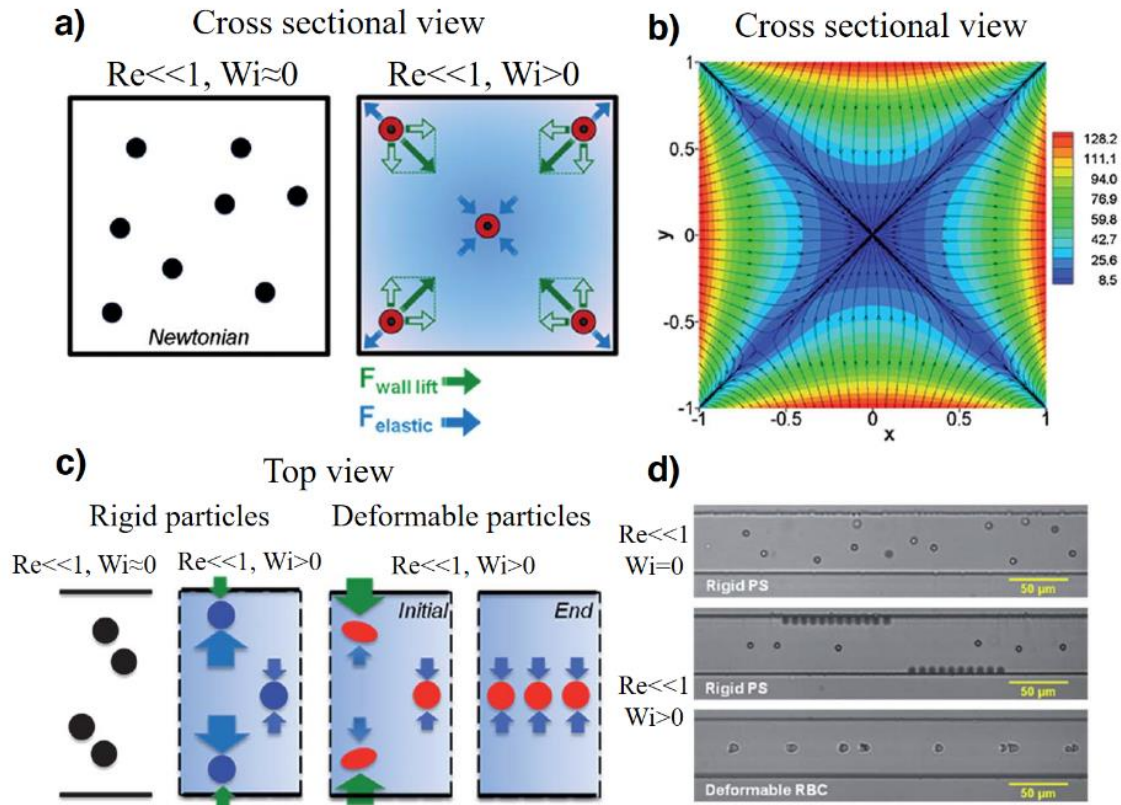


Figure 2-5: Mechanisms of focusing for deformable particles. a) A cross-sectional view of randomly dispersed particles in inertialess Newtonian fluids (left schematic), and applied forces on deformable particles in an inertialess viscoelastic flow (Right schematic). b) Lateral displacement velocity profiles for inertialess viscoelastic flow. c) Top view illustration of focusing position for rigid particles (left one) and cases of ($Re \ll 1, Wi = 0$) and ($Re \ll 1$ and $Wi > 0$), as well as soft particles for Re lower than 1 and $Wi > 0$. d) Particle and deformable RBC focusing positions. Adapted with permission from Royal Society of Chemistry [76].

Being inspired by this research, Kim et al. [29] studied the focusing of submicron particles (500, 200 and 100nm) and DNA in a diluted PEO solution (500 ppm) through a straight square and rectangular channel with 5×5 and $30 \times 10 \mu m^2$ dimensions. As mentioned earlier, focusing of the submicron particles are extremely difficult due to the diffusion phenomenon (Brownian motion). Their results showed a distinct difference in focusing positions between the flexible DNA molecules and rigid particles. While DNA molecules mainly equilibrated in a single band along the centerline, rigid particles focused at multiple equilibrium positions (Figure 2-6).

Focusing positions of rigid particles at the center and corners implies that the particle migration happens mainly due to the elasticity force. In addition, according to the Re numbers used in this study ($\sim 10^{-3}$), one line band focusing in λ -DNA and T4-DNA can be correlated to the wall-repulsive deformability force (Figure 2-6 b).

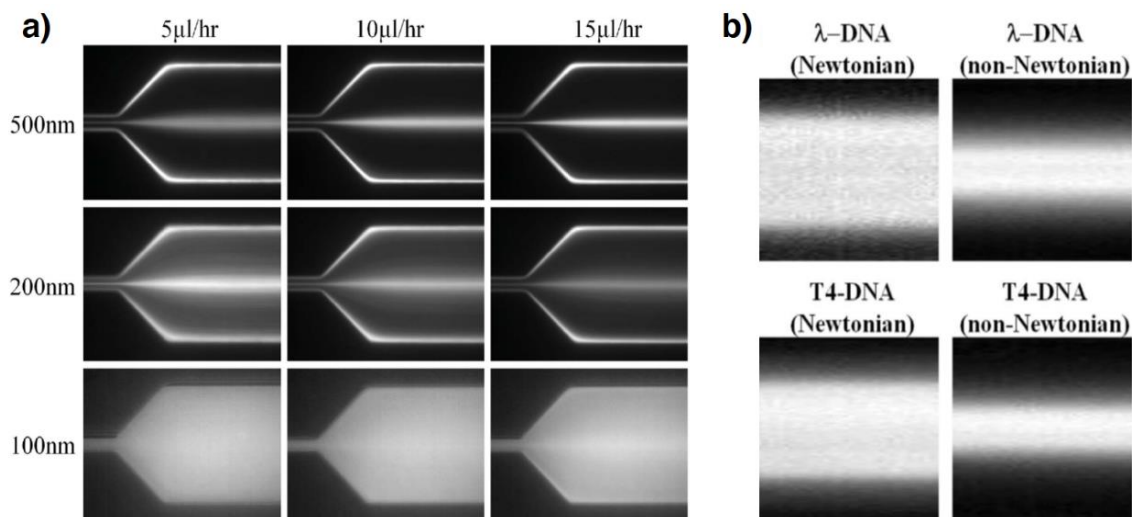


Figure 2-6: Focusing positions of beads and DNA in Newtonian and non-Newtonian solutions. a) Focusing positions of rigid particles with 100, 200 and 500 nm diameters at the channel outlets, located 4 cm downstream from the inlets. b) Focusing of the λ -DNA and T4-DNA molecules in a Newtonian and a viscoelastic medium at a pressure of 4 psig. Adapted with permission from Royal Society of Chemistry [29].

Later on, Lim et al. [57] compared the focusing of rigid spherical beads, anisotropic poly(ethylene glycol) particles and WBCs using hyaluronic acid (HA) solution at high flow rates (up to 50 ml/min). They quantified the deformation of WBCs by measuring the AR (a_x/a_z) parameter. According to Figure 2-7 a, by increasing the viscosity of the solution and increasing the molecular weight of the HA solution, the AR values increase. Distinct particle streaks at the channel center showed that elastic forces are dominant compared to the shear-thinning effects (Figure 2-7 b). Also, it was shown that while anisotropic PEG particles are almost scattered everywhere in the water, they were completely aligned at the channel center for HA solution at flow rate of 20 ml/min (Figure 2-7c). These findings have proven that particle focusing is achievable at Re numbers beyond previously observed limits by controlling the synergetic effects of elasticity and inertia.

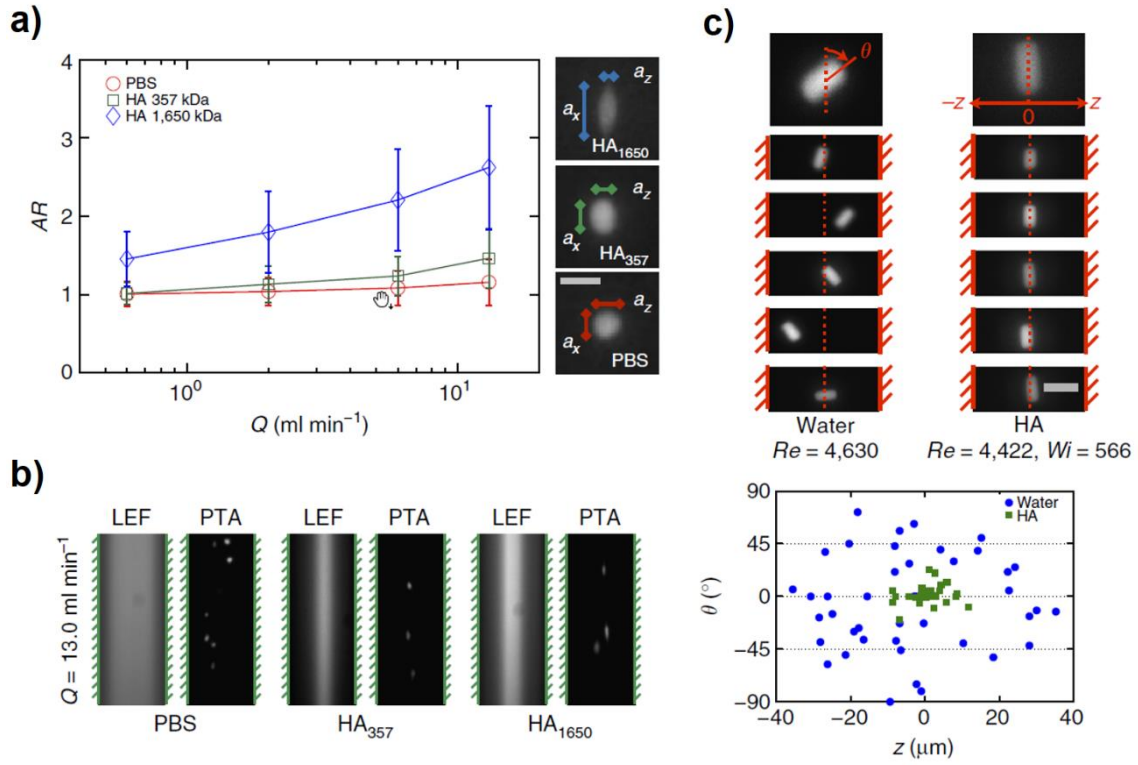


Figure 2-7: Focusing of the PEG particles and WBCs based on deformability, shape and solution elasticity. a) WBCs deformation for PBS, and HA solutions with low and high molecular weights of 0.357 and 1.65 MDa, respectively. WBCs deformation is expressed by aspect ratio ($AR = a_x/a_z$). b) Long exposure fluorescence and particle trajectory analysis (PTA) pictures of WBCs for PBS, low, and high molecular-weight HA solutions at flow rate of 13 ml min⁻¹. c) PTA pictures of anisotropic PEG particles in 1.65 MDa HA solution at flow rate of 20 ml min⁻¹. PEG particles' lateral positions and their inclination angle (θ) are depicted in the HA solution (green) and water (blue) for each particle. Adapted with permission from Springer Nature [57].

Following this research, several studies have been performed to explore the effects of solution rheology, flow rate, aspect ratio, and particle size on the focusing phenomenon in elasto-inertial systems. Seo et al. [77, 78] explored elasto-inertial focusing in straight circular and square channels for PVP and PEO solutions with molecular weights of 360 KDa and 4 MDa, respectively. As Figure 2-8 a shows, the shear-thinning behavior of the PEO and PVP solution are completely different. While viscosity of the PEO solution noticeably decreases with shear rate growth, the PVP solution viscosity remains approximately constant over the given shear rates. They showed that dispersed particles in the PEO ($M_w=4\text{MDa}$) solution can be focused more effectively at low flow rates compared to the PVP solution. However, in the PEO solution particles began scattering by increasing the flow rate (Figure 2-8 b) while remaining focused in the PVP. This stems from the fact that increasing the flow rate decreases the viscosity of PEO solution noticeably, causing the inertial force to become stronger and comparable to the elastic

force in the core region. As a result, slightly off-center particles are affected by the shear gradient force and move towards the walls, whereas ones that are exactly located on the channel center remain untouched as the shear force is zero at the channel center. Results also revealed that particles in a viscoelastic solution experience different values of elastic force according to their size, as this force strongly depends on the gradient of the first normal stress around the particle. The gradient of the first normal stress decreases when the particle size declines, which consequently decreases the applied elastic force on the particle. As a result, larger particles focused at the center more quickly and effectively compared to the smaller particles. Besides, there is a neutral surface inside the tube where elastic force direction changes. The particles initially positioned between the neutral surface and the wall move towards the tube wall, while the rest laterally migrate to the center and focus at the tube center. This neutral surface shifts towards the channel centerline by increasing the shear-thinning effects and flow rates.

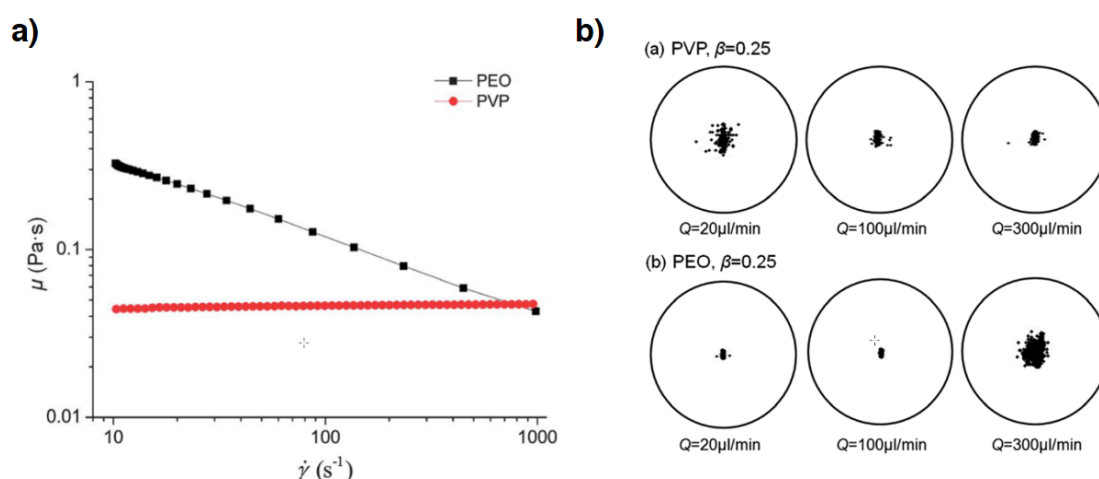


Figure 2-8: Effects of solution property on the focusing positions. a) Viscosities of the 1% wt. PEO, and 8% wt. PVP solutions versus shear rate. The PEO solution viscosity noticeably changes with shear rate and represents a strong shear-thinning behavior, while the viscosity of PVP solution remains constant. b) Focusing positions in a circular channel for PEO and PVP solutions under different flow rates. Adapted with permission from RSC Publishing [77].

Giudice et al. [69] also examined the impacts of solution rheology on focusing behaviors in a straight square microchannel by altering the level of shear-thinning and elasticity. They showed that particles migrate towards the channel center at low flow rates due to the presence of the elastic force. However, by increasing the flow rate particles migrate outwards as a result of shear-thinning. In addition, they [79] investigated the effect of shear-thinning on the cells' and

particles' lateral displacements using 0.8 wt% hyaluronic acid. Results showed that while NIH 3T3 cells move towards the channel center for all tested Deborah numbers, Jurkat cells migrate to the walls or channel centerline as a function of both the elastic capillary number (Ca_{el}) and Deborah number (De) (Figure 2-9). Capillary number ($Ca_{el} = \eta Q / GH^3$) defines the particle deformability, where G and H are the object storage modulus and channel height, respectively. Ca_{el} is the ratio between the solution viscous force and the elastic force caused by the object deformability which is zero for rigid particles. The Deborah number ($De = \lambda Q / H^3$) is the ratio between the fluid relaxation time (λ) and the flow characteristic time (H^3 / Q) which can be used to quantify the fluid viscoelasticity. While focusing positions for rigid particles shift to the channel center by increasing the De number, highly deformed cells migrate towards the walls and less deformed cells focus at the center.

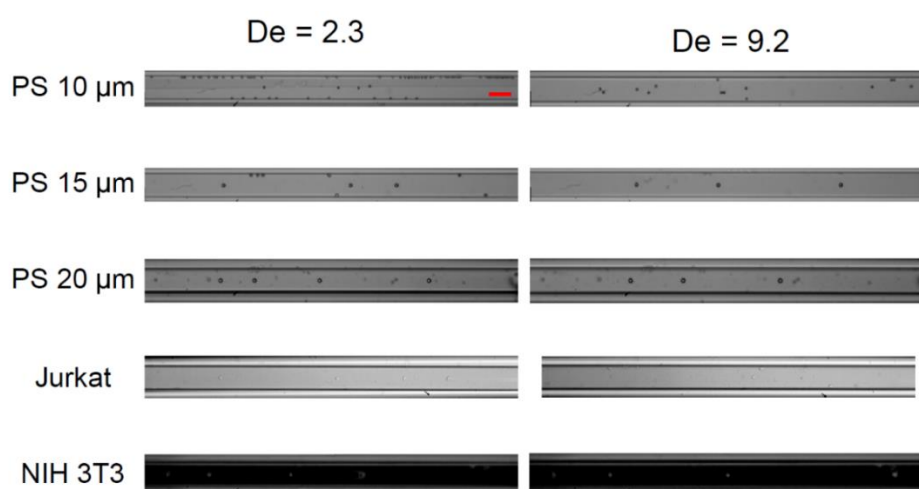


Figure 2-9: Focusing positions of deformable cells and rigid particles at 7.5 cm from the channel inlet. Adapted with permission from American Chemical Society [79].

Following this research, Xiang et al. [58] thoroughly investigated the effects of blockage ratio, aspect ratio and solution property on the lateral migration of dispersed particles in straight rectangular channels using PVP and PEO solutions. Results showed one, two, and three distinct focusing positions can be obtained by tuning the combined effects of inertia and elastic forces. Additionally, it was shown that in a rectangular channel with a high aspect ratio (1/3), all three focusing bands merged together to form a wider band at higher flow rates. For the PEO solution (2000 ppm), particles were scattered throughout the channel at flow rate of 1 μ l/min, while at

slightly higher flow rates (20 $\mu\text{l}/\text{min}$), particles found new focusing positions at two lines around the centerline (Figure 2-10 a). By increasing the flow rate to more than 40 $\mu\text{l}/\text{min}$, a third focusing band appeared at the channel center. However, with further increase in the flow rate to 120 $\mu\text{l}/\text{min}$, particles at the central region started defocusing. They observed that before defocusing phase both focusing bands around the centerline first slightly shifted towards the central streak and then gradually migrated to the channel wall, while the central focusing position remained untouched for all flow rates (Figure 2-10 a). They performed the same experiment for Newtonian and 8 wt. % PVP solution over a wider range of flow rates (1–80 $\mu\text{l}/\text{min}$). It was shown that in the PVP solution, particles laterally move to form a single band at the channel center at very low flow rates, while in Newtonian solutions focusing happens at higher flow rates, in which particles focus close to the middle of the longer sides (Figure 2-10 b, c). In contrast to the PEO solution, multi-train focusing positions was not observed in the PVP and Newtonian solutions under the same Weissenberg number and Reynolds number. This is due to the fact that for inertia-less regimes ($Re_c \sim 0.05$), the PEO solution has weaker elasticity ($Wi = 0.29$) compared to that of the PVP solution ($Wi = 3.74$). As a result, while in the PEO solution no focusing behavior was observed at this Reynolds number, particles equilibrate remarkably around the center in the PVP solution. Additionally, for the same value of elasticity, particles in both PEO and PVP fluids focus at different lateral locations. In contrast to the PVP solution where particles focus at the channel center, in the PEO solution, they concentrate at two symmetrical locations on both sides of the centerline (Figure 2-10 b, c). This is caused by the competition between elasticity and inertial forces. In this experiment, the elasticity of PEO solution was 11 times smaller than that of the PVP solution, indicating that viscoelastic force in PVP solution dominated the inertial forces, causing particles to focus at the channel centerline.

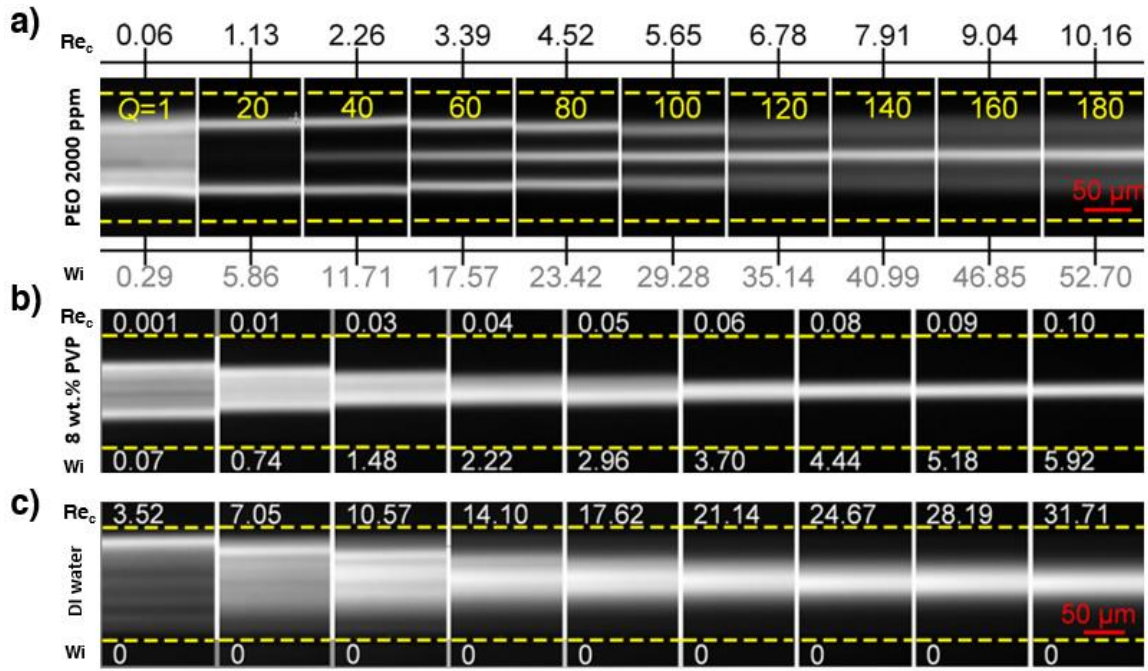


Figure 2-10: Particle equilibrium positions for a) PEO (2000 ppm), b) PVP (8 wt. %) and c) DI water under different flow rates for a rectangular channel with AR of 1/3. Adapted with permission from AIP Publishing [58].

However, for the PEO solution with the elasticity of order one, inertial forces are comparable to the viscoelastic force and push particles slightly towards the walls, which consequently causes particles to concentrate at two positions. For the case of Newtonian fluids, particles remain dispersed due to the lack of center-directed elastic force even for Re numbers up to 10.

In 2017, Holzner et al. [80] for the first time investigated the effects of polymer length and viscoelasticity on the focusing of bacteria and mammalian cells, using PEO solutions with a low concentration (500 ppm) and molecular weights of 0.4 and 1 MDa over a wide range of flow rates. The viscosity for 0.4 and 1 MDa PEO solution showed different correlations to the shear rate. While the viscosity of the PEO solution with 0.4 MDa molecular weight remains constant over a broad range of flow rates, that of the 1 MDa molecular weight displays nearly shear-thinning behavior. Results showed that at a constant flow rate by increasing the polymer length Re declines and Wi increases as both viscosity and relaxation time rises with molecular weight. In addition, for PEO solution with higher molecular weight, cell focusing happens more quickly at the channel centerline. However, working with low molecular weight solution is better for cell sorting as it avoids cell aggregation [80]. Also, compared to the 1 MDa PEO

solution, the 0.4 molecular weight offers a broader range of flow rates for one-line focusing. Additionally, they observed that formation of a one-line cell focusing takes more time at higher flow rates (22 $\mu\text{L}/\text{min}$) since cells are pushed away more effectively from the center by augmentation of the inertial forces at higher flow rates. Interestingly, their results demonstrated that focused cells at the channel center stop rotating as a result of their symmetric location in the flow profile, which is highly interested in high-resolution imaging. However, in pure inertial systems, cells continue to rotate after focusing as the equilibrium positions are either two or four next to the walls.

In another fascinating research, Yang et al. [23] investigated particle migration in different straight rectangular channels for various flow rates and solution concentrations. They showed that shear-thinning effects in PEO solution can be considered negligible up to 2000 ppm concentration. Numerical results also showed that minimal N_1 regions became wider by increasing the channel aspect ratio (confinement effects), causing a wider focusing band at the mid-plane of the channel. Besides, in high aspect ratio channels, the transition from one-band to double-band focusing occurs when inertial forces overcome the elastic force. Using the same approach, Go et al. [81], aligned erythrocytes in the centerline of a straight rectangular channel. They showed that in contrast to hardened erythrocytes and rigid spheres, previously focused erythrocytes at the center start scattering when the flow rate increases. Normal erythrocytes undergo extra deformability lift force, generated by the asymmetric deformation of the cells, which repels them away from the wall. This phenomenon develops a cell-free layer close to the walls even at very low flow rates where inertial forces are negligible. Results also showed that erythrocytes display three different forms of motion in pressure-driven flows regarding the applied shear rate and fluid viscosity. The motion behaviors include the spinning phase where cells rotate with the vortices in the shear flow, rotating phase in which cells periodically change their angular velocity and tank-treading phase in which particles flow with the main stream at a constant angle to the streamlines. In fluids with very low viscosity, RBCs orient randomly

due to the combination of all motion phases, which makes the optical imaging troublesome. However, in fluids with higher viscosities ($\mu \geq 0.01$ Pa·s), RBCs take a constant orientation. Recently, Li et al. [24] studied the pure and combined effects of fluid inertia, viscoelasticity, and shear-thinning on the particle migration through a straight rectangular channel. Results showed that due to the pure elastic force in Boger fluids particles migrate towards the channel center, while for a pseudoplastic fluid particles focus at five points (center, and corners) due to the pure shear-thinning effect. The same behavior was observed in a research by Xiang et al. [82] where 6 and 10 μm particles were focused in a straight circular channel using PEO ($M_w=2$ MDa) and PVP ($M_w=360$ KDa) solutions. They showed that PEO solution can focus particles at the center more effectively than the PVP solution for flow rates lower than 30 $\mu\text{l/min}$. Whereas, for higher flow rates particles start to gently move towards the walls due to the augmentation of the PEO shear-thinning property. Their device efficiently focused diluted blood cells at the channel center for flow rate of 10 $\mu\text{l/min}$.

In contrast to the previous studies which were performed using conventional non-Newtonian solutions (PEO, PVP, and HA), Yang et al. [83], in a novel study, compared the effects of PEO and hydroxypropyl cellulose (HPC) solutions on the focusing behavior of the 5, 10, 15 μm particles. Results interestingly showed that while in PEO solution larger particles have more tendency to focus at the center, in HPC solution smaller particles equilibrate at the center and larger particles focus at both sides closer to the walls. They assumed that this behavior is due to the fact that in typical viscoelastic solutions (*i.e.*, PEO or PVP) the normal stress (τ_{xx}) and the shear stress (τ_{xy}) are stronger near the channel walls, causing particles to migrate laterally towards the channel center. However, in contrast to typical non-Newtonian solutions, not only τ_{yy} is not negligible in HPC solution, but also stronger than τ_{xx} and τ_{xy} which causes particles to form a double line focusing positions (Figure 2-11 a, b). Results showed that different solution concentration is required for particles of different size. For instance, the highest

separation resolution for 5 and 10 μm particles was achieved at 1000 ppm HPC, while the best separation resolution for 10 and 15 μm particles occurs at 2000 ppm HPC.

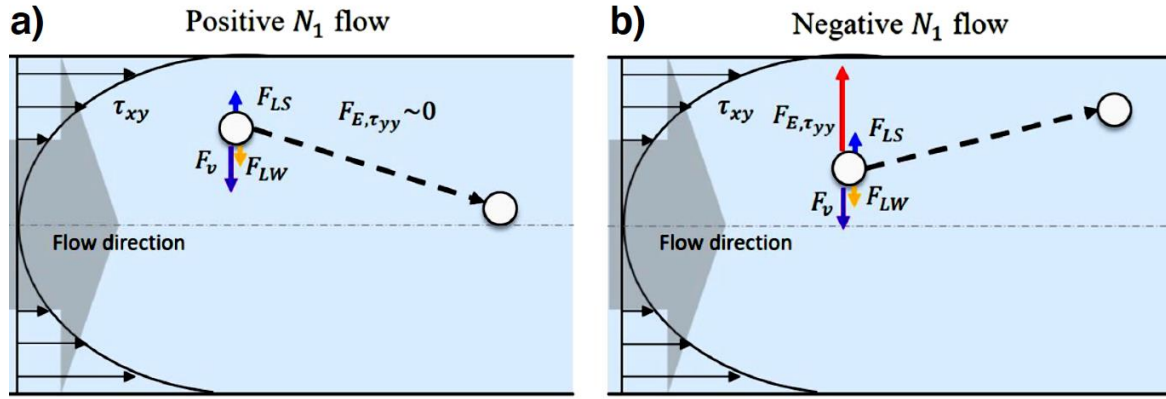


Figure 2-11: Schematic of the focusing mechanisms in non-Newtonian fluids. a) Particle focusing behavior in a positive N_1 flow, where τ_{yy} is negligible and particles focused at the channel center. b) Particle lateral migration in a negative N_1 flow where $F_{E,\tau_{yy}}$ outweighs the $F_{E,\tau_{xx}} + F_{\tau_{xy}}$. Here $F_{E,\tau_{yy}}$ and $F_{E,\tau_{xx}}$ are the elastic forces and F_v is the viscous force from τ_{xy} . Adapted with permission from Springer Nature [83].

In 2019, for the first time, Tang et al. [84] studied the elasto-inertial focusing in a straight channel with various cross-sections fabricated by fused deposition modeling (FDM) 3D printer. They investigated particle focusing in straight square, triangular, and circular channels over a wide range of flow rates. Results showed that single-line focusing caused by viscoelasticity in the triangular channel was closer to the channel bottom than those of the square and circular channels, which is of great interest for the cytometry application by enhancing the detection sensitivity. In contrast to the previous researches were all about particle focusing and the fundamentals of particle/cell migration in elasto-inertial systems, there are some efforts which used sheathless straight channels to separate particles/cells size-dependently. Based on the type of the straight channel, three approaches can be used for particle separation size-dependently.

2.4.1.1.2 Simple straight with a sudden expansion

The first approach is to initially focus particles at different locations based on their size or deformability, followed by a sudden expansion to increase the distance between focusing bands [85]. However, this approach is not robust enough, as focusing streaks might not have enough distance. Additionally, finding the condition where particles focus at different locations is

difficult and needs an accurate calculation of inertial and elastic forces. In 2015, using this approach, Liu et al. [86] separated two binary mixtures of RBCs and *E. coli* bacteria, and RBCs and MCF-7 cells at very high-throughput. They compared denaturized PEO solution to its newly prepared counterpart and realized that while both solutions have the same elastic modulus, the denaturized PEO solution has lower and constant viscosity, which can increase the focusing efficiency over wider flow rates (Figure 2-12 a, b).

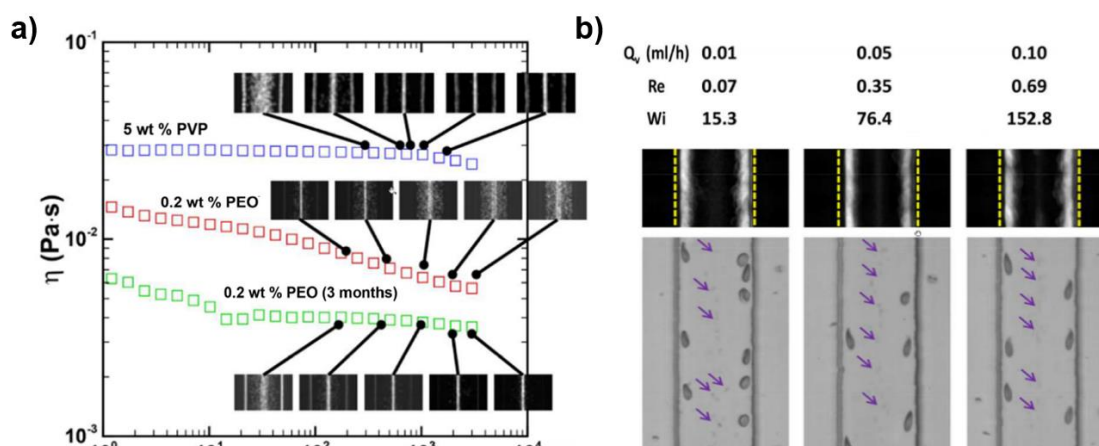


Figure 2-12: Focusing and separation of beads and *E. coli*. a) The shear-thinning behavior of the used solutions. The denaturized 0.2 wt. % PEO solution and the 5 wt. % PVP solution show constant viscosities at different shear rates, while the lately prepared PEO solution (0.2 wt. %) demonstrates shear-thinning behavior for all measured shear rates. Focusing positions in a channel with $H = 50 \mu\text{m}$ and aspect ratio of two for the $5 \mu\text{m}$ particles and mentioned liquids show that shear-thinning effects considerably influence the focusing positions, especially at higher Re numbers. b) Complete separation of RBCs and *E. coli* was attained by using the denaturized PEO medium (0.2 wt. %). As shown, *E. coli* (marked by arrows) were focused at the centerline and RBCs focused along both sides. Adapted with permission from American Chemical Society [86].

In the same year, Lu et al. [87] investigated the separation of peanut and spherical particles through a straight rectangular channel in a viscoelastic solution. The results showed that the transition from one line focusing to two starts at different flow rates based on the particle's shape. Also, particles of different shapes equilibrate at different positions under the same flow conditions, facilitating the sheath free particle separation with high purity. Using the same approach, Li et al. [88] continuously separated drug-treated *C. neoformans* cells from normal cells. They observed that larger abnormal-shaped cells stay farther away from the channel center compared to the regular-shaped cells with smaller size. The best separation efficiency was achieved at the flow rate of $100 \mu\text{l/h}$, PEO concentration of 1000 ppm, and aspect ratio of

2. Recently, Nam et al. [89] isolated *Candida albicans* (C. albicans) from blood using 0.1% hyaluronic acid (HA) solution. As shown in Figure 2-13, while *Candida* cells focused tightly at the channel center (2 μm), WBCs focused closer to the side walls and were harvested from side outlets.

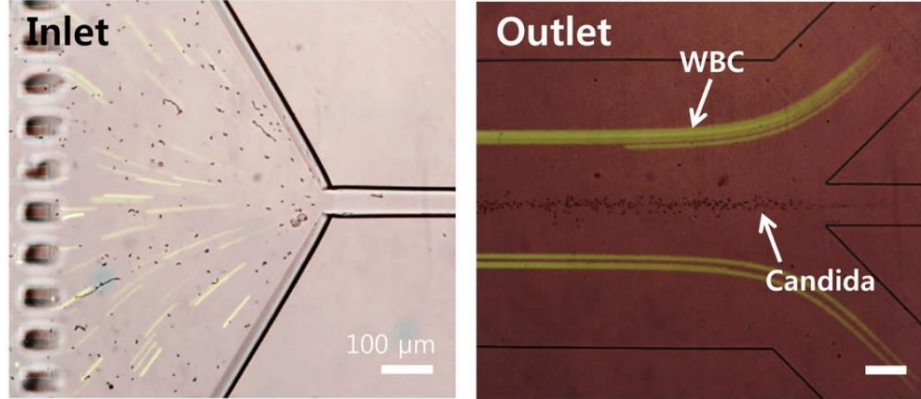


Figure 2-13: Separation of the candida and WBCs sample at flow rate of 100 $\mu\text{l}/\text{min}$. Fluorescent images of WBCs and bright-field microscopic images of candida were stacked to demonstrate the distinctly separated cells at the channel outlet. Adapted with permission from Springer Nature [89].

2.4.1.1.3 Multi-stage bifurcation

The second approach to separate particles in sheathless straight channels is to use multi-stage bifurcation channels. In this approach, the first stage is designed for pre-alignment of particles at the center (as all particles in this stage meet the criteria for focusing ($a/D_H > .07$)) and the second stage is for separation. When previously focused particles hit the first bifurcation, they are divided into two streams and enter the second stage from the inner side of the channel (Figure 2-14). Throughout the second stage, while larger particles get affected by elasto-inertial forces and migrate towards the channel center, lateral migration of the smaller particles are negligible and they move with the flow close to the wall. The lateral migration velocity in this system can be measured by:

$$\frac{V_E}{V_m} \sim Wi \left(\frac{a}{h} \right)^2 \frac{\partial \dot{\gamma}}{\partial x} \quad (2-22)$$

with V_m and V_E being the flow mean velocity and lateral migration velocity. The parameter $\dot{\gamma}$ also indicates the localized shear rate in the channel. By designing a sudden expansion in the

second stage, the distance between larger and smaller particles increases, causing high-efficiency separation at the second bifurcation [90].

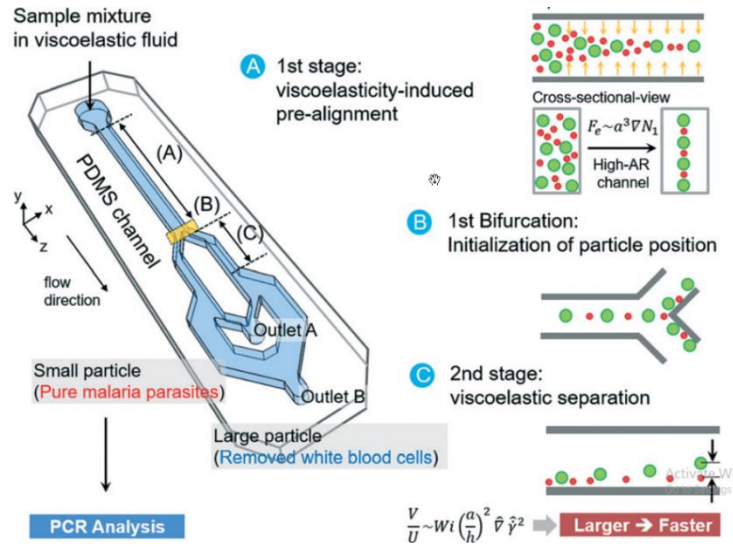


Figure 2-14: Schematic of a two-stage straight channel for sheathless particle separation. The device is comprised of (A) the 1st stage for aligning the particles at the channel center by elasto-inertia forces, (B) the 1st bifurcation to focus all the particles next to the inner walls at the entrance of the second stage (C) the 2nd stage for elasto-inertial particle separation. Small particles remain untouched and are harvested at outlet A whereas large particles migrate toward the center and are harvested from outlet B. Adapted with permission from Royal Society of Chemistry [90].

The simplest device in this category was used by Nam et al. [91] comprised of a straight circular channel connected to a high aspect ratio rectangular bifurcation responsible for the separation of particles size-dependently. All particles were focused at the center of the straight circular channel and separated based on their size via a sudden expansion in the bifurcation part. Later on, they [92] developed their device and fabricated a novel 2-stage microfluidic system to separate 5 and 10 μm particles using elasto-inertial flow with high-efficiency of 99%. They separated MCF-7 cells from leukocytes at flow rate of 200 $\mu\text{l}/\text{min}$ and purity of 97% to showcase the ability of their system for separation of biological samples. In another work [90], using the same device, they filtered malaria parasite from WBCs using a viscoelastic solution with purity of 99% and high-throughput of 400 $\mu\text{l}/\text{min}$ for PCR detection. As shown in Figure 2-15, WBCs were collected from the first outlet and malaria cells were harvested at the second outlet. Later on, Tan et al. [93] used this device to separate WBCs from diluted blood in a viscoelastic solution. They evaluated the effects of hematocrit, flow rate, and PVP concentrations on the separation efficiency and finally achieved a high-throughput of 150

$\mu\text{l/min}$ for 1% PVP and 0.01% hematocrit. They realized that by increasing the hematocrit to more than 10%, WBCs remained dispersed between RBCs due to the high cell-cell interactions.

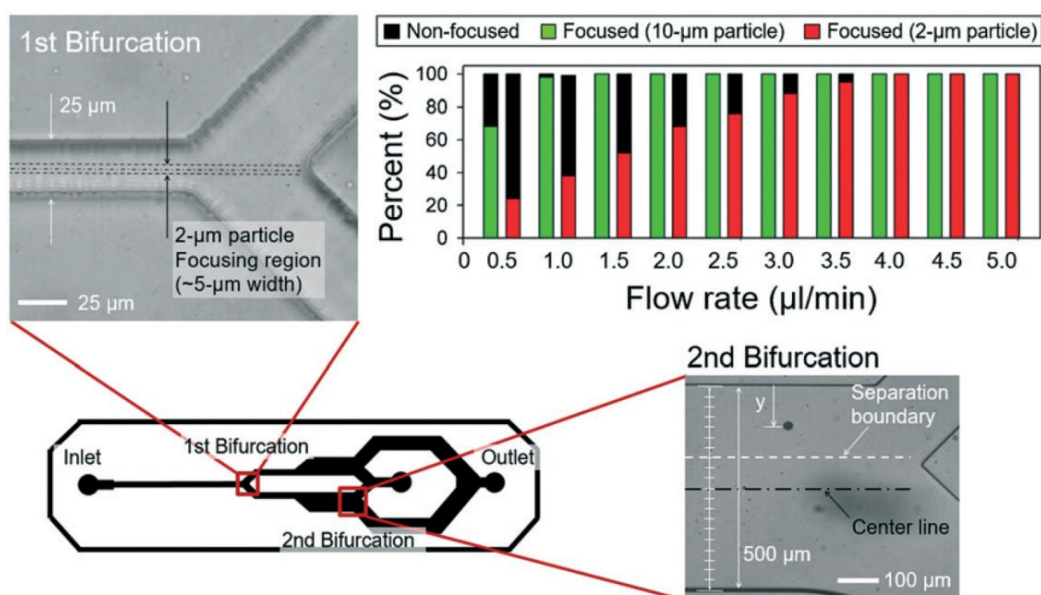


Figure 2-15: Sheathless elasto-inertial focusing and separation of rigid polystyrene particles through a multistage bifurcation straight channel. (Top-left) focusing of 2 μm particles at the 1st bifurcation. (Top-right) Ratio of non-focused and focused particles at the bifurcation region for different flow rates. While 10 μm particles start focusing from 1 $\mu\text{l/min}$, 2 μm particles start focusing from $Q = 4 \mu\text{l/min}$. 2nd bifurcation shows the separation of 2 and 10 μm particles. Adapted with permission from Royal Society of Chemistry [90].

2.4.1.1.4 Side wells

The last approach to separate particles in a sheathless straight channel is to generate secondary flows by adding side wells to the channel. Figure 2-16 demonstrates the schematic of particle focusing through a channel with side wells, as well as flow field and focusing positions in a cross-section 10 μm away from the last cavity in the axial direction, for two cases of Newtonian (Figure 2-16 bI) and non-Newtonian solutions (Figure 2-16 bII) [94]. In a normal straight rectangular channel without side cavities and for Newtonian fluids, particles equilibrate at two positions close to the middle of longer sides due to the effects of two-opposing wall-induced and shear gradient lift forces. However, by adding side wells, secondary flows form through the channel which exert extra drag forces and shift the final focusing positions towards the cavity side (Figure 2-16 bI). Nonetheless, for non-Newtonian fluid, particles are first pushed towards the center by elastic force and then migrate towards the non-cavity side by Dean vortices (Figure 2-16 bII).

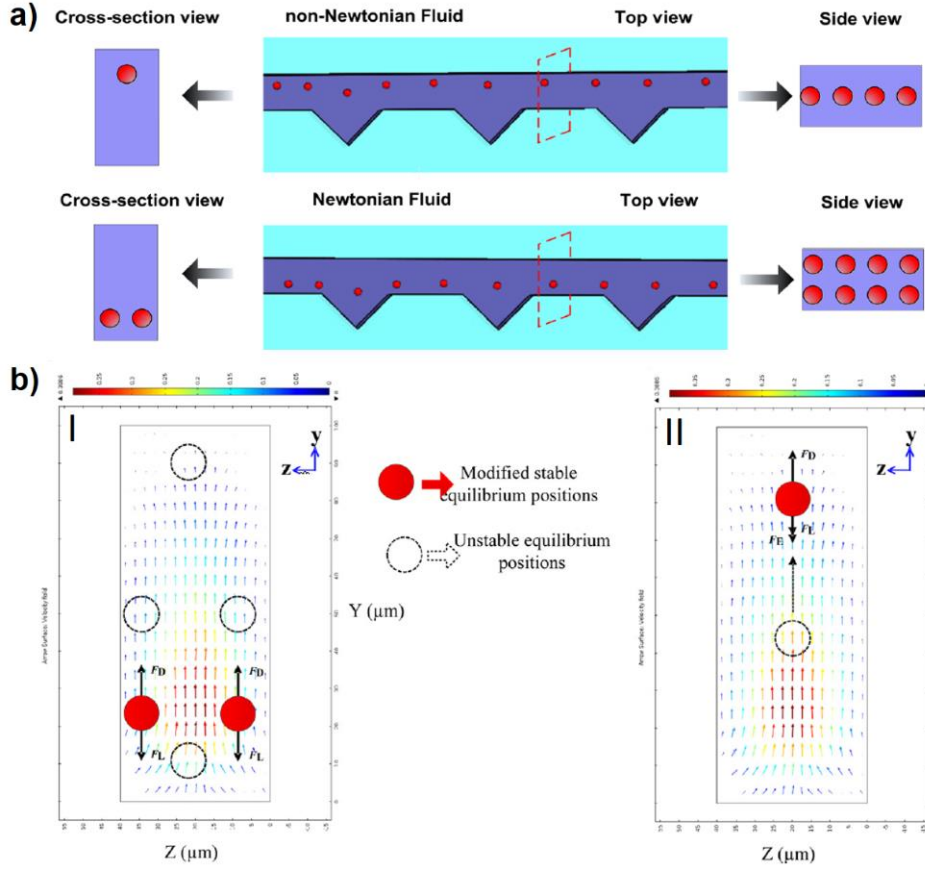


Figure 2-16: particle focusing phenomenon in a straight channel with side wells. a) Schematic of the straight channel with cavities. For non-Newtonian fluid, particles equilibrate on the non-cavity side, while for Newtonian fluid they focus close to the cavity side. b) Secondary flows and schematic of the focusing positions 10 μm away from the last cavity in the axial direction for two cases of I) Newtonian, and II) non-Newtonian solutions. Adapted with permission from AIP publishing [94].

Using this approach, Yuan et al. [94] studied the combined effects of elasticity and Dean drag force on the focusing behavior of the 3, 4.8 and 13 μm particles in a straight channel with expansion-contraction cavity arrays (ECCA) for a wide range of flow rates. Results showed that while for Newtonian solution particles focus at the cavity side due to the inertial and dean effects, for viscoelastic solution particles concentrate on the opposite cavity side as a result of extra elastic force. Following this research, they studied the effects of viscoelasticity on the plasma extraction using the same device [95]. They first characterized the device by using 3, 4.8, and 10 μm particles representing platelets, RBCs, and WBCs, respectively. Benefitting from Dean flow in cavities, the ECCA device offers plasma extraction with high purity of 99.99% after the second filtration. Also, they studied the effects of viscoelasticity and ECCA geometry on the particle separation under different conditions [96]. Results showed that in a

simple straight channel while particles remained scattered everywhere for the Newtonian solution, extra elastic force arising from the non-Newtonian property of the PEO (1000 ppm) solution sorted particles size-dependently, in a way that smaller and bigger particles focused at the center and both sides, respectively. For ECCA channel and PEO solution, focusing positions shifted towards the non-cavity side due to the combined effects of elasticity and of Dean flows. It should be noted that, due to the extra Dean drag force generated by cavities, two line focusing positions for larger particles changed to one line close to the non-cavity side. Using this device yeast cells and the human Jurkat cells were separated with the purity and recovery of 24% and 99.6% for Jurkat cells, respectively.

2.4.1.2 Spiral channels:

Particles flowing in a spiral channel within a non-Newtonian fluid and finite inertia experience Dean drag, viscoelastic force, and inertial migration. A combination of elasto-inertial lift and Dean flow enable microfluidic systems to precisely focus and position microparticles. In these systems, channel dimensions, solution rheology, aspect ratio, particle size, and Re number are the key factors to control particle migration. Particles in elasto-inertial spiral systems are simultaneously affected by Dean drag, viscoelastic and inertial forces which can be simplified for flow inside a rectangular cross-section by the following equations [97]:

$$F_{Elastic} \sim 8a_p^3 \lambda \left(\frac{Q}{hw^2} \right)^3 \quad (2-23)$$

$$F_{Inertial} \sim \frac{1}{4} \rho Q^2 a_p^4 \left(\frac{(w+h)^2}{(hw)^4} \right) \quad (2-24)$$

$$F_{Drag} \sim \frac{4\rho Q^2 a_p}{R(w+h)^2} \quad (2-25)$$

Where λ and Q are the relaxation time of viscoelastic solution and flow rate, respectively. As can be seen, particle diameter (a_p) and flow rate noticeably affect these forces due to the strong correlation between them. Therefore, particles with different sizes are assumed to migrate with different lateral velocities, making spiral channels a suitable choice for size-dependent separation. In 2013, for the first time, Lee et al. [98] studied the coupled effects of elasticity

and Dean drags on particle migration in a spiral rectangular channel. Various particles, flow rates, and solution concentrations were tested to achieve multiplex focusing positions aiming at separating 1.5 and 10 μm particles. They showed that channel aspect ratio has a significant effect on particle focusing, and the focusing bands shift towards the outer wall by increasing the particle size. Later on, Xiang et al. [97] investigated the fundamentals of elasto-inertial focusing in rectangular spiral channels for different flow rates, channel radii, and channel aspect ratios using PEO and PVP solutions. Results for the first time showed a six-stage focusing model associated with the competition between inertial, elastic, and Dean drag forces (Figure 2-17). They showed that by precise control over these forces single line focusing at the center of the channel can be achieved with high-throughput of 100 $\mu\text{l}/\text{min}$. In another study [99], the same group accurately controlled particle migration in a similar device, by optimizing the concentration of PVP solution. Based on their findings, at high concentration, particles focus in a single line at the channel centerline by the dominated viscoelastic force. However, by decreasing the PVP concentration particles migrate towards the outer wall region. They declared that one line focusing at the channel center for PEO solution was not observed due to the shear-thinning effect.

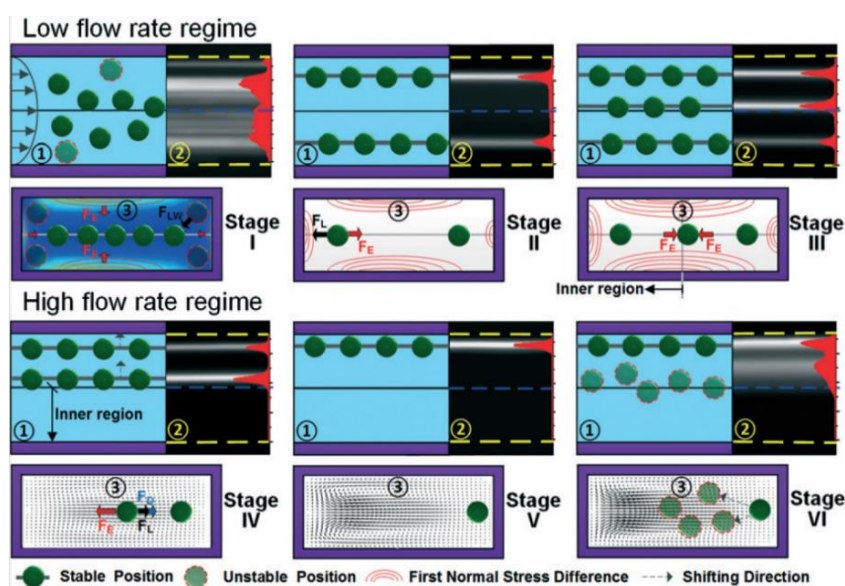


Figure 2-17: Demonstration of the different elasto-inertial focusing stages in a spiral channel. At each stage, a couple of graphs demonstrating the possible equilibrium positions and particles behavior including (1) schematic of the particle focusing positions (2) the corresponding fluorescence image as well as intensity profile (3) flow vectors, inertial force and elastic force applied on the particles, are provided. Adapted with permission from Royal Society of Chemistry [97].

2.4.1.3 Serpentine channels:

The mechanism of particle focusing in serpentine and spiral channels are the same, which means particles are affected by the same forces. However, in contrast to spiral channels, the position of inner and outer walls in serpentine channels continually changes, which consequently alters the direction of secondary flows. In pure inertial systems, this structure makes larger particles to focus at the channel center while smaller ones mostly concentrate on both sides. There is only one paper studying the elasto-inertial focusing phenomenon in the serpentine channel. In 2019, Yuan et al. [59] focused Jurkat cells (ATCC) in a serpentine channel in both Newtonian and viscoelastic solutions. They showed that elastic effect and Dean vortices formed in serpentine channel accelerate the focusing and reduce the channel length (Figure 2-18). Also, investigation on cell viability before and after the tests proved that while PEO solution has negligible effects on cell viability, focusing throughout the serpentine channel may have a negligible adverse impact on cells.

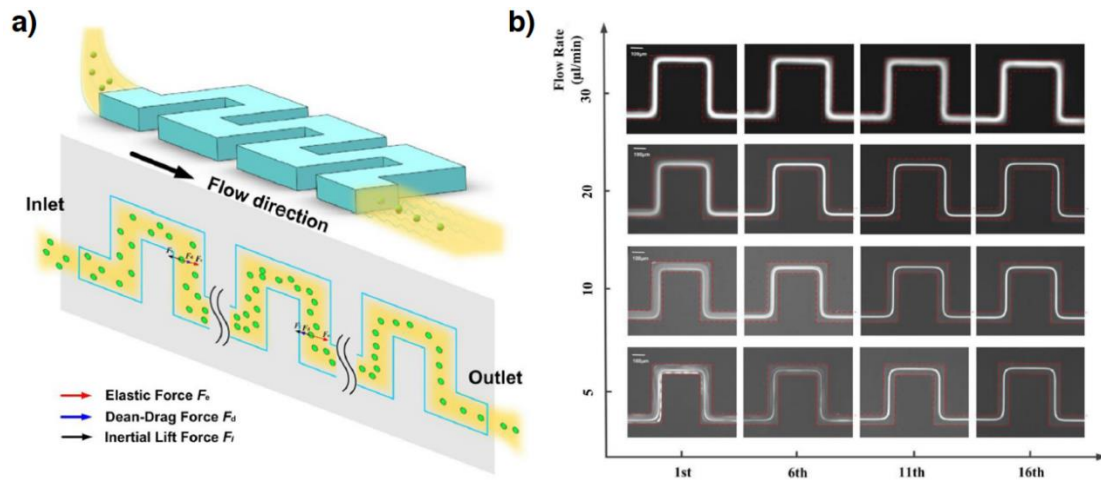


Figure 2-18: a) Graphic demonstration of particle focusing in a serpentine channel for PEO solution. b) Focusing behaviors at different zigzag turns and low rates. Adapted with permission from Springer Nature [59].

Table 2 demonstrates all the studies performed on the sheathless elasto-inertial systems. As can be seen, in non-Newtonian systems, straight channels are the most common device used for particle sorting. In contrast to the higher throughput of the spiral channels for particle focusing in elasto-inertial systems, there are limited studies on its applications. It might be due to the

inability of this approach to accurately separate particles size-dependently, causing particles to focus at the same position. However, it needs more studies and characterization to claim such a statement firmly. In addition, serpentine channel in elasto-inertial applications seems to be weak, since not only it makes focusing positions to overlap, but also decreases the throughput of the similar inertial device.

Table 2: Studies performed on the elasto-inertial microfluidics within sheath-less microchannels

Reference	channel structure (μm^2)	Particle (μm)	Solution	throughput	purpose
Straight channel					
Yang 2011 [55]	Straight square 50×50	5.9 and 2.4	8 wt% of PVP ($M_w=360$ KDa) PEO ($M_w=2$ MDa)- 50, 100, 250 and 500 ppm	N/A	Studying focusing
yang 2012 [76]	straight rectangular 50×50, 75×75	6, fresh and rigidified RBCs	6.8 wt. % PVP, $M_w=360$ KDa	0.24 mL/h	Separation of RBCs and WBCs
Kim 2012 [29]	straight rectangular 5×5, 30×10	1 μm , 500nm, 200nm, 100 nm and DNA	PEO $M_w=2$ MDa, 500 ppm	15 $\mu\text{L/hr}$	focusing
Seo 2014 [77]	Straight Tube $\pi \times 150 \times 150$	7, 15 and 30	1% wt. PEO ($M_w=4000$), .8% wt. PVP ($M_w=360$ kDa)	N/A	Studying focusing
Seo 2014 [78]	Straight square 300×300	30 and 50	8 wt.% PVP ($M_w=360$ kDa), 1 wt.% PEO ($M_w=4000$ kDa)	N/A	Studying focusing
Ahn 2015 [85]	straight rectangular 50×50	4.5 and 2.3	0.01, 0.025, 0.05, and 0.1 wt. % PEO $M_w=2$ MDa	160 $\mu\text{L/h}$	Separation
Liu 2015 [86]	straight rectangular, H=10 and 50, AR=1,2,4	1, 3, 5, 15, MCF-7 and (RBCs), Escherichia coli (E. coli)	PEO ($M_w=4$ Mda) and PVP ($M_w=3.6 \times 10^5$ g/mol)	0.1 ml/h	Separation
Lu 2015 [87]	straight rectangular 50×15, 50×25, 50×40, 50×100	4.18 μm , peanut-shaped with 3.5 μm -diameter/ 6 μm -length	PEO $M_w=2$ MDa, 500, 1000, and 2000 ppm	150 $\mu\text{L/h}$	Separation
Del Giudice 2015 [69]	straight, rectangular 100×100	10	0.1, 0.8, 1.6 wt. % PEO $M_w=4000$ kDa	N/A	Effects of rheology on focusing
Nam 2015 [91]	Straight circular, rectangular- 2 stage separation H=45, W=45, 40	5 and 10	8 wt. % of PVP $M_w=360$ KDa	0.1 $\mu\text{L/min}$	separation
Nam 2015 [92]	straight rectangular 2 stage- $D_H=50$ and 104	5, 10, MCF7 and leukocytes	5 wt. % PVP 0.1 (w/v) % HA	200 $\mu\text{L/min}$	separation of the MCF7 from leukocytes
Yuan 2015 [94]	straight channel with expansion- contraction cavities (ECCA) 100× 45	3.2, 4.8 and 13	PEO $M_w=2$ MDa, 500 ppm	60 $\mu\text{L/min}$	Focusing
Yuan 2016 [100]	straight channel with expansion- contraction cavities (ECCA) 100× 40	3, 4.8, 10, platelet, RBC and WBCs	PEO $M_w=2$ MDa, 500, 1000, 2000 ppm	50 $\mu\text{L/min}$	Plasma separation
Kim 2016 [75]	Straight square 50×50	6, 10 and 15	DNA, 2.5, 5, 10, and 50 ppm	640 $\mu\text{L/h}$	Studying focusing
Xiang 2016 [58]	straight rectangular 100×50, 50×50, 150×50	10, 5 and 2	8 wt. % PVP 360 KDa, 0.05 wt. % PEO 2MDa.	N/A	Studying focusing
Go 2016 [81]	straight rectangular 500×50	7 μm , hardened and normal erythrocytes	3 wt. % PVP, $M_w=360$ kDa	50 $\mu\text{L/min}$	focusing
Nam 2016 [90]	Straight rectangular- 2 stage separation 25×250	2 μm , 10, malaria and white blood cells	0.1% HA	400 $\mu\text{L/min}$	Separation
Hong 2016 [101]	Sheath Straight channel with side well-50× 50	1	PEO $M_w=2$ MDa, 250 and 500 ppm	N/A	Mixing
Tan 2017 [93]	straight rectangular 2 stage- H=125, W=25,50,500	2, 6, and 15	1% PVP, $M_w=360$ KDa	150 $\mu\text{L/min}$	separation of WBCs (0.01% hematocrit)
Holzner 2107[102]	straight, rectangular 30×30, 43×43 and 50×50	HL-60 (13 μm) and Human B-lymphoid cell lines (10.5 μm), E.coli Bacteria(1 μm wide and 1-5 μm long)	PEO 0.4 and 1 MDa, 500 ppm	N/A	Studying focusing
Yang 2017 [23]	straight rectangular 25×25, 25×50, 25×100	6, 10 and 15	PEO $M_w=2$ MDa, 500 to 4000 ppm	N/A	Studying focusing
Yuan 2017 [96]	straight channel with expansion- contraction cavities (ECCA) 50× 30	5,13, yeast cells and the human Jurkat cells	PEO $M_w=2$ MDa, 1000 ppm	20 $\mu\text{L/min}$	Separation
Giudice 2017[79]	straight square 100× 100	6, 10, 15, 20 and Jurkat and NIH 3T3 cells	0.8 wt. % hyaluronic acid	2 $\mu\text{L/min}$	Studying the focusing and separation

Li 2018 [88]	straight rectangular 50×15, 50×25, 50×40	5 and 7	PEO M_w = 2 MDa, 500, 1000, and 2000 ppm	100 μ L/h	Separation
Xiang 2019 [82]	straight circular $\pi \times$ (50×50 - 75×75)	5 and 10	PEO M_w =2MDa and PVP M_w = 360 KDa	30 μ L/min for PEO and 60 μ L/min for PVP	Studying focusing
Tang 2019 [84]	straight (triangular, square, circular)	15	0.3 wt. % Hyaluronic acid (HA) M_w = 265 kDa	100 μ L/min	focusing
Yang 2019 [83]	straight rectangular (AR=2)	5, 6.5, 10, and 15 μ m	PEO M_w = 2 MDa, 2000 ppm and hydroxypropyl cellulose (HPC) M_w = 1 MDa, 100ppm	N/A	focusing
Nam 2019 [89]	straight rectangular 50×25	2, 13, candida cells and WBCs	0.1% HA	100 μ L/min	Separation
Spiral channel					
Lee 2013 [98]	spiral rectangular 100×25	1.5, 5 and 10	PEO M_w =1MDa, 500, 1000, 3000, and 5000 ppm	N/A	Physics of focusing and separation of 1.5 and 10 microparticles
Xiang 2016 [97]	spiral rectangular 140,190,215×50	5 and 10	6.8 wt.% PVP (360 KDa), PEO(2MDa)	N/A	Physics of focusing
Xiang 2018 [99]	spiral rectangular 140×50	10	8.0 wt% PVP (360 KDa)	120 μ L/min	Separation
Serpentine channel					
Yuan 2019 [59]	Serpentine rectangular 100×45	13 and Jurkat cells (ATCC)	PEO M_w =2MDa 0, 500, 1000, ppm	20 μ L/min	focusing

2.4.2 Sheath flow

2.4.2.1 Straight channels

Sheath flow systems are typically used for squeezing, separation and washing purposes and functions by introducing two or more fluids at the channel inlets with different velocities. The flow with lower velocity, which contains cells or particles, is the sample flow, and the other particle-free fluids are called the sheath flow (Figure 2-19 a). In these systems the larger particles are affected by inertial and elastic forces and laterally move to the sheath fluid, while smaller particles remain scattered in the sample flow and follow the flow streamlines[103]. According to the design and target of the system, both sample and sheath flows can be Newtonian or non-Newtonian and pumped from any of the inlets. For example, for particle washing and separation in an elasto-inertial system with two inlets, the sample fluid is usually non-Newtonian causing particles to migrate easily from the sample fluid to the Newtonian sheath flow. According to Figure 2-19 b, for the case of two inlets and non-Newtonian sample, the elastic and wall-induced lift forces should overcome the opposing shear gradient lift and Stokes' drag forces for efficient particle migration [103]. In these systems, characterizing the rheology of the non-Newtonian solution is of great importance, as the low concentrations prevent particles from migrating to the sheath flow. As shown in Figure 2-19 ci, particles pass

through the channel without any noticeable cross-stream migration, due to the lack of elastic force.

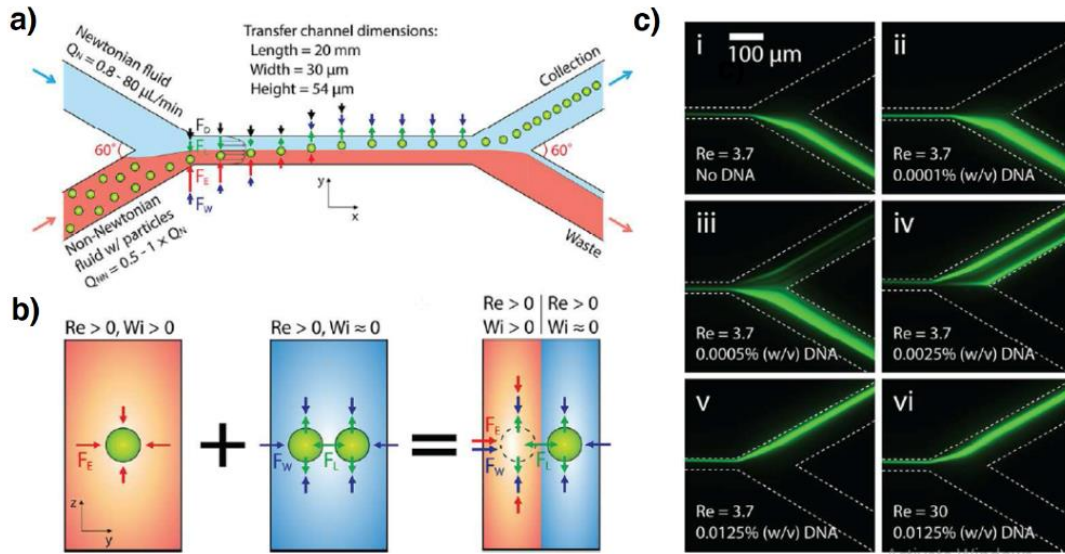


Figure 2-19: Transverse movement of particles from non-Newtonian sample fluid to the Newtonian sheath flow. a) Schematic of the sheath flow microchannel for particle washing. b) Cross-sectional view of the channel which demonstrates the applied forces on particles. c) Fluorescent images showing particle migration strongly relies on the DNA concentration in the sample flow. Adapted with permission from American Chemical Society [103].

However, by increasing the concentration of the DNA solution (sample flow), particle migration starts happening (Figure 2-19 ci-vi). For the sheath flow systems with three inlets, samples can be pumped from either middle inlet or lateral inlets. For the case where sample flow is in the middle and sheath flows are on both sides, the best result can be obtained when the sample fluid is non-Newtonian and sheath flow is Newtonian [30]. In this case, larger particles are pushed towards the Newtonian/viscoelastic interface by synergetic effects of elastic and shear gradient lift forces and penetrate to the sheath flow while smaller particles remain untouched and move with the main streamline. For the reverse condition where the sample flow is pumped from both sides and the sheath flow is injected from the middle inlet, effective separation can be achieved when the sample fluid is Newtonian and sheath flow is non-Newtonian. For this condition, inertial and elastic forces oppose each other on the Newtonian/viscoelastic interface. While on the interface, the elastic force is towards the channel wall and controls particle penetration to the core region, for particles penetrated to the core region the elastic force changes its direction and pushes them towards the channel center.

Therefore, the concentration of the non-Newtonian fluid should be precisely optimized to allow larger particles to migrate towards the sheath flow while preventing smaller particles from penetration. Excessive concentration of the non-Newtonian solution can block migration of both particles to the core flow. Nonetheless, very low concentrations may cause both large and small particles to migrate towards the channel center and reduces the effectiveness of the device [104]. Due to the difficulty of analysis in sheath flow elasto-inertial systems, there are only a few studies on its applications in straight channels and almost no investigations in curved channels. The promising results of this approach for sorting and separation of submicron particles make further study of these systems a crucial need.

The earliest research on the sheath flow elasto-inertial microfluidics was carried out by Nam et al. [105], to separate platelets from diluted blood with the throughput and efficiency of 4.5 $\mu\text{l}/\text{min}$ and 99%, respectively. They injected samples from side inlets and sheath flow (PEO solution) from the middle inlet to pinch the samples to the side walls (Figure 2-20 a). As shown in Figure 2-20 b, while 1 μm particles remained scattered on the sample flows and collected from side outlets, 5 μm particles migrated to the channel center due to the strong elasto-inertial forces applied on them. In designing these systems, we should make sure that bigger particles meet the criteria for focusing ($a_p/D_h > 0.07$) and vice versa for smaller particles.

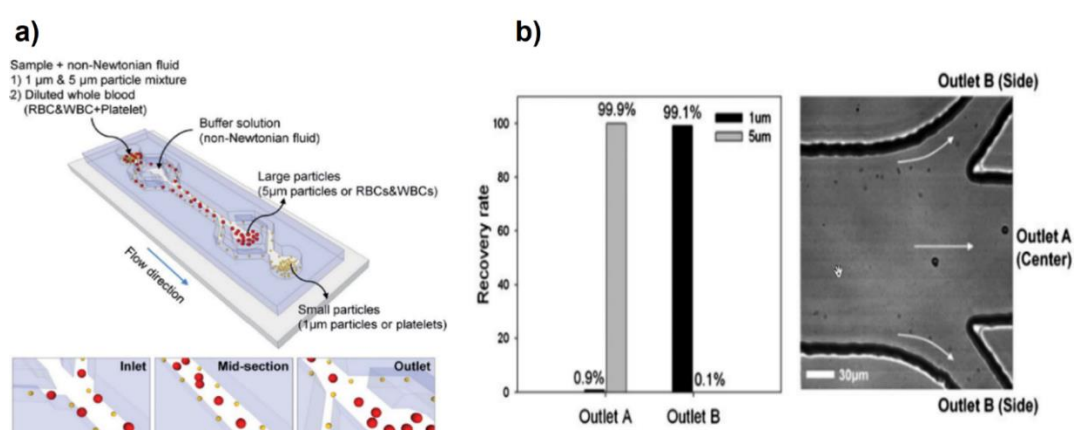


Figure 2-20: a) Schematic illustration of sheath flow elasto-inertial particle separation using viscoelastic fluid flow in a straight microchannel. b) Separation of particles at the outlet, showing while 1 μm particles remained untouched and collected from side outlets, 5 μm particles moved to the center and harvested from the middle outlet. Adapted with permission from Royal Society of Chemistry [105].

Following this research, Kang et al. [56] studied the effect of DNA-laden flow on the focusing and separation of 1, 2.3, 4.5 and 10.5 μm particles within a straight circular and rectangular channel. The medium for the sheath fluid was considered to be the same as sample flow. Results showed that due to the larger size and longer relaxation time of DNA compared to the synthetic polymers (for example, PEO), DNA increases the viscoelasticity of its diluted solution more noticeably. Also, they showed that the working flow rate for DNA solution is almost 10 times higher than that of the PEO solution. Using the same approach, Lim et al. [106] investigated the effect of first and second normal stress differences (N_1 and N_2) on the lateral displacement of dispersed particles. They utilized PEO ($M_w = 2 \text{ MDa}$) and PAA ($M_w = 5 \text{ MDa}$) solutions as they both generate a nonzero N_1 and a shear-thinning viscosity. However, the PAA solution also yielded a nonzero N_2 . Results showed that in the PAA solution, the secondary flows, perpendicular to the main flow, are enhanced by the nonzero second normal stress difference. They also demonstrated a strong influence of N_2 on the particle migration and illustrated the various size-dependent forces applied on particles. As Figure 2-21 a-b show, while 10 μm particles (blockage ratio is equal to 0.2) migrated toward the channel centerline for all tested conditions, focusing patterns of 1 μm particles in PEO and PAA solutions are noticeably different and affected by the extra force arising from the second normal stress difference.

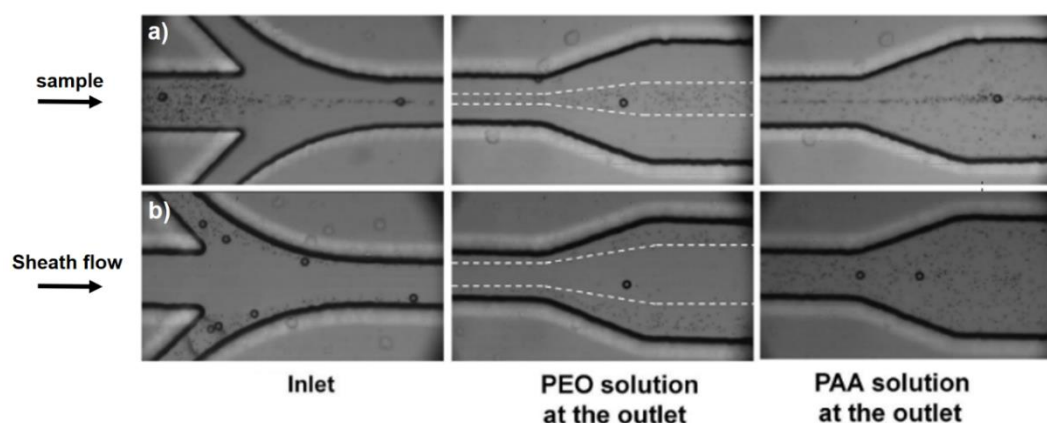


Figure 2-21: Comparison of particle lateral migration in different viscoelastic fluids within a rectangular microchannel ($AR=2$) for two conditions of side and central sheath flow. a) The sample is pumped through the middle inlet, and b) sample is pumped from the side walls. For a 500-ppm PEO solution, for both conditions, smaller particles move along the streamlines while 10 μm particles equilibrate at channel center. For 100-ppm PAA solution, 10 μm particles focused at the channel center while 1 μm particles scattered as a result of secondary flows generated by second normal stress differences (N_2). Adapted with permission from Springer Nature [106].

Following this work, Lu et al. [87, 107] separated 3 and 10 μm particles by an elasto-inertial pinched flow in a T-shaped microchannel (Figure 2-22). This device is the simplest design for sheath flow separation applications. However, due to the 90° junction between sheath and sample inlets, increasing the sample flow rate can increase the mixing more significantly compared to the systems with a lower angle between inlets. This device functions most effectively for the Re of order 1, making it suitable for the applications with a limited amount of samples. Their findings showed that the aspect ratio significantly affects the separation efficiency due to its effects on the deflection of particles.

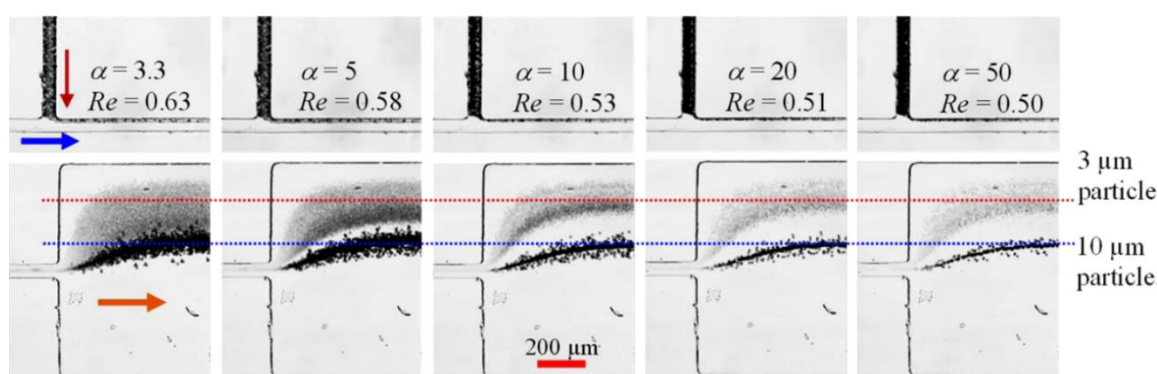


Figure 2-22: Elasto-inertial pinched flow in a T-shaped microchannel. Stack images at the inlet (top row) and outlet (bottom row) of the channel, showing the sheath flow separation of 3 and 10 μm particles for PEO solution with 1000 ppm concentration. By increasing the α (the ratio of sheath and sample flows), separation efficiency increases. The red and blue dotted lines are utilized to help to visualize the impacts of α on the focusing positions at the outlet. Adapted with permission from American Chemical Society [107].

They tested various fluid elasticity and flow rate to find the best condition for achieving the highest focusing positions gap. They realized that PEO solution with 1000 ppm concentration and flow rate of 100 $\mu\text{l/h}$ lead to the best separation efficiency.

Enhanced capabilities of sheath flow elasto-inertial systems for separation of submicron particles make them an appropriate option for bacteria separation. Bacteria possess a wide diversity of sizes and shapes and are generally between 0.5 to 5 micrometer. In 2017, for the first time, Faridi et al. [25] separated bacteria from whole blood using a sheath flow straight channel. Whole blood was pumped from side inlets while the non-Newtonian sheath flow (PEO-500 ppm) was introduced from the central inlet, pinching the whole blood towards the

side walls. Due to the center-directed elastic force, larger blood cells migrate to the channel center, while bacteria remain scattered in the sample next to the walls. Results successfully showed the separation of bacteria from undiluted blood at a high throughput of 60 $\mu\text{l}/\text{min}$ and efficiency of 73%. Following their work, Tian et al. [104] separated platelets (2–3 μm) from *Staphylococcus aureus* (1 μm) size-dependently with high purity of 100 % using a co-flow of diluted PEO (100 ppm) and Newtonian solutions. They tested different scenarios for pumping the sample and sheath fluids considering Newtonian and non-Newtonian solutions for both (Figure 2-23 a). Results showed that the highest separation efficiency and purity were achieved by pumping the PEO (100 ppm) as a sheath flow from the middle inlet and Newtonian sample from both sides at flow rates of 2.4 ml/h and 0.3 ml/h, respectively (Figure 2-23 b, c). They also showed that using a higher concentration of PEO solution causes 2 μm particles (platelets) to trap at the PEO/Newtonian solution interface which reduces the separation efficiency.

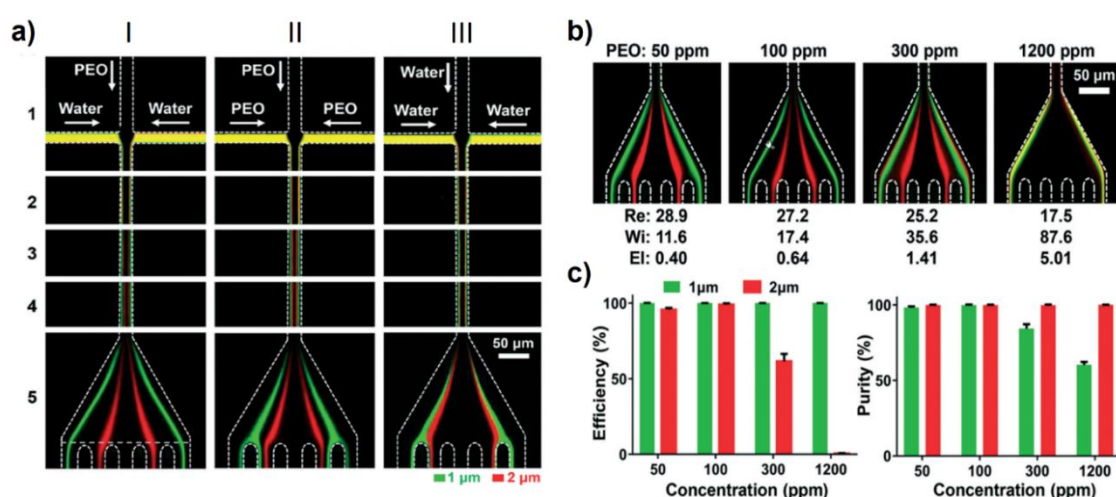


Figure 2-23: Separation of a mixture of 2 μm (red) and 1 μm (green) particles for different sample/sheath flow conditions: aI) Newtonian /viscoelastic, aII) viscoelastic/viscoelastic, and aIII) Newtonian/Newtonian. PEO solution with 100 ppm concentration was used for the viscoelastic medium. b) Particle trajectories for different PEO solution concentration at the channel outlet. c) Separation purities and efficiencies of 1 and 2 μm particles at different PEO solution concentrations ranging from 50 to 1200 ppm. Adapted with permission from Royal Society of Chemistry [104].

Recently, exosomes have drawn significant attention among scientists as therapeutic vehicles and potential diagnostic biomarkers for several diseases such as infectious diseases, cancer, and neurodegenerative disorders [108-110]. Exosomes, as one of the smallest extracellular vesicles (EVs) with diameter ranging from 30 to 200 nm, contain proteins and nucleic acids from their

originating cells and play pivotal roles in intercellular communications [111]. Even though exosomes are rich in our body fluids (e.g., urine, blood, saliva, and synovial fluid) the co-existence of other extracellular vesicles in our biofluids has great impacts on the precise analysis of exosomes. There is a crucial need to separate exosomes from other suspended EVs for better interpretation of the information carried by exosomes. There are few efforts on the purification and isolation of the exosomes using non-Newtonian sheath flow systems. In 2017, Liu et al. [112] separated exosomes from extracellular vesicles (EVs) using label-free, continuous viscoelastic sheath flow in a straight rectangular channel with high purity of 90% and exosomes recovery of 80% (Figure 2-24 a). Both sample and sheath flow were diluted by 0.1 wt% PEO. Sheath fluid was introduced from the middle channel and samples were pumped from side walls. Results showed that large EVs concentrated at the channel center due to the elasticity effects, while exosomes remained scattered in sample flows close to the walls and were collected from both sides (Figure 2-24 b).

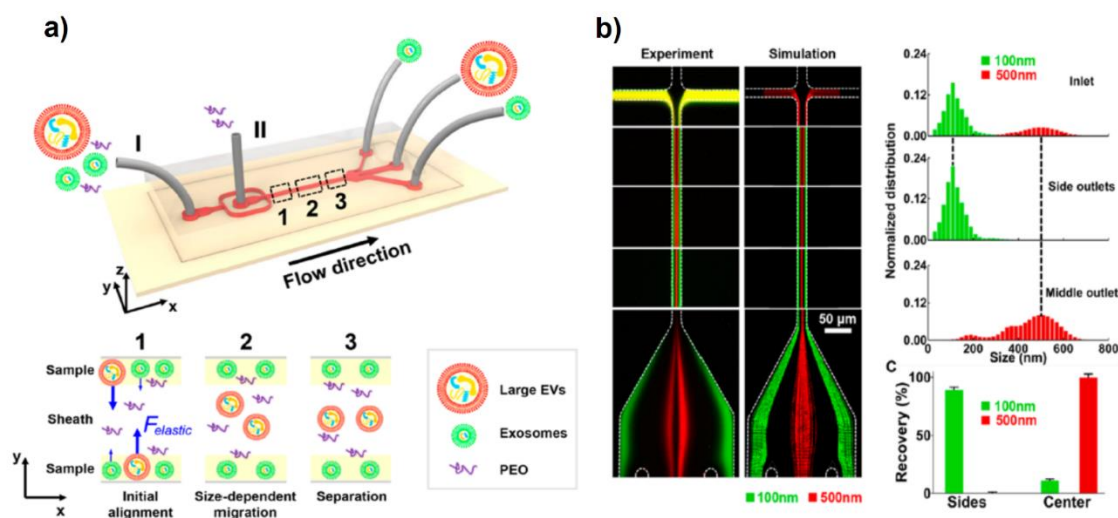


Figure 2-24: a) Schematic illustration of the microfluidic device for exosome isolation. b) Experimental and numerical results, showing the trajectories and separation of the 500 nm (red) and 100 nm (green) fluorescent particles. It also demonstrates the recovery rate for each particle as well as normalized distribution at each outlet. Adapted with permission from American Chemical Society [112].

In another work [30], the same group separated extracellular vesicles (EVs) with diameters ranging from 30 nm to larger than 1000 nm. EVs are generally categorized into three subpopulations including exosomes (30 to 200 nm), microvesicles (200 to 1000 nm) and apoptotic bodies (larger than 1000 nm) depending on their size and biogenesis. By pumping a

non-Newtonian sample (λ -DNA medium) from the middle inlet and Newtonian sheath flows (TBE) from side walls, they were able to separate these EVs size-dependently at flow rates of 50 $\mu\text{l/h}$ and 5000 $\mu\text{l/h}$ for the sample and sheath flows, respectively. Results showed 91% recovery and 96% separation efficiency for exosomes, 92% recovery and 94% separation efficiency for microvesicles, and 89% recovery and 93% separation efficiency for apoptotic bodies.

Although viscoelastic solutions have been proven to increase the focusing and sorting efficiency, it is of great importance to measure the flow instabilities caused by adding synthetic polymers to Newtonian fluids. Kim et al. [113] fundamentally studied the flow instabilities in a 90° curved microchannel for viscoelastic solutions of different concentrations over a wide range of flow rates (Figure 2-25 a). Results showed that instabilities in PEO solution happen when the PEO concentration is as low as 50 ppm. Interestingly these instabilities increase when concentration reaches the 500 ppm followed by a decrease when concentration approaches 3000 ppm (Figure 2-25 b). They concluded that the flow instability is more probable to happen in low viscosity and weak elastic-polymer solutions.

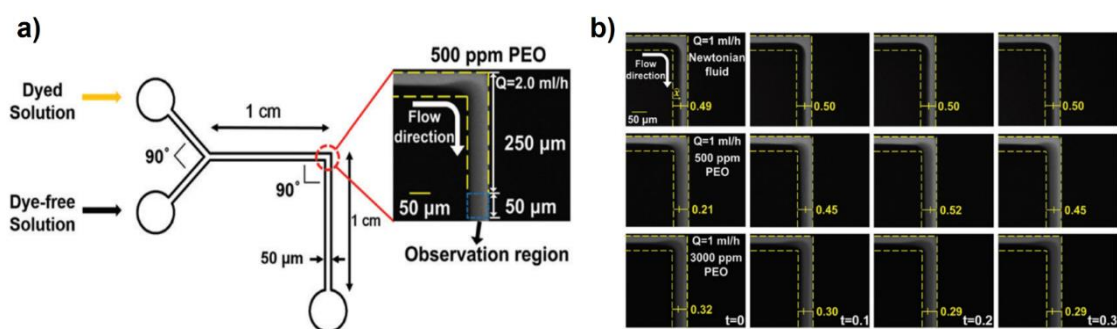


Figure 2-25: flow instabilities in a 90° curved microchannel a) Schematic illustration of the used microchannel for investigation of the flow instabilities for PEO solution. The microchannel geometry is almost a square ($50 \times 55 \mu\text{m}^2$). b) The flow dynamic behaviors, which is visualized with dye-free and dyed streams. The time interval between two successive images is 0.1 s. Adapted with permission from Royal Society of Chemistry [113].

Table 3 shows previous investigations carried out on the sheath flow elasto-inertial systems. It can be seen that all these studies were limited to the straight channel of rectangular and square geometries. This is due to the difficulty of microfabrication for channels with non-rectangular geometries, and the complexity of the particle migration analysis in co-flow systems.

After a thorough review of the literature and categorizing different systems used in elasto-inertial microfluidics, in the following section, the fabrication process of these devices will be explained. This helps investigators to not only learn the current methods of microchannel fabrication but also pave the way for proposing new fabrication methods suitable for inertial microfluidic applications.

Table 3: Studies performed on the sheath flow elasto-inertial microfluidic systems.

Reference	channel structure (μm^2)	Particle (μm)	Solution	throughput	purpose
Straight channel					
Nam 2012 [105]	straight rectangular 50×50	1, 5 and diluted blood	PEO 2MDa, 500 ppm	Sheath: 4 $\mu\text{l}/\text{min}$ Samples: 0.5 $\mu\text{l}/\text{min}$	Separation
Kang 2013 [56]	straight rectangular 52×50	1, 2.3, 4.5, 5.8 and 10.5	0.05 wt. % PEO 2MDa, λ -DNA (5 ppm)	Total of 100-2000 $\mu\text{l}/\text{h}$	focusing
Lim 2014 [106]	straight rectangular 100×50	1 and 10	PEO (2MDa, 500ppm) and PAA(Mw = 5MDa, 100ppm)	Total of 4.5 $\mu\text{l}/\text{min}$	Focusing
Lu 2015 [87]	straight square 50×50	1 μm and 5 μm /platelets diluted blood	PEO (2 MDa), 500 ppm	Sheath: 1 ml/h Samples: .1 ml/h	separation
Lu 2015 [107]	straight square 25×50	3,10	PEO (2 MDa), 50 to 3000 ppm	Sheath: 100 $\mu\text{l}/\text{h}$ Samples: 5 $\mu\text{l}/\text{h}$	Focusing/separation
Ha 2016 [103]	Straight rectangular 30×54	2 and 10	0.01% λ -DNA	Sheath: 80 $\mu\text{l}/\text{min}$ Samples: 40 $\mu\text{l}/\text{min}$	Washing and separation
Faridi 2017 [25]	straight rectangular 50 μm × 65	2, 5,10, bacteria and undiluted blood	PEO Mw = 2 MDa , 250, 500, 750 and 1000 ppm	Sheath: 360 $\mu\text{l}/\text{h}$ Samples: 30 $\mu\text{l}/\text{h}$	Separation
Tian 2017 [104]	straight rectangular 50×20	1, 2 Staphylococcus aureus, and platelets	PEO 2MDa, 100 ppm	Sheath: 2.4 ml/h Samples: 0.3 ml/h	separation
Liu 2017 [112]	Straight sheath 20×50	Exosomes from Extracellular Vesicles (100nm and 500nm)	PEO=600 kDa (0.1 wt. %)	Sheath: 2.4 ml/h Samples: 0.3 ml/h	separation
Kim 2017 [113]	Straight rectangular 50×55	1	PEO 2MDa, 250, 500 ppm	Sheath: 1 ml/h Samples: 1 ml/h	Mixing
Liu 2019 [30]	Straight rectangular 40×37	0.1, 0.2, 0.3, 0.5 and 2	150 ppm λ -DNA	Sheath: 500 $\mu\text{l}/\text{h}$ Samples: 50 $\mu\text{l}/\text{h}$	EXOs, MVs and ABs separation

2.5 Mold development of inertial microfluidic devices

Microfabrication is one of the most important stages in microfluidic researches since the efficiency and accuracy of the results are strongly related to the precision of the fabricated channels. There are different microfabrication techniques, but only a few of them are suitable for inertial microfluidic applications. This stems from the fact that many of the proposed methods lack enough surface quality, precision, and transparency which are essential for inertial microfluidic researches. Among all fabrication techniques suitable for inertial microfluidic applications, softlithography by PDMS is a gold standard for replicating microchannels. In this method a degassed mixture of PDMS and curing agent should be poured on a master mold, and then put in an oven at 65 °C for two hours. Finally, the cured PDMS should be peeled off and bonded to another substrate to make the final channel. However, master mold fabrication has

been always troublesome in this method due to the limitations of the available microfabrication techniques. In this section, all these techniques and their advantages and disadvantages are thoroughly explained.

2.5.1 Photolithography

Photolithography or optical lithography is a process to pattern some parts of a thin film (called a wafer) as a master mold. The schematic illustration of this process by negative photoresist is depicted in Figure 2-26. This approach employs light to start the polymerization reactions and copy the patterns on the photoresist through photomasks. SU-8 was first developed in the 1990s and has been increasingly used for microfabrication due to the high-resolution of the fabricated molds [114]. The technical process of SU-8 photolithography can be illustrated as follows. First, the surface of the wafer should be cleaned by acetone, methanol or other wet chemical treatment. Then, the wafer should be put on a hot plate (120°C) to drive off any moisture that may be present on its surface. To increase the adhesion between photoresist and the wafer an adhesion promoter such as hexamethyldisilazane (HMDS) can be applied. Following this, the light-sensitive material (mostly SU-8) is dropped onto the middle of the substrate (normally a silicon wafer) surface and spin-coated with a predefined rotational acceleration and speed (Figure 2-26 a). After that, the photoresist will be exposed to UV lights through a photomask to form the patterns on the uncured photoresist (Figure 2-26 b). Finally, the wafer is put on a hot plate for post-baking and immersed in a developer to wash the non-exposed or exposed regions based on the type of photoresist (Figure 2-26 c). This method can precisely produce extremely small structures, down to submicron sizes. However, the main drawbacks of this method are the expensive requirements, adroit operator, time-consuming, and inability to fabricate non-rectangular and non-planar geometries. Using this approach, many devices have been fabricated for cell isolation, blood fractionation, cell separation, and filtration, but all of them limited to the rectangular and square cross-sections. However, these inadequacies prevent

investigators from creating complex geometries, which are essential for many microfluidic applications.

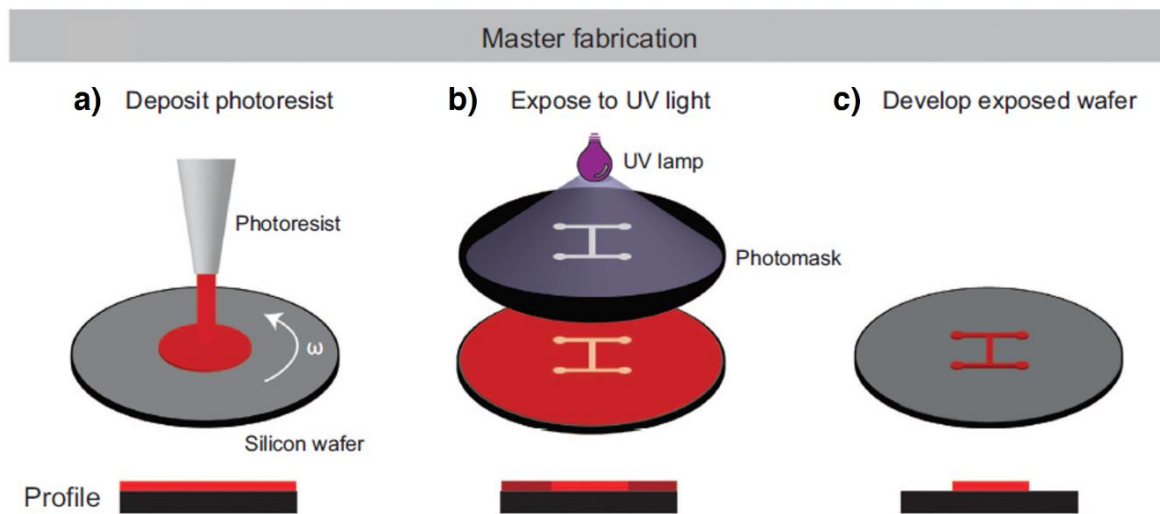


Figure 2-26: Schematic illustration of the mask fabrication by photolithography. a) Depositing photoresist on a silicon wafer, followed by spin coating to make a uniform layer on the wafer. b) Exposing the photoresist to the UV light through the mask. c) Washing the non-exposed or exposed regions by developer. Adapted with permission from Springer Nature [115].

2.5.2 Laser cutting:

Laser cutting is a method that utilizes a laser to cut different materials and is normally employed for industrial manufacturing purposes. Recently femtosecond and CO₂ laser ablation have been used to fabricate inertial microfluidic channels [116-119]. In laser ablation, the targeted pattern is fabricated by removing material from the surface of solid base (e.g. PMMA) through exposing it to a laser beam (Figure 2-27 a). While for high laser intensities, the material directly transforms to plasma, it is heated and evaporates for low laser intensities. Generally, in laser ablation the material is exposed to a pulsed laser; however, it can be irradiated to a continuous wave laser as long as the laser flux is high enough. After ablation, the debris produced during the ablation process must be cleaned from the structure [114]. Studies showed that among PMMA, cyclic olefin polymer (COP) and PS materials only microfabrication with PMMA can be used for inertial microfluidic applications since the PS and COP lose their transparency during the ablation process. Therefore, PMMA is the only feasible thermoplastic polymer for the construction of microfluidic channels using femtosecond laser among the mentioned materials [120]. While microfabrication with laser ablation is straightforward, the

limitation of fabricating curved geometries and requiring expensive equipment hindered its wide use. In addition, while CO₂ laser ablation can create triangular cross-sections with high aspect ratio as a negative master mold, double casting noticeably adds complexity to the fabrication process [121].

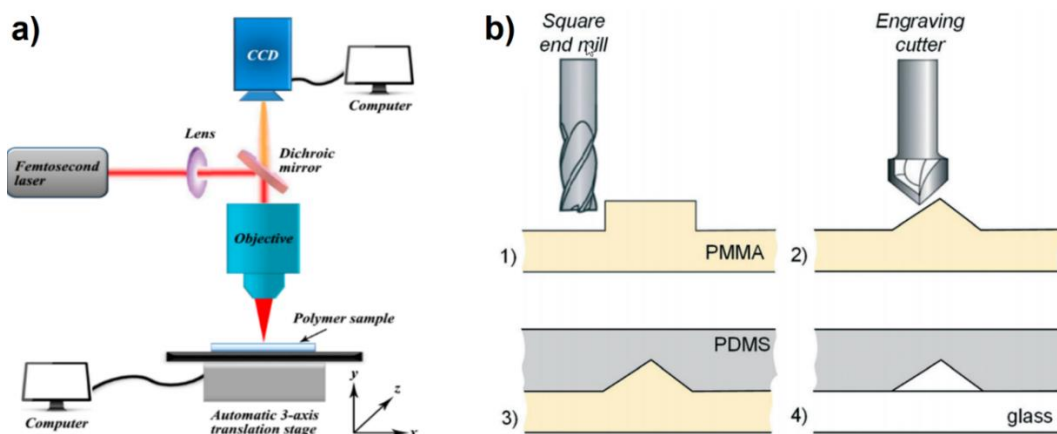


Figure 2-27: Schematic illustration of the mold fabrication by a) femtosecond laser ablation [114], and b) mechanical machining. Adapted with permission from Royal Society of Chemistry and MDPI [121].

2.5.3 Mechanical machining

Machining refers to any types of processes involves cutting a piece of raw material into a desired size and shape by an accurately controlled material-removal procedure known as subtractive manufacturing. There are different types of machining operations including drilling, turning, and milling, each of them is capable of creating a certain geometry and surface texture. For microchannel fabrication, generally, the master mold is fabricated by micro-milling on an aluminum block or PMMA sheet [122]. In micro-milling, a rotating tool with several cutting edges gradually moves relative to the material to create the final structure (Figure 2-27 b). For a long time, micromachining has been used to fabricate rectangular and trapezoidal molds for inertial microfluidic applications [122]. However, recently by engraving the cutter of milling machine, Mukherjee et al. [121] were able to fabricate straight triangular channel. Another approach to creat master mold is to use a cutting tool to make a scratch on the surface of the mold by using a sharp cutting device made of harder material [123]. While creating straight triangular geometry with milling and scribing methods are simple, controlling the

geometry and angles are very difficult especially for non-rectangular geometries. In addition, scribing approach not only generates a negative master mold which arises a double-casting issue for fabrication of the sealed microchannels, but also limits the integration of other channels with these triangular channels.

2.5.4 Etching:

Etching involves elimination of layers from the surface of a wafer by chemical materials during the manufacturing process. This method is a complex process module, in which every wafer undergoes several etching steps prior to the construction of the final design on the wafer (Figure 2-28). In general, for most etch steps, some parts of the wafer should be covered by an etching resistant material (mask) to protect it from the etchant. Some etchants erode the substrate in all directions (isotropic) and produce cavities under the mask; however, modern systems require sharp edges and well-controlled features, which makes use of anisotropic etches a crucial need. There are two types of etching for microfabrication including dry etching (plasma-phase) and wet etching (liquid-phase). The wet etching process is time-consuming and controlling the edges and the angles are troublesome in this method. Most of the etchants are isotropic and erode in all direction equally which reduces the accuracy of the final structure (Figure 2-28 a). Therefore, anisotropic wet etching (crystallographic etching) is more common due to its enhanced capabilities to erode in specific directions (Figure 2-28 b). The anisotropic etchants etch crystalline materials (e.g. silicon) at very different rates according to the direction of the erosion and exposed crystal face. Among various anisotropic wet etchants available for silicon, potassium hydroxide (KOH) has been widely used for microfabrication. This chemical shows an etch rate selectivity almost 400 times lower in $\langle 111 \rangle$ crystal directions than in $\langle 100 \rangle$ directions [124].

In dry etching, plasma is used to generate active free radicals to react at the surface of the silicon wafer. It should be noted that as neutrally charged particles attack the silicon wafer from all directions, this process is classified as isotropic. To address this difficulty, reactive-ion

etching (RIE) and Deep reactive-ion etching (DRIE) were introduced to fabricate microfluidic systems accurately. Using this method, Kim et al. [125] have constructed triangular channels with 90° and 70.6° tip angles to study the particle migration in non-rectangular cross-sectional geometries. Although etching is capable of mold fabrication with dimensions down to the nanometer, difficulty of controlling the geometry and angles limits its extensive use for creating master molds for inertial microfluidic applications. Also, anisotropic wet etching is typically limited to few geometries as a result of crystallography.

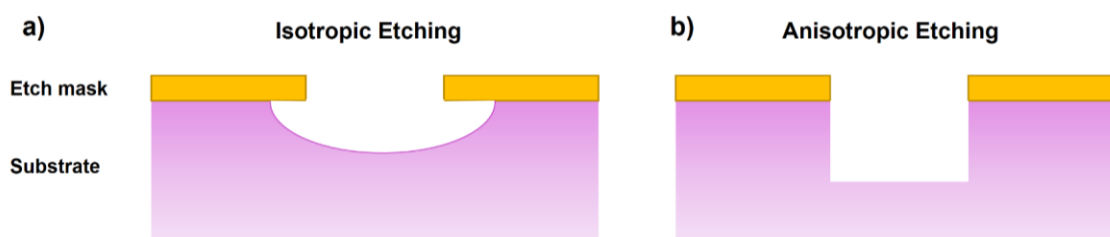


Figure 2-28: Schematic illustration of the mold fabrication by a) isotropic etching, and b) anisotropic etching.

2.5.5 Embedding micro-wire

Embedding micro-wire is another approach for fabrication of circular microchannels. In this method, wire of the desired diameter is embedded in an uncured PDMS. When the PDMS is cured, the wire is gently pulled out of the PDMS block [82, 126]. Despite the simplicity of this approach for microchannel fabrication, this method is limited to the straight circular channel, as wire removal in more complex channels can damage and rupture them. Apart from micro-wire, there are other materials which can be used as an embedded-mold; however, they have not employed for microchannel fabrication due to the low quality of the replicated channels and difficulty of mold removal from PDMS.

2.5.6 Hot embossing:

Hot embossing technology is a flexible and low-cost fabrication method which involves precise stamping of a pattern in a polymer material softened by increasing its temperature just above the melting point (Figure 2-29) [127]. It uses glass or polymer substrates to imprint planar structures created on a master stamp. The stamp employed to pattern the polymer can be

produced by different ways such as LIGA (**L**ithographie, **G**alvanoformung, **A**bformung), machining using a computer numerical control (CNC) tool (for making large features), and micromachining from silicon. So far, various polymers have been hot-embossed successfully with micron/submicron-sized features, such as PMMA and polycarbonate [128]. This method is mainly employed for patterning wells and micro-channels for fluidic devices. The advantages of this method are the capability to function with a variety of polymers, and the ability for rapid prototyping and high volume production with microscale features. However, all the channels in this approach should be planar with orthogonal geometries which limits the use of this method for fabrication of the 3D structures and 2D structures with non-conventional geometries. There are few studies used hot embossing for the fabrication of rectangular microchannels suitable for inertial microfluidic applications [129]. However, as mentioned earlier, these studies are restricted to the rectangular geometry and lack enough design flexibility which is vital in inertial microfluidic researches.

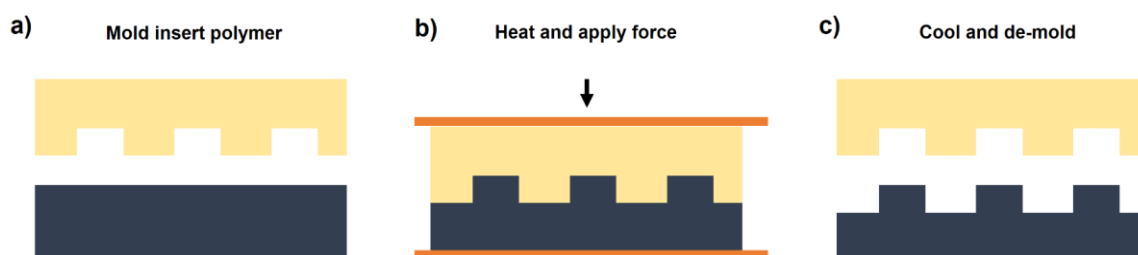


Figure 2-29: Schematic illustration of the mold fabrication by hot embossing method. a) Illustration of the stamp and the base. b) Heating the base and the stamp followed by pressing the structures together. c) Cooling and de-molding to fabricate the final structure.

2.5.7 3D printing:

Recently, additive manufacturing or 3D printing has emerged as a powerful platform for the fabrication of 2D and 3D structures with complex geometries. This technology can produce 3D objects with material being added together (such as powder grains or liquid molecules), typically layer by layer. One of the key benefits of additive manufacturing is the capability to create complex structures or geometries readily while requiring only a digital 3D model or a CAD file. Based on the type of material and printing method this technology can be classified

to different groups. Among them, SLA/DLP, FDM, and multi-jet are the machines that have been widely used for microfluidic applications.

In 1986, Chuck Hull introduced Stereolithography (SLA) and commercialized it at 3D Systems [130]. SLA has two important configurations: constrained surface approach (bat configuration) and free surface approach (bath configuration) [131]. In both configurations structures are constructed layer-by-layer by controlling the photo-polymerization of a liquid resin spatially. This process can be performed with either a digital light projector (DLP) or a scanning laser [132]. The bath design is the conventional setup for SLA machines in which a precise UV beam produces a planar geometry on a substrate immersed in a tank containing photoactive resin which polymerizes under illumination (Figure 2-30 a). After finishing each layer, the substrate moves further down into the resin, and the UV beam starts patterning the next layer on top of the former layer. Between every two consecutive layers, a blade levels the resins' surface to make sure a uniform layer of liquid before the next round of UV exposure. In this approach resin waste, extensive cleaning procedures, and chemical reactions with air are the main concerns. However, in bat configuration the object is constructed on a mobile substrate (picker) similar to a bat hanged from a ceiling (Figure 2-30 b). The picker is suspended over the resin tank, and the UV light source is positioned below the reservoir, which possesses an optically clear surface, and a non-adherent layer to prevent the printed object from sticking to the picker. The bat approach has numerous benefits compared to the bath systems which makes it more popular in stereolithography technique [133]. Although the height of the printed structure is not limited in bat setup compared to the bath configuration, each under-printing layer is confined to the resin vat and the previously cured layer. This may cause the cured resin to stick to the bottom of vat, which consequently leads to the deformation or breaking of the object when the picker is elevated from the vat [134]. Despite the great benefits of SLA/DLP printers for construction of directly printed parts [135], this method is not proper for creating microchannels owing to the difficulty of residual removal from the printed microchannels.

Moreover, the poor optical transparency of the current resins averts particle tracking for both fluorescent and non-fluorescent particles [136].

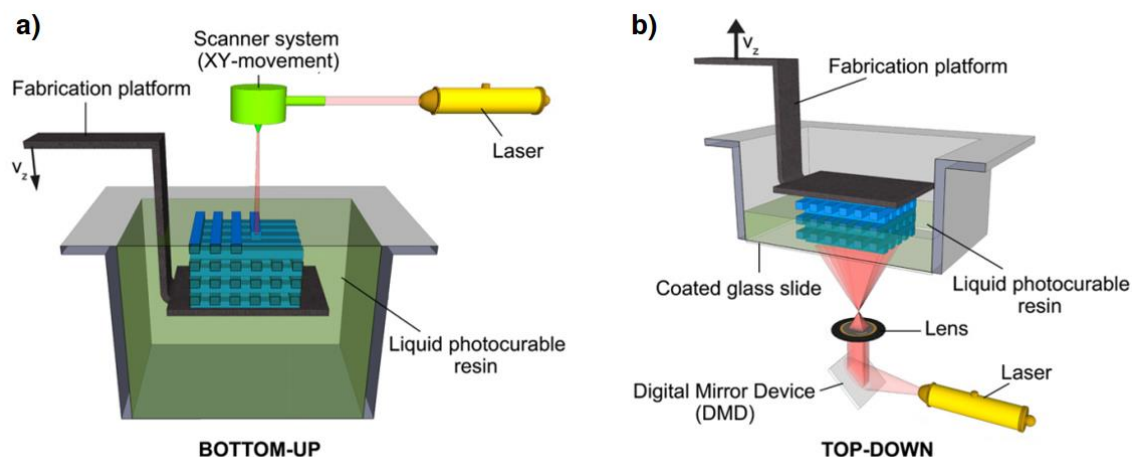


Figure 2-30: Schematic illustration of a) SLA, and b) DLP 3D printers. Adapted with permission from Elsevier [134].

In addition to the SLA and DLP 3D printers, fused deposition modeling (FDM) printer is one of the most broadly used 3D printing technologies. In FDM machine thermoplastic materials (in the form of filament) are extruded via a nozzle with high temperature to construct three-dimensional structures layer-by-layer [137]. The nozzle includes a temperature controller that keeps the filament temperature slightly above its melting point, causing the filament to easily flow through the nozzle. When one layer is printed, the build plate moves downward allowing the extrusion nozzle to print another layer on top of the previously printed layer. Recently, FDM printer has used to fabricate microchannels with non-rectangular geometries for inertial microfluidic applications [84]. However, mold fabrication with this method is troublesome as the printer nozzle needs to be modified for each shape and the final channels lack enough surface quality.

2.6 Applications of non-Newtonian systems

Non-Newtonian microfluidic systems have a myriad of applications in biomedical and biological researches. As mentioned earlier the presence of additional viscoelastic force in these systems cause particle focusing to happen for smaller particles and over a wider range of flow rates. Non-Newtonian systems can be utilized primarily for focusing, separation, washing,

stretching and mixing of particles and cells, which will be explained comprehensively in the following sections.

2.6.1 Particle focusing

The earliest application and goal of non-Newtonian systems were to focus particles for flow cytometry, high quality image processing, and pre-alignment for particle separation. There are several efforts on the focusing of bioparticles or cells using sheath or sheathless flow systems in straight and curved channels. For flow cytometry and image processing applications the desired focusing position is one line focusing at the channel center, where particles completely align with flow without any vibration and additional rotation [138, 139]. In Newtonian systems, particles focus at asymmetric positions, allowing them to freely rotate in their equilibrium position which makes the image processing troublesome. Benefitting from fluid viscoelasticity, Asghari et al. [138] developed a microflow cytometry in a straight capillary without need for any co-flow or other actuation mechanism to detect particles with cytometer throughput of around 750 events/s (Figure 2-31 a).

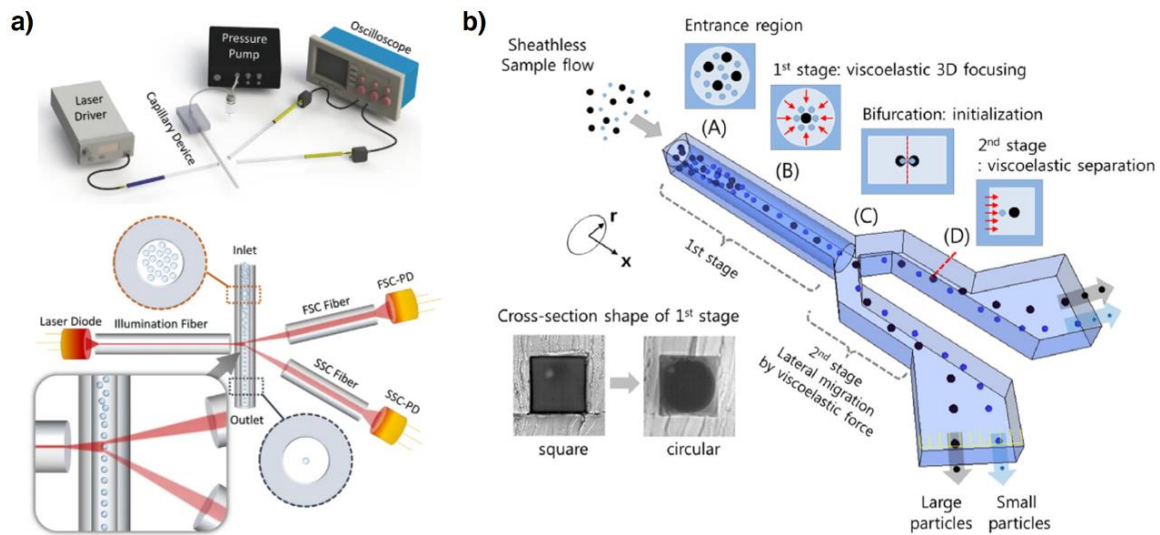


Figure 2-31: a) Schematic illustration of sheathless microflow cytometer and assembled components including chip, pressure pump, oscilloscope, laser diode and laser driver [138]. b) pre-alignment of the particles using non-Newtonian fluid. Adapted with permission from Springer Nature and Elsevier [91].

Dannhauser et al. [139] utilized 3D cell focusing in viscoelastic fluids and light scattering camera to characterize the morphological properties of RBCs. Also, effective viscoelasticity-

induced focusing in the channel centreline can noticeably increase the separation efficiency. Nam et al. [91] separated particles of different size by pre-aligning the particles in a circular channel connected to a high aspect ratio rectangular bifurcation (Figure 2-31 b).

2.6.2 Particle separation

Separation of a mixture of suspended particles has many practical applications in different disciplines. Most of the devices developed in inertial microfluidic researches aim at increasing the separation efficiency. There are several structures and designs for particle separation, all explained carefully in section 2.4. Generally, these devices were used for exosome, bacteria, cells, and particle separation. For instance, Liu et al. [86] separated RBCs and *E. coli* bacteria at very high-throughput using PEO solution. In another study, Faridi et al. [25] separated bacteria from whole blood using a sheath flow straight channel. Recently, Nam et al. [89] isolated *Candida albicans* (*C. albicans*) from blood using 0.1% hyaluronic acid (HA) solution. Benefitting from sheath flows, Liu et al. [112] separated exosomes from extracellular vesicles (EVs) in a straight rectangular channel. The same group separated extracellular vesicles (EVs) with diameters ranging from 30 nm to larger than 1000 nm [30].

2.6.3 Fluid exchange and cell washing

Washing and fluid exchange of particles and cells have various applications in clinical analysis and biology [26, 27]. Conventional methods for washing and fluid exchange (e.g., centrifugation) is time-consuming, not continuous and may damage the cells due to the high-speed rotation. Recently, microfluidic methods have proved to be good alternatives by increasing the efficiency and throughput of the washing process. Generally, passive techniques for cell washing are carried out in Newtonian solutions, which requires intricate designs and external forces for proper functioning. However, additional elastic force in non-Newtonian microfluidic systems to some extent addresses the mentioned issues, making them a better option for particle washing and fluid exchange. Using a non-Newtonian sheath flow system (Figure 2-32), Yuan et al. [31] washed and separated Jurkat cells from their culture medium. As

can be seen, larger particles are pushed to the Newtonian solution and washed throughout the channel while smaller particles remain in the sample fluid and exit the channel from the other outlet. Ha et al. [103] separated 10 and 2 μm particles with the same approach with high throughput of 6700 particle/s.

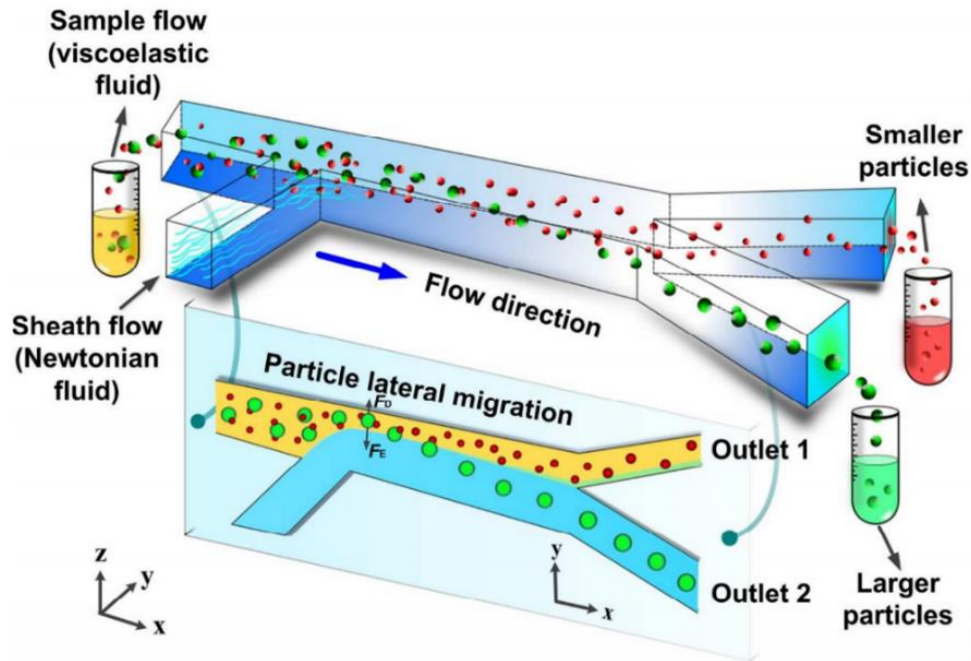


Figure 2-32: Schematic illustration of the non-Newtonian microfluidic device for cell washing. Adapted with permission from American Chemical Society [31].

2.6.4 Cell stretching measurement

Cell deformability is a promising approach for the diagnosis of diseases and controlling the quality of stem cells [140, 141]. There are several approaches to stretch cells and observe their deformability [142, 143]. Among them, inertial microfluidic platforms have recently garnered significant attention due to their high-throughput, simplicity, and cost-effectiveness [144]. Proper single-line focusing and flow stagnation is essential for effective cell stretching. Due to the enhanced capability of elasto-inertial systems for single-line particle focusing, Cha et al. [28] measured the cell deformability using viscoelasticity-induced particle migration at the conjunction of two straight channels (Figure 2-33 a), which showed a higher detection efficiency compared to its Newtonian counterpart. As Figure 2-33 b demonstrates, particles are aligned at the channel center more accurately in viscoelastic solution, which increases the stretching sensitivity.

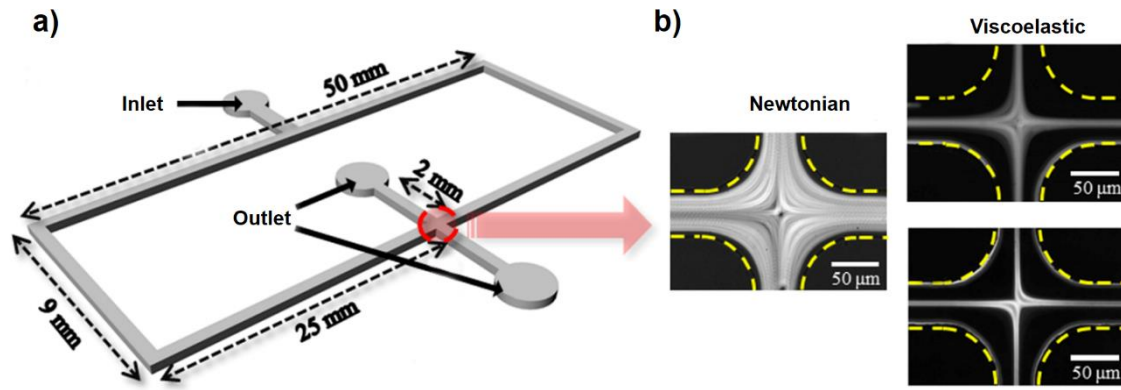


Figure 2-33: a) Schematic illustration of the device used for measuring the cell deformation. b) focusing results for Newtonian and viscoelastic solutions, showing the enhanced particle focusing in viscoelastic solution, which increases the sensitivity of the measurements. Adapted with permission from American Chemical Society [28].

2.6.5 Mixing

In contrast to the focusing applications, Hong et al. [101] proposed a microfluidic mixer based on the elasto-inertial instabilities formed by the presence of a low viscosity polymer solution (PEO) within a straight channel with side wells which functions appropriately over a wide range of flow rates (Figure 2-34 a). The presence of vortices in side wells generate lateral fluid motion, which consequently improves the efficiency of mixing (Figure 2-34 b).

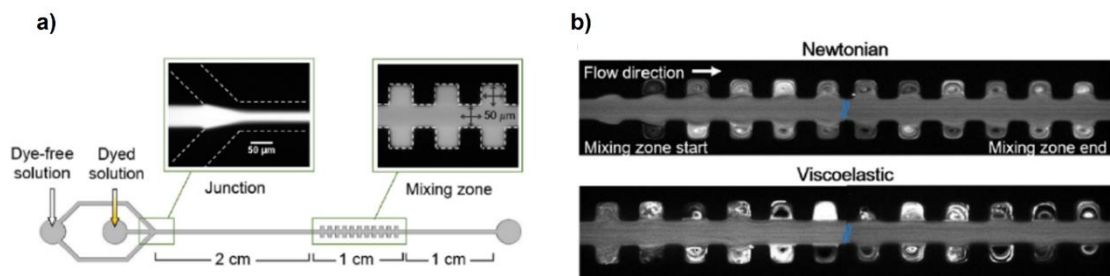


Figure 2-34: Microchannel used for the elasto-inertial mixing experiments. a) A viscoelastic or Newtonian fluid is pumped into one inlet, and the same fluid with fluorescent dye is pumped through the other inlet at the same flow rate. b) The mixing vividly happens at the side well locations. Adapted with permission from AIP Publishing [101].

2.7 Conclusion

In this chapter, the fundamentals of particle migration and its applications in non-Newtonian fluids through different channels were studied. The combined effects of inertia, viscoelasticity and dean drags were studied, and conditions in which these forces come into effect were explained. It was shown that, despite the capability of spiral channels for high-throughput

applications, few studies have been performed on its applications in elasto-inertial systems. Also, most of the investigations on elasto-inertial systems are focused on practical applications while very few studies devoted to the fundamentals. Therefore, in chapter four, we systematically investigate the focusing phenomenon in a non-newtonian solution for different conditions of flow rate, channel geometry, blockage ratio to achieve a profound knowledge about the particle migration in these systems.

A brief review on the microfabrication methods also showed that while there are different approaches for fabrication of microchannels suitable for inertial microfluidic applications, each has some downsides including low resolution, accuracy, time-consuming fabrication process, and cost. Therefore, finding a robust and easy fabrication method with acceptable channel accuracy and surface quality is still of great importance. To address the mentioned drawbacks in the previous methods, in chapter five and six, we develop two new workflows, based on wax 3D printing and DLP 3D printing, to readily fabricate non-planar microchannels suitable for inertial applications. Based on the proposed methods, for the first time, we fabricated some new complex channels and studied the fundamentals of elasto-inertial focusing in these channels. In addition, we used these channels for different practical applications (cell separation and focusing) to showcase their compatibility for biological applications. Also, by optimizing the geometry we introduced new geometries with enhanced efficiency for cell focusing and cell separation compared to the traditional rectangular channels under the same condition. Finally, in chapter seven, benefitting from the non-Newtonian property of blood and Zweifach-Fung effect, a novel design for plasma extraction is introduced.

3

Chapter Three: Methodology of sample preparation, device fabrication and experimental setup

3.1 Introduction:

In inertial microfluidic systems, the quality of results strongly relies on different parameters such as quality of the microchannels, human errors, accurate characterization of the working media, and quality of the technologies used for measurements and imaging. This chapter is categorized into four parts including solution characterization, sample preparation, device fabrication, and experimental setup to briefly explain how the mentioned criteria were satisfied. More detailed information can be found in the corresponding chapter.

3.2 Characterization of the PEO solution

In elasto- inertial microfluidic systems, elasticity and shear-thinning effects noticeably alter the focusing positions by changing the shear rate and elastic force. Two parameters that significantly affect the shear-thinning and viscoelasticity of the solution are the molecular weight of the polymer and solution concentration. Increasing the value of these two parameters intensifies the shear-thinning effects and elasticity. While elastic force is recognized as a positive force which directs the particles towards the channel center and modifies the focusing, shear-thinning effects cause particles to become unfocused and decrease the focusing efficiency. Therefore, in this section, we prepared various PEO solutions (Sigma-Aldrich) with different molecular weights and concentrations to analyze the effect of these parameters on particle focusing behaviors and to find the tightest focusing conditions for downstream analysis in elasto-inertial microfluidic systems. First, five different solutions with concentrations ranging from 500 ppm to 2500 ppm were made by adding PEO ($M_w=2\text{MDa}$) to PBS solution. After that, PEO polymers with molecular weights of 1 and 4 MDa were used to compare the effect of molecular weight on the focusing phenomenon. Figure 3-1 shows the focusing of 5 μm particles for different PEO ($M_w=2\text{MD}$) solution concentrations and flow rates. As can be seen, the tightest focusing band occurs around 1500 ppm for all flow rates. For concentrations lower and higher than 1500 ppm, the focusing bandwidth slightly increases. This behavior can be explained by the simultaneous effects of viscoelasticity, inertia and shear-thinning property.

Although at low concentration PEO solutions (500 ppm) the shear-thinning effects are negligible and elastic force pushes the particles toward the channel center, it is not strong enough to eliminate the impact of wall-directed shear gradient lift force at the core region, preventing particles from being tightly focused at the channel center. With increasing the PEO concentration to 1000 ppm, elastic force becomes more dominant and the focusing position becomes tighter around the channel core region. This behavior continues up to around 1500 ppm, where the focusing band has its narrowest form. From 2000 ppm, the focusing band starts widening showing that the shear-thinning effect comes into account.

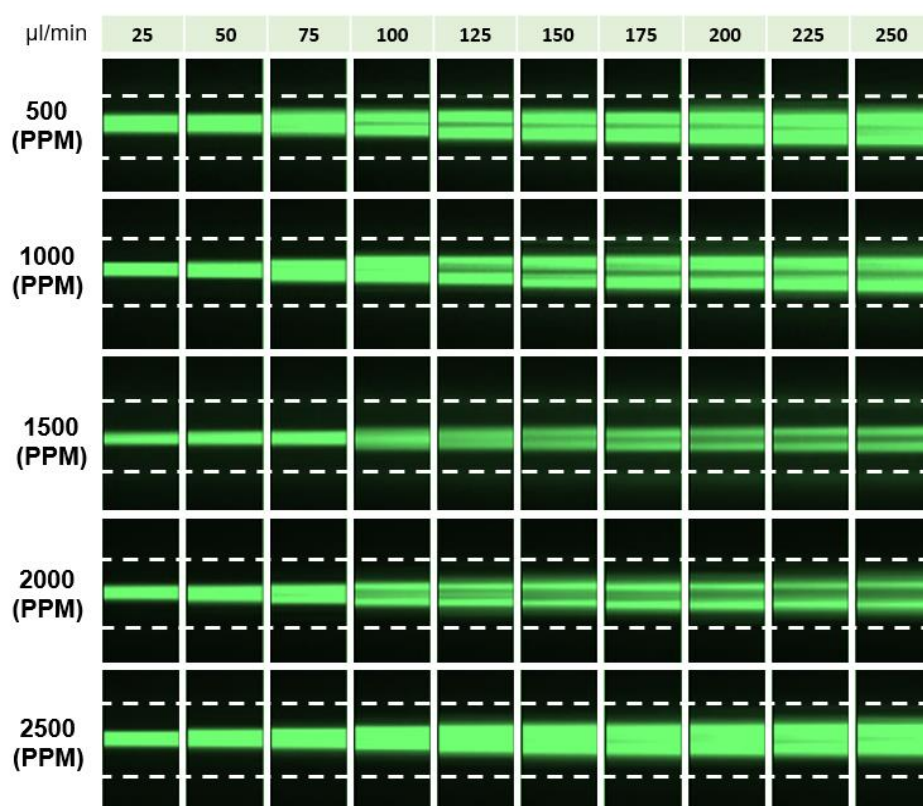


Figure 3-1: Focusing positions in a straight square channel for PEO solution with molecular weight of $M_w=2\text{MDa}$ at different concentrations. As can be seen, for PEO solution with the concentration of 1500 ppm, the tightest focusing band has been achieved.

It seems from 2500 ppm onward, the shear-thinning property overcomes the viscoelastic force and particles begin to move towards the walls. It is worth mentioning that the shear-thinning property causes the viscosity to decrease by increasing the shear rate. Therefore, in the core region, the shear-thinning effect not only reduces the elastic force but also increases the shear gradient lift force, causing particles to defocus slightly. As shown in Figure 3-1, the focusing

band becomes wider for all conditions by increasing the flow rate. This stems from the fact that for both low and high concentrated solutions, increasing the flow rate, intensifies the inertial forces and shear-thinning effects.

Similar experiments have been performed for 13 μm particles and the same behaviors have been observed (Figure 3-2). However, the focusing bands become tighter for 13 μm particles over a wider range of flow rates as elastic force increases noticeably with the particle size increase.

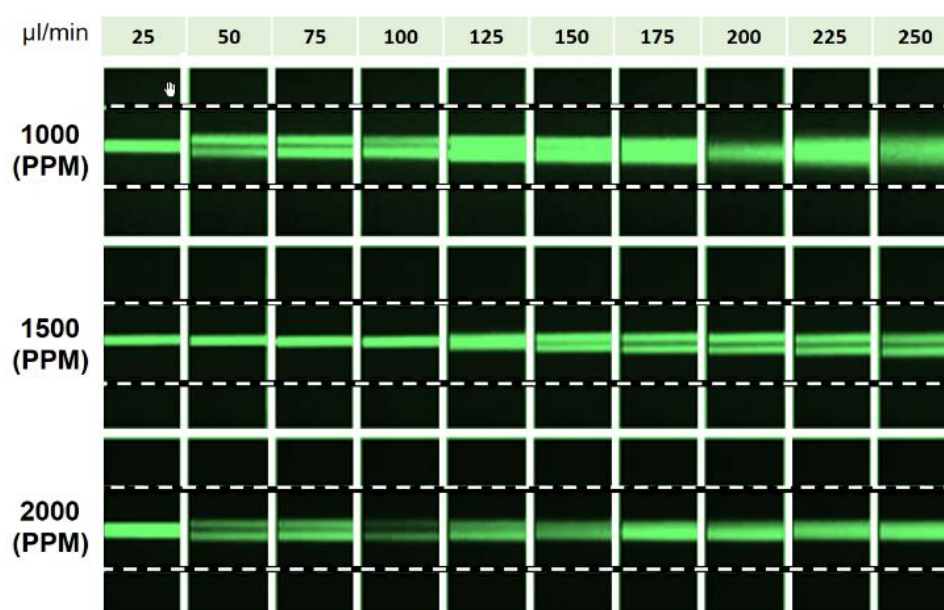


Figure 3-2: Equilibrium positions for 13 μm particles in a straight square channel which shows that the tightest focusing band for PEO solution with $M_w=2\text{MDa}$ occurs at 1500 ppm.

After investigating the effect of solution concentration and obtaining the optimal concentration for tightest focusing bandwidth, it is now time to study the effect of polymer molecular weight on focusing phenomenon. To this end, three PEO solutions with different molecular weights of 1, 2 and 4 MDa were made. According to Figure 3-3 by increasing the molecular weight from 1 to 2 MDa, focusing bandwidth decreases slightly, showing that the elasticity force strengthens while the shear-thinning effects are still negligible. However, for 4 MDa PEO solution, since the shear-thinning effects dominate the elastic force, particles start defocusing. Based on these characterizations, it is quite clear that there is an optimum value for solution concentration and molecular weight in sheathless straight channels which gives the tightest focusing. For our

experiment, the tightest focusing occurs for 2 MDa molecular weight and 1500-2000 ppm solution concentration.

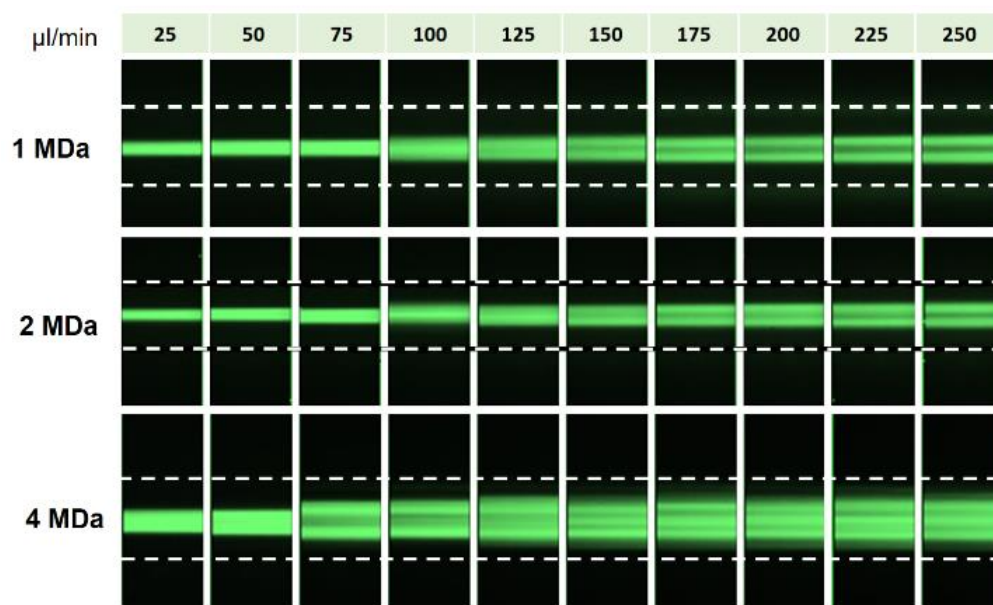


Figure 3-3: Equilibrium position for 13 μm particles in a straight square channel which shows the tightest focusing band occurs at 1500 ppm for PEO ($M_w=2\text{MDa}$) solution.

3.3 Sample preparation

Throughout this research, mixture of Newtonian or non-Newtonian solutions with different particles and cells are used for various applications. We use fluorescent 3, 5, 10, 13, and 50 μm particles with 5×10^4 particle/ml concentration to visualize the particle trajectories for all solutions. However, in each chapter, cell concentrations are measured based on the best separation or focusing conditions. To study the fundamentals of particle focusing in straight channels, we use PEO solution with 2MDa molecular weight and 2000 ppm concentration. For the focusing of the yeast cells, 3×10^6 cells/ml solution is used. The detailed information about cell culture and sample preparation are provided in the corresponding chapter.

3.4 Device fabrication

One of the most challenging steps in inertial microfluidic studies is the microchannel fabrication process. Throughout this study, we use different fabrication processes and propose new fabrication workflows. Each method is thoroughly explained in the corresponding chapter, but here we will explain the overall fabrication workflows for each study.

In chapter four, all the channels are created by micro-milling on an aluminum mold and tested for the quality and accuracy of the channels. Figure 3-4 shows the results of the analysis for the square channel, which shows less than 6% error in dimensions between the designs and fabricated channels.

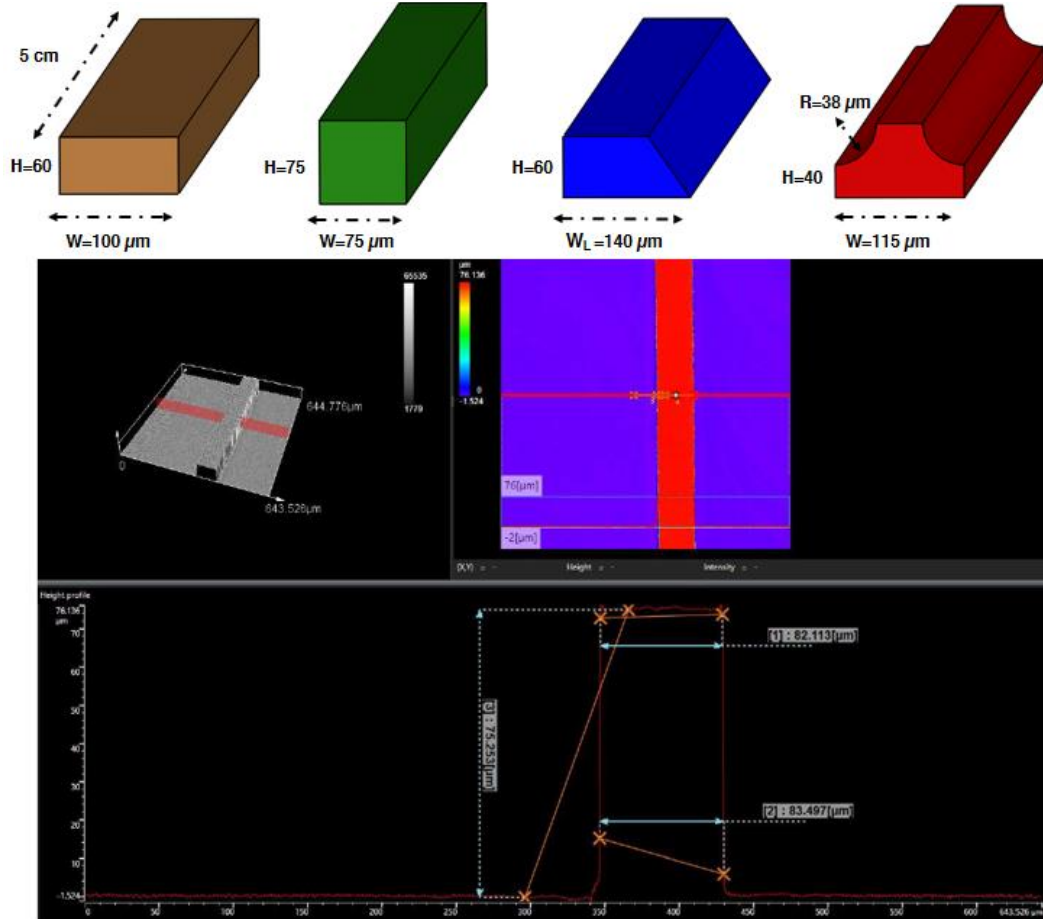


Figure 3-4: Inspection results for the Aluminum mold. It shows approximately 6% errors in dimensions. The same characterization has done for other geometries and almost the same dimension error has been obtained. It should be noted that we proposed a new complex straight channel with higher focusing capabilities, fabricated by cutting the upper corners of the rectangular channels.

In chapter five, we propose wax 3D printing method since micro-milling is unable to fabricate non-planar geometries (i.e., curved circular or triangular channels). For the first time, we tailor this printing technology to create microchannels with arbitrary cross-sections. We create different straight and curved channels with rectangular, trapezoidal, triangular, and circular geometries to demonstrate the ability of this method for microfabrication as well as

analyzing the focusing phenomenon in curved non-conventional geometries. The technical information is provided in chapter five. Despite the simplicity of fabrication process in wax 3D printing method, the fragility of the printed channels and the resolution of the current wax printing machines prevent further down-scaling the channel dimensions.

In chapter six, we propose a new methodology for fabrication of direct-3D-printed microchannels with arbitrary cross-sections suitable for inertial microfluidic applications. Using DLP technology and optimizing the printing parameters as well as benefitting from double-adhesive tapes and transparency of the PMMA sheets, we addressed many of the limitations and difficulties scientists have experienced during the fabrication process by conventional methods. More information about the characterizations and fabrication workflow is provided in chapter six.

In chapter seven, we fabricate the channels by casting PDMS on a mold created by photolithography on a silicon wafer. Photolithography is a key standard for the fabrication of the planar geometries which was thoroughly described in the previous chapter. The detailed information and geometrical parameters are explained in chapter seven.

3.5 Experimental setup and Image processing

After the fabrication of microfluidic devices, they are mounted on an inverted microscope (Nikon Eclipse Ti) and connected to the syringe pump (Nexus 3000) by 1.5 mm tubes. Different cameras are employed to observe the fluorescent particles' and cells' trajectories in the channels. To observe the yeast cells and fluorescence particles, high speed (Phantom- VEO 640L) and 14-bit CCD cameras (NIKON DS-Qi1Mc) are used, respectively. The exposure time and microscope objective are set to 60 μ s and 10X for bright-field imaging and 800 ms and 10X for fluorescence microscopy. For visualizing the 50 μ m particles and microcarriers, the exposure time and long-working-distance objective are set to 400 ms and 4X, and 60 μ s and 4X, respectively. All the image analyses and post-processings have been performed by the ImageJ software.

4

Chapter Four: Experimental and numerical study of Elasto-Inertial focusing in straight channels

(PAPER I)

Introduction

Elasto-inertial microfluidic has been a flourishing area of research in recent years due to its capabilities to accurately control and manipulate particles. In this chapter, we investigated the effects of channel geometry, corner angle, aspect ratio, blockage ratio, elasticity, and flow rate both experimentally and numerically on the particle migration in elasto-inertial systems. Based on our findings, we proposed a new channel with higher capabilities for tighter particle focusing over wider flow ranges. We showcased the capability of the channel for particle sorting by focusing of the yeast cells at high- throughput of 100 $\mu\text{l}/\text{min}$.

Authors' contributions:

1) Mohammad Amin Raoufi:

Designing all the channels, characterizing the PEO solution to get the best focusing conditions, running all the experiments, understanding the fundamentals and equations for elasto-inertial systems, writing the algorithm for DNS simulation, writing more than half of the paper.

2) Ali Mashhadian:

Running the simulations, writing some parts of the manuscript

3) Hamid Niazmand, Mohsen Asadnia, Amir Razmjou, and Majid Ebrahimi Warkiani

Revising the paper

Paper details:

***This chapter has been published in *Biomicrofluidics* journal.**

I. Raoufi M.A., Mashhadian A., Niazmand H., Asadnia M., and Warkiani M.E, Experimental and numerical study of Elasto-Inertial focusing in straight channels. Biomicrofluidics, 2019. Doi. 10.1063/1.5093345

*The paper is presented here with the permission of AIP Publishing.

Experimental and numerical study of Elasto-Inertial focusing in straight channels

Mohammad Amin Raoufi^{1,2,3‡}, Ali Mashhadian^{4‡}, Hamid Niazmand³, Mohsen Asadnia², Amir Razmjou⁵, and Majid Ebrahimi Warkiani^{1,6*}

¹*School of Biomedical Engineering, University of Technology Sydney, NSW, 2007, Australia*

²*School of Engineering, Macquarie University, NSW, 2109, Australia*

³*Department of Mechanical Engineering, Ferdowsi University of Mashhad, Mashhad, Iran*

⁴*Department of Mechanical Engineering, Sharif University, Tehran, Iran*

⁵*UNESCO Center for Membrane Science and Technology, School of Chemical Science and Engineering, University of New South Wales, Sydney, 2052, Australia*

⁶*Institute of Molecular Medicine, Sechenov First Moscow State University, Moscow 119991, Russia*

[‡] Both authors contributed equally to this manuscript

Corresponding Author: Majid Ebrahimi Warkiani (*majid.warkiani@uts.edu.au*)

Abstract

Elasto-inertial microfluidics has drawn significant attention in recent years due to its enhanced capabilities compared to pure inertial systems in control of small microparticles. Previous investigations have focused mainly on the applications of elasto-inertial sorting, rather than studying its fundamentals. This is because of the complexity of simulation and analysis, due to the presence of viscoelastic force. There have been some investigative efforts on the mechanisms of elasto-inertial focusing in straight channels; however these studies were limited to simple rectangular channels and neglected the effects of geometry and flow rates on focusing positions. Herein, for the first time, we experimentally and numerically explore the effects of elasticity accompanying channel cross-sectional geometry, and sample flow rates on the focusing phenomenon in elasto-inertial systems. The results reveal that increasing the aspect ratio weakens the elastic force more than inertial force, causing a transition from one focusing position to two. In addition, it was shown that increasing the angle of a channel corner causes the elastic force to push the particles more efficiently towards the center over a larger area of the channel cross-section. Following on from this, we proposed a new complex straight channel which demonstrates a tighter focusing band compared to other channel geometries. Finally, we focused *saccharomyces cerevisiae* cells (3-5 μm) in the complex channel to showcase its capability in focusing small-size particles. We believe that this research work improves the understanding of focusing mechanisms in viscoelastic solutions and provides useful insights into the design of elasto-inertial microfluidic devices.

Keywords: *Elasto-Inertial microfluidics; Viscoelastic solution, Particle focusing; Direct numerical simulation; Saccharomyces cerevisiae cell*

4.1 Introduction

Microfluidics deals with the manipulation and precise control of flows geometrically restricted to sub-millimeter scales. Microfluidic devices can be categorized as either passive or active, depending on the source of the manipulating forces [11]. While majority of microfluidic devices work in a Stokes flow regime and at low-Reynolds number ($Re = \rho_f U_{max} D_H / \mu$, where ρ_f is the fluid density, U_{max} is the maximum flow velocity, D_H is the hydraulic diameter and μ is the fluid dynamic viscosity) [12, 145-147], inertial microfluidic devices work within intermediate Re numbers between Stokes and turbulent regimes [17, 148]. The lateral migration of flowing particles inside a tube was first discovered by Segré and Silberberg about 60 years ago [18]. However, inertial microfluidics was first demonstrated by Di Carlo et al. [67] in 2007, and since then has been widely used for variety of applications including cell isolation [149-152], blood fractionation [153, 154], cell separation [155, 156], cytometry [157, 158] and filtration [122, 159, 160].

Conventional inertial microfluidic devices have been working with Newtonian solutions flowing through patterned non-structured channels such as spiral, serpentine, and expansion-contraction with rectangular, square and trapezoidal cross-sections [151, 161, 162]. While these devices have been capable of sorting bioparticles for various biomedical applications, their usage has been limited to particles larger than 6 microns (*i.e.* larger than a red blood cell (RBC)) due to the strong correlation between particle size and inertial lift forces [163]. To passively control smaller microparticles in Newtonian solutions, either the channel length has to be increased, making the device footprint impractical, or the channel hydraulic diameter needs to be reduced [66, 164], which increases the pressure drop to an extent that the whole device becomes impractical.

To address this problem, investigators have recently started to use viscoelastic solutions such as polyvinylpyrrolidone (PVP), polyacrylamide (PAA), and Polyethylene oxide (PEO). For example, Faridi et al. [165] used sheath viscoelastic flow to separate 5 and 2 μm particles,

as the 5 μm particles focus at the center while the 2 μm particles remain scattered in the pinched flow near the channel walls. In another study, using expansion-contraction cavities, Yuan et al. [94] focused 3.2 and 4.8 μm particles in 500 ppm PEO solution. In viscoelastic fluids, due to the extra viscoelastic forces arising from the gradients of normal stresses ($N_1(\dot{\gamma}) = \sigma_{XX} - \sigma_{YY}$, $N_2(\dot{\gamma}) = \sigma_{YY} - \sigma_{ZZ}$), particle focusing can happen even in a very low Re numbers [47, 97]. It has been proven that fluid elasticity directs flowing particles towards the lowest shear gradient regions, which are the centerline and corners for a rectangular Poiseuille flow [76] and the centerline for cylindrical Poiseuille flow [77]. So far, several research has been performed on the applications of elasto-inertial microfluidics including cell stretching measurements [28], size-based cell separation [86, 105], sheath flow particle separation [112], sheathless particle focusing [55, 91], and Dean-flow-coupled elasto-inertial particle focusing [94, 96] with particle sizes ranging from tens of microns down to nano-scale. However, only a limited number of studies have focused on the fundamentals and mechanisms of elasto-inertial focusing. For example, in 2016, Xiang et al. [97] studied elasto-inertial focusing in curved channels both numerically and experimentally. Their results revealed that the contribution of Dean forces in focusing is only important at high flow rates causing the particles to focus near the outer edge of the channel. Yang et al. [55] experimentally investigated the effects of elasticity on particle focusing in a straight rectangular channel and observed even a low level of elasticity can cause particles to focus at the channel center. Li et al. [70] carried out a numerical study of the lateral migration of spherical particles through a square channel. They showed that secondary flows around particles and shear-thinning effects tend to push the particle towards the channel wall. Patankar et al. [166] investigated the effect of viscoelasticity on lateral migration of a single particle by the direct numerical simulation method. They showed that in an Oldroyd-B fluid, elastic shear stress has an insignificance effect on the lift force, and the major impact of viscoelasticity is on the pressure. Seo et al. [77] studied the effect of flow rate, blockage ratio, and the shear-thinning properties of PEO and PVP solutions on the focusing of 15 μm particles

in a straight channel. Their results showed that while under pure viscoelastic condition particles focus at the center and the corners of the channel, under the combined effect of inertia and elasticity the particles focus at the center of the channel. The channel geometry used in these studies was rectangular, for ease of fabrication and simulation. While informative, none of these prior research has experimentally and numerically studied the effects of channel geometry, solution viscoelasticity and sample flow rate on the focusing behavior of elasto-inertial systems.

In this paper, we commenced with experimental investigation of the focusing patterns of 10 and 5 μm particles in square, rectangular and trapezoidal straight channels using a viscoelastic solution (PEO). Then, by modeling particle fluid interactions using a direct numerical simulation method (DNS), for the first time, we studied the effect of channel geometry and corner angle on particle focusing in viscoelastic solutions. Based on that work, we proposed a novel complex straight channel in order to achieve tighter focusing compared to other channels under the same conditions. The complex channel was first numerically modelled and then tested with 5 and 3 μm particles for validation and comparison with other channels. Finally, as a proof of concept, we showcased focusing of *saccharomyces cerevisiae* cells (3-5 μm size) through the complex channel to prove its suitability for focusing of biological samples.

4.2 Numerical Simulation

4.2.1 Background

The lateral movement of neutrally buoyant particles in a shear-thinning viscoelastic solution flowing through a microchannel mainly originates from four different lift forces, including shear gradient (F_s), wall induced (F_w), Magnus (F_Ω) and elastic (F_E) forces. Generally, inertial forces can be considered negligible unless the particle size becomes comparable to the characteristic length of the channel, $a/D_H > 0.07$ where a and D_H are particle diameter and channel hydraulic diameter respectively [67]. Figure 4-1a shows particle focusing in a straight rectangular channel and the corresponding forces for both Newtonian and viscoelastic solutions. As can be seen in wall-bounded Poiseuille flow, shear gradient lift force arising from

the relative velocity difference around the particle pushes the particles away from the channel center [167]. On the other hand, wall induced lift force originating from the unbalanced pressure distribution over the particles adjacent to the walls repels the particles away from the walls [44]. This pressure dissymmetry caused by fluid flow deceleration between the wall and its adjacent particles increases the pressure in this region and consequently pushes the particles towards the channel center [168]. The Saffman force can be considered zero for a buoyant particle in a Poiseuille flow, since the Stokeslet flow originating from a particle lagging relative to the shear flow is balanced by the Stokeslet velocity field generated by the curvature of the bulk flow [167]. Asmolov derived an equation for the net inertial lift force (F_L) on a rigid sphere in a Poiseuille flow caused by shear gradient and wall induced forces as follow [64]:

$$F_L = C_L \rho_f \gamma^2 a^4 \quad (4-1)$$

where C_L denotes the dimensionless lift coefficient, γ represents the shear rate, ρ_f is the solution density and a is the diameter of the particle.

Magnus force originates from the rotation of the sphere particles in an inertial flow and can be described by the following equation [169]:

$$\vec{F}_\Omega = \frac{1}{8} \pi r a^3 \rho_f (\vec{u}_f - \vec{u}_p) \times \vec{\Omega} \quad (4-2)$$

where Ω is the vector of angular velocity of the sphere, and u_p and u_f represents the sphere and flow axial velocity respectively. This force is taken into account in regions where the wall induced and shear gradient lift forces balance each other.

Viscoelastic force arising from the solution viscoelasticity pushes the particles towards the regions with lower shear stress values and can be described as [97]:

$$F_E \sim a_p^3 \nabla N_1(\dot{\gamma}) \quad (4-3)$$

Where ∇N_1 and $\dot{\gamma}$ are the gradient of first normal stress difference and average (characteristic) shear rate. For most viscoelastic fluids, $N_2(\dot{\gamma})$ values are very small and can be considered negligible compared to the corresponding $N_1(\dot{\gamma})$ values under most conditions [106].

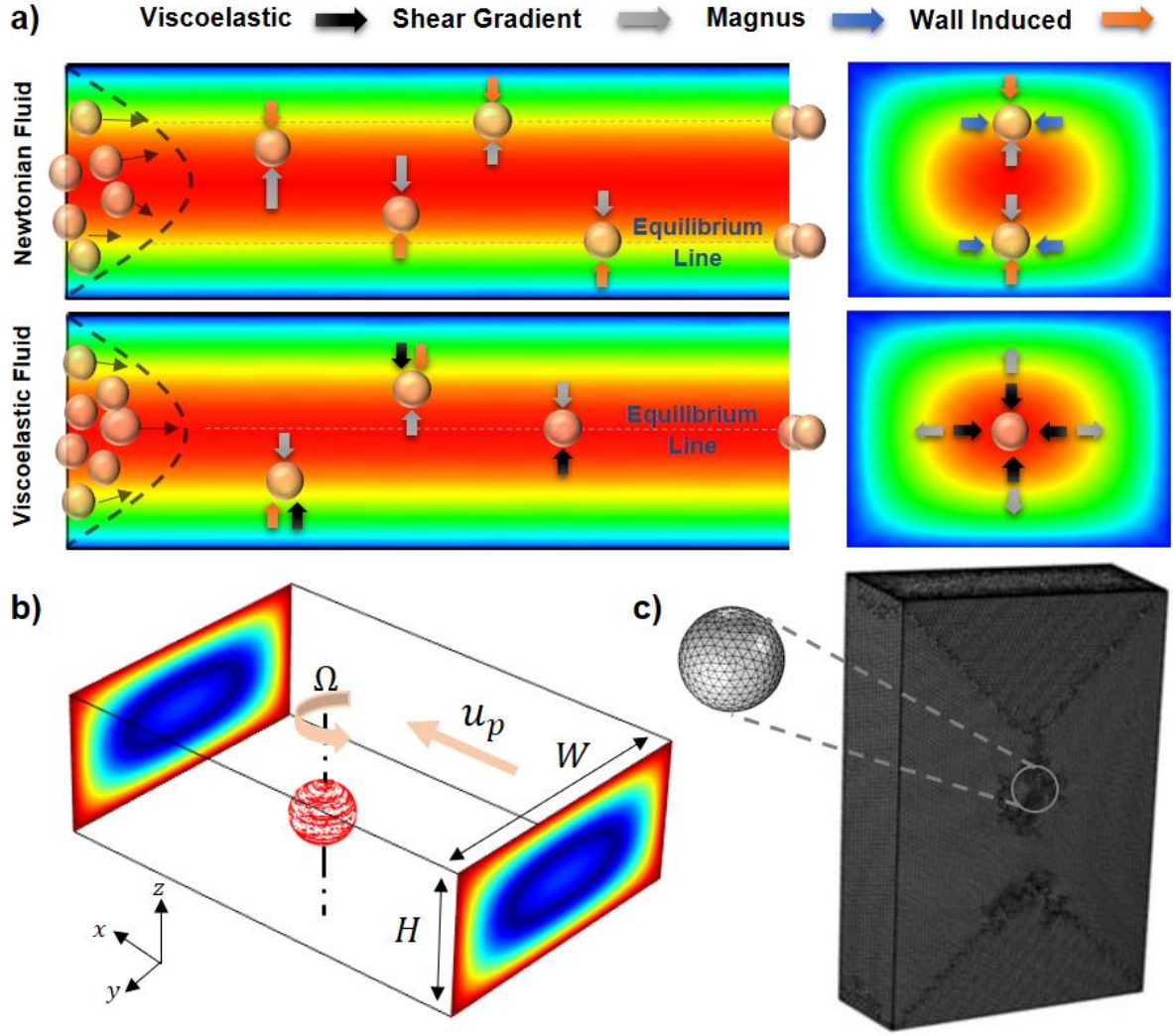


Figure 4-1: a) Different equilibrium positions and their corresponding forces for Newtonian and viscoelastic solutions in a straight rectangular channel. b) Schematic of the particle modeled in a portion of a rectangular channel for DNS. c) Mesh configuration for the portion of the channel with a length of $20a$, and boundary mesh on the surface of the particle.

4.2.2 Direct numerical simulation method (DNS)

In this study, the DNS method was used to precisely model the interactions between flow and particles and to measure the elasto-inertial forces acting on the particles [170]. To this end, flow field through the channel is first calculated using continuity and momentum equations (Eq. (4-4) and (4-5)) by considering the particle as an obstacle only permitted to have free rotational movement (Fig. 1b).

$$\nabla \cdot \mathbf{u} = 0 \quad (4-4)$$

$$\rho \left(\frac{\partial \mathbf{u}}{\partial t} + (\mathbf{u} \cdot \nabla) \mathbf{u} \right) = -\nabla p + \eta_s \nabla^2 \mathbf{u} + \nabla \cdot \boldsymbol{\tau} \quad (4-5)$$

In Eq.5, τ and η_s are the polymeric part of the extra stress tensor and the Newtonian viscosity of the fluid, respectively [74]. It should be noted that in the case of Newtonian fluid, τ is equal to zero. Yang et al. [23] experimentally proved that for low concentration of PEO solution (less than 2500 ppm) the shear-thinning property of the PEO solution can be considered negligible. Since elasticity has more effects on particle migration than the shear-thinning behavior of the PEO solution (2000 ppm) [23, 147], Oldroyd B equation (Eq. (4-6)) is used to calculate the extra stress tensor used in Eq.5.

$$\tau + \lambda \left(\frac{\delta \tau}{\delta t} + u \cdot \nabla \tau - \nabla u^T \cdot \tau - \tau \cdot \nabla u \right) = \eta_p (\nabla u + \nabla u^T) \quad (4-6)$$

where λ and η_p indicate the relaxation time and polymeric viscosity, respectively [74]. The value of relaxation time (λ) and viscosities of the PEO solution (η_p) were measured using a capillary breakup extensional rheometer (CaBER-1, ThermoHakke) and a rotational rheometer (MCR- 301, Anton Paar) respectively, which are $\lambda_{mean} = 0.0106$ s and $\eta_p = 0.031$ for PEO solution (2000 ppm).

After solving the momentum equation and obtaining the flow field, particle linear and angular acceleration are obtained based on Newtown's second law (Eq. (4-7) and (4-8)) by integrating the total stresses over the particle's surface in all three directions.

$$m \frac{du_p}{dt} = \oint_{\partial V_p} \left[\underbrace{-PI + \eta_s (\nabla u + \nabla u^T)}_{\text{Inertial part}} + \underbrace{\tau}_{\text{Elastic part}} \right] \cdot n \, dS \quad (4-7)$$

$$I \frac{d\Omega_p}{dt} = \oint_{\partial V_p} r \times \left\{ \left[\underbrace{-PI + \eta_s (\nabla u + \nabla u^T)}_{\text{Inertial part}} + \underbrace{\tau}_{\text{Elastic part}} \right] \cdot n \right\} dS \quad (4-8)$$

The total stress tensor is divided into two separate inertial and elastic parts (Eq. (4-7) and (4-8)) which enables us to measure the effects of each force individually (The whole algorithm for DNS method and lift forces calculation flowchart can be seen in Figure 2-3). According to Figure 4-1b a moving wall and slip velocity boundary conditions are used for the channel walls and the particle's surface, respectively. Also, laminar inflow and outflow conditions are considered at the channel inlet and outlet correspondingly. The boundary conditions for the

channel and particle with their corresponding values are presented in Table 4. In this table, U and \vec{r} indicate the mean inlet velocity and vector of particle position. Also, as was shown in Figure 4-1b, \vec{u}_p and $\vec{\Omega}$ represent the particle axial and angular velocities. Our investigation shows that utilizing 0.5 million elements for the channel and an element size of $0.1a$ on the particle's surface ensures the independency of simulation results with the number of mesh elements (Figure 4-1 c). The flowchart for the calculation of lift forces applied on a particle located at point (y_1, z_1) is depicted in Figure 2-3. Initially, the particle was assumed to be at rest, and its angular and axial velocities were set to zero. Utilizing the second-order upwind scheme, flow field around the particle was solved based on the given boundary conditions (Table 4). Then, by means of Eqs. 7 and 8, particle axial and angular velocities were measured to update the boundary conditions. At the next iteration, flow field was solved again with the updated values of the boundary conditions from previous iteration. This iterative solution stops when the absolute values of axial force in X direction ($|F_x|$) and angular momentums in y and z directions ($|M_y|$ and $|M_z|$) are less than a defined threshold. Finally, when the solution converged, lift forces on y-z plane (F_y and F_z) were calculated for further analysis on particle lateral migration.

Table 4: Boundary conditions of the system

Boundary	Boundary condition	Value
Inlet	Laminar inflow	$U - u_p$
Outlet	Laminar outflow	$U - u_p$
Channel walls	Moving wall	$-u_p$
Particle surface	Slip velocity	$\Omega \times r$

The surface plot of the elasto-inertial lift force can be calculated by repeating the aforementioned steps for all different points of the cross-section. After solving the flow field around particles and measuring the lift forces, particles' trajectories to their final equilibrium positions need to be simulated. The momentum equation for a single particle is:

$$m_p \ddot{\vec{x}}_p = \vec{F}_{Drag} + \vec{F}_{Inertial\ lift\ force} + \vec{F}_{Elastic\ lift\ force} \quad (4-9)$$

Eq. 9 was used to predict and measure particle trajectories relative to its original position. The main flow drag force (F_D) on the particle surface (with diameter of a) was calculated using Stokes drag equation [171] as follows:

$$F_{Drag} = 3\pi\mu U_D a \quad (4-10)$$

In this equation, μ is the solution viscosity and U is the mean velocity. In addition, elastic and inertial lift forces on each cross-section can be measured by interpolation of the lift forces obtained at some specific predefined points across that cross-section.

4.3 Experimental setup

To investigate the effects of viscoelasticity on particle focusing, 0.1 gr polyethylene oxide (PEO, Sigma-Aldrich, $M_w = 2000$ kDa) was dissolved in a 50 ml PBS running Max buffer (Sigma-Aldrich) to make 2000 ppm PEO solution. Then 3, 5, and 10 μm fluorescent polystyrene particles (Magsphere-Pasadena, California) were added to the PEO solution to make a final solution with a concentration of 5×10^4 particle per ml. Also, *saccharomyces cerevisiae* cells (Sigma-Aldrich- Yeast from *Saccharomyces cerevisiae*) were added to PEO solution to make 3 million per ml yeast solution. The prepared solutions were loaded into the 10 ml BD plastic syringe and derived through the channels by a Nexus 3000 syringe pump. After assembling the fluidic tubes to the microchannels, they were mounted on the stage of an inverted fluorescence microscope (Nikon Eclipse Ti) for further analysis. To visualize the focusing of yeast cells and fluorescence particles, the bright-field and fluorescence images were captured using a high speed (Phantom- VEO 640L) and 14-bit CCD cameras (NIKON DS-Qi1Mc). The microscope objective and the exposure time were set to 10X and 60 μs for bright-field imaging and 10X and 800 ms for fluorescence microscopy. All the analysis and post-processing on the captured photos have been performed by the free IMAGEJ software.

4.3.1 Device structures and fabrication

Four different square, rectangular, trapezoidal and complex straight channels with the same length and hydraulic diameter of 5 cm and 75 μm were designed to investigate the effect of channel geometry on elasto-inertial focusing. Figure 4-2 shows the cross-sectional optical micrograph of the channels with their corresponding dimensions.

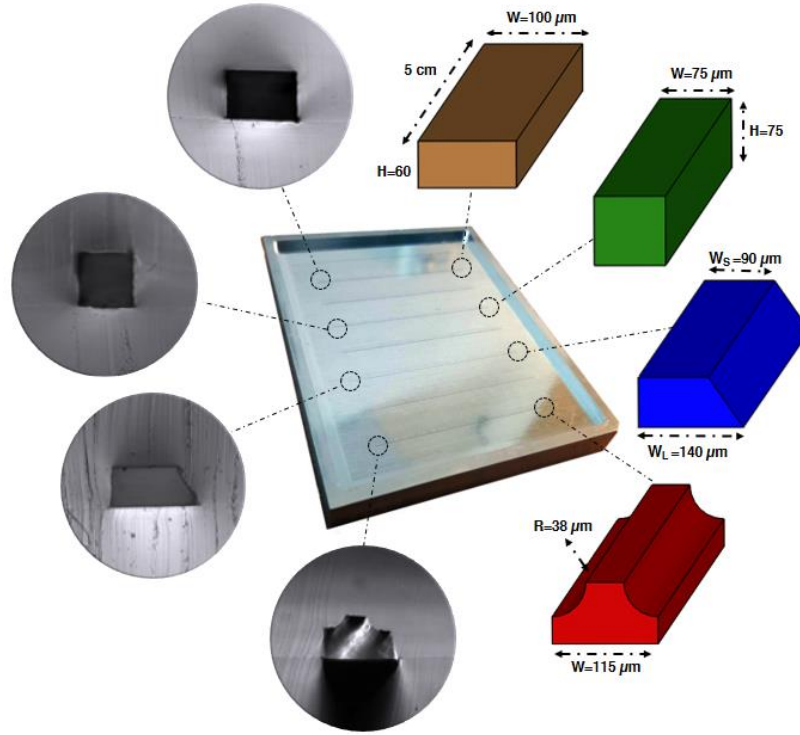


Figure 4-2: Schematic of the channels with corresponding dimensions and cross-sectional optical micrograph of the PDMS microfluidic chips.

Microfluidic devices were fabricated via soft lithography on aluminum master mold by pouring 10:1 degassed mixture of polydimethylsiloxane (PDMS, Sylgard 184, Dow Corning) and curing agent on the molds. Then, after 2 hours of curing in an oven at 65 $^{\circ}\text{C}$, a cured PDMS block was carefully peeled off from the master mold and its inlet and outlet punched through for fluidic access. Finally, the PDMS block was cleaned by 2-propanol to remove the dust and debris, and bonded to a cleaned PDMS slab using oxygen plasma cleaner (Harrick Plasma, PDC-002). It should be noted that the complex channel mold can be easily fabricated by milling a rectangular geometry on an aluminum mold, followed by cutting the upper edges to form the final shape.

4.4 Results and discussion:

Firstly, elasto-inertial focusing in a straight square channel is investigated to better understand the physics of focusing in viscoelastic fluids. Then the effect of flow rate, velocity gradient, channel geometry and corner angles on focusing patterns are comprehensively studied. On the basis of that work, we proposed a new complex channel to obtain a tighter focusing band compared to the other channels under the same hydrodynamic conditions. Finally, we showcased the focusing of 3 μm particles and *saccharomyces cerevisiae* cells in the complex channel.

4.4.1 Physics of elasto-inertial focusing

Fig. 3a shows the focusing of 10 μm particles in the straight square channel for different flow rates and solutions. As can be seen, for the Newtonian solution and flow rates less than 75 $\mu\text{l/min}$, particles remain scattered within the given channel length as the inertial force is not strong enough to push entire particles towards their equilibrium positions. However, for $Q \geq 100 \mu\text{l/min}$ four distinct focusing bands form due to the strengthening of inertial forces. But for the PEO solution, focusing starts to occur at very low flow rates. It begins with five bands (at corners and the center) at 1 $\mu\text{l/min}$, followed by one and four focusing bands for flow rates up of 75 $\mu\text{l/min}$ and more than 100 $\mu\text{l/min}$, respectively (focusing of 10 μm particles can be seen in supplementary movie 1, (<https://aip.scitation.org/doi/suppl/10.1063/1.5093345>)).

In order to explain these focusing behaviors, we numerically modeled the lateral migration of a dispersed particle in the PEO viscoelastic solution inside the square channel for flow rates of 1 and 25 $\mu\text{l/min}$ (Figure 4-3b). It is shown that by increasing the flow rate, by transitioning from a pure elastic to an elasto-inertial regime, the number of focusing bands decreases from five to one. Figure 4-3 c and d show the distribution of inertial and elastic lift forces for a flow rate of 1 $\mu\text{l/min}$. In central regions (particle a), shear gradient force pushes the particles towards the walls, while elastic force acts in the opposite direction and drives particles to focus at the center. By approaching towards the middle of the side walls (particle b), wall induced and

elastic forces become strong and unidirectional towards the channel center, which lowers the chance of focusing in these regions.

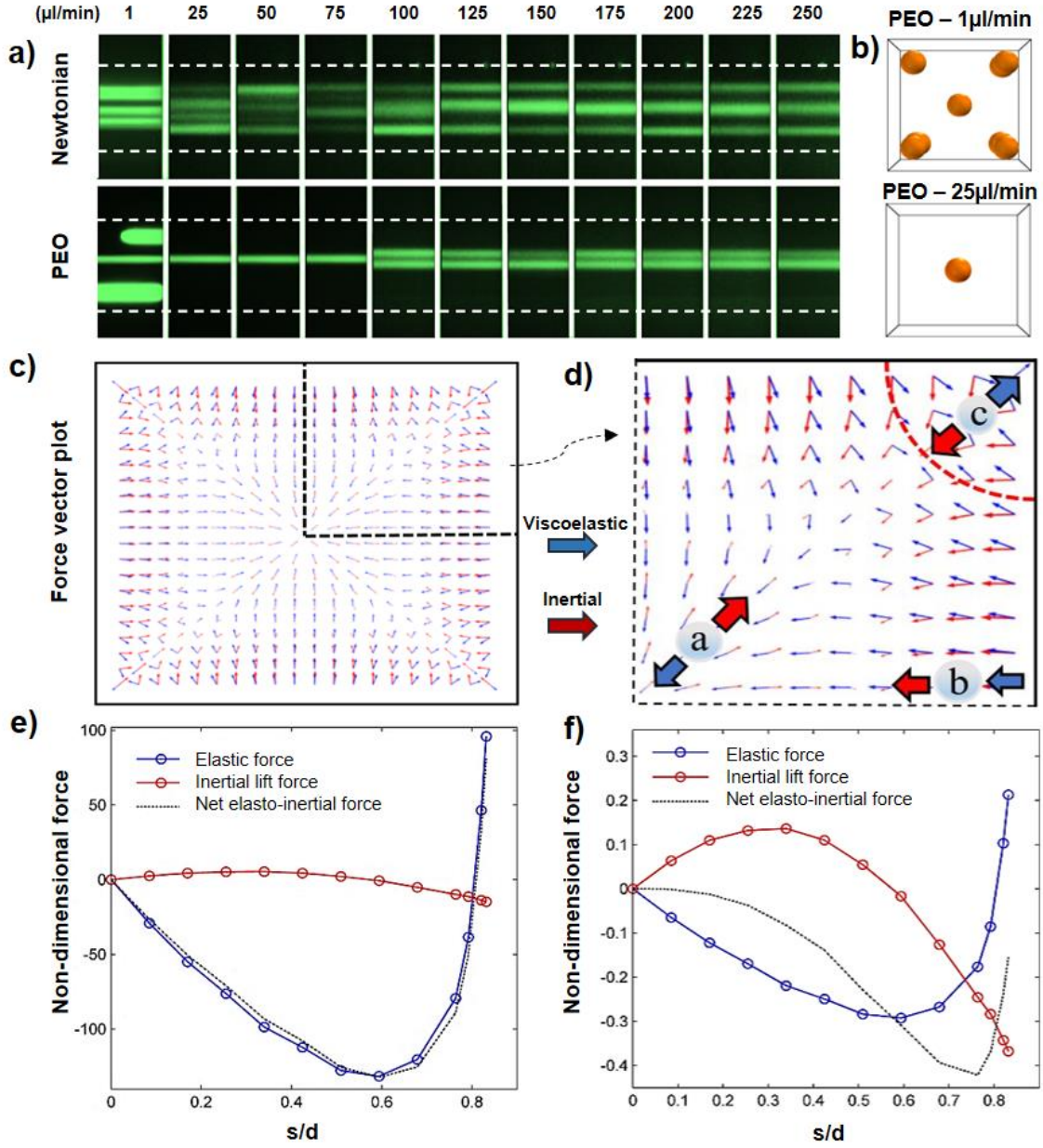


Figure 4-3: The mechanism of elasto-inertial focusing in the square channel. a) Experimental results for focusing positions of 10 μm particles. b) Numerical results indicating the focusing positions in PEO solution for flow rates of 1 and 25 $\mu\text{l/min}$. c) and d) The inertial and elasticity force vector plot in the cross-section of the channel. e) and f) Non-dimensional applied elasto-inertial forces on the particles for flow rates of 1 and 25 $\mu\text{l/min}$, respectively.

Around the corners (particle c), the elastic force is weak and towards the corner which can be balanced by the opposing inertial lift force. As discussed, equilibrium positions mainly form in the regions where inertial and elastic forces can balance each other (diagonal directions (particle a and c)). To better describe the competition between inertial and elastic forces to form one and

five focusing positions, lift forces are measured along the diagonal direction from the center (s) for flow rates of 1 and 25 $\mu\text{l}/\text{min}$ (Figure 4-3 e and f). The lift forces are made non-dimensional with respect to the term $\rho U_{max}^2 a^4 / H^2$ for each of the conditions. In these figures, the positive and negative values denote the force direction towards the channel center and corner, respectively. As shown in Figure 4-3 e, at low flow rates (1 $\mu\text{l}/\text{min}$), the net lift force values are mainly negative (except the regions close to the corners which noticeably increase) with two points equal to zero (at center and $s/d \approx 0.8$). Therefore, particles in the central region focus at the center, and the rest migrate towards the four focusing positions near the corners. In contrast, by increasing the flow rate to 25 $\mu\text{l}/\text{min}$ (Figure 4-3f), inertial forces become stronger near the corners and repel the particles from the walls. It can be seen that the net elasto-inertial force is negative for all the points on the diagonal resulting particles to focus at the center.

To better understand how elastic and inertial forces act on a particle, first normal stress difference ($N_1 = \tau_{xx} - \tau_{yy}$) is shown inside the channel, and inertial and elastic stresses are depicted on the surface of the particle in Figure 4-4. As shown in Figure 4-4 a, while N_1 has maximum values near the walls, it has considerably smaller values around the channel center and corners. Streamlines around the particle are depicted in Figure 4-4 b. There are three types of streamlines: open streamlines away from the particle, reverse streamlines near the particle changing its direction and spiraling streamlines which after several rotations around the particle move away due to the presence of the wall near the particle. The distributions of non-dimensional inertial and elastic stresses with respect to the $0.5 \rho U^2$ on the surface of the particle are depicted in Figure 4-4 c and d, respectively. These contours are presented from a view direction shown in Figure 4-4 a. As can be seen, the inertial stress is maximum on one side and minimum on the other side, while the elastic stress distribution is more complex with maximum and minimum values at different parts. It can be seen that the highest and lowest values for both inertial and elastic forces are of the same order at the given flow rate (25 $\mu\text{l}/\text{min}$).

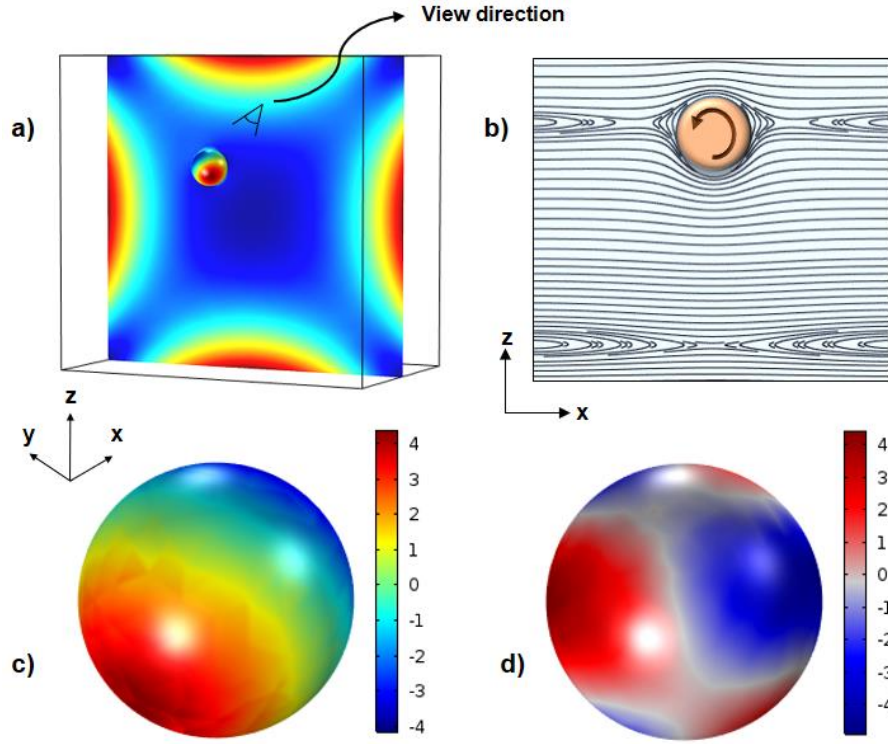


Figure 4-4: a) Contour of first normal stress difference (N_1) and pressure in the cross-section of the channel and over the particle, respectively, for flow rate of $25 \mu\text{l/min}$. b) Streamlines around the particle in x-z symmetry plane. c) Distribution of inertial stress on the surface of the particle. d) Distribution of total elastic stress tensor.

4.4.2 Particle trajectories in a viscoelastic fluid

In this part, particle trajectory through the square channel is presented to illuminate the mechanisms of focusing in viscoelastic solutions. According to Figure 4-5, the migration of particles to their equilibrium positions can be divided into two stages for both Newtonian and viscoelastic solutions. For Newtonian fluids (Figure 4-5 a), initially particles migrate quickly to the minimum inertial lift regions (curves parallel to the walls (Figure 4-5 aII)) due to the strong shear gradient and wall induced lift forces at the corner and near the walls respectively. Then, Magnus force pushes the particles slowly towards their final equilibrium positions (Figure 4-5 a III). However, in viscoelastic fluids (Figure 4-5 b), particles first move towards the minimum elastic lift regions (diagonal directions (Figure 4-5 bII)), and afterwards migrate diagonally towards the minimum shear gradient point (Figure 4-5 bIII) (The two-stage focusing model can be seen in supplementary movie 2, (<https://aip.scitation.org/doi/suppl/10.1063/1.5093345>)).

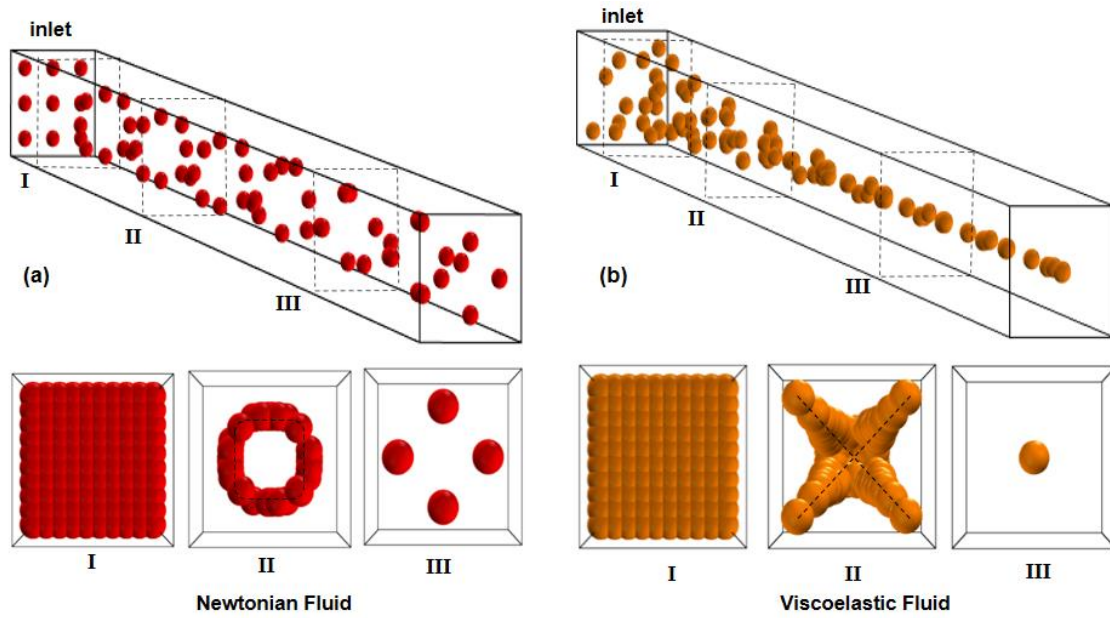


Figure 4-5: Particle trajectories of Newtonian a) and viscoelastic fluid b) in various cross-sections of the straight channel. The black dash lines in the Newtonian fluid are minimum lift force line and in the viscoelastic fluid are the minimum shear line.

4.4.3 Effect of velocity gradient on focusing pattern

Detailed investigation of the velocity gradient as one of the practical tools in particle sorting is of great importance. As inertial forces are strongly correlated to the shear rate ($F_L \propto \gamma^2$), changes in flow rate and velocity gradient can noticeably alter the focusing positions. It should be noted that flow rate increase in wall-bounded Poiseuille flow increases the velocity gradient, and subsequently strengthens the inertial forces. Figure 4-6 a shows the focusing patterns of 10 μm size particles through the rectangular channel with an aspect ratio of 1.6 for different flow rates. At low flow rates (25 $\mu\text{l/min}$) particles only focus at the channel center but increasing the flow rate to 50 $\mu\text{l/min}$ causes focusing to occur in two bands. The side view shows a single line focusing for all the given flow rates, so lift forces were investigated on the horizontal symmetry plane along the Y-axis (Figure 4-1 b) to elucidate the transition from one to two-line focusing. As previously mentioned, inertial and elastic lift forces oppose each other near the center of the channel and the interaction between these two forces defines the final focusing positions. Figure 4-6 b and 6c demonstrate the non-dimensional lift forces along the Y direction in the symmetry plane for flow rates of 25 and 50 $\mu\text{l/min}$. In these figures, negative values of elastic force are presented to better compare the magnitude of elastic and inertial forces. Due to symmetry, the

forces are only studied in the first quarter of rectangular cross-section. For flow rate of 25 $\mu\text{l}/\text{min}$ (Figure 4-6 b), elastic force is stronger than inertial force everywhere which causes all the particles to focus at the center. However, for 50 $\mu\text{l}/\text{min}$ flow rate (Figure 4-6 c), there are two regions near the center (separated by the dashed black line), in which elastic and inertial forces are dominant. Although inertial force is dominant between the center of the channel and $y/h = 0.42$ ($h=H/2$), elastic force is stronger on the other side of the dashed line from $y/h = 0.42$ to the wall.

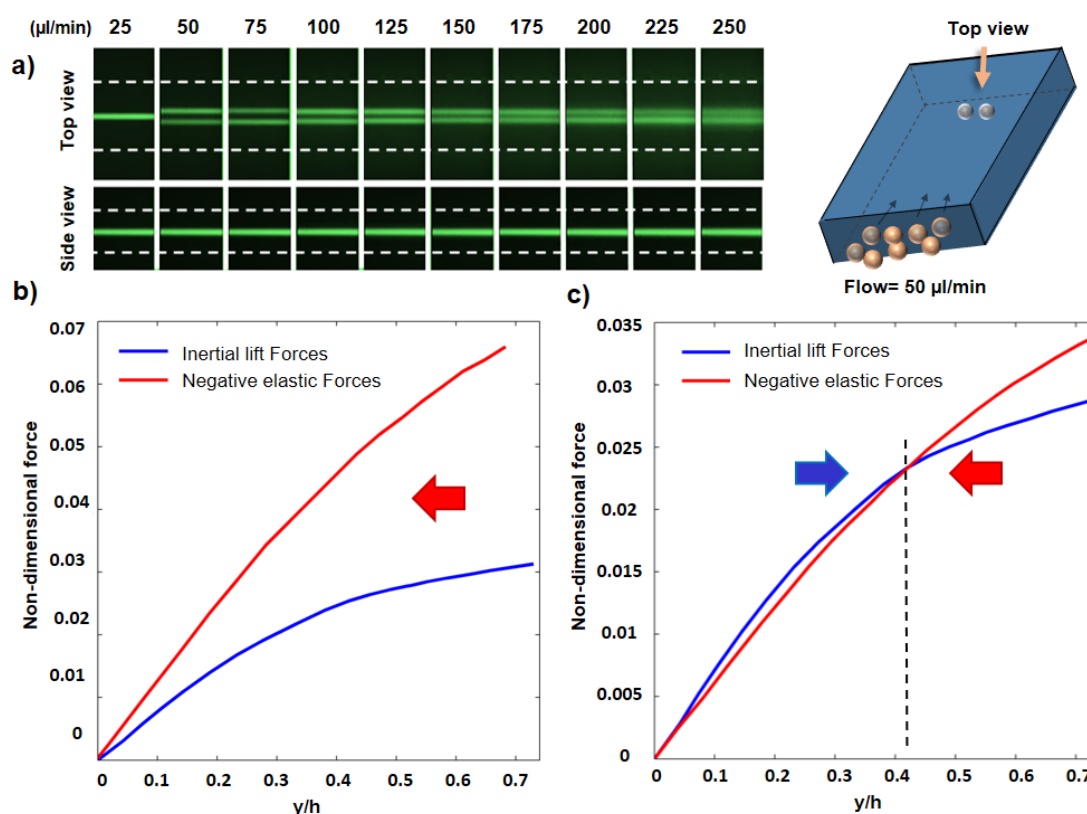


Figure 4-6: Elasto-inertial focusing in rectangular channel. a) Top and side views of equilibrium positions for a rectangular channel with an aspect ratio of 1.6. b) and c) Non-dimensional inertial lift force and negative value of non-dimensional elastic force near the center of the channel for two different flow rates of 25ml/min b) and 50ml/min c). Curve intersections are the equilibrium positions.

As a result, while particles in central region are pushed towards the walls, at around $y/h = 0.42$, elastic force becomes stronger and pushes the particles in the opposite direction, causing them to reach equilibrium at $y/h = 0.42$ (about 12.5 μm) distance from the center (The two-line focusing model for viscoelastic solution can be seen in supplementary movie 3, (<https://aip.scitation.org/doi/suppl/10.1063/1.5093345>)).

4.4.4 Effect of Geometry on focusing

In inertial microfluidic systems, channel geometry has proven to play a pivotal role in controlling particle movements due to the strong correlation between inertial forces and the characteristic length of the channel. While many efforts have been performed to increase the efficiency of these systems by employing trapezoidal, semicircular and triangular channels [123, 172], no one has previously explored the effects of shape non-orthogonality and corner angles on particle sorting. In this section, to evaluate how geometry can affect the focusing behaviors, firstly the impacts of aspect ratio on the lift forces are explained. Afterwards, elastic force along the bisector of various corner angles are evaluated to determine the effects of corner angle on viscoelastic forces. Finally, based on the results of these investigations, a new complex channel is proposed to obtain tighter focusing bands than can be achieved with conventional straight channels.

Figure 4-7 a shows focusing of 10 μm particles in trapezoidal, square and rectangular straight channels with the same hydraulic diameter. It can be clearly seen that for flow rates of 50 and 75 $\mu\text{l/min}$, the square channel has one focusing band, while the rectangular channel has two. To explain this focusing behavior we note the correlation between inertial and elastic forces with the width of the channel along the Y-axis. Toward the center of the channel, the inertial and elastic forces scale as $F_L \propto \rho_f U_m^2 a^3 / W$ [66] and $F_e \propto a^3 \eta_p \lambda \nabla \dot{\gamma}^2 \propto a^3 \eta_p \lambda U_m^2 / W^3$ [19], respectively. Also, the core fluid in square channel is more confined to the walls rather than rectangular channel which one side is noticeably longer than the other side. Therefore, by increasing the width of the cross-section (W) the elastic force decreases more rapidly than the inertial force, which induces the focusing position to increase to two bands in the rectangular channel at lower flow rates.

Since the elastic force is closely proportional to normal stress difference (∇N_1), Figure 4-7 b shows the ∇N_1 contours in trapezoidal, square and rectangular channels instead of elastic

force. As can be seen, increasing the angle of the corner results in stronger elastic force around it.

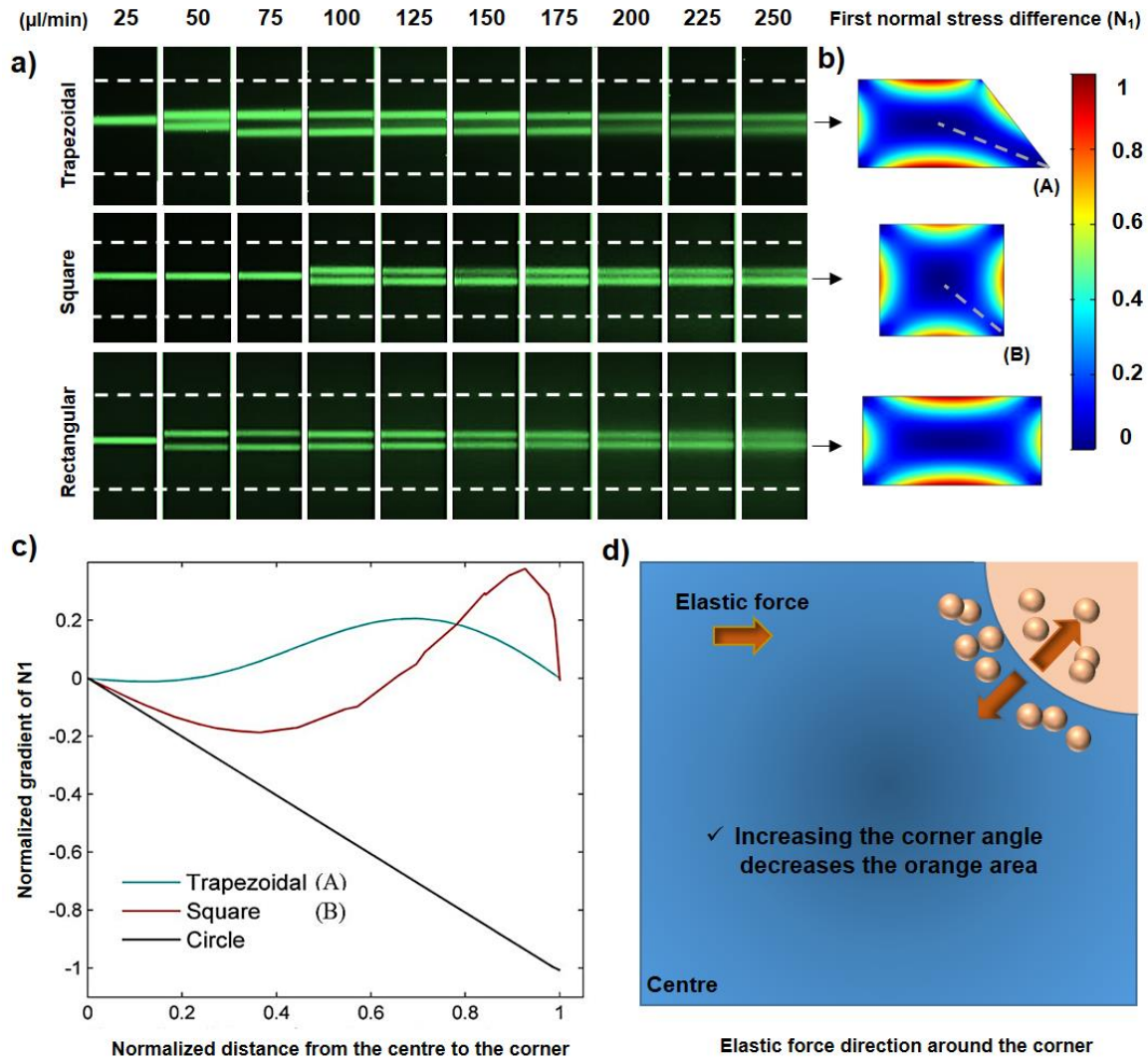


Figure 4-7: a) Top views of the particle trajectories in trapezoidal, square and rectangular channels. The transition from one to two focusing bands occurs at a higher flow rate in square channel under the same conditions. b) First normal stress difference contours in the corresponding channels. c) Effects of corner angle on normalized gradient of N_1 as an indicator of elastic force. Corners A and B have angles of 50° and 90° respectively. A circular channel is assumed to have the corner angle of 180° . d) Direction of elastic force in the first quarter of square cross-section. The direction of elastic force in the blue region is always towards the center while in the orange region is in the opposite direction.

According to Figure 4-7 a, in the trapezoidal channel, for flow rates of 75-150 $\mu\text{l/min}$, the focusing band in the proximity of the “50-degree corner” slightly shifts towards this corner, proving that the elastic force in this region is weaker than the other corners. To better describe the effects of corner angle on viscoelastic force, ∇N_1 values are measured along the line connecting the center to the corners A and B (shown in Figure 4-7 b) and the radial direction in

a circular channel. All the channels assumed to have the same hydraulic diameter of $75\mu\text{m}$ and flow rate of $25\ \mu\text{l}/\text{min}$ to equalize the hemodynamic conditions. According to Figure 4-7 c, increasing the angle of the corner has two significant effects on ∇N_1 . First, the regions in which ∇N_1 has negative values increases, which means elastic force can drive the particles towards the center more effectively. Second, the value of elastic force rises, indicating this force becomes stronger. As shown for the circular channel with angle of 180° , since the value of ∇N_1 is negative everywhere, the elastic force pushes the particles towards the center from all the regions. However, for trapezoidal and square geometries, there are some regions around the corners where the elastic force acts in the opposite direction and inhibits the tight single band focusing at the center. Figure 4-7 d shows one of these regions (orange quadrant) around the corner of the square channel. Since increasing the corner's area can increase the elastic force and changes its direction towards the center (as for a circular channel), it might be possible by some modification in the rectangular geometry (as the most common cross-section used in inertial microfluidic systems) to obtain tighter focusing for wider range of Reynolds number and concentrate smaller microparticles more accurately.

As a summary of previous sections, we concluded that in order to improve focusing, the following points should be considered:

1. The corner angle of the cross-sections should be as large as possible. This encourages particle migration towards the center of the channel.
2. At the same hydraulic diameter, the core flow needs to be as confined as possible in all directions. This causes particles to remain focused at the center for higher flow rates.

4.4.5 Designing the complex channel

In this section, based on our understanding about the mechanisms of elasto-inertial focusing, we proposed a new complex straight channel to obtain a tighter particle focusing band for smaller microparticles and wider range of flow rates. According to Figure 4-7 d, this geometry is designed by cutting the upper corners of the rectangular channel (as shown in Figure 4-2) and

resizing the sides to have the same hydraulic diameter as other channels. This geometry modification promotes focusing by two mechanisms. Firstly, compared to the rectangular channel, wider corners in complex channel shrink the regions where elastic force is directed towards the corners. In addition, it causes the elastic force to become more dominant in the core region and improves focusing there. Secondly, due to its non-linear shape, the core flow around the center of the channel is more confined and have more similar values in both vertical and horizontal directions, causing the channel to have tighter focusing at higher flow rates. Figure 4-8a shows the elasto-inertial focusing positions of 5 μm particles through the square, rectangular and complex channels for wide range of flow rates. It can be seen that, in contrast to square and rectangular channels, the complex channel has single-band focusing at flows up to 100 $\mu\text{l/min}$. In addition, as shown by intensity profile in Figure 4-8 c, the complex channel has tighter focusing compared to the rectangular and square channels at 100 $\mu\text{l/min}$ flow rate. For flow rates greater than 100 $\mu\text{l/min}$, although the focusing band splits in complex channel, it still shows an enhanced focusing in the central region (Figure 4-8 d). It should be noted that while the complex channel has longer width compare to its counterpart geometries, interestingly it has tighter focusing, which makes this channel is a better option for flow cytometry and particle separation applications. Figure 4-8 b represents the viscoelastic and inertial lift forces in a cross-section of complex channel. According to the N_1 contours shown in Figure 4-8 bI, elastic forces are stronger in the complex channel and are more unidirectional towards the channel center, compared to the other channels. After verifying the tighter focusing in complex channel, we modified its dimensions ($W=100$, $H=30$, and $R=38$) to focus 3 μm particles (Figure 4-8 II). Interestingly, the 3 μm particles remain focused up to a flow rate of 100 $\mu\text{l/min}$. Finally, as a proof of concept, we showcased the focusing of *Saccharomyces cerevisiae* cells (3-5 μm) with flow rate of 75 $\mu\text{l/min}$ (Figure 4-8 bIII). Dashed circles show the position of yeast cells at the central region of the channel (focusing of the 3 μm particles and yeast cells in the complex channel can be seen in supplementary movie 4, (<https://aip.scitation.org/doi/suppl/10.1063/1.5093345>)).

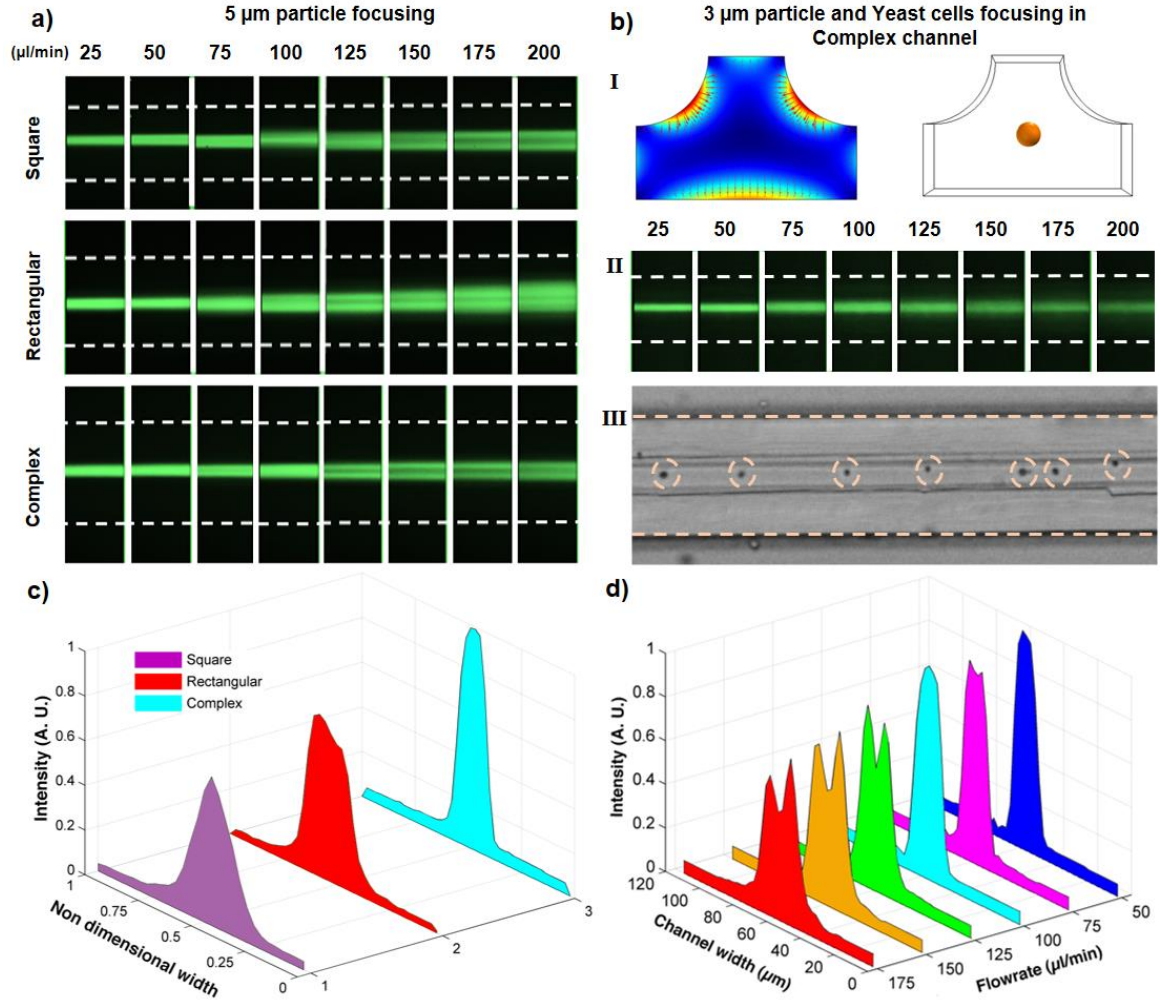


Figure 4-8: focusing positions in square, rectangular and complex channels. a) Top view focusing positions of 5 μm particles, which shows for all the flow rates the complex channel has tighter focusing compared to the conventional channels. bI) Elasto-inertial force vector plot in the modified complex channel and the focusing position for 3 μm particles. bII) Top view focusing of the 3 μm fluorescent particles in the modified complex channel. bIII) Focusing of the yeast cells in the complex channel for flow rate of 75 $\mu\text{l/min}$. c) Intensity profiles for the focusing of 5 μm particles at flow rate of 100 $\mu\text{l/min}$ which shows a tighter focusing in complex channel. d) Intensity profiles for focusing of 5 μm particles through the complex channel.

4.5 Conclusion

In this work, we experimentally and numerically studied the elasto-inertial focusing in different straight channels to investigate the effects of cross-sectional geometry accompanied by viscoelasticity on the focusing phenomenon. We presented a two-stage elasto-inertial focusing model within straight channels, in which particles first move towards the lowest elastic force regions (diagonal directions in rectangular and square channels), and then diagonally migrate to their final equilibrium positions. Furthermore, for the first time, we explored the effects of corner angle on the viscoelastic force. The results revealed that increasing the angle

of the corner not only strengthens the elastic forces but also directs them more towards the channel center, even in areas near the corners. Also the core flow needs to be as confined as possible in all directions to have the best focusing at the center. We then studied the effects of velocity gradient and aspect ratio on the focusing positions. We found that increasing the channel width weakens the elastic force more than the inertial force, causing one focusing band in a square channel to increase to two bands in a rectangular channel. Based on our findings, we developed a novel complex channel design to obtain a tighter focusing under the same conditions. We were able to use elasto-inertial forces to focus 3 μm particles in the complex channel at high flow rate of 100 $\mu\text{l}/\text{min}$. Finally, as a proof of concept, we showcased the elasto-inertial focusing of the *Saccharomyces cerevisiae* cells (3-5 μm) with high-throughput of 75 $\mu\text{l}/\text{min}$. We are of the opinion that our findings will provide a deeper understanding of the fundamentals of elasto-inertial focusing and will serve as a strong basis for further design of complex channels.

4.6 Supplementary material

Supplementary movie 1 shows the numerical results for the focusing of 10 μm particles in square channel for Newtonian and viscoelastic solutions. Supplementary movie 2 shows the Modelling of two stage focusing in straight square channel for both Newtonian and viscoelastic solutions. Supplementary movie 3 shows the Simulation results for the elasto-inertial focusing of 10 μm particles in a rectangular channel for flow rate of 50 $\mu\text{l}/\text{min}$. Supplementary movie 4 shows the focusing of 3 μm particles and yeast cells at the center of the complex channel numerically and experimentally (the concentration of the yeast cells is 3 million per ml).

4.7 Acknowledgment

This research work is supported by the national health and medical research council via the career development fellowship (APP1143377) and the Australian research council through discovery project grants (DP170103704 and DP180103003).

5

Chapter Five: Wax 3D printing of inertial microfluidic channels with complex geometries

(PAPER II)

Introduction

In this chapter, we introduce a new fabrication workflow to easily create microchannels of arbitrary cross-sectional geometries suitable for inertial microfluidic applications. Then, we study the particle focusing behaviors in straight and curved channels with different geometries using both Newtonian and non-Newtonian solutions. Finally, we propose a complex spiral channel and use it for separation of stem cells from microcarriers with separation efficiency of 98%.

Authors' contributions:

1) Mohammad Amin Raoufi:

Proposing the fabrication workflow, designing all the channels, characterizing the solutions, running all the experiments, analyzing the results, preparing the samples writing the entire paper, and making some of the figures.

2) Sajad Razavi Bazaz:

Making some of the figures and revising the paper.

2) Omid Rouhi:

Helping in the fabrication process

3) Mohsen Asadnia, Hamid Niazmand, Amir Razmjou, and Majid Ebrahimi Warkiani

Reviewing the paper.

***This chapter is submitted to the Soft Matter.** Submission number: SM-ART-10-2019-002067.R1

Wax 3D printing of inertial microfluidic channels with complex geometries

Mohammad Amin Raoufi^{1,2,3}, Sajad Razavi Bazaz², Hamid Niazmand³, Omid Rouhi¹, Mohsen Asadnia¹, Amir Razmjou⁴, and Majid Ebrahimi Warkiani^{2,5*}

¹ School of Biomedical Engineering, University of Technology Sydney, NSW, 2007, Australia

² School of Engineering, Macquarie University, NSW, 2109, Australia

³ Department of Mechanical Engineering, Ferdowsi University of Mashhad, Mashhad, Iran

⁴ School of Chemical Science and Engineering, University of New South Wales, Sydney, 2052, Australia

⁵ Institute of Molecular Medicine, Sechenov First Moscow State University, Moscow 119991, Russia

*Corresponding Author: Majid Ebrahimi Warkiani (majid.Warkiani@uts.edu.au)

Abstract:

Inertial microfluidics has emerged over the past decade as a powerful tool to accurately control cells and microparticles for diverse biological and medical applications. Many approaches have been proposed to date in order to increase the efficiency and accuracy of inertial microfluidic systems, including altering flow rates, solution properties, and channel geometries. However, the effects of channel cross-section and solution properties (Newtonian or non-Newtonian) have not been fully explored, primarily due to limitations in current microfabrication methods. In this study, we overcome many of these limitations using wax 3D printing technology and softlithography through a novel workflow, which eliminates the need for use of silicon lithography and polydimethylsiloxane (PDMS) bonding. We have shown that by adding dummy structures to reinforce the main channels, optimizing the gap between the dummy and main structures, and dissolving the support wax on a PDMS slab to minimize the additional handling steps, one can make various non-conventional microchannels with hydraulic diameters as small as 250 μm . These substantially improve upon previous wax printed microfluidic devices where the working area falls into the realm of macrofluidics rather than microfluidics. We assessed the robustness of the proposed method by fabricating different straight and curved microchannels while evaluating them for particle and cell separation. Results revealed a surface roughness of 1.75 μm for the printed channels, which does not affect the performance of inertial microfluidic devices used in this study. Channels with complex cross-sections were fabricated and then analyzed to investigate the effects of viscoelasticity and superposition on the lateral migration of the particles. Finally, as a proof of concept, 180 μm microcarriers were separated from human Mesenchymal Stem Cells (hMSCs $\sim 10\text{-}25\ \mu\text{m}$) using an optimized channel with maximum cell-holding capacity, demonstrating the suitability of these microchannels in the bioprocessing industry.

Keywords: *Wax 3D Printing; Inertial Microfluidics; Particle Separation; Computational fluid dynamics; Stem Cells*

5.1 Introduction

Inertial microfluidics refers to the accurate control of flows and microparticles confined to the channels with micrometer dimensions, without requiring external forces. In these systems, particles of different sizes can be sorted using inherent inertial lift and drag forces for use in biomedical and industrial applications [11]. This technique has several advantages over conventional particle sorting methods, including low sample volumes, high-throughput, low cost, and fast processing. Lateral migration of microparticles was first observed around 60 years ago [173], followed by several experimental and theoretical studies about the underlying physics [64, 174-177]. This phenomenon was not widely employed by researchers until the availability of advanced microfabrication technologies enabled investigators to precisely fabricate microchannels with characteristic dimensions comparable to the microparticle/cell sizes. These advancements allowed researchers to fabricate microchannels of various shapes, including straight, spiral, serpentine, and expansion-contraction for a myriad of applications such as microfiltration [165, 178], droplet generation [179], flow cytometry [180, 181], fluid mixing [182, 183], and cell separation [15, 152, 184, 185]. In addition to inertial forces in straight microchannels, secondary flows in curved channels or around obstacles give extra controllability to inertial microfluidics by applying an extra viscous drag force perpendicular to the main flow direction [186-189]. Secondary flows, wall induced forces, and shear gradient lift forces are strongly dependent on the channel size and geometry; hence, significant efforts have been made to produce complex microchannels, with the aim of improving particle focusing [123, 125, 190-192].

Microfluidic devices can be categorized into two groups based on the channels' connectivity and shape, namely two-dimensional (2D) (planar) and three-dimensional (3D) microdevices [193]. In planar microfluidic systems, all the channels are arranged on a same plane regardless of their size, while 3D devices consist of non-planar channels and crossover features which form a more complex 3D structure. The SU8 photolithography technique is the most well-

known patterning method to fabricate planar structures on silicon wafers [194]. In the past, many planar microchannels with rectangular and square cross-sections have been fabricated using the silicon softlithography technique to manipulate cells and microparticles within inertial microfluidic systems [15, 180, 195-199]. Although this approach has been the basis of many microfluidic device developments, some major drawbacks such as the requirement for expensive microfabrication equipment, skilled operators, and an inability to build non-planar structures impeded its widespread utilization [55, 200]. Silicon direct etching (wet or dry) [201, 202] and mechanical machining (i.e., micro-milling [60, 121]) are other options for producing 2D structures, mainly for non-rectangular cross-sections [203-205]. Using these approaches, multiple groups reported the fabrication of polydimethylsiloxane (PDMS)-made trapezoidal, circular, and triangular microchannels, resulting new insights into the physics of inertial microfluidics, and the emergence of new applications of these devices [123, 159, 172, 206, 207]. In addition, other techniques such as hot embossing [207, 208] and laser cutting [117-119] have been also used for fabrication of microchannels in glass and polymers; however, these approaches require sophisticated equipment, making them less viable options for rapid prototyping.

Lately, additive manufacturing (AM) or 3D printing has been extensively explored for fabrication of functional microfluidic devices (*i.e.*, micromixers, microvalves, and micropumps [147]), including microchannels from a variety of polymeric materials. In 2014, Lee *et al.* used stereolithography apparatus (SLA) to fabricate a 3D helical trapezoidal channel in order to separate antibody-functionalized magnetic nanoparticle clusters from *Escherichia coli* (EC) bacteria using a combination of Dean drag and inertial lift forces [135]. Despite the great benefits of SLA 3D printing for the fabrication of microfluidic components (and also master molds for PDMS casting), this technique is not suitable for the production of microchannels because of the difficulty of removal of the support residuals. More importantly, the optical

transparency of the existing resins is not sufficient to allow particle tracking using both fluorescent and non-fluorescent particles [136].

More recently, embedded template-assisted method (*i.e.*, soft lithography using dissolvable molds) has emerged as a cost-effective and straightforward technique to create 2D and 3D microchannels. A wide variety of materials such as polylactic acid (PLA), sugar [209], acrylonitrile butadiene styrene (ABS) [210], and liquid metals [211] have been proposed as a sacrificial (or template) material; however, some major drawbacks such as inadequate resolution of templates, distortion of PDMS microstructures, and presence of residual materials in channel networks limit their adaptation for inertial microfluidic applications [211]. Fused deposition modeling (FDM) 3D printing is a new method for making sacrificial molds for the fabrication of channels with non-conventional geometries [84]. Despite the capability of this method for fabrication of non-rectangular channels, the difficulty of modifying printing nozzles and the inferior surface quality of the resulting printed objects hinder its widespread adoption.

In order to address these issues, in this study, we report a new approach for the fabrication of PDMS microchannels using a wax 3D printer, enabling rapid prototyping of complex structures while avoiding solid-to-solid bonding. We have developed a new technique for fabrication of microchannels of arbitrary cross-sections by introducing dummy structures to support the main parts and dissolving the support wax on a PDMS slab to minimize the additional handling steps. Various straight and curvilinear microchannels have been fabricated using our proposed methodology. Then, focusing of micron-size particles at different flow rates was observed and analysed for both Newtonian and viscoelastic fluids to demonstrate the suitability of the printed microchannel for inertial microfluidic applications. Finally, separation of stem cells from microcarriers was demonstrated in a novel wax printed spiral channel, showcasing the suitability of this technique for the bioprocessing industry.

5.2 Materials and methods

5.2.1 Design and fabrication process

Figure 5-1 shows all steps from design to casting of the microfluidic channels via the wax 3D printing method. As per the workflow presented in Figure 5-1 A, SolidWorks 2016 software (Dassault Systemes SolidWorks Corporation, Waltham, MA, USA) was first used to design the channels (Figure 5-1 A I). At this step, it is vital to design specific dummy structures to prevent breakage/collapse of microchannels during the post-processing steps, as the main channels are extremely fragile. Figure 5-1 A I shows a single-curved microchannel reinforced by a dummy structure in the center. Although the dummy structure is not connected to the main channel, it prevents the main channel from breakage during the peel-off step because the design is printed as a single block comprising two structures (the main channel and the dummy structure printed by castable wax) connected together by the support wax (Figure 5-1 B II). It should be noted that the dummy structure needs to be symmetrical and separate from the main channel to prevent distortion and to allow easy disconnection from the main channel during removal of the support wax. The gap between the main channel and the dummy structure should be selected carefully, as large gaps can prevent the structure from being printed homogeneously, causing the channel to collapse during the peel-off process, while minute gaps can lead to unwanted adhesion between the dummy and main structures. We found that the optimum gap between the dummy and main structures is 250-500 μm . The gap is intended to be filled with support wax during the printing step, resulting in a homogeneous structure. In Figure 5-1 B II, only the dummy structure (in blue) and the support wax (in red) are visible, whereas the main microchannel is covered by support wax.

Following the design modeling, these models were saved as a stereolithography file (.STL) and exported to Modelwork and Analyzer software (SolidScape, Inc., USA) for further modification. In the next step, the wax printer machine (SolidScape S350- SolidScape, Inc., USA) printed the complete structure layer by layer (Figure 5-1 A II, and B I) using additive and

subtractive manufacturing. Each layer is generated by depositing droplets of molten wax, followed by a cooling process for solidification. At the end of each layer, a cutter trims back the structure surface for the next layer to be printed. The machine works with two different types of wax including Midas Castable Material (SolidScape, Inc., USA) to create the main structure, and Melt Dissolvable wax (SolidScape, Inc., USA) to support all the undercuts and overhangs during the fabrication process. Various layers of support wax can be printed beneath the main structure on the build plate to protect the main channel. Since inertial microfluidic channels are extremely fragile, at least 30 layers of support wax are essential to prevent them from any damage during the peel-off process. Once the part has been printed, it can be easily detached from the build plate by placing the plate onto a hot plate for 30 min at 55 °C, then sliding a thin nylon wire under the part. After the detachment of the printed structure from the build plate, it needs to be immersed in a BIOACT VSO (Vantage Specialty Chemicals, USA) solvent at 55 °C for 30 minutes to remove and dissolve the support wax (Figure 5-1 B III, and A III). The temperature must be lower than 55 °C, as higher temperatures can deform the structure. The VSO solvent only dissolves the support wax and is chemically unreactive with castable counterparts. Dissolving the support wax must be performed on a cured PDMS (Sylgard 184 Silicone Elastomer Kit, Dow Corning, MI, USA) substrate in order to support the final structure, eliminating the need for manual handling of parts after the removal of support wax (Figure 5-1 B IV). When the support wax is completely dissolved, the detached dummy structures and the solvent are removed from the PDMS substrate (Figure 5-1 B V and VI). After the mold fabrication, a degassed mixture of 10:1 PDMS and curing agent was poured over the 3D wax structure and cured in an oven at 55 °C for 5 hours (Figure 5-1 B VII, and A IV). The cured PDMS was punched using a Uni-Core™ Puncher (Sigma-17 Aldrich Co. LLC, SG) at the inlet and outlet of the channels for fluidic access and wax cleaning.

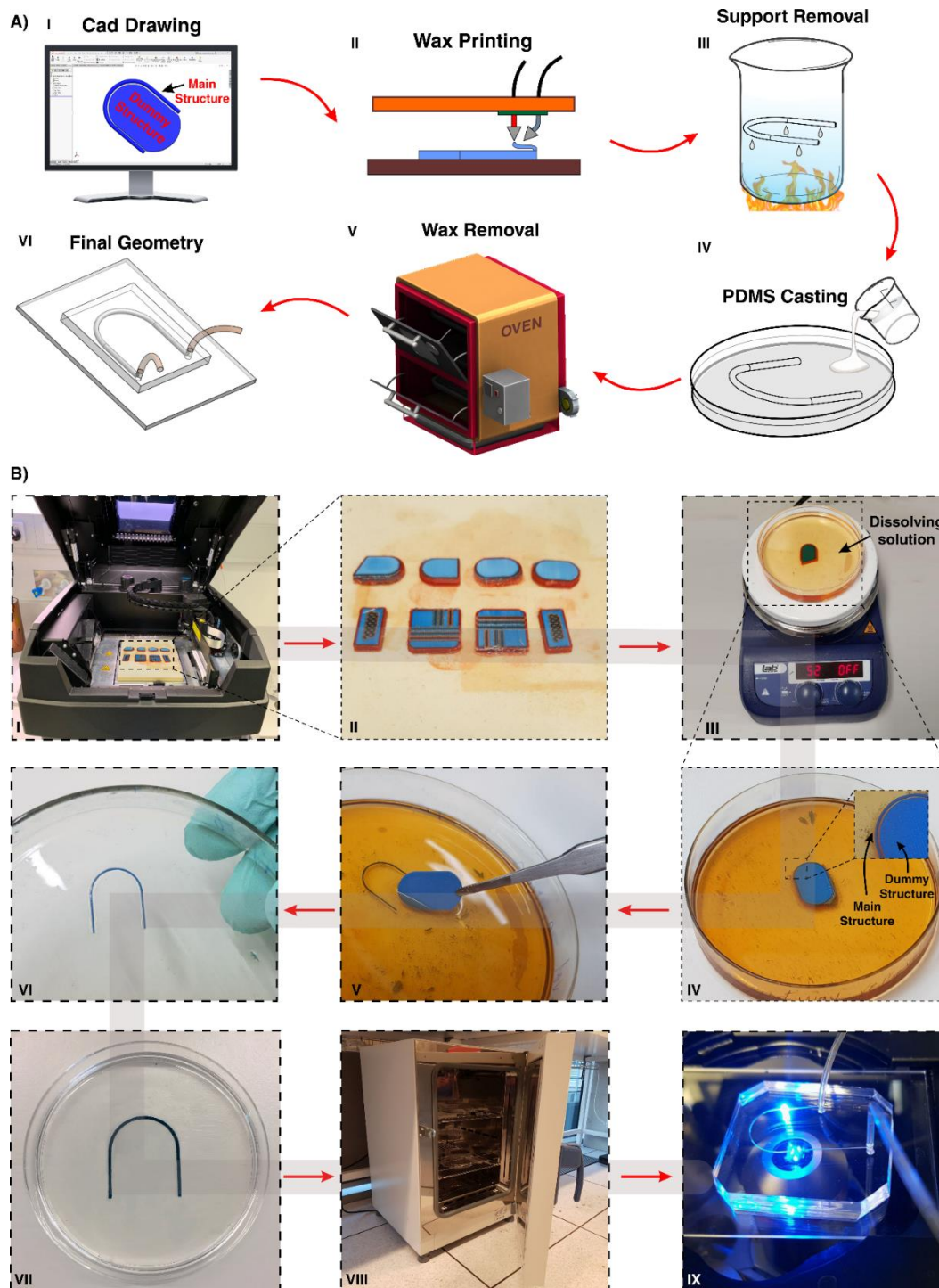


Figure 5-1: Microchannel fabrication process by the wax printing approach. A) Schematic illustration of the proposed workflow for the fabrication of microchannels. A I) Channels design using CAD software. A II) and B I). Printing models with the wax 3D printer. The main microchannel is supported by the blue dummy structure in the middle and is covered by the supporting wax. The large dummy structure in the middle serves to protect the main channel from breaking during post-processing. B II) Fabricated channels on the build plate which are placed on a hot plate for detachment. A III), and B III) Dissolving the support wax by immersing the chip in the BIOACT VSO solvent on a hot plate. B IV) Dissolution of the support wax (red) causes the main microchannel to appear gradually. The channel rests on a thin PDMS slab once the support wax was completely dissolved. B V) Dummy structure removal by tweezers. B VI) Cleaning the PDMS slab with new solvent and drying. A IV), and B VII) Pouring uncured PDMS on the fabricated wax channel. A V), and B VIII) Punching the cured PDMS at the inlet and outlet, and put it in the oven at a temperature of 115 °C. A VI), and B IX) The final microchannel after flushing the melted wax, and cleaning the channel with Acetone.

Finally, the 3D printed mold was removed from the PDMS by melting the wax in an oven (Figure 5-1B VIII, and A V) at a temperature of 100–115 °C and flushing the channels with acetone at room temperature (Figure 5-1 B IX, and A VI). Using this approach eliminates the time-consuming PDMS bonding step and prevents the leakage at high flow rates since PDMS layers merge together during the curing process. It has been proven that acetone has negligible effects on the PDMS-made channels and can be used to clean the channels without damaging the device and altering its properties [212].

5.2.2 Experimental setup

In this experiment, all images were captured using an inverted epi-fluorescence microscope (Nikon Eclipse Ti) equipped with a monochrome CCD camera (NIKON DS-Qi1Mc) and a CoolLED pE300. The exposure time and long-working-distance objective were set to 400 ms and 4X, respectively. A high-speed camera (Phantom- VEO 640L) with 7000 fpm and 60 μ s exposure time was used to take the images of microcarrier separation from stem cells. Fluorescent microbead (phosphorex-USA) suspensions (5×10^4 per mL) were loaded in 10 mL BD plastic syringes with Luer-Lok® tips and pumped through the microchannels using a Nexus 3000 syringe pump. In addition, the mixture of Dry Cytodex 3 microcarriers (GE Healthcare, the volume fraction of 0.15%) and stem cells (fat-derived hMSCs, the average concentration of 0.6×10^5 cells/mL) was driven continuously through the microchannels by a peristaltic pump (Shenchen, LabV1, China).

Fat-derived hMSCs were first cultured in a T175 tissue culture flask in a humidified incubator at 37 °C and 5% CO₂ and then passaged in a high-glucose Dulbecco's modified Eagle's medium (DMEM, Life Technologies) supplemented with 1% Penicillin-Streptomycin (10,000 U/mL, Life Technologies Holdings Pte Ltd), 10 ng/mL bFGF (Sigma-Aldrich) and 10% fetal bovine serum (FBS, Life Technologies). After 80% confluency, they were washed with Mg²⁺ and Ca²⁺ free DPBS and dissociated by 25% trypsin and 0.53 mM EDTA. Finally, cells were suspended in the five-fold diluted culture medium to neutralize the trypsin, harvested

by centrifugation, and re-suspended in the culture medium with desired cell concentration. Microcarriers were hydrated by 1X, Mg^{2+} and Ca^{2+} free phosphate buffer saline (PBS) for three hours, and then washed by PBS before autoclaving. Finally, the microcarriers were stocked and suspended with the volume fraction of 0.15%.

In order to make a Newtonian sample, 100 μ L of fluorescein (green) was diluted in 15 mL of Auto MACS buffer (Miltenyi Biotec). The viscoelastic solution was also made by adding 0.1 g of polyethylene oxide (PEO, Sigma-Aldrich, Mw = 2000 kDa) powder to 50 mL of AutoMACS buffer solution. In order to measure the viscoelasticity of the PEO solution, relaxation time (λ) and viscosity of the PEO solution (η_p) were measured by a capillary breakup extensional rheometer (CaBER-1, ThermoHakke) and a rotational rheometer (MCR-301, Anton Paar), respectively, as $\lambda_{mean} = 0.0106$ s and $\eta_p = 0.031$. All the solutions and tests were made and performed at room temperature (27 °C). It should be noted that peristaltic pumps produced some small pulsation; however, as we used a pressure damper, and given the flexibility of PDMS-made channels, this had no effect on the flow profile and particle focusing.

5.2.3 Surface characterization

The surface of the PDMS device replicated from the wax printed mold was examined by a 3D laser microscope (Olympus LEXT OLS5000) with an LMPLFLN 10x LEXT objective lens (Olympus). Profilometry images were used to analyze the surface morphology, surface roughness, and step heights. The surface roughness was evaluated as arithmetical mean height (S_a), which measures the average magnitude of variation in the height of individual points, compared with the arithmetical mean of the corresponding surface.

5.3 Results and discussion:

5.3.1 Wax 3D printer

The nominal resolution of the S350 Wax 3D printer used in this study is 6 μ m in the Z axis (layer thickness) and 24 μ m in the X and Y axes. Nevertheless, based on our findings, the smallest printable dimension for rectangular cross-section is approximately 75 μ m in width and

50 μm in height (hydraulic diameter $\sim 60 \mu\text{m}$), whereas for non-rectangular geometries this value increases to 200 μm . We decided to fabricate different channels with 250 μm hydraulic diameter in order to evaluate the printing quality for different geometries and to compare the effect of channel cross-sectional geometry on particle migration under similar hydrodynamic conditions.

5.3.2 Characterization of microfluidic devices

The surface finish of PDMS replica and its performance strongly depend on the fabrication procedure [36]. Conventional soft lithography techniques using microfabricated molds are not able to produce microchannels with non-planar cross-sections (e.g., triangular, circular), especially in curvilinear geometries. In addition, bonding a PDMS slab to another PDMS layer or a glass slide requires tedious micro-scale alignment and surface treatments (oxygen plasma, adhesive, ultrasonic, etc.), all of which can result in leakage at the interface of two surfaces. Here, we have proposed a new methodology based on the wax 3D printing and soft lithography capable of overcoming mentioned issues. To this end, we fabricated straight, curved, and spiral microchannels with different cross-sections (i.e., circular, rectangular, triangular and complex) as shown in Figure 5-2 A and C. Careful characterization of fabricated microchannels using this approach revealed that all geometries have a good surface finish with S_a of $\sim 1.75 \mu\text{m}$ (Figure 5-2 B) and are close to the designed structures dimensionally (errors of less than 3%). To better illustrate the quality of the fabricated channels, a magnified view of the triangular channel is presented. As can be seen, while the fabrication workflow precisely makes the sharp edges, the triangular tip was printed imperfectly due to the printing resolution and geometrical constraints in X-Y directions. The required time for printing can vary as a function of channel size and the resolution value in the Z direction. For the objects printed in this study with 6 μm Z resolution, the time required was around 6 hr. It should be noted that the transparency of the final microchannels is comparable with that of PDMS, as the printed wax channels were used only as a sacrificial template for the PDMS casting. To the best of our knowledge, inertial

focusing in curved circular and triangular microchannels has not been studied previously due to the difficulty of their microfabrication using conventional techniques. More importantly, the utilization of dummy structures proposed in this study (i.e., to reinforce the main channels during the peel-off from the print bed) allowed us to create high-quality microchannels, not reported in the previous studies [182, 212, 213].

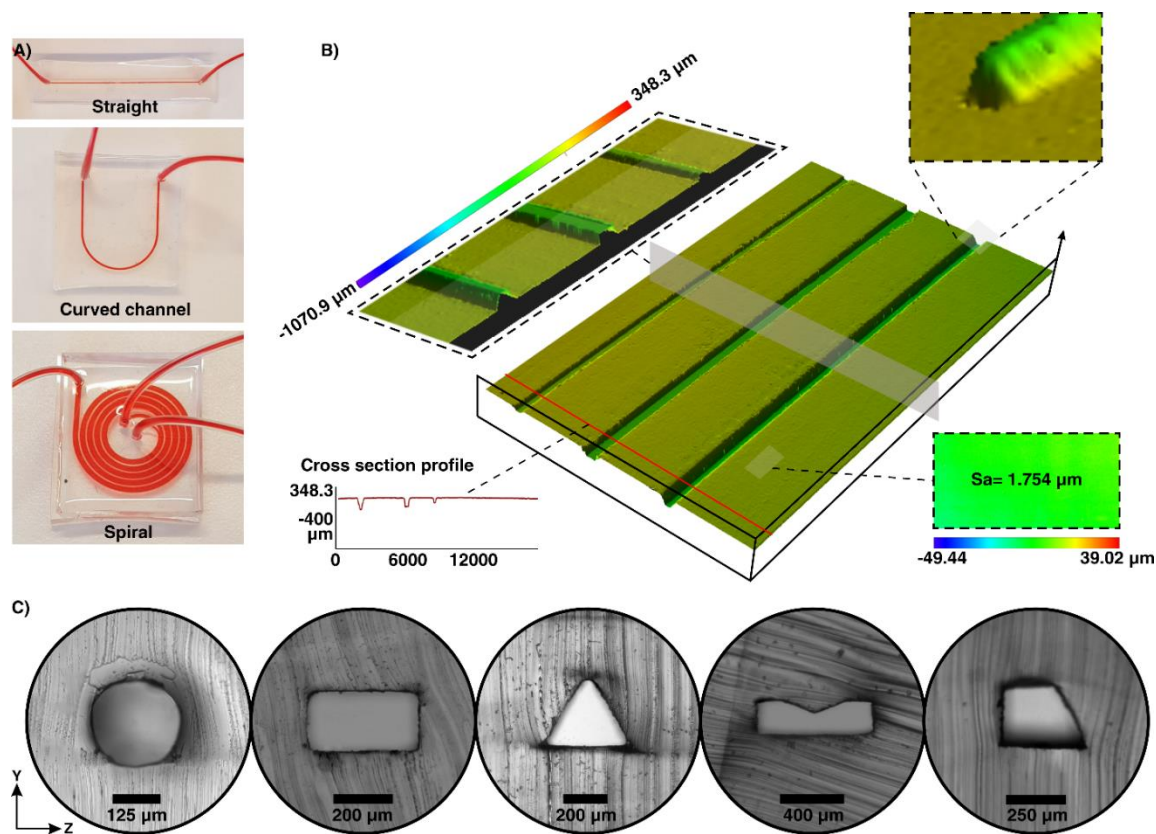


Figure 5-2: A) Top view images of the PDMS devices used for particle sorting. B) Characterization of the wax printed channels using a profilometer device. It shows the printed channels from different angles, and surface roughness ($1.75 \mu\text{m}$). C) Cross-sectional optical micrograph of the PDMS microfluidic chips.

Figure 5-2 C demonstrates cross-sections of different curved and straight microchannels fabricated by the wax printing method, which was further used for particle migration analysis in Newtonian and non-Newtonian solutions. All single curved channels (triangular, rectangular and circular cross-sections) share the same hydraulic diameter of $250 \mu\text{m}$ and curvature radius of 6.5 mm , for consistency of hydrodynamic conditions in each channel.

5.3.3 Numerical Simulation Results

In order to study the effects of channel geometry on the flow field and Dean vortices, three different circular, triangular, and rectangular curved channels with the same hydraulic diameter were numerically modeled in Comsol 5.3a, a commercially available software based on finite element method. For this purpose, the continuity and Navier Stokes equations for a laminar incompressible Newtonian flow were solved as follows:

$$\nabla \cdot V = 0 \quad (5-1)$$

$$\frac{\partial V}{\partial t} + \rho(V \cdot \nabla)V = -\nabla P + \mu \nabla \nabla^2 V \quad (5-2)$$

where P is the static pressure, V is the velocity vector, ρ is the fluid density, and μ is the dynamic viscosity of the fluid. For the Newtonian solution, ρ and μ were considered to be 998.2 kg/m^3 and $0.001002 \text{ kgm}^{-1}\text{s}^{-1}$, respectively. As shown in Figure 5-3, the curvature at the start of the bend in the channel acts as an obstacle and pushes the flow towards the inner wall. However, shortly after this, the flow shifts towards the outer wall and returns circumferentially to the inner wall, due to the presence of a centrifugal force caused by the curvature. These secondary flows, or Dean vortices, push the main flow outward and cause the velocity profile peak to occur near the outer wall. However, due to the changes in geometry, the maximum value of the velocity in each cross-section differs from the corresponding value in the other geometries. While the maximum velocity in the triangular channel is approximately 0.91 m/s , it drops to around 0.86 m/s in the circular and rectangular channels. Also, each channel has its range of helicity (defined in Eq.(5-3)), based on its shape. Helicity is the strength of Dean vortices in helical flows and is a practical variable to quantitatively evaluate secondary flows in curved channels, as a high value of helicity implies stronger Dean vortices and consequently more mixing [214].

$$H = \omega \cdot v \quad (5-3)$$

where H is the helicity, and ω and v indicate the angular and axial velocity, respectively. As shown in Figure 5-3, at the same flow rate, the rectangular geometry has lower value of maximum helicity (≈ 400) compared to other channels (≈ 600).

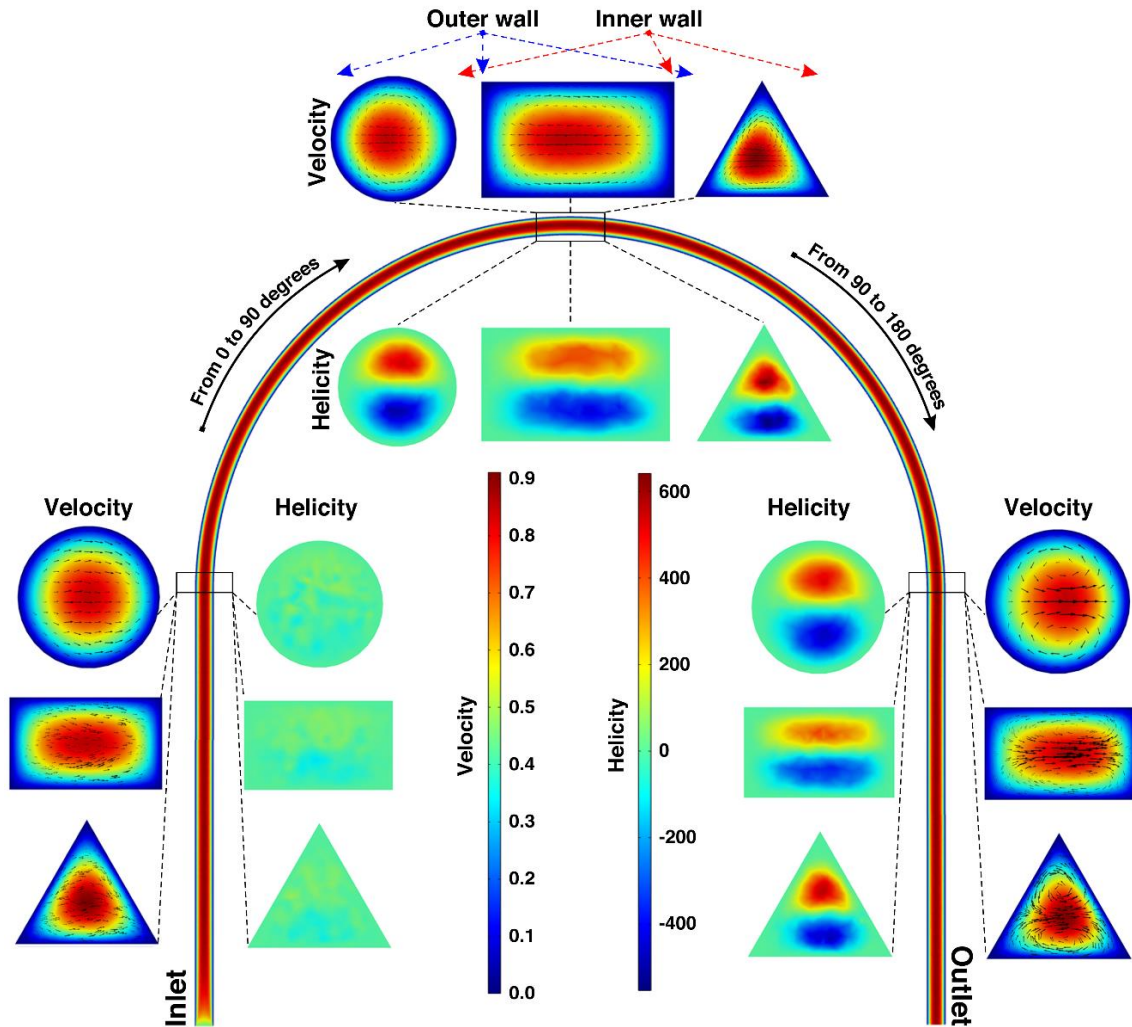


Figure 5-3: Velocity and helicity contours for circular, rectangular and triangular single curved channels for the flow rate of 1.1 ml/min. Through the curved part, the maximum velocity region gradually moves towards the outer wall. Rectangular and triangular channels have the least and most helicity, respectively.

So for high-throughput applications in spiral and curved channels where Dean drag is dominant compared to other inertial forces, rectangular geometry is more suitable than other cross-sections, due to its lower value of helicity. Figure 5-3 also shows that the location of the maximum helicity regions varies in each channel, which noticeably alters the focusing positions in each channel. Generally, particle focusing happens in the regions where secondary flow drag

is weak and can be balanced by inertial forces. At high flow rates, Dean vortices dominate the other inertial forces, and particles remain scattered throughout the channel [215].

5.4 Experimental Results

This section consists of three parts. First, we demonstrated the particle migration in a single curve channel with various cross-sections. Second, the particle behavior inside a straight channel with trapezoidal and complex cross-sections (a superposition of two trapezoids) was evaluated. Finally, as a proof of concept, we investigated using an optimized channel design for separation of human mesenchymal stem cells (hMSCs) from microcarriers.

5.4.1 Curved Channels

During the last decade, curved and spiral channels have been extensively used to separate cells and particles (e.g., cancer cells, bacteria, and algae) from complex biofluid solutions [11]. As a result, finding a new method to fabricate curved channels with better separation efficiency is of great importance. In this part, focusing of $50\text{ }\mu\text{m}$ fluorescent particles is investigated for a wide range of flow rates in order to evaluate the functionality of the proposed fabrication method for inertial microfluidic applications.

In general, particle focusing in microchannels occurs when the diameter of flowing particles (a) is comparable to the characteristic length of the channel (D_H) ($a/D_H > 0.07$) [67]. Furthermore, for an appropriate value of blockage ratio ($a/D_H \sim 0.2$), focusing can occur even in a single-curved channel [216]. Typically, inertial forces can be divided into four categories, namely, wall-induced (F_w), shear gradient (F_s), Magnus (F_Ω), and elastic lift (F_E) forces. F_w is a repulsive force which pushes the particles away from the walls, while F_s acts in the opposite direction and forces the particles towards the walls. The Magnus force originates from the particle rotation and is due to the asymmetric shear stress on the particles. It causes particles to migrate circumferentially towards final equilibrium positions and only becomes significant wherever F_w and F_s substantially balance each other [217]. The viscoelastic force (F_E), arising from the non-Newtonian behavior of the solution, pushes the particles towards the low shear

stress regions. As shown in Figure 5-4 A, since the blockage ratio meets the criterion for single curve focusing ($a/H = 0.2$), particles can be focused in all of the curved channels. While all these channels have the same hydraulic diameter of $250\ \mu\text{m}$, due to the nonlinearity of their shapes, each channel has its own focusing behavior. As can be seen, for a Newtonian solution, particles focus close to the inner wall, where the secondary flow drag and inertial lift forces balance each other for a wide range of flow rates and all the cross-sections used. However, the focusing band and position vary between cross-sections. The triangular structure has the highest helicity value (based on numerical results in section 5.3.3); nevertheless, the particles are mainly concentrated in the center of the channel due to the presence of sharp corners and strong wall-induced lift forces towards the channel center. On the other hand, the additional elastic force arising from the non-Newtonian property of the PEO solution pushes the particles away from the inner wall and causes a new focusing position to form near the outer wall due to the synergistic effect of Dean drag and elastic forces (Figure 5-4 B). Near the outer wall, the outward Dean and shear gradient lift forces are balanced by the opposing wall-induced and elastic lift forces, resulting in particles reaching an equilibrium at this position. Figure 5-4 A also shows that for the non-Newtonian solution at a flow rate of $0.5\ \text{ml/min}$, particle migration towards the outer wall happens more gradually, since secondary flows are weaker in the rectangular channel than for the other channel geometries. Besides, it can be observed from the same figure that in the non-Newtonian solution, the focusing position of particles did not change for varying flow rates in circular and triangular cross-sections; However, in rectangular channels, higher flow rates resulted in the focusing band moving closer to the outer wall.

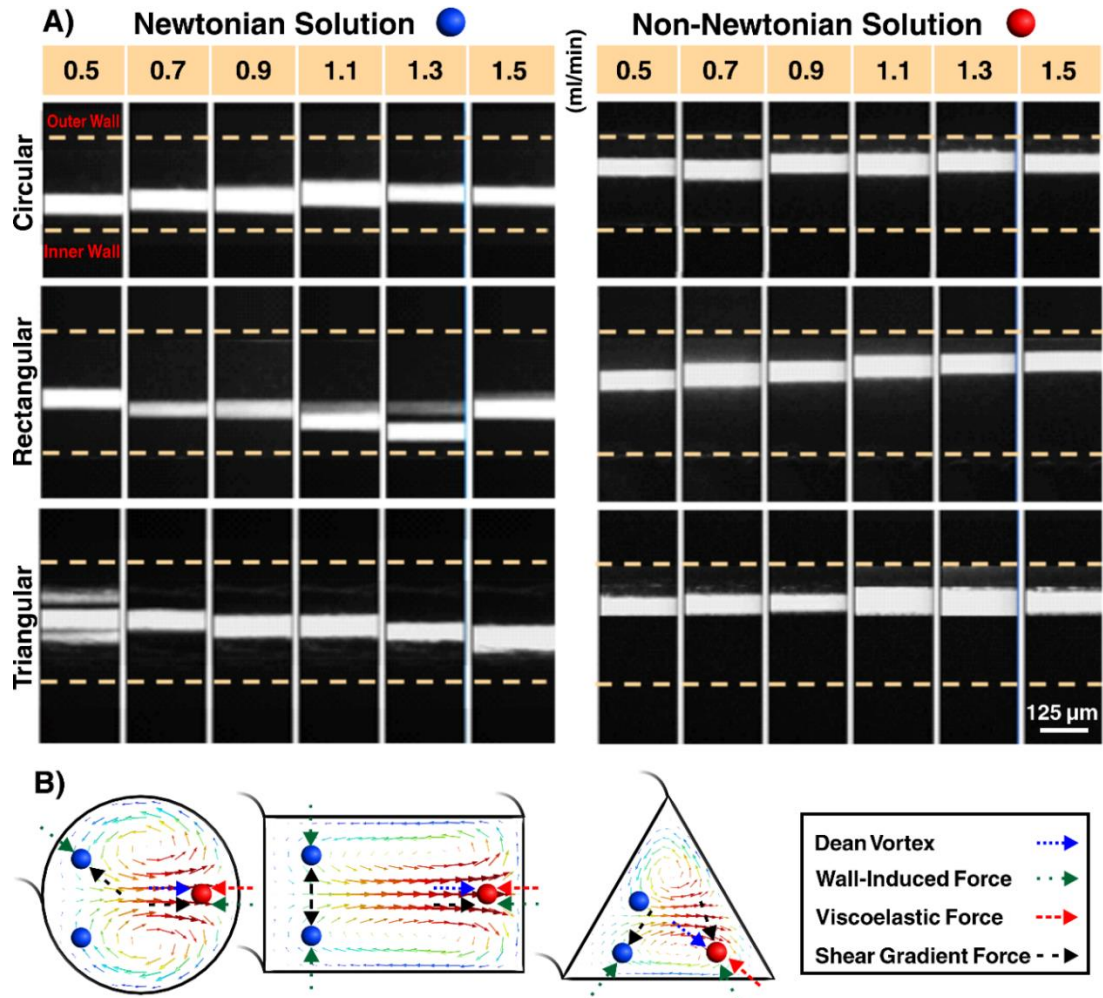


Figure 5-4: Focusing of 50 μm particles through circular, rectangular, and triangular curved channels under different flow rates at $\theta = 180^\circ$. A) Fluorescence microscopy results for the Non-Newtonian solution (PEO (2000 ppm)) and Newtonian solution (PBS) which shows a distinct focusing near the outer and inner walls, respectively. B) Cross-sectional view of the channels which shows the Dean vortices, inertial, and elastic lift forces, and the equilibrium positions for the flow rate of 1.1 ml/min.

5.4.2 Straight Channels

Trapezoidal microchannels have recently proved to have higher efficiency and better resolution (i.e., distance between two particle streaks) in particle separation in comparison to conventional microchannels such as rectangular and square channels due to the non-linearity of their cross-section [159].

In this section, the effects of a trapezoidal cross-section on particle migration for Newtonian and non-Newtonian solutions were investigated and then the superposition of two trapezoidal cross-sections to form a complex geometry was evaluated. Figure 5-5 shows that in straight channels, focusing happens predominately due to the F_W , F_s , F_E , and F_Ω forces. Figure 5-5 A

illustrates that particles equilibrate near the vertical side for the straight trapezoidal channel in the Newtonian solution at a flow rate of 0.5 ml/min. As can be seen in Figure 5-5 B, dispersed particles initially migrate laterally towards the focusing line where F_w and F_s balance. Then, particles move vertically towards the equilibrium positions under the effect of F_Ω . By increasing the flow rate, the equilibrium positions migrate towards the slanted wall. This is due to the particles' tendency to migrate to regions where the flow rate is lower, minimising the shear stress and pressure gradient on the particles. Conversely, in the complex channel, the focusing positions diverge into two bands, each located in one trapezoidal section, and remain fixed for all flow rates tested. Although the cross-sectional area of the complex channel is almost twice the size of the single trapezoidal channel, the focusing phenomena are still manifest, which suggests that this method can be used to increase the channel cross-sectional area for high-throughput applications (e.g., sample concentration) without diminishing the inertial forces. Providing dual outlets can thus allow separation of distinct output samples. For non-Newtonian solutions, however, particles concentrate at the channel center for both trapezoidal and complex geometry. This is due to the additional viscoelastic force which is stronger around the walls and pushes the particles towards the channel center (Figure 5-5 B) where F_E is at its minimum range and can be balanced by the opposing inertial forces. As can be seen in Figure 5-5 A, while particles find an equilibrium position at the center of the trapezoidal channel for all the given flow rates, for the complex channel, they focus in the narrowed area between the two trapezoidal geometries. The tight single focusing band shows the potential of the complex channel for flow cytometry applications.

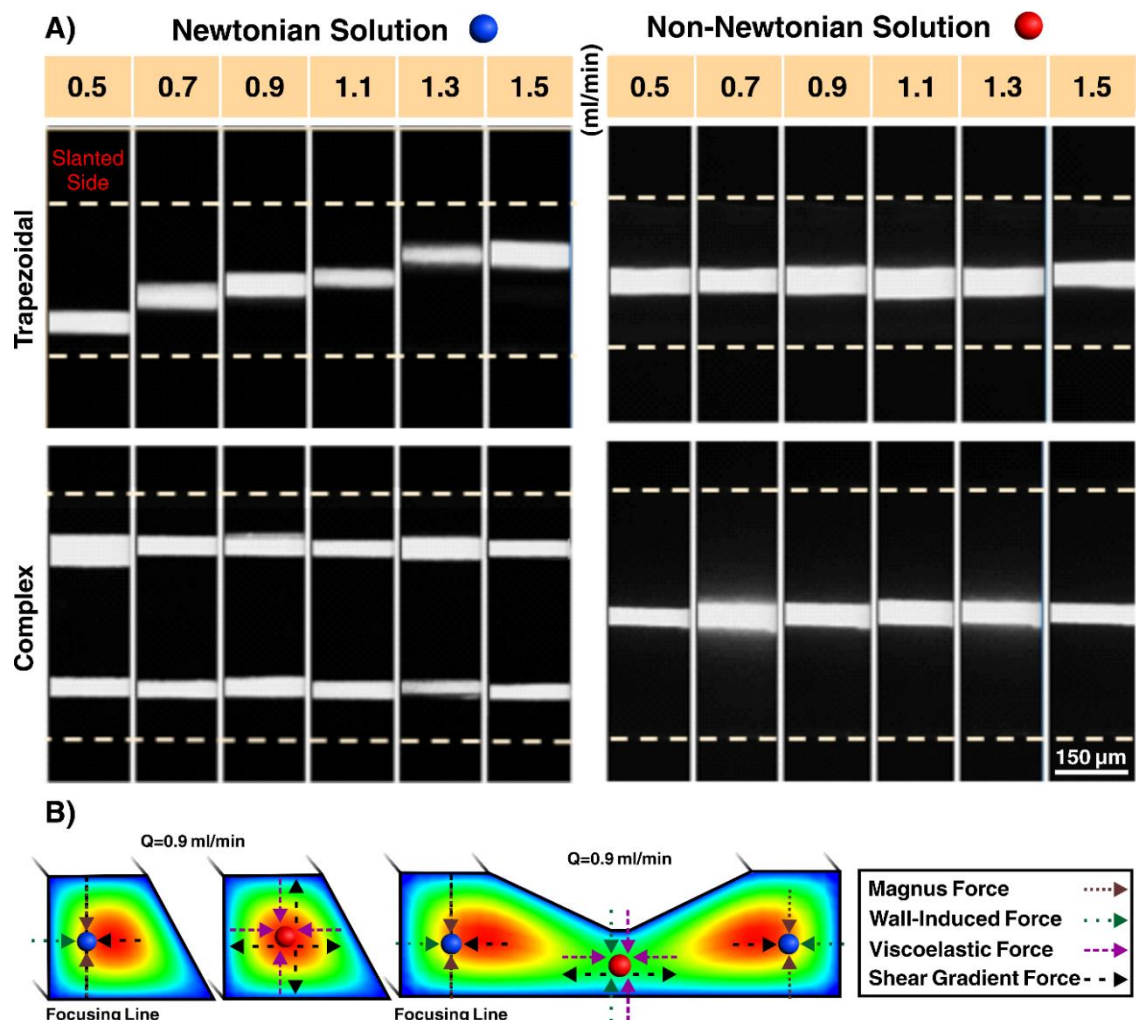


Figure 5-5: Focusing of 50 μm particles within straight trapezoidal and complex channels under different flow rates. A) Focusing results for the Non-Newtonian solution (PEO (2000 ppm)) and Newtonian solution (PBS) captured by fluorescence microscopy. For PEO solution, particles focus at the center for all flow rates and channels. However, for the PBS solution and the complex channel, particles focus at both sides for all the flow rates. Equilibrium positions in trapezoidal channel move towards the slanted wall by increasing the flow rates. B) Cross-sectional view of the channels which shows the inertial and elastic forces as well as equilibrium positions for a flow rate of 0.9 ml/min.

5.4.3 Separation of microcarriers from Mesenchymal Stem Cell

Due to the rapid development of cell-based therapy techniques, high-throughput and effective methods are required to grow adherent cell types such as hMSCs. Large-scale manufacturing of stem cells using microcarriers (100–300 μm) in a perfusion bioreactor is proven to be a promising approach; however, downstream separation and purification of the cells from microcarriers has remained a big challenge in the bioprocessing industry [206]. Here, as a proof of concept, a wax-printed spiral complex channel is used to filter microcarriers from the hMSCs (Figure 5-6 A). To mimic the condition of a bioreactor, a mixture of 180 μm microcarriers and

hMSCs were prepared in a PBS solution and then pumped into the spiral channel by a peristaltic pump at flow rate of 10 ml/min. To prevent sedimentation of the microcarriers, the suspension was continuously mixed by a stirrer during the experiment. Throughout the channel, cells and microcarriers are affected by the secondary forces and rotate with the secondary flows. After 4 loops, microcarriers focus on the inner side of the channel, where Dean drag and inertial forces balance each other. However, stem cells remain dispersed because the blockage ratio for stem cells is smaller than 0.06; hence, the effect of the inertial forces on them is negligible. Figure 5-6 B I and B II show the microcarriers collected from the inner outlet and the stem cells harvested from the outer outlet after the second pass, respectively. The microcarrier separation efficiency and the cell recovery rate were approximately 98% and 93%, respectively, demonstrating the ability of the complex spiral channel to fractionate microcarriers and cells effectively. The harvested cells were cultured in a plastic tissue culture and formed a cell monolayer within 3 days, confirming their viability for downstream assays (Figure 5-6 B III). Besides, multipotency test was performed to evaluate the quality of the stem cells for differentiating into osteoblasts, adipocytes, and chondrocytes. The results demonstrated that the multipotency of the collected hMSCs was totally retained and not compromised. Trilineage differentiation into osteogenic, chondrogenic, and adipogenic lineages after 28 days showed that staining was positive for the 3 differentiated lineages, as shown in Figure 5-6 C. Lipid vacuole formation was visualized using Oil Red O which confirmed adipocytic phenotype (Figure 5-6 C II). Glycosaminoglycan complex stained by Alcian Blue showed chondrocytic phenotype (Figure 5-6 C III), and positive staining of the mineralized matrix by Alizarin Red S demonstrated osteoblastic phenotype (Figure 5-6 C I).

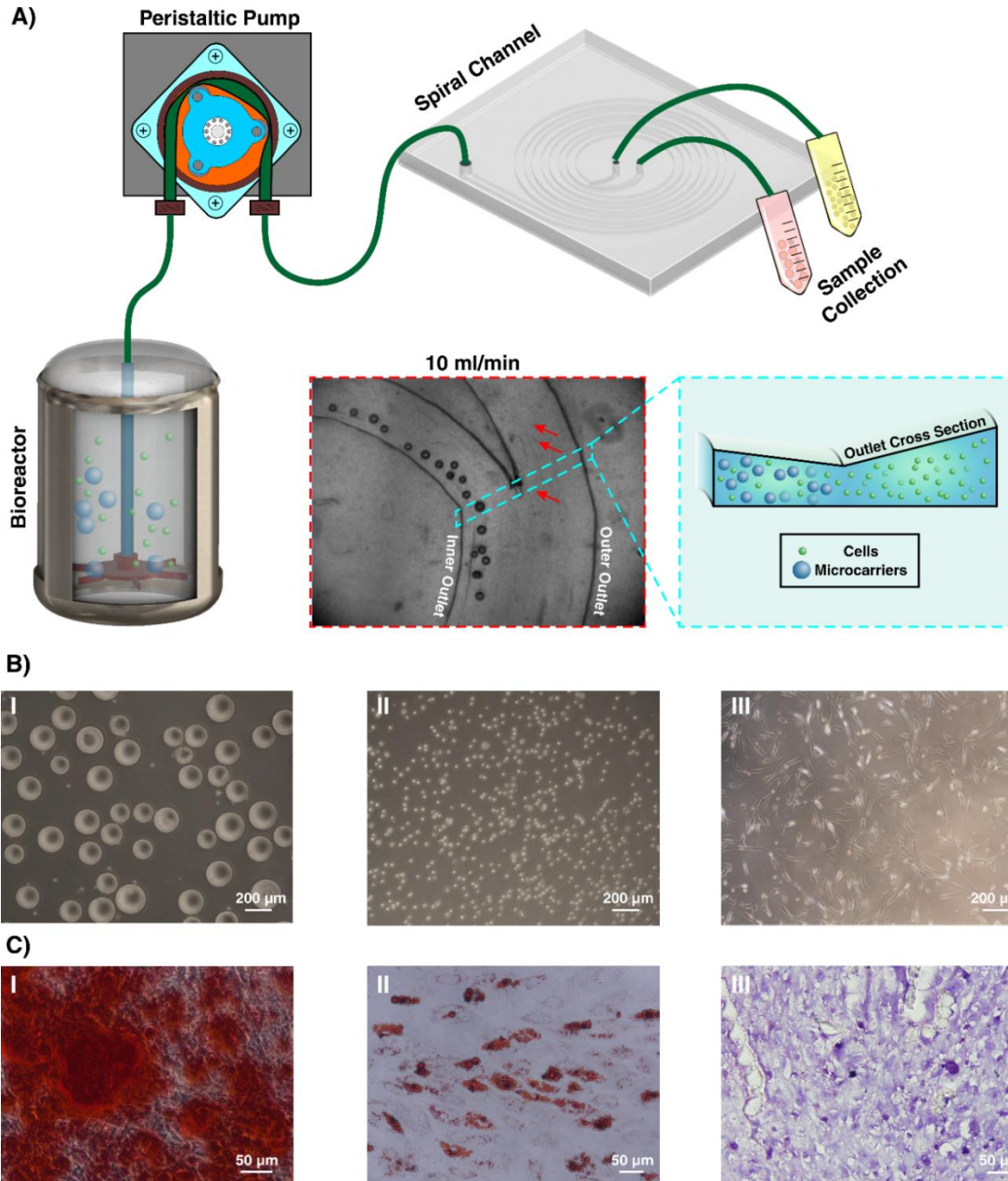


Figure 5-6: Microcarrier separation from stem cell suspensions. A) Schematic model of the setup which shows the suspension in a bioreactor injected into the microchannel at 10 ml/min by a peristaltic pump. Before the bifurcation, microcarriers migrate to the inner wall and can be extracted there. Red arrows indicate the cells flowing through the outer outlet. B I) Collected microcarriers from the outer outlet. B II) Harvested stem cells from the inner outlet after the second pass. B III) stem cell monolayer formation after 3 days. C) Multipotency assay of collected hMSCs stained by Alizarin red, Oil Red O, and Alcian blue to demonstrate I) Osteogenic, II) Adipogenic, and III) Chondrogenic differentiation, respectively.

5.5 Conclusion

Sacrificial 3D printed molds have been used in fabrication of microfluidic devices, where PDMS elastomer has been cast into a wide range of dissolvable materials such as sugar alcohol isomalt [218], polyvinyl alcohol (PVA) [219], polyethylene glycol (PEG) [220], and

acrylonitrile butadiene styrene (ABS) molds [221]. Although the use of these materials is a step forward in simplifying the fabrication of microfluidic chips, the resolution of microchannels obtained using these template-assisted techniques is not high enough to meet the requirement of inertial microfluidics.

In this paper, we overcome many of these limitations by employing a high-quality wax 3D printer and softlithography through a novel workflow, which eliminates the need for use of harsh chemicals, multiple cleaning steps and more importantly PDMS bonding. We have shown that by adding dummy structures to reinforce the template and dissolving the support wax on a PDMS slab to eliminate the additional handling steps, one can make various microfluidic microchannels with any arbitrary cross-section. Careful characterization of fabricated microchannels using this approach revealed that all geometries have a good surface finish with Sa of ~ 1.75 , reproducing the intended design with dimension errors of less than 3%.

In addition, focusing of $50\text{ }\mu\text{m}$ particles in Newtonian and non-Newtonian solutions, for various curved and straight channels was demonstrated to highlight the suitability of this technique for inertial microfluidics. Systematic analysis of curved microchannels using numerical simulations revealed that rectangular-shape channels have lower helicity values compared to the circular and triangular geometries at similar flow rates. As such, for high-throughput focusing applications, a rectangular channel is preferable, as it has lower helicity values and consequently less particle mixing. As expected, experimental results revealed that the focusing positions in Newtonian and non-Newtonian solutions are quite different, due to the extra viscoelastic force applied on the particles. For the Newtonian solutions, particles find equilibrium close to the inner wall of the curved channels, while for the non-Newtonian solutions, equilibrium positions move towards the outer wall due to viscoelastic force. In straight channels, for a trapezoidal shape and Newtonian solution, increasing the flow rates resulted in a migration of the focusing line from the vertical side to the slanted side. However, for the non-Newtonian solution, particles focused at the center of the channel for all the tested

flow rates. While the cross-sectional area of the complex channel is almost twice the size of the single trapezoidal channel, distinct focusing in the complex channel showed the potential of the superposition technique for high-throughput applications. Finally, as a proof of concept, we fabricated a spiral channel with a maximum cell-holding capacity able to separate microcarriers from MSCs with over 98% efficiency. We believe this new method for fabrication of complex inertial microfluidic channels will open up avenues for researchers to explore new physics and develop new applications for the promising field of microfluidics.

5.6 Acknowledgment

This research work is supported by the Australian research council through discovery project grants (DP170103704 and DP180103003) and the national health and medical research council via the career development fellowship (APP1143377).

6

Chapter Six:3D-Direct-Printing of Inertial Microfluidic Devices

Introduction

In this chapter we propose a new fabrication workflow based on the 3D printing technology to facilitate the microchannel fabrication, especially with non-conventional geometries. So far, inertial microfluidics has been broadly investigated, resulting in development of various applications particle or cell separation. The lateral migrations of these particles within a microchannel are strictly dependent on channel design and its cross-section. In this study, by gaining the efficiency of additive manufacturing, we have proposed a new method for fabrication of inertial microfluidic devices. In this way, the parts are first printed via a high-resolution 3D printer, and then are bonded to a PMMA slab. Although structuring via usage of a commercial-grade 3D printers is becoming comparatively easy, reliable, accurate, and rapid assembly to provide a leakage-free interface for inertial microfluidic application remains a challenging issue.

Authors' Contributions:

1) Sajad Razavi Bazaz and Omid Rouhi:

Designing the channels, Optimizing the printing configuration, writing most of the manuscript.

2) Omid Rouhi:

Optimizing the printing configuration and running the tests.

3) Mohammad Amin Raoufi:

Designing and Running the tests for spiral channels, designing and analyzing the Saffman-Taylor finger tests, writing the introduction, characterizing the channels, and image processing.

4) Fatemeh Ezheian:

Cell culture and cell analysis

5) Mohsen Asadnia, and Majid Ebrahimi Warkiani

Revising the paper

This chapter is prepared for submitting to scientific reports.

3D-Direct-Printing of Inertial Microfluidic Devices

Sajad Razavi Bazaz^{1‡}, Omid Rouhi^{1‡}, Mohammad Amin Raoufi^{1,2}, Fatemeh Ezheian, Mohsen Asadnia², Majid Ebrahimi Warkiani^{1,4*}

¹*School of Biomedical Engineering, University of Technology Sydney, Sydney, New South Wales 2007, Australia*

²*School of Engineering, Macquarie University, New South Wales 2109, Australia*

⁴*Institute of Molecular Medicine, Sechenov University, Moscow, 119991, Russia*

[‡] Co-first authors

* Corresponding Author: Majid Ebrahimi Warkiani (majid.warkiani@uts.edu.au)

Abstract

Inertial microfluidics has been broadly investigated, resulting in development of various applications, mainly for particle or cell separation. The lateral migrations of these particles within a microchannel are strictly dependent on channel design and its cross-section. Nonetheless, fabrication of these microchannels is a continuous challenging issue for microfluidic community, where the most studied channel cross-sections are limited to only rectangular and more recently trapezoidal microchannels. As a result, a huge amount of potential remains intact for other geometries with cross-sections difficult to fabricate with standard microfabrication techniques. Recently, there is a growing body of interest in versatile and low-cost microfluidic devices where their fabrication process is straightforward, rapid, and universal; also, has the potential of industrial mass production. In this study, by leveraging on the benefits of additive manufacturing, we have proposed a new method for fabrication of inertial microfluidic devices. In our proposed workflow, parts are first printed via a high-resolution DLP-SLA 3D printer, and then bonded to a PMMA sheet. Although fabrication of microfluidic components using commercial-grade 3D printers is becoming comparatively easy, development of a robust protocol to produce a leakage-free interface for inertial microfluidic application remains a challenging issue. Accordingly, we have proposed a cost-effective, reliable and reproducible method, relying on a high-pressure double adhesive tape. Our characterizations revealed that produced chips can withstand up to 150 psi pressure with minimum interference of the tape to the total functionality of the device. In this way, there are three key features that differentiate the proposed approach from existing fabrication methods which are restricted to a certain extent. The first is its universal nature for direct fabrication of a plethora of existing inertial microfluidic devices as exemplified for fabrication of straight, spiral, serpentine, curvilinear, and contraction-expansion arrays, indicating the potential to exploit underlying physics in various channel geometries. Second, the total time frame, from designing a part to starting the experiment just took less than two hours, representing a huge amount of saving time for inertial microfluidic community. Third, the proposed workflow can be adopted at production levels, enabling large-scale production of inertial microfluidic systems.

Keywords: 3D printing; Hard chip; Inertial microfluidics; Microfluidics,

6.1 Introduction

Particle/cell regulation and manipulation often involve intricate interaction between particulates and the surrounding carrier flow. The advent and emergence of microfluidic systems herald new hopes in developing miniaturized devices. In particular, utilizing these devices offer such unique advantageous over conventional methods such as high-throughput, less sample consumption, and low cost, thereby opening new avenues for discovery of new phenomena [11]. These fluid handling systems are typically categorized as either active or passive. In active systems, particle sorting occurs by applying external forces which require a long time to influence particle migration, making them a less viable commercially option. On the other hand, inertial platforms only rely on intrinsic hydrodynamic forces between particles and their surrounding fluid and function at higher flow rates. Hence, inertial microfluidic devices are envisioned as the next milestone for particle separation. As in inertial microfluidic systems lateral migration of particles strongly depends on the channel geometry [162], an accurate and robust fabrication method is undoubtedly a crucial need for achieving a highly functionalized device.

Although theoretically straightforward, the fabrication process of inertial microfluidic devices involves challenging engineering issues, including the difficulty of alignments in micro/nano scales and limitations of fabrication for channels with nonlinear geometries. Microfabrication contains a myriad of approaches; nonetheless, few of them are suitable for inertial applications. This stems from either lack of enough accuracy for the fabrication of complex channels within microscale or poor transparency of the device for particle trajectories and live monitoring [135, 209, 211, 222]. Despite the promising future of inertial microfluidics in many disciplines, its applications are yet limited because of inefficient and expensive fabrication methods available, each of which are capable of fabricating specific geometries and cross-sections. Therefore, developing a new fabrication strategy capable of constructing a variety of geometries and structures easily and straightforward is of significant importance.

Improving fabrication techniques can not only reduce the fabrication time and cost but also will benefit the microfluidic community in exploring new physics by facilitating the creation of non-conventional microchannels [84, 123].

So far, several microchannels (i.e., straight, spiral, and serpentine) with different cross-sections have been proposed to enhance particle sorting via optimizing the effects of inertia and Dean drag forces. [121, 122, 152, 196, 223]. These devices are mainly fabricated by casting PDMS on a master-mold due to the suitability and biocompatibility of the PDMS material for live monitoring and biological applications. Conventionally, master molds were created by lithography-based approaches, which results in channels with rectangular geometry. [194, 197]. While this approach has been the basis of many microfluidic device developments, inability to build non-orthogonal and non-planar structures, time-consuming process, and the requirement for expensive fabrication equipment hampered its widespread applications [224]. Silicon direct etching (wet and dry) [201] is another alternative for fabrication of 2D master molds, mainly for non-orthogonal geometries (i.e., trapezoids, and triangles). Using this approach, Kim et al. [123] managed to fabricate two triangular channels with tip angles of 70.6° and 90° to study the particle migration in triangular geometry. However, anisotropic wet etching is typically limited to few geometries due to the crystallography issues. To address this difficulty, the same group recently fabricated a triangular channel mold by scribing a brass work-piece with a diamond-tipped tool [125]. Despite the simplicity of this method for mold fabrication, scribing is limited to very few geometries and creates a negative mold which needs double PDMS casting to construct a sealed channel.

Mechanical machining [203, 204] is a well-established approach capable of creating non-rectangular cross-sections. Although micro-milling is incapable of creating curve cross-sections and sharp-edge bifurcations due to the mechanical limitations and curvature at the tip of the mill, respectively, it has been widely employed for constructing inertial microfluidic channels

with trapezoidal and triangular geometries [121]. Our group fabricated myriads of spiral trapezoidal channels to passively separate and filter different types of cells and particles [172]. Laser cutting [116, 117, 119, 225] is another technique for the fabrication of master molds or direct-channels in polymers and glasses. Various microfluidic devices have been fabricated to sort particles size-dependently using femtosecond laser irradiation and CO₂ laser ablation techniques [225, 226]. Despite the simple fabrication process, the complexity of building non-rectangular cross-sections, poor surface finish, and requiring a time-consuming etching step making them less user-friendly.

Hot embossing [207, 208] is an attractive method for rapid prototyping and high volume production of microfluidic systems with microscale features. Wang et al. recently sorted bovine WBCs within a low-aspect-ratio rectangular channel made by roll-to-roll (R2R) hot embossing technique. Nonetheless, requiring sophisticated equipment and inability to build non-rectangular cross-sections make this approach restricted to the conventional channels.

Another tactic to make microchannels is to embed metal micro-wires as a template inside a block of PDMS and remove them easily after PDMS curing by exerting a little tension [82]. In spite of the simplicity of this method in fabrication of circular channels, PDMS block rupturing or distortion and the presence of residuals in microchannels during and after the template removal restricts its manipulation in microfluidics applications [227, 228].

Recently, additive manufacturing or 3D printing has emerged as a powerful platform to fabricate 3D functional microfluidic systems from a variety of polymeric materials. This outstanding technology enables investigators to build microstructures with complex shape and geometry (i.e., micromixers, microchannels, microvalves, micropumps, etc.) in a short time. Benefiting from Stereolithography apparatus (SLA) technique, Lee et al. directly fabricated a 3D helical trapezoidal microchannel to separate magnetic nanoparticle clusters from *E. coli* (EC) bacteria [135]. However, due to the poor transparency of the fabricated channel, imaging (whether fluorescent, bright field or high speed) was not feasible through the channel. Besides,

their fabrication process limited to the dimensions in the range of millimeter and hundreds of microns which is not suitable for most of the inertial microfluidic applications. More lately, 3D printing of sacrificial molds has gained significant attention due to its simplicity and cost-effectiveness. Benefitting from fused deposition modeling (FDM) printer, Tang et al. [84] fabricated various microchannels with unconventional cross-sections to study the effect of geometry on elasto-inertial focusing. However, requiring different nozzle's tip and insufficient resolution of templates (due to the thermoplasticity of the ABS filaments) make this method impractical for many microfluidic applications.

To address these inadequacies, we have developed a robust protocol for large-scale manufacturing of inertial microfluidic systems. Thanks to the capabilities of DLP-SLA 3D printing, we have printed a wide range of microchannels with different geometries, capable of performing particle and cell focusing for a large range of Re numbers. The approach makes use of high-pressure double adhesive tape that perfectly binds 3D printed microchannels with optically transparent acrylic sheets, producing a leakage-free interface for inertial microfluidic applications. The bonding strength is quantified and the compatibility of the concept for fabrication of new generation of inertial microfluidic devices is evaluated using surrogate particles.

6.2 Materials and method

6.2.1 Fabrication Method

Inertial microfluidics has gained much attention. However, fabrication limitation hinders its further development. For the fabrication of a simple straight channel via softlithography, several days must spend (from CAD drawing to PDMS casting) to test the results. More importantly, re-iteration leads to spending the same amount of time, resulting in compiling lots of projects in the stage of just brainstorming. To address all these issues, we have proposed a new fabrication method capable of fabricating various inertial microfluidics devices in less than 2 hours (from CAD drawing to experimental testing). This leads to a revolution for further

expansion of the potential of this platform. Gaining the efficiency of additive manufacturing, we have used 3D printed microfluidic devices for chip manufacturing.

Gaining the efficiency of PMMA transparency and 3D direct printing, we have proposed a new fabrication method for fabrication of inertial microfluidic devices with various cross-sections and designs. Generally, parts printed by SLA 3D printers have great precision. However, since these parts are based on liquid resin, residual monomers and oligomers on their surface impede their further usage for PDMS casting and require extra steps for post-processing. Moreover, these materials are not capable of bonding with PDMS or glass slides. Some research groups try to bond the resin with its liquid resin, however, since the channel geometry is small enough, the liquid resin will penetrate inside the microchannel due to the capillary forces and disturb the cross-section and functionality of the devices. As such, we have proposed the use of a high-stress double adhesive tape for bonding of the resin chip with a PMMA layer. This tape is capable of withstanding high-pressure stress which results in bonding of these two layers. At first, the desired pattern designed in the Solidworks. Thereafter, it will be translated to .stl file to be suitable for 3D printer language. Afterward, based on the setting of the 3D printer, the parts will be printed. As the dimensions used in the inertial microfluidics are tiny and small, the printer must have high-quality. The printers used in this study is a MiiCraft Ultra 50 3D printer (MiiCraft, Hsinchu, Taiwan) with the printing area of 57×32×120 mm where the nominal XY resolution is 30 μm . The imported file must be carefully sliced to create an accurate geometry after the printing process. The slicing in Z direction can be adjusted from 5 to 200 μm with increment of 5 μm . Slicing option is related to the design pattern of the geometry. In the geometries where ramp or step exist, the thickness layer should be small, whereas for planar or orthogonal structures, higher thickness layer is suitable.

6.2.2 Preparation of Bead Suspension

Fluorescent microbeads (Fluoresbrite® Microspheres, Polysciences Inc, Singapore) 15 μm in diameter were added to the MACS® buffer with 0.01% volume fraction. The main usage of

MACS® buffer was to prevent nonspecific adhesion of microbeads to the walls and tubing of the microchannel. Also, spiral and micromixer microchips were washed with MACS® buffer (after being soaked in a water bath (Thermoline, Australia) at 37 °C for 10 min) to prevent the formation of bubbles inside the microchannel.

6.2.3 Bonding quality test

Inertial devices are operated at high flow rates; hence, the bonding technique must provide enough strength to prevent leakage from the interface. To evaluate the bonding quality of our proposed technique, a simple 3D-printed straight channel featuring 50 μm height, 200 μm width, and 4 mm length was bonded to a 2 mm transparent PMMA layer, and a high-pressure (to evaluate wide ranges of applied pressure inside the channel) syringe pump (Chemyx Fusion 4000, Chemyx, TX, USA) was used to inject fluids inside the channel while a 6ml syringe size was utilized to increase the maximum applied pressure to 587.90 psi. The bonding is stable up to a pressure where Saffman-Taylor fingers appear around the inlet, in which the most pressure in the channel present. Saffman-Taylor fingers are generated by the movement of a viscous fluid within a porous material. As the bonded adhesive tape forms a porous zone within a connecting part, this theory is applicable for bonding evaluation. An increase in the applied pressure leads to developments of the Saffman-Taylor fingers until the bonding fails. A brightfield microscope (DP80, Olympus, Tokyo, Japan) mounted on an inverted microscope (IX73, Olympus, Tokyo, Japan) was used for monitoring the bonding integrity. All recorded data were obtained immediately after bonding of 3D printed channel to the PMMA slab.

6.2.4 Surface characterization

For the purpose of double adhesive tape surface characterization, a 3D laser microscopy (Olympus LEXT OLS5000) and an LMPLFLN 20x LEXT objective lens (Olympus) was used. Arithmetic mean deviation (R_a) and arithmetical mean height (S_a), the arithmetic mean of absolute ordinate $Z(x, y)$ documented across a line and region respectively, were chosen to assess the surface quality of the tape.

6.2.5 Cell culture conditions

DU145 cells (human prostate cancer cell line) were cultured and expanded under normal culture condition (37° C and 5% CO₂) using Roswell Park Memorial Institute medium (RPMI, Thermofisher) supplemented with 10% fetal bovine serum (FBS, Gibco), and 1% Penicillin Streptomycin (Pen/Strp, Gibco). To reach to a homogeneous suspension of single cells, semi-confluent cultures were incubated with the sufficient amounts of TrypLE (Gibco) for 5 min. Following centrifugation, cells were counted and resuspended in phosphate buffer saline (PBS) at the almost concentration of 10⁶ cells/ ml. DU145 cells were then passed through the both PDMS-based and 3D printed microchannel. For all further experiments, results are compared to untreated cells as the control group.

6.2.6 Morphological analysis and cell viability assay

In order to evaluate the immediate effect of passing the channel on the cell viability, Live-dead assay was carried out using Live and Dead Cell Assay kit (Abcam) directly following the test. Collected single cell suspension was incubated at the concentration of 5×10⁵ cell/ ml in the staining solution, regarding the kit manufacturer's instruction. For this purpose, cells were incubated for 10 min at room temperature and analyzed by flowcytometry (Olympus CKX53) equipped with the CytExpert software. Live and dead cells were detected by green (λ excite/emit =488/515 nm) and red (λ excite/emit =488/617 nm), respectively. For further study of the short-term impact of the channels, the viability of passed DU145 cells was assessed after 24 hours culturing under growing condition. Fluorescent microscopic imaging was performed for adhered cells to distinguish live cells (with green cytoplasm) from dead ones (with red nucleus). The morphology of the attached cells was monitored under an inverted microscope (Olympus DP80) for up to five days until they reach confluency. Furthermore, the morphological feature of both test and control cells was visualized by fluorescence staining of cytoskeleton after 3 days. The F-actin filaments were labeled by Phalloidin- FITC following

fixation and permeabilization by 4% paraformaldehyde (PFA) and 0.2% Triton X-100 (all from Sigma), respectively.

6.2.7 Real-time PCR analysis

The probable influence of shear stress on the expression of a set of genes related to proliferation and survival was measured using real-time PCR (BioRad CFX 96 thermocycler). Briefly, channel departed DU145 cells were moved to the culture dish and kept under normal culture condition for one day. Next, total RNA from three independent experiments were extracted by using PureLink™ RNA Mini Kit and cDNA were synthesis by applying Revert Aid First Strand cDNA Synthesis Kit. Real-time PCR was performed using specific TaqMan primer sets and TaqMan PCR Master Mix (all from Thermofisher) with following cyclic conditions: 95°C for 10 min, followed by 40 cycles of 95°C for 10 s, 60°C for 1 min and 72°C for 10 s temperature.

6.3 Results and discussion

6.3.1 fabrication and characterization of the 3D printed channels

For the last two decades, PDMS, as a silicon-based organic polymer, has been a boon for the microfluidic community, the fabrication of which is through softlithography. Sampling the literature for PDMS microchannels shows a myriad of new emerging applications in microfluidic fields, including micromixing, droplet generator, and single cell analysis microdevices. However, fabrication of PDMS microchannel requires cleanroom facilities, skillful users, and variety of equipment (i.e., spin coater, hot plate, etc.). More importantly, the gas permeability of this material can be pretty beneficial or undercut applications related to biological studies. Although theoretically straightforward, scaling up of PDMS channels for commercialization application in inertial flows is challenging since these devices are flexible and prone to rupture or collapse in high flow rates. In addition, inflammation and hysteresis feature of PDMS creates a big question mark regarding the exact focusing position of particles. This becomes more serious for numerical analyzers where the “wall boundary condition” is not

truly correct in inertial flows within PDMS channels. It is not surprising that the results of numerical simulations must be validated with hard chips rather than soft (PDMS-based) microchannels. Apart from all the issues mentioned, fabrication limitation of soft lithography hinders the discovery of new phenomena in various geometries or cross-section. For instance, inertial and Dean drag forces developed within a triangular curved microchannel has never been reported in the literature. As such, Parallel efforts and substantial strides are being made by microfluidic technologists toward fabrication of inertial microfluidic devices. As was mentioned in the introduction, different groups make attempts and deliver their proposal for new fabrication method of microfluidic devices, either of which requires dexterous users, advanced facilities, and still not optimize for all geometries. Nevertheless, there is still no consensus about the optimum protocol for the fabrication of unconventional inertial microfluidic devices.

In this study, we have proposed a novel approach for fabrication of microfluidic devices based on 3D printing method, as shown in Figure 6-1. Gaining the efficiency of a high-resolution 3D printer, the desired geometry is printed while its face is outer and the base is attached to the build plate. This method is particularly significant since various cross-section in inertial microfluidics is of interest. However, printing parameters and options need to be optimized for fabrication of a channel with proper dimension. The slice thickness in Z direction, curing time of each layer, and the total thickness of the part are the most critical issue to have a channel with the highest degree of quality. Various cross-sections, ranges from right hand or isosceles triangular to hexagonal were fabricated and the best optimized parameters were identified. Then, the channel needs to be bonded permanently to another substrate to create a close network of microchannels. For this aim, various scenarios were examined. Bonding the part to another glass slide, PDMS slab, or PMMA sheet via oxygen plasma device, coat a layer of resin on surface of a glass slide and then UV curing, use mixture of PDMS, curing agent, and liquid resin (with various aspect ratios) to develop a new resin-based PDMS layer are among the trials.

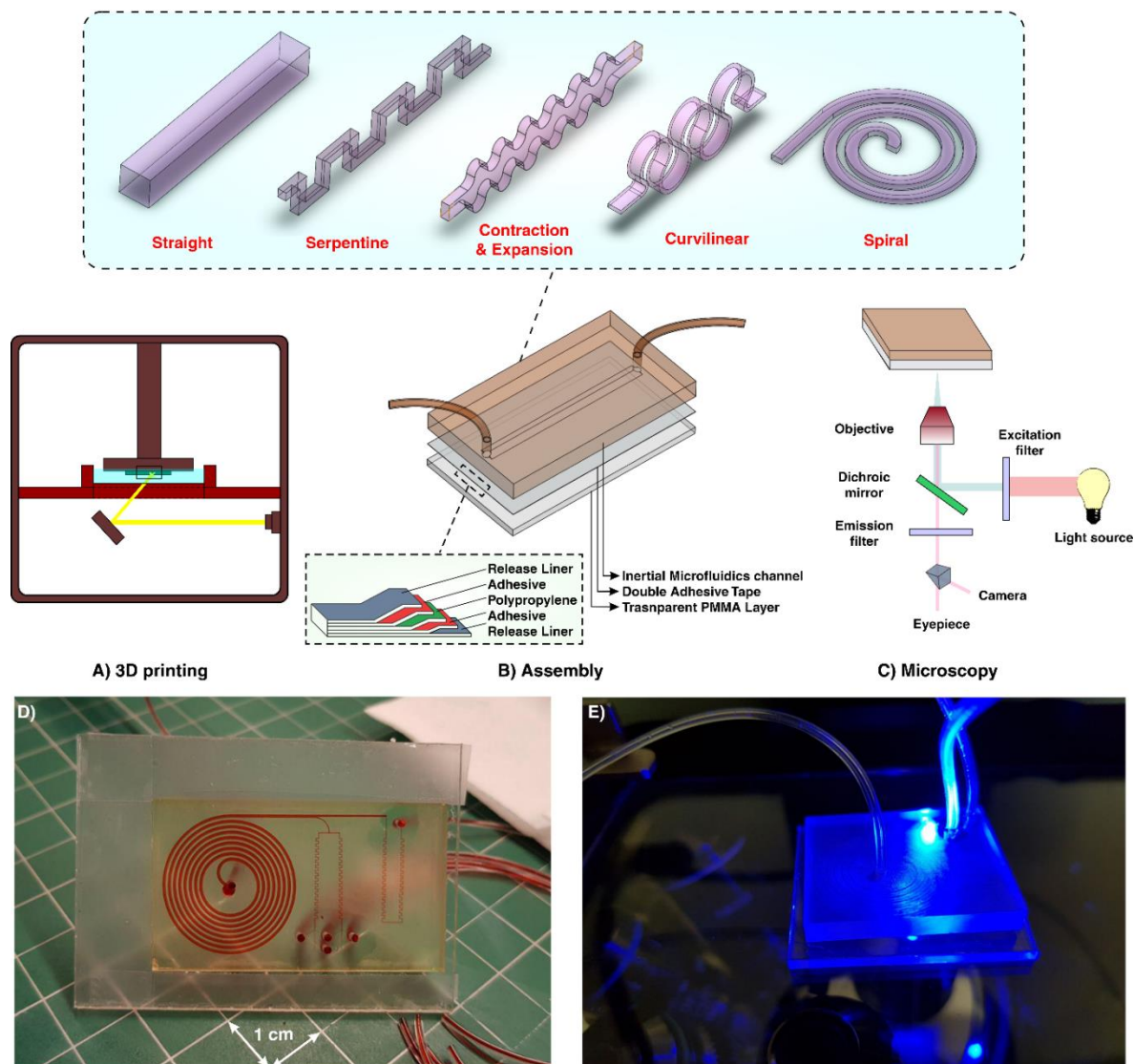


Figure 6-1: Schematic illustration of the proposed workflow for fabrication of inertial microfluidic devices. A) the desired channel geometry was printed by a high-resolution SLA/DLP 3D printer B) after cleaning the part by IPA, it was bonded to a PMMA sheet by means of a high-pressure double adhesive tape. C) benefitting from the transparency of the PMMA slab, high-speed, fluorescent, bright field, or phase contrast microscopy can be performed from the bottom side of the channel D) an actual complicated inertial microfluidic device containing a spiral and serpentine microchannel. E) fluorescent microscopy from the bottom side of the channel.

After careful evaluation, permanent bonding of 3D-printed part to a PMMA sheet or glass slide via a double adhesive tape is selected from a pool of try and errors. A transparent double-coated pressure-sensitive adhesive tape (ARcare®, Adhesive Research) having 25.4 μm clear polyester film coated with AS-110 acrylic medical grade adhesive was cut with a similar size of 3D printed inertial part, manually placed over the design, and pressed with a simple tweezers or fingers until no bubble was elucidated at the interface of the part and PMMA sheet.

Gaining the efficiency of PMMA transparency, these devices are amenable to the bright field, phase contrast, fluorescent, or high-speed microscopy. Figure 6-1 provides an overview of fabrication process. What stands out in Figure 6-1 is that the whole process, from CAD designing to imaging, only takes less than 3 hours, portraying the versatility of the method for inertia microfluidic fabrication. Perhaps the most significant feature of these devices is that they are immune to the inflammation, whereas PDMS as a soft material has a nonlinear inflammation behavior toward the flow rates which makes the interpreting the results, quite challenging. This provides further support for the hypothesis that numerical simulations results must be validated by hard chips rather than soft ones. The step by step fabrication process is depicted in Figure 6-1.

In order to investigate the bonding quality, a simple 3D-printed straight channel having 50 μm height, 200 μm width, and 4 mm length was bonded to a transparent PMMA layer. To this end, the device was monitored and two criteria were considered. First, the time point in which Saffman-Taylor fingers appear, and second, when the device obtains its stability (i.e., no inflammations appears after 5 min) (Figure 6-2 A). As a given 3D-direct printed part has a finite holding force capacity, it is of significant importance to establish rubrics to guide the setup of an operable 3D printed inertial microfluidic device. Hence, the results are mapped in a 2D diagram for users to identify the behavior of channel at the presence of pressure inside the channel, as shown in Figure 6-2 B. The results illustrate that the holding strength of double-adhesive tapes was able to achieve a leak-proof interface between the 3D-printed part and PMMA sheet, not only at typical operating pressure reported in literature [229], but also more than the capability of PDMS in withstanding high-flow rates conditions. Looking at Figure 6-2 B reveals that the area highlighted with light green is the safe zone area of the experiment where no Saffman-Taylor fingers appear during the stability of the channel interface. In the pressure more than 82.6 psi, Saffman-Taylor fingers began to appear, however, shortly after their

appearance, the system became stable and no leakage or bonding collapse was identified during the experiment.

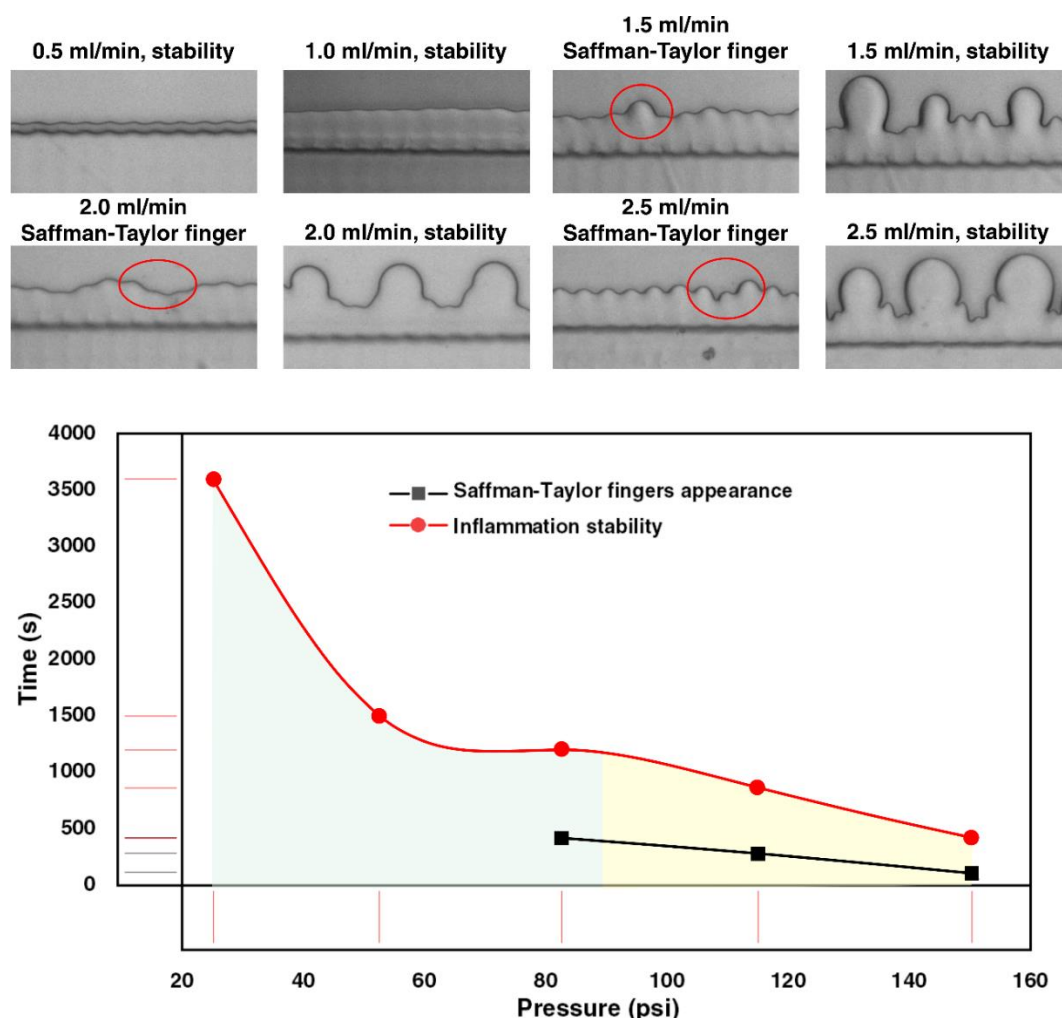


Figure 6-2: Analyzing the Saffman-Taylor finger criteria for the bonding test in a microchannel versus the applied pressure. The results show that there is not any evidence of channel burst and the more the flow rate, the faster the creation of Saffman-Taylor fingers.

Also, the results show that there is not any evidence of delamination, inflammation, deformation, or channel burst, all of which are common in PDMS-based inertial microfluidic devices. Thus, the bond strength is more than enough for inertial microfluidic applications. The surface characteristics of the double adhesive tape were also investigated via a profilometer. Prior to commencing the evaluation, the double adhesive tape was bonded from one side to a PMMA slab and was characterized from the other side (after the release liner was gently removed from its top surface). As Figure 6-3 illustrates, the roughness of the tape is homogenous, in the submicron range. The roughness across two different crossing lines was

about 250 nm and across an area was around 240 nm. This nanometric rugosity indicates that the roughness of the tape does not impose any challenging issue to inertial microfluidic applications.

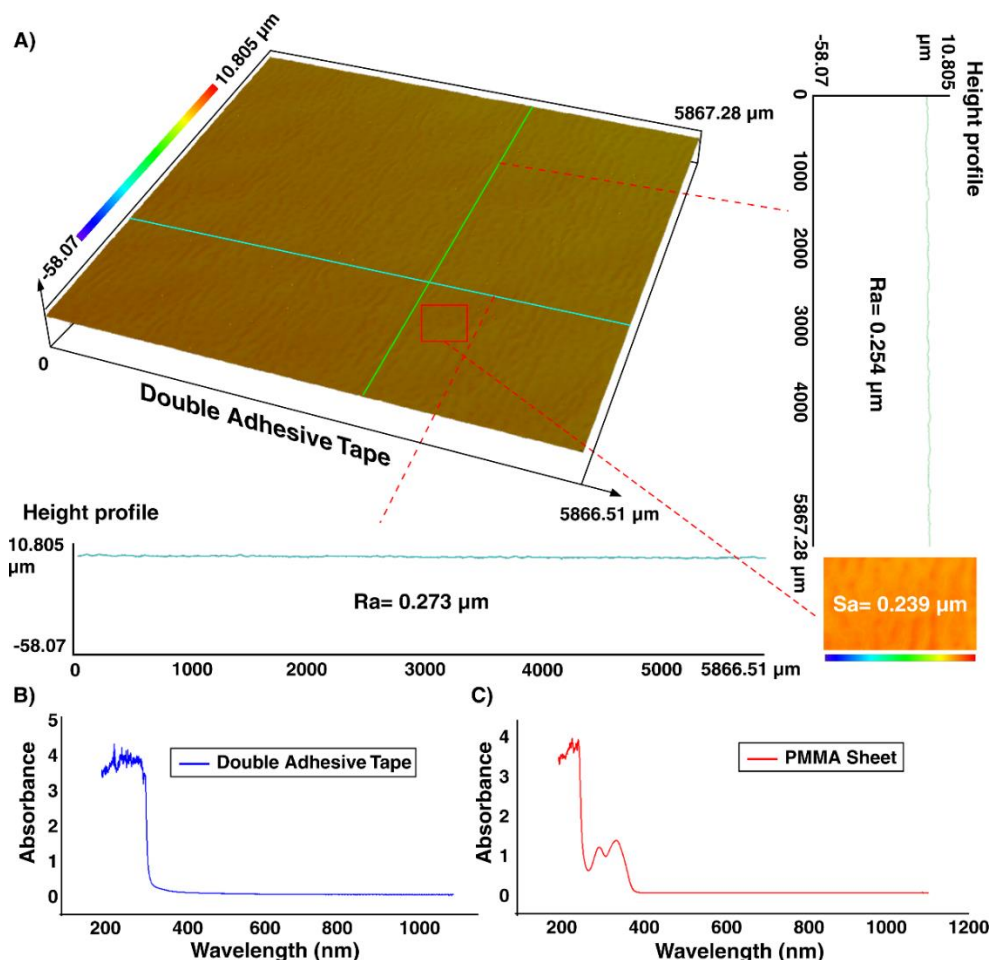


Figure 6-3: A) Surface topography of the double adhesive tape. Results show that the tape has homogenous roughness which does not impose any interference on the channel performance. The amount of absorbance of B) double adhesive tape and C) PMMA sheet. Results show that these two materials are transparent for visible spectra range.

Although optically transparent, the optical characteristics of the PMMA slab and double adhesive tape were evaluated to identify the possibility of fluorescence imaging. Hence, the UV-visible absorbance spectra for a wide range of wavelengths from 200 to 1100 nm were recorded via a spectrophotometer (Cary 60 VU-Vis spectrophotometer, Agilent Technologies). Looking at Figure 6-3 B and C reveals that the light loss is negligible for both PMMA and double adhesive tape within the visible spectrum, resulting in no trace of autofluorescence residual.

6.3.2 Straight microchannel

Although the first evidence of particle migration was illustrated in channels with circular cross-sections, limitations in microfabrication have forced investigators to converge on the focusing of particles in straight channels with rectangular cross-sections. These straight structures entail the unique feature of massive parallelization and are the simplest design among others. The required channel length for inertial particle migration to the equilibrium positions is $L_f = \pi\mu H^2 / \rho U_m \alpha^2 f_L$ where f_L is estimated in the range of 0.02 to 0.05 for (H/W) from 2 to 0.5, and the corresponding flow rate for inertial migration is calculated as $Q \approx 2\pi\mu W H^3 / 3\rho L \alpha^2 f_L$ [17]. Channel Reynolds number ($Re = \rho U D / \mu$) and particle Reynolds number ($Re_p = Re \frac{\alpha^2}{H^2}$) are two dimensionless number for characterization of particle migration in a straight microchannel. When particle Re is much smaller than 1, viscous drag becomes dominant and particles follow the streamline. Increasing the particle Re makes inertial forces to be dominant and inertial particle migration becomes obvious in the microchannel [11].

Particle migration within a straight channel strictly dependent on its cross-section. In square straight microchannels (with aspect ratio AR (width/height) of 1), particles migrate to four equilibrium positions located at the center of each wall. Changing the cross-section to rectangular disturbs this focusing pattern where in a rectangular straight microchannel with aspect ratio 0.5, focusing positions reduce to two at the center of each wall [11]. This migration behavior was explained by Zhou and Papautsky where they illustrated two-stage particle migration phenomenon [217]. Further increase in the aspect ratio results in the more unpredicted focusing behavior of particles. Generally, channels with high aspect ratio result in a reduction of stable focusing positions. However, exceeding from a critical Re value leads to an increase in the number of stable equilibrium positions which is a function of particle size, channel dimensions, and Re . based on reported experimental results, $Re_c = 697(AR/\kappa)^{-0.79}$ ($4.5 \leq AR/\kappa \leq 60, 5 \leq Re \leq 660$) was identified [230]. The abovementioned results elucidate that particle focusing strongly affects by channel cross-section. However, due to the

fabrication limitations, correlation of focusing behavior to the cross-sectional geometry was not systematically investigated. Recently, triangular and semi-circular cross-sections were fabricated using Si anisotropic etch with potassium hydroxide [123], a brass for mold fabrication [125], FDM for creation of sacrificial mold [84], and unconventional micromilling [121].

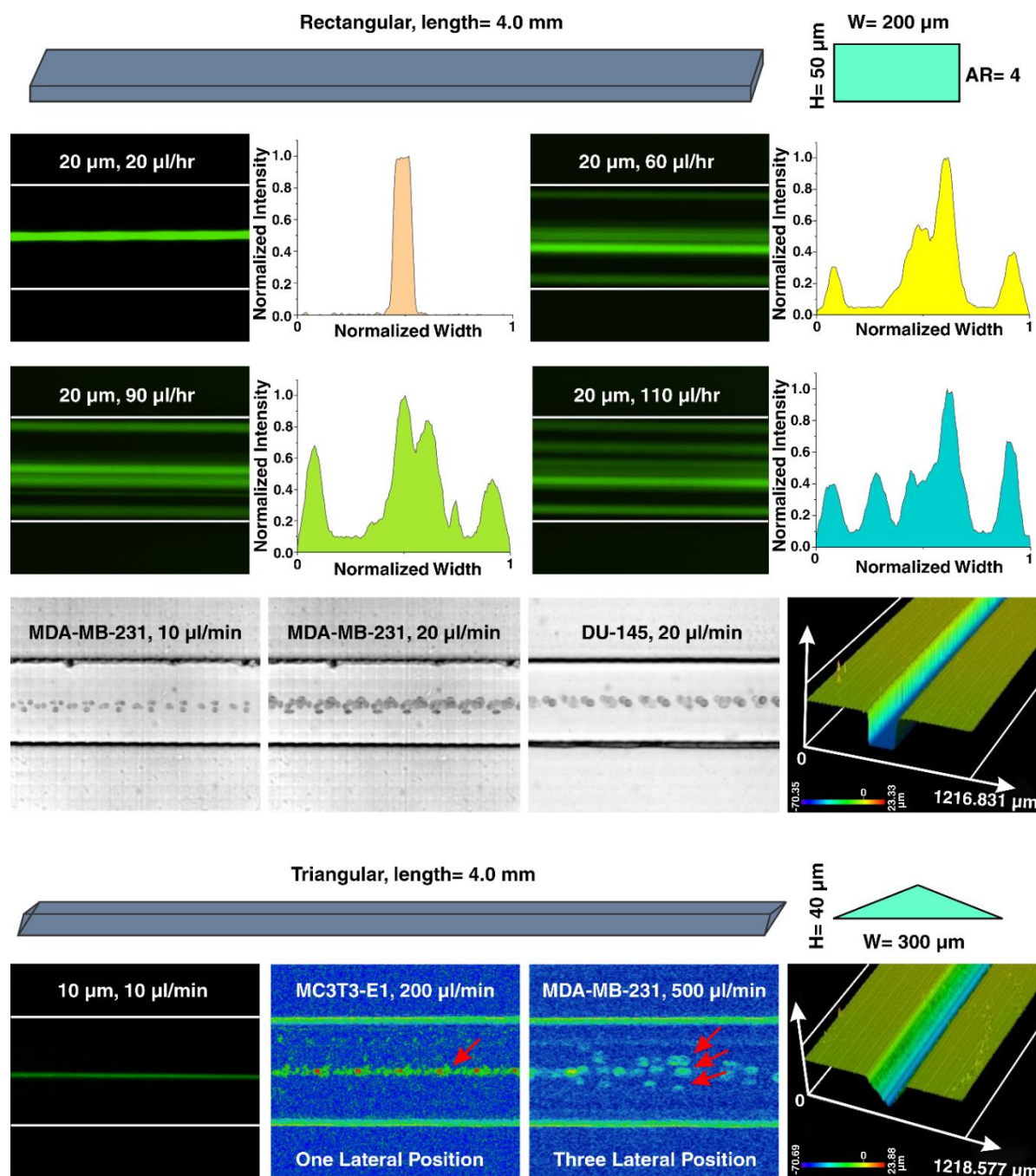


Figure 6-4: inertial focusing in a rectangular and triangular straight microchannel. From the top view, in the rectangular microchannel, particles occupy the center of the channel as their focusing position in moderate flow rates. In triangular microchannel also, particles first migrate to one focusing position and then this increases to three separate points.

However, critical fabrication limitations restrict further investigation on the dependency of triangular angle or right-hand triangular on focusing pattern of the particles. Here, as a showcase, a straight microchannel with rectangular cross-section and aspect ratio of 4 was fabricated and the results are illustrated in Figure 6-4. As the results indicate, for low Re, 20 μm particles focus at the center of the long wall of the cross-sections. Nonetheless, the focusing pattern for particles at higher Re does not obey a specific role. As the results are clear, increasing the flow rates leads to generation of additional focusing position within the microchannels where side walls are also added to the equilibrium positions of particles. Furthermore, to showcase the versatility of the proposed method, a triangular straight microchannel was fabricated and the results are shown in Figure 6-4. The results are completely in line with those reported in the literature where 10 μm particles occupy one lateral position in the channel for low flow rates. For high flow rates, this equilibrium position increases to three points which are highlighted by MDA-MB-231 inside the channel.

6.3.3 Spiral Microchannel

Spiral defines as a curve winding around a center point with continues decreasing or increasing manner. When flow passes the curvature, velocity mismatch occurs in the curve section of the channel, which results in the generation of secondary flows. In inertial microfluidics, spiral microchannel has progressed significantly, and nowadays most of the particle/cell separations are applied using these microchannels [231]. De is used for the characterization of secondary flows within the channel. Intuitively, smaller channel curvature or larger channel size or Re leads to higher Dean number, thereby imposing stronger secondary flows within the channel. For a given De, average transverse Dean velocity ($U_{De} = 1.84 \times 10^{-4} De^{1.63}$) and Dean drag force ($F_D = 3\pi\mu U_{De}\alpha = 5.4 \times 10^{-4}\pi\mu De^{1.63}\alpha$) can be identified. However, the exact behavior of particle migration at the downstream of the fluid was not thoroughly investigated, and all results are based on experimental data. The most appealing feature of spiral inertial microfluidics is its high-throughput where 2100 particles per second can be processed [180].

Particle sorting is one the most significant applications of the spiral microchannels. Previously, the potential of a rectangular spiral microchannel for continues and simultaneous isolation of 10, 15, and 20 μm based on softlithography has been investigated (Figure 6-5 AI) [232]. Dean flow dynamics for a low-aspect ratio rectangular spiral microchannel was also thoroughly explored [233]. Beyond simple rectangular spiral microchannel, various geometry modifications for regulation of Dean forces and performance enhancement have been proposed. Benefitting from micromilling (Figure 6-5 AII), redistribution of lateral focusing positions in trapezoidal spiral microchannels has been used for separation of particles with different sizes where smaller particles focused along the outer wall, whereas larger ones migrate toward the inner wall [234]. This superior advantage has been widely investigated by our group, among other groups, for CTC isolation [235], circulating fetal trophoblasts separation [236], blood plasma separation [237], zonal chondrocyte separation [238], isolation of microcarriers from mesenchymal stem cells [206, 239], microalgae cell separation [156], and mixed age eggs separation [240]. Also, multiplexing using stack of attached PDMS layers to boost the throughput of these systems was illustrated previously [122, 237]. However, most of the aforementioned applications are just doable by utilizing cleanroom facilities or employing conventional micromachining (e.g., metal machining or laser cutting) for fabrication of the microchannel. Besides, micromachining has its own limitations such as inability to make sharp corners or difficulty in making spiral loops close to each other. These challenges highlight an unmet need for fabrication of spiral microchannels using a versatile method which is robust and can surmount aforementioned issues.

Despite all progress in spiral inertial microfluidics, there is not any report of a spiral with cross-sections rather than rectangular or trapezoidal shape. In other words, a huge amount of potential remains intact on study of spiral microchannels with different cross-sections (Figure 6-5 AIII). For this aim, for the first time, we have fabricated a spiral microchannel with right-hand triangular cross-section (Figure 6-5 B) where the width and height are 600 and 210 μm ,

respectively. As the results illustrate in Figure 6-5 C, there is a tight band focusing of particles with diameter more than $9.7\ \mu\text{m}$. Also, the focusing band becomes double for $20\ \mu\text{m}$ particles and flow rate of $4\ \text{ml/min}$. The dimensions (Figure 6-5 D) and surface profilometry (Figure 6-5 E) of the cross-section shows the accuracy of the proposed method for fabrication of right-hand triangular spiral microchannel.

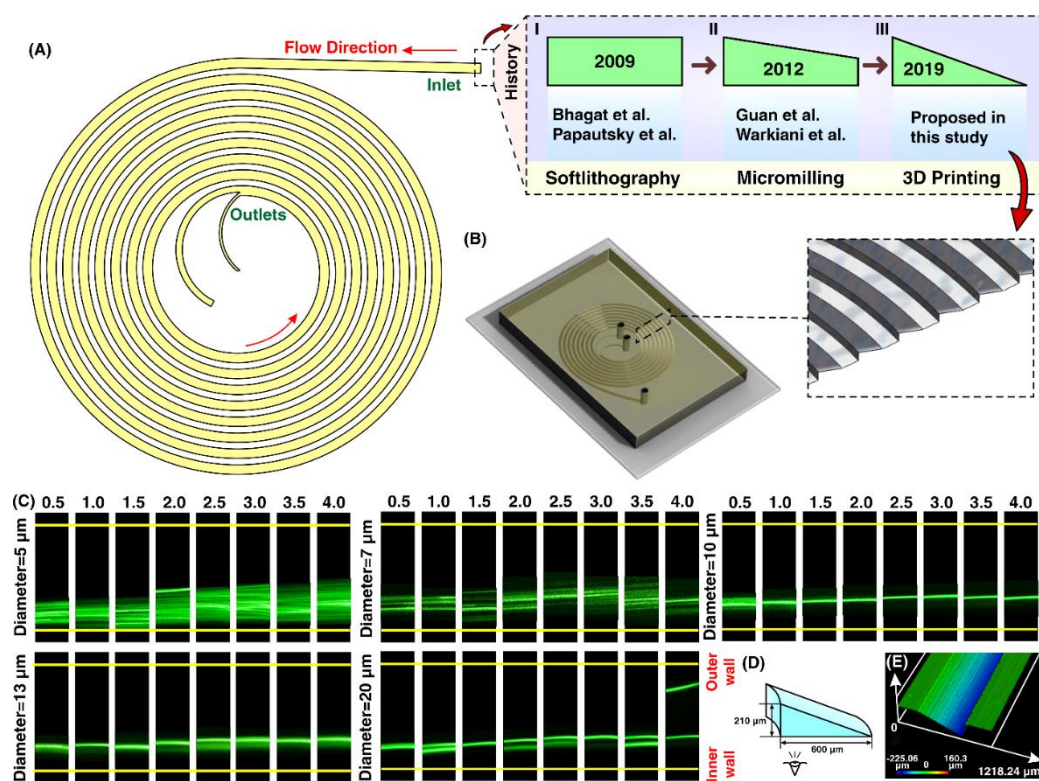


Figure 6-5: A) Illustration of a spiral microchannel with triangular cross-section where the fluid direction is from outside to inside. I) Firstly, several groups (e.g., Bhagat et al. [180], Papautsky et al. [195, 233], etc.) have shown the capability of rectangular spiral microfluidics for such applications as flow cytometry for microparticle/cell separation. The fabrication method was based on softlithography. II) gaining the efficiency of micromilling, many groups (e.g., Guan et al. [234], Warkiani et al. [172], etc.) made an attempt to get advantage of trapezoidal spiral microchannel for particle/cell filtration and fractionation. III) In this study, for the first time, we have shown the fabrication of a right-hand triangular spiral microchannel with the aid of additive manufacturing. B) Schematic illustration of the microchannel where the inset shows the cross-section of the microchannel. C) Focusing positions of particles with sizes ranging from 5 to $20\ \mu\text{m}$. D) dimensions of the right hand triangular spiral microchannel where the inner wall is $210\ \mu\text{m}$ and the width is $600\ \mu\text{m}$. The hydraulic diameter of this channel is similar to a spiral with trapezoidal cross section and dimension of $80\times 130\times 600\ \mu\text{m}$. E) Surface profilometer of a right hand triangular cross section, which shows the accuracy of the fabrication process.

Sheath flow systems function by introducing two or more flows at the channel inlets and have shown a great promise for particle separating, squeezing, and washing. Despite the high capability of these systems for particle sorting, the difficulty of controlling the effective parameters and complexity of an accurate design make them less user-friendly. Here, a sheath

flow spiral channel (Figure 6-6) was readily fabricated and tested for particle separation at various sample-to-sheath flow rate ratios. Results demonstrated that previously pinched particles in the sample flow can focus distinctly at different positions, making this device a suitable candidate for PBMC separation applications. This phenomenon strongly depends on the particles' diameter and the ratio of sample-to-sheath flow rates.

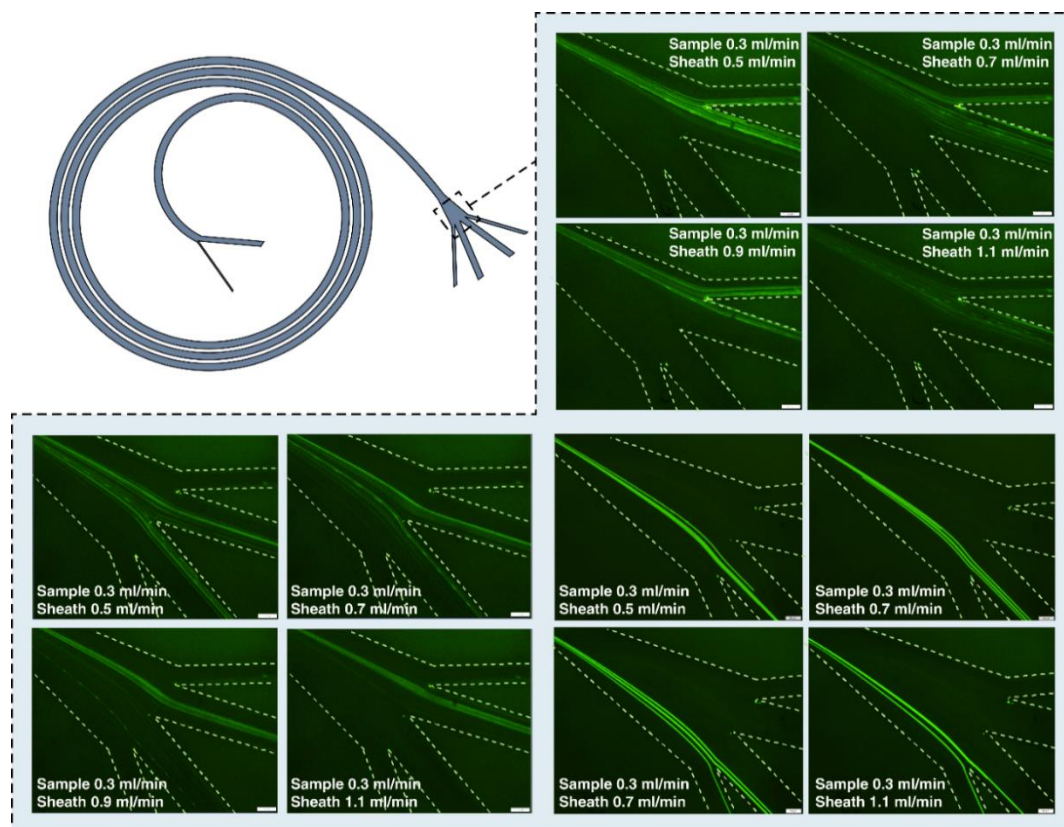


Figure 6-6: Focusing of the 7, 15 and 20 μm particles within a sheath flow trapezoidal spiral channel for PBMC separation.

These results illustrate the versatility of this method where various cross-sections can easily be fabricated in less than two hours with high robustness and stability. As results are clear, the device is capable of working in high flow rate with the presence just sample flow or sample flow and sheath flow while the hardness of the chip adds extra solidity to the device.

6.3.4 Sinusoidal Microchannel

Similar to the spiral microchannels, particles undergo the dean drag forces throughout the serpentine channel due to the non-linearity of its structure. However, in the sinusoidal microchannel, the curvature direction changes in each loop, resulting in variable secondary

flows that change the focusing behaviors significantly (Figure 6-7). This design was firstly developed by Di Carlo in 2007 and its capabilities for particle sorting was evaluated over a wide range of Dean numbers [67]. Application of this microchannel was even expanded where it was used for high-throughput separation of micron and sub-micron bioparticles (cyanobacteria) [241] and also was used for fabrication of a microfluidic concentrator for harvesting of cyanobacteria [242]. In addition, in a comprehensive study, design principles of curvilinear microchannels were investigated and a map for various focusing phenomenon was provided [243]. The dependency of curvature angle on lateral migration of particles was also evaluated [244] and various cell lines with their possible focusing efficiency were investigated [245].

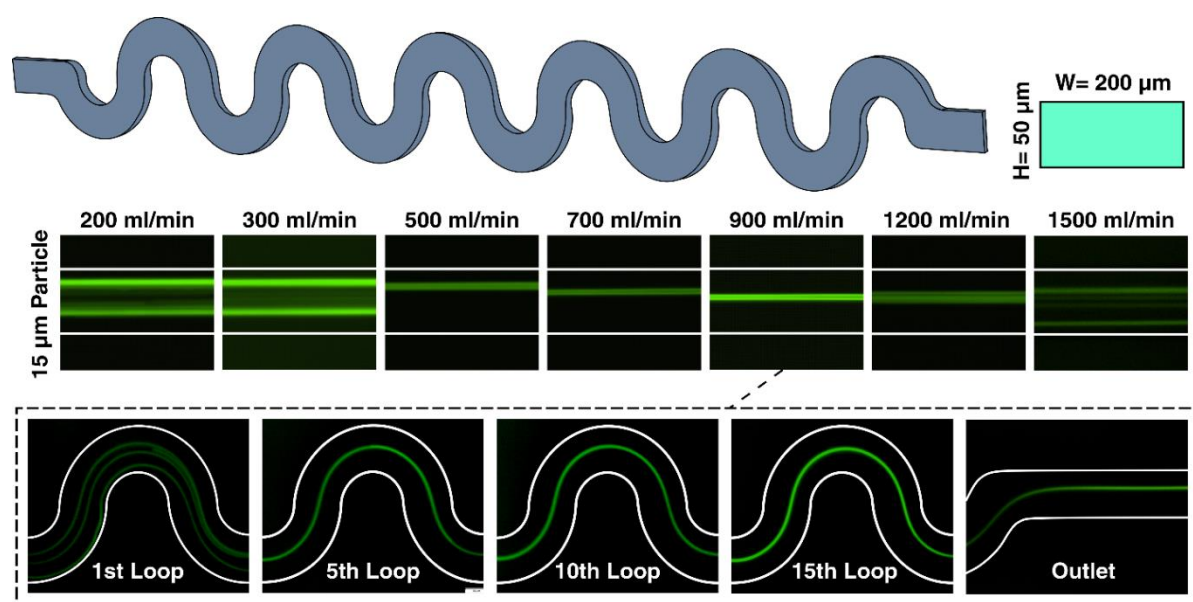


Figure 6-7: inertial microfluidics in a curvilinear microchannel. The results show that the equilibrium position of the particle depends on the flow rate and it can change from one to multi-focusing positions.

In order to showcase the feasibility of our model, a curvilinear microchannel with rectangular cross-section was designed, fabricated, and evaluated. Looking at Figure 6-7 reveals that 15 μm particles first occupy two focusing positions, while by increasing the flow rate the focusing band reduces to a single line close to the channel center which is consistent to the results previously reported [243].

6.3.5 Serpentine

The serpentine channel proves to have a unique feature for focusing of particles with different sizes. Generally, particle focusing achieved when $a/D_h > 0.07$ and $R_p \sim 1$. However, additional dean drag in serpentine microchannel leads to the focusing of particles with smaller diameter compared to mentioned criteria. These devices have the potential of parallelization along their vertical direction to amplify their throughput. This channel demonstrates three different focusing patterns by increasing the flow rate including two-sided focusing, transition focusing, and central single line focusing. If inertial effects dominate the secondary flows, particles occupy two lines near the walls. In contrast, the dominance of secondary flows results in a single-line focusing at the channel center. If these two effects have the same order, particles focus as a wide streak.

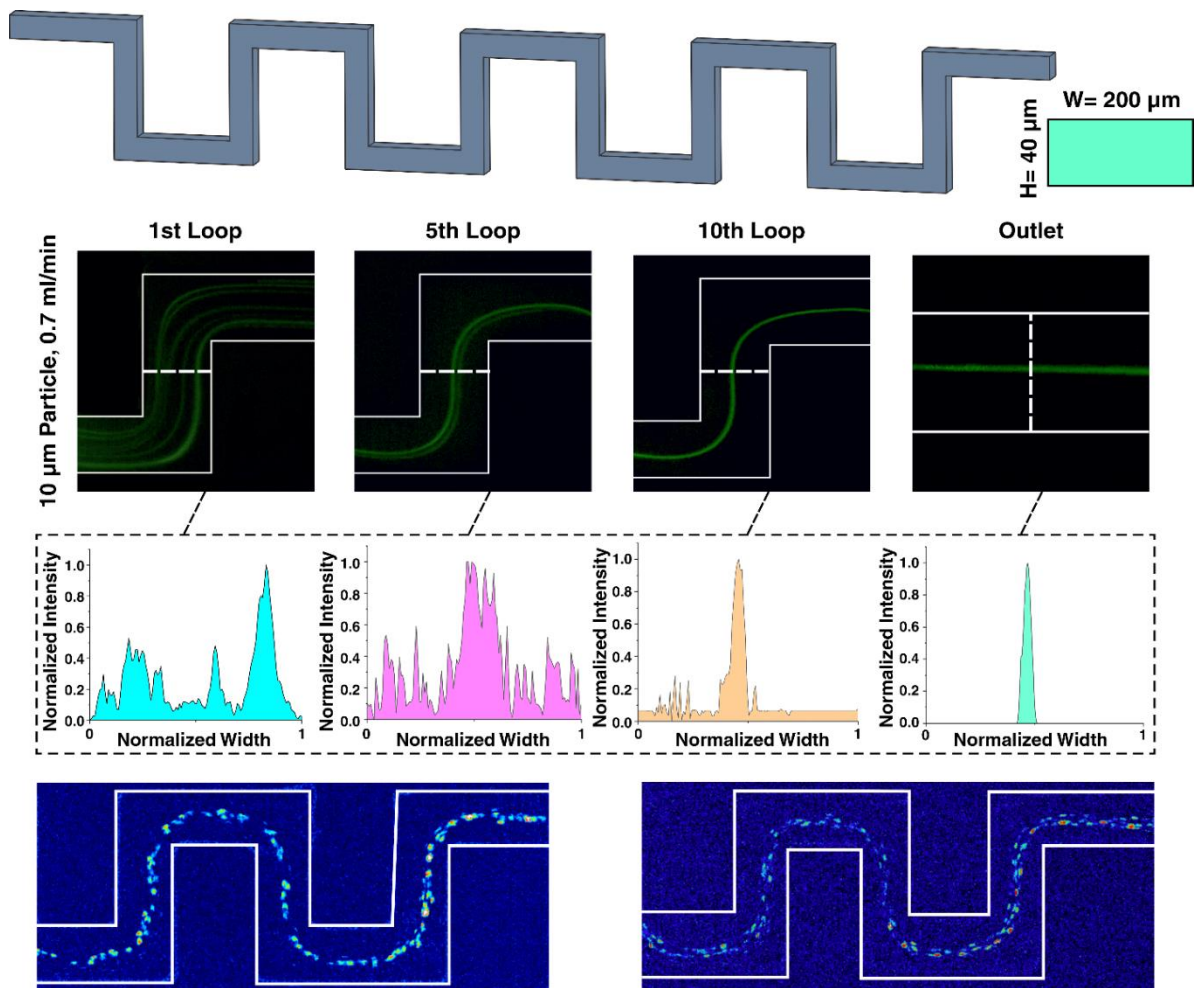


Figure 6-8: inertial microfluidics in a serpentine microchannel. The number of lateral positions depends on the flow rate apply at the entrance of the channel.

To compare the particle focusing behaviors within a 3D printed serpentine channel with PDMS-made one, we used a serpentine microchannel with cross-section of $200 \times 40 \mu\text{m}$ (H×W) and 15 loops, similar to the one employed by Zhang et al. [162]. Figure 6-8 elucidates that $10 \mu\text{m}$ particles can be focused at the center of channel in the 10th loop, and occupy central equilibrium position at the outlet of the channel, which is also demonstrated at the normalized intensity profiles. More importantly, the performance of the device was tested with two different cell lines (Hela cells and MC3T3-E1) and the results are consistent with those reported in the literature [162].

6.3.6 Contraction-expansion array

Deformation of a straight channel by adding and subtracting a specific design creates the so-called geometry of contraction-expansion (CE) arrays microchannels. In this channel, particles with small size migrate towards the wall while bigger particles focus at the center of the channel. In these array-based microchannels, pairs of helical vortices and secondary flows developed in the expansion section of the channel due to the abrupt change in cross-section alter the lateral migration of particles. For larger particles, inertial forces are dominant and particles are focused at the channel centerline. However, for smaller particles, secondary flows are dominant which create a new focusing zone near the side walls [246]. This mechanism was broadly used for separation of Malaria disease [15], plasma from whole blood [247], CTCs [248], and various particle sizes [246]. The geometry of contraction-expansion arrays used in this study is adopted from Jiang and co-workers [249]. The particle size of 7 and $15 \mu\text{m}$ are examined and the results are shown in Figure 6-9, and based on above-mentioned theories, smaller particles tend to occupy near the side walls while larger particles migrate to the center of the microchannel. Altogether, the proposed method facilitates the rapid fabrication of inertial microfluidic devices which are difficult or impossible to fabricate with conventional techniques. Since two of the most important applications of inertial microfluidic devices are

cell separation and cellular studies, how the cells will be affected by hard chips need to be evaluated.

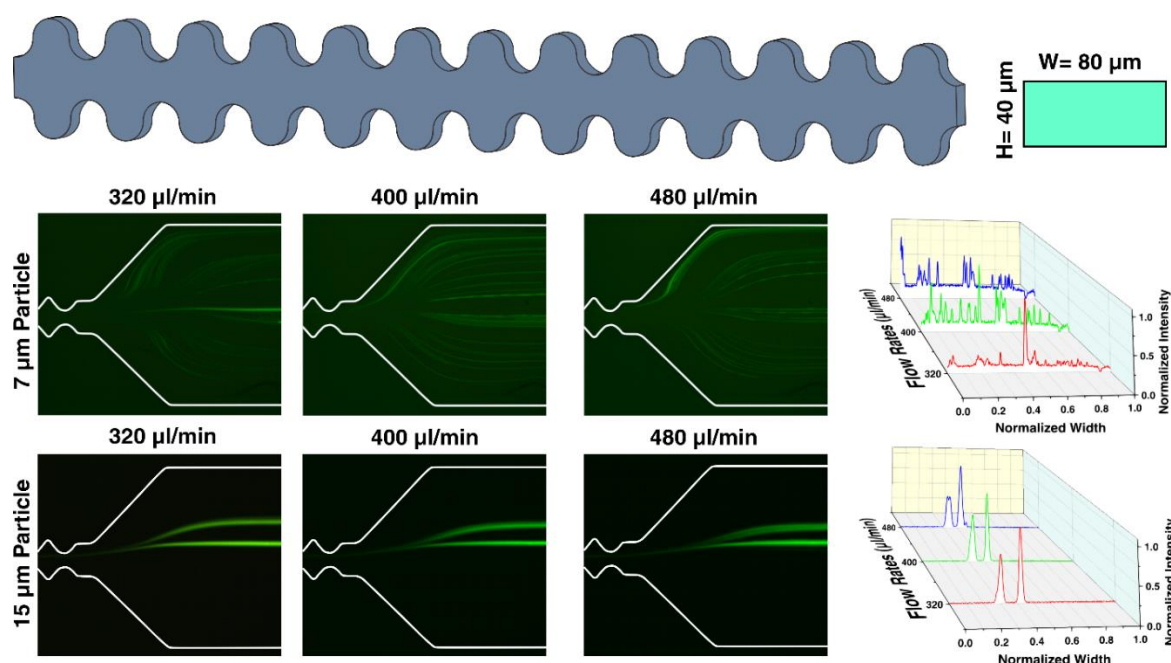


Figure 6-9: inertial microfluidics in a contraction-expansion arrays microchannel. Results show that particles with smaller diameter tend to focus on the side of the channel while larger particles usual occupy the center of the channel.

6.3.7 Cell activity assessment

Since most of the applications of the inertial microfluidics are related to biology and medicine, the viability and biocompatibility of the printed devices should be carefully evaluated. To this end, the DU145 cells collected from the channel outlet and a controlled sample were cultured under the same condition. According to Figure 6-10 A, both cells adhere to the culture plastic dish and resemble morphological features closely similar to each other. Indeed, the processed cells exhibited normal distribution of cytoskeletal F-actin subsequent to primary proper expansion during a usual period time (Figure 6-10 B). They presented suitable proliferation rate and reached the confluent state after five days, similar to the control cells. Real-time PCR analysis revealed the balanced expression of genes related to the general activities and stress response in the treated and untreated cells (Figure 6-10 C). In fact, the expression of *GAPDH* and *CDKN2A* confirmed that neither cellular metabolism nor cell cycle progression were

affected by traveling through the channel. We also did not find any significant changes in the expression of *TXNIP* and *MAPK14* as the two well-known regulators of cellular stress.

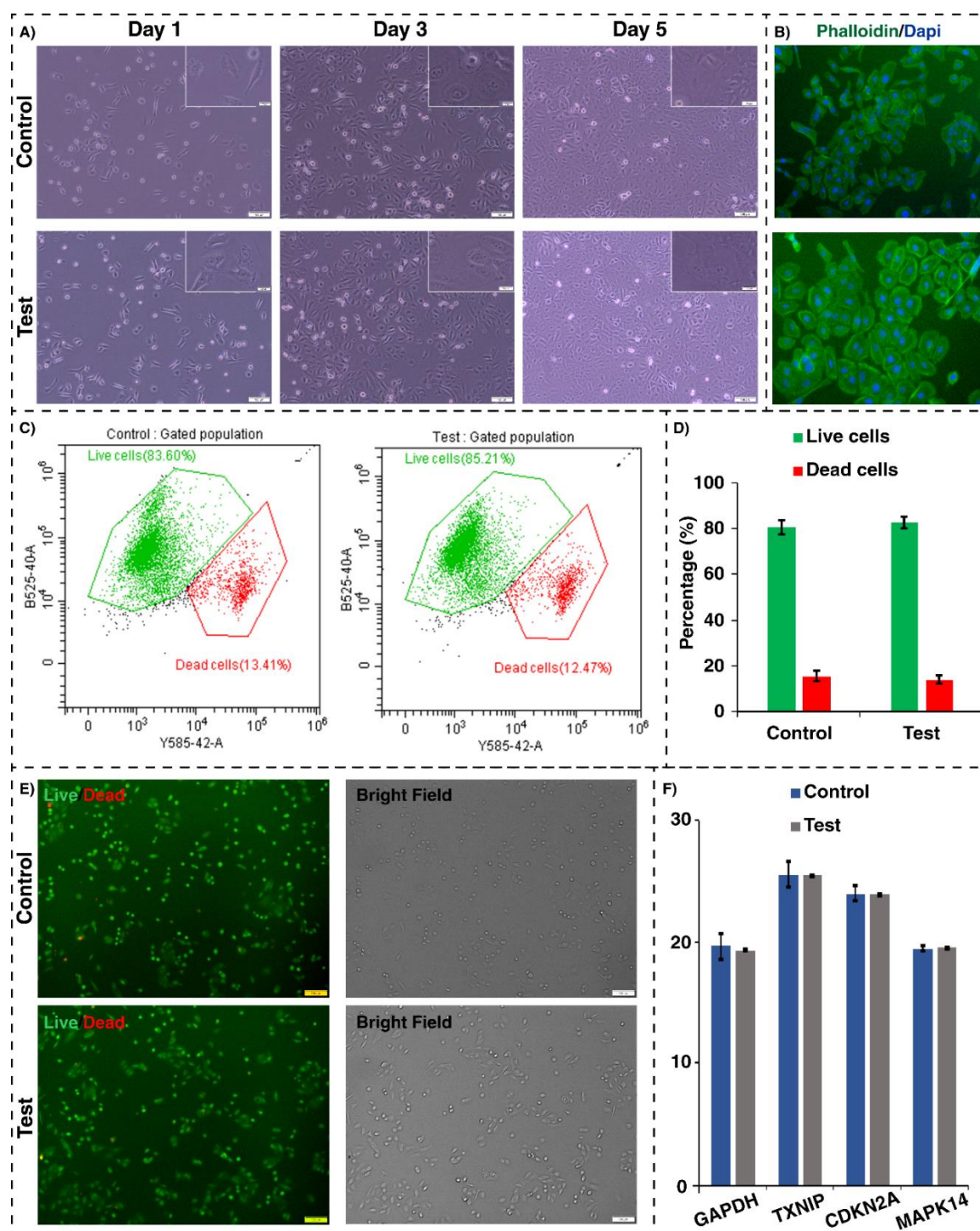


Figure 6-10: Characterization of DU145 cells after passing the channel. A) Monitoring the morphological feature of the cells during five days post-experiment, compared to the control group. B) Fluorescent staining of F-actin filaments in expanded cells on day 5 (green= phalloidin-FITC, blue= nucleus). Cycle of threshold (Ct) value (expression level) for GAPDH (cellular metabolism-related gene), CDKN2A (cell cycle regulatory gene), TXNIP and MAPK14 (genes involved in cellular stress response). Results are expressed as mean \pm SEM from three independent experiments. C) Representative plot and D) mean value \pm SEM of flowcytometric analysis of live/dead population for control and test group. E) Fluorescent imaging of live/dead dual stained cells after one day culture in normal condition. Scale bars are equal to 100 μ m in large images and 20 μ m in insets.

Furthermore, evaluation of cell viability immediately after passing the channel showed the appropriate percentage of live/dead cell population, compared to the control group. Figure 10E displays representative flowcytometric plots of dual stained cells and the mean value of each population resulted from the three independent experiments shown in Figure 6-10 D. Moreover, according to microscopic images shown in Figure 6-10 E, there is not any noticeable difference in live/ dead population of cells between test and control group after one day.

6.4 Conclusion

The main aim of this study is to propose a new fabrication method for inertial microfluidic devices. The proposed method involves 3D direct printing of a channel with desired channel type and geometry via a high-resolution SLA/DLP 3D printer (in this study, we use Miicraft). As the prevalent challenge of Resin microchannels is their bonding and assembly, we have proposed a novel bonding technique based on a double adhesive tape to a transparent PMMA slab. Since the utilized PMMA is transparent, these devices are capable of bright field, phase contrast, fluorescent, and high-speed microscopy. The bonding quality was evaluated by Saffman-Taylor finger criterion and the results showed that the device is capable of withstanding pressure as high as 150 psi (nearly triple of the value reported for PDMS). Using this strategy, we were not only able to retrofit a variety of previously inertial microfluidic devices into 3D-direct-printed microfluidic devices (e.g., straight with rectangular and triangular cross-section, spiral, curvilinear, serpentine, and contraction-expansion array), but also new channel designs and cross-sections, which are implausible to be fabricated conventionally, were designed, fabricated, and evaluated. To this end, for the first time, we have fabricated a right-hand triangular spiral microchannel and the results reveal promising focusing behavior within the channel. Uniquely, previously established inertial microfluidic devices as well as newly developed channels and cross-sections can easily be adapted into this 3D-direct-printing fabrication method with a time frame less than 2 hours. We are of the opinion

that the proposed fabrication method can benefit inertial microfluidic community to rapidly develop their desired microchannel and discover new physics and phenomena remained intact in this area.

6.5 Acknowledgment

M.E.W. would like to acknowledge the support of the Australian Research Council through Discovery Project Grants (DP170103704 and DP180103003) and the National Health and Medical Research Council through the Career Development Fellowship (APP1143377).

7

Chapter Seven: A novel microfluidic device for extraction of plasma by considering the non- Newtonian characteristics of human blood

Introduction

In this chapter, we demonstrate a new microfluidic design for blood plasma separation which employs three major principles, including the Zweifach-Fung effect, plasma skimming phenomenon, and acceleration-declaration effect. For this purpose, particle trajectories within several microchannels under different conditions were numerically modeled to find out the best configuration for high separation efficiency. The final design was then experimentally tested with 7 μm fluorescent particles to test the validity of the numerical results and showcase the efficiency of our device for blood plasma separation.

Authors' contributions:

1) Sajad Razavi Bazaz:

Designing the channels, performing numerical simulations, analyzing the results, Image processing.

2) Mohammad Amin Raoufi:

Device fabrication, Running the tests, writing some parts of the manuscript, helping in the numerical simulations, and revising the entire paper.

2) Alireza Zabihi Hesari:

Assisting in the numerical simulation part.

3) Steven Vasilescu, Mohsen Asadnia, Ali Abouei Mehrizi, and Majid Ebrahimi Warkiani
Reviewing the paper.

This chapter is prepared for submitting to Micromachines.

A novel microfluidic device for extraction of plasma by considering the non-Newtonian characteristics of human blood

Sajad Razavi Bazaz¹, Mohammad Amin Raoufi^{1,3}, Alireza Zabihi Hesari², Ali Abouei

Mehrizi^{2,*}, Steven Vasilescu¹, Mohsen Asadnia³, Majid Ebrahimi Warkiani^{1,4*}

¹*School of Biomedical Engineering, University of Technology Sydney, Sydney, New South Wales 2007, Australia*

²*Department of Life Sciences Engineering, Faculty of New Sciences and Technologies, University of Tehran, Tehran, Iran*

³*School of Engineering, Macquarie University, New South Wales 2109, Australia*

⁴*Institute of Molecular Medicine, Sechenov University, Moscow, 119991, Russia*

Corresponding Authors: Abouei@ut.ac.ir; M.warkiani@unsw.edu.au

Abstract

There is arguably no more important biofluid than blood when considering the often essential role it plays in diagnostics and therapeutic applications. The analysis of blood components enables healthcare practitioners to make informed decisions on patient care by providing information on organ function, mineral content and the presence of pathogens. In order to effectively analyze blood samples, there is a need to accurately fractionate the components of interest. Although such conventional methods as membrane filtration and centrifugation for blood processing have been effective in producing relatively pure fractions, they are labor-intensive, time-consuming, and more importantly are not ideal for processing low volume samples. Over the past decades, microfluidic-based approaches have garnered significant interest as an alternative for blood processing due to their accurate control over fluid behavior and the ability to downsize the required sample volume. These methods are typically aimed at increasing the separation efficiency and purity efficiency, as two of the most important parameters for evaluating the device effectiveness. However, these parameters are often inversely proportional, which makes finding an optimal design with desirable PE and SE noteworthy. To accomplish this, we demonstrate a new microfluidic design for plasma extraction which employs three major principles, including the Zweifach-Fung effect, plasma skimming phenomenon, and acceleration-deceleration effect. For this purpose, particle trajectories within several microchannels under different conditions were numerically modeled to find out the best configurations for high separation efficiency. After the investigation of PE for each daughter channel, a new design for the construction of the last bifurcation was proposed which culminated in a SE and PE of 86.18% and 94%, respectively. The final design was then experimentally tested with 7 μm fluorescent particles to test the validity of the numerical results and showcase the efficiency of our device for blood plasma separation. We believe that this device can be adopted easily in clinics for high-throughput blood sample processing.

Keywords: Blood plasma separation; Microfluidic device; Non-Newtonian model; Zweifach-Fung effect; Plasma skimming phenomenon

7.1 Introduction

Blood has several basic components, including plasma, red blood cells (RBCs), white blood cells (WBCs), and platelets and contains a wealth of pathophysiological information that can be extracted. In the interest of accessing this information, blood fractionation and blood plasma separation have become appealing areas of research that are based on separation of the blood into its basic components for diagnostic and therapeutic analysis. There are numerous applications in human health monitoring and disease detection that benefit from blood processing [250]. Plasma in particular, is widely used for the diagnosis and prognosis of several diseases such as cancer, malaria, and HIV. For many diseases such as leukemia and hyperviscosity, the exchange of blood plasma alone is used as a standard therapy [251]. It also plays a crucial role in analyzing electrolyte, glucose, lactate, and total cholesterol concentrations [252]. Furthermore, it can facilitate the process of polymerase chain reaction (PCR)—generating a myriad of copies of a particular DNA sequence [253].

Conventional methods of blood plasma separation can be categorized into centrifugation [254] and filtration techniques [255]. While these methods possess a high purification efficiency (PE) they are otherwise time-consuming, costly, and labor-intensive processes. Microfluidics is a current-state-of-the-art technology well-suited to developing blood processing alternatives. The advantages of microfluidic technology include portability, low volume consumption, precise fluid control, and rapid fluid processing, each of which are rewarding features, especially for POC diagnostics [256]. Microfluidic devices have made considerable contributions to biology, pharmacy, and biochemistry due to their ability to precisely control and manipulate fluids and particles. Among the numerous intriguing applications of microfluidics, fluid separation continues to play an important role and can be categorized into phase separation [257], particle/cell separation [258], droplet separation [259], and chromatography [260] techniques.

Generally, cell-plasma separation microfluidic devices can be grouped into the two main categories of active and passive. Active systems function with external forces such as magnetic [261], dielectrophoresis [262, 263], and acoustic [264, 265] to selectively guide targeted blood components. These systems depend on the integration of external devices and complicating setups which make them generally expensive. Despite their high PE, these methods have some by-products such as joule heating during electrophoresis [266] which limits their wider use for practical applications. On the other hand, passive methods, including hydrodynamic, crossflow, dead end filtration, centrifugation, sedimentation, inertial, and Zweifach-Fung separation techniques rely on hemodynamic forces, microchannel geometries, and biophysical effects [267].

Among common passive separation techniques, dead-end filtration methods usually suffer from filter clogging [268]. In order to prevent the fouling of elements, cross-flow filtration has been utilized [269]. This method has the potential to solve the problem of blocking; however, the separation efficiency (SE) falls outside an acceptable range. Periodic reverse flow could be utilized to reduce the fouling elements of the cross-flow membrane; however, this entails additional costs and energy, adding to the list of disadvantages for this approach [270, 271]. Another standard technique, centrifugation, has been found to provide the highest PE, but it suffers from certain critical issues such as cost, hemolysis, and difficulty of integrating into LOC systems which hinders its utility for POC applications [272-274]. Another method is the sedimentation approach which is based on the natural aggregation and sedimentation behavior of cells at low shear rates. However, its usability is limited by the time required for complete separation [275, 276]. Recently, inertial microfluidics has emerged as a powerful platform for biological applications and blood-plasma separation. However, inertial systems generally function at high flow rates, and strong shear stress may cause haemolysis *in vitro* and damage blood components, impacting diagnostic processes [277].

One of the best known microfluidic methods for blood plasma separation with high purity and separation efficiency at moderate flow rates is based on two principles including Zweifach-Fung [278] and plasma skimming phenomenon [279]. These principles have considerable influence on the PE and SE. A review of relevant literature shows that a microfluidic device based on the Zweifach-Fung effect was fabricated by Kersaudy-Kehoas *et al.* [280]. In their work, geometric design was based on one constriction in the form of a rectangular shape in the main channel; this aimed to create a shear stress zone to centrally localize cells and was supported by 20 bifurcation channels on each side of the main channel. The widths of the main channel and daughter channels were $100\ \mu\text{m}$ and $20\ \mu\text{m}$, respectively, and the constriction width and length were $25\ \mu\text{m}$ and $300\ \mu\text{m}$, respectively. Mussel and human blood were utilized as the input of the experiments and the PE were 96% and 60.8%, approximately; meanwhile, the SE was 40%. By improving the channel design, the same team [281] suggested a geometry consisting of four plasma channels running beside the main channel at a 45° angle with a constriction before each plasma channels. The width of the main channel was $100\ \mu\text{m}$ while the width of plasma channels used was either 10 or $20\ \mu\text{m}$. Ultimately, with this device, they reported 100% purification efficiency and only 30% SE (1.8% hematocrit) with the $20\ \mu\text{m}$ plasma channel and 5% SE (35% hematocrit) with the $10\ \mu\text{m}$ plasma channel. Although the PE was considerable, the SE was extremely low, and as a result, the amount of recovered plasma was not adequate for downstream assays. Fekete *et al.* [278] proposed an alternative geometry by modifying the effective parameters, including side channel width, main channel width, hydrodynamic resistance ratio, and bifurcation angle. Their results showed that by changing the hydrodynamic resistance ratio, the PE and SE would not exceed 80% and 25%, approximately. By refining the proposed geometry, Shamsi *et al.* [282] suggested a geometry with a new bifurcation type to reduce the hydrodynamic resistance of daughter channels seen in Fekete's design, resulting in PE and SE of 70.% and 66.8%, respectively. The accuracy of blood processing is extremely reliant on the PE and SE being as high as possible. Therefore,

improvements in microchannel design are essential for blood plasma separation with high PE and SE values.

The main aim of this study is to propose a new microfluidic device with enhanced capabilities for blood plasma separation based on the Zweifach-Fung effect and plasma skimming phenomenon. The device consists of a main straight channel, five daughter channels, and a curved outlet. To exploit the efficiency of acceleration-deceleration phenomenon, a constriction was planted before each daughter channel to increase the PE of the channel. Blood was modeled with a non-Newtonian power-law model—a comprehensive non-Newtonian model of blood—to consider non-Newtonian effects of blood and its components. By using the best arrangement of daughter channels, different values for PE and SE are investigated and reported. Also, the PE of each channel was evaluated and a new constriction for the last bifurcation was proposed. In the end, the proposed design was fabricated and tested via $7\ \mu\text{m}$ particles to evaluate the functionality of the devices.

7.2 Methodology for simulations and Experiments

7.2.1 Geometry design

Figure 7-1 demonstrated the geometrical parameters of the proposed plasma extraction device. In this figure, the width of main channel is constant at $40\ \mu\text{m}$, while the width of daughter channels increases gradually from $15\ \mu\text{m}$ at the inlet to $50\ \mu\text{m}$ at the outlet.

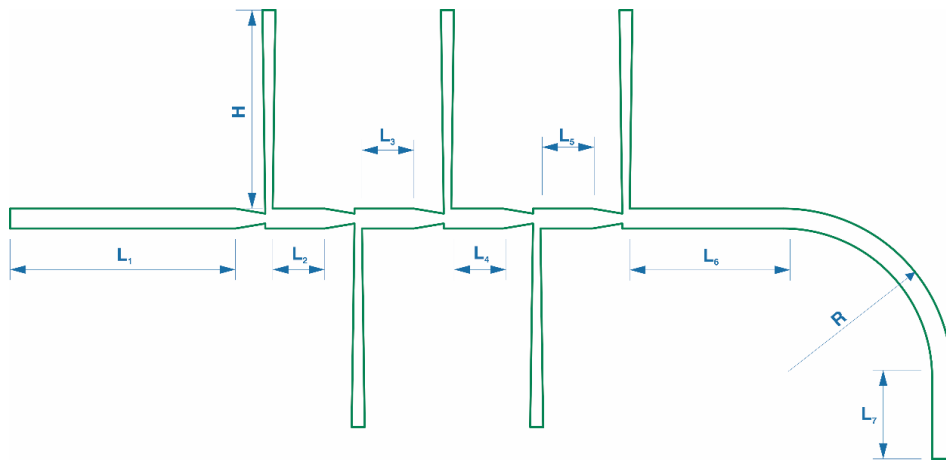


Figure 7-1: Geometrical parameters of the proposed plasma extraction device

In addition, L_1 is 2440 μm , L_2 , L_3 , L_4 , and L_5 are the same and 110 μm , L_6 is 900 μm , L_7 is 2000 μm , R is 500 μm , the small base of trapezoid and its altitude are 20 and 60 μm , respectively, the angle between the main and the centerline of daughter channels is 90 degrees, and H is 2700 μm . All sizes have been chosen based on the chip manufacturer specifications and based on existing literature [278]. The selected geometry is illustrated in the XY plane. For three-dimensional simulation and experimental works, the depth of the microchannel is taken as 10 μm in Z direction. The hydrodynamic resistance of a rectangular channel with the height of h and width of w can be calculated by Eq. (7-1) as shown below [283]:

$$R_h \approx \frac{12\mu L}{wh^3(1 - 0.630 h/w)} \quad (7-1)$$

with L and μ being the microchannel length and the viscosity of the liquid, respectively. Comparing the hydrodynamic resistance of the rectangular and diffuser shaped channels is beyond the scope of this research, but it has been proven that a diffuser shaped microchannel has less hydrodynamic resistance than a rectangular one [282]. It should be noted that Zweifach-Fung effect has some major limitations on the dimensions of the channel while the dimensions of the diffuser shaped microchannel must be adapted to suit the diameter of RBCs. Thus, the width of the entrance and outlet for each trapezoidal daughter microchannel is selected in a way to accommodate these conditions.

7.2.2 Numerical simulation

In order to find the flow field and particle trajectories in the proposed designs, Ansys fluent 19 software is used to carry out the simulations. To this end, first, continuity and momentum (Navier-Stokes) equations (Eqs. (7-2) and (7-3)) are solved to obtain the flow field in the entire domain.

$$\nabla \cdot \mathbf{V} = 0 \quad (7-2)$$

$$\rho \mathbf{V} \cdot \nabla \mathbf{V} = -\nabla P + \mu \nabla^2 \mathbf{V} \quad (7-3)$$

where V , ρ , P are the velocity vector, density, and pressure, respectively. To solve these equations, bloodstream is considered as a steady-state, laminar, and homogeneous flow. RBCs trajectories are modeled using a Lagrangian approach by injecting them into the mainstream with a relative velocity of zero and considering them as rigid spherical particles with a diameter of $7\ \mu\text{m}$ and density of $1125\ \text{kg/m}^3$. The convergence criterion for all parameters (continuity and velocity components) is set to be 10^{-8} . A uniform velocity of $2\ \text{m/s}$ is applied at the main inlet, while pressure outlet boundary condition is set at all the outlets. The Knudsen number is used to determine the slip boundary condition and is defined by equation (4) [147]:

$$\text{Kn} = \frac{\lambda}{L_s} \quad (7-4)$$

where λ is the mean free path of molecules and L_s is the characteristic channel dimension. No-slip boundary condition is satisfied when the Knudsen number is lower than 10^{-3} . When the Knudsen number increases, the continuum theory cannot be reasonably used. The molecular structure of gasses and liquids are dissimilar. It is easy to extract the mean free path from standard published tables for gasses. For liquids, however, it is quite different. Due to the density of the fluids, the space between molecules is less than in gasses. Lattice space δ could be used instead of λ for measurement, the formula of which is defined by Eq. (7-5) [284]:

$$\delta = \left(\frac{\bar{V}_1}{N_A} \right)^{\frac{1}{3}} \quad (7-5)$$

where \bar{V}_1 denotes the molar volume and N_A represents the Avogadro number. For the microchannel used in this study, with the width and depth of 40 and $10\ \mu\text{m}$, the Knudsen number is calculated to be 2×10^{-5} , approximately. Therefore, no-slip boundary condition and continuum theory are completely satisfactory.

By using Newton's second law, particle motion can be illustrated with Eq. (7-6) [285]:

$$\frac{d\vec{v}_p}{dt} = \vec{F}_{\text{drag}} + \vec{F}_{\text{pressure}} + \vec{F}_{\text{virtual mass}} + \vec{F}_{\text{other}} \quad (7-6)$$

where \vec{F}_{drag} is the drag force per unit particle mass that acts on each particle which is defined as Eq. (7-7) [286]:

$$\vec{F}_{drag} = \frac{18\mu}{\rho_p d_p^2} \frac{C_d Re_p}{24} (\vec{v} - \vec{v}_p) \quad (7-7)$$

here, μ is the molecular viscosity of the plasma, d_p , ρ_p , and \vec{v}_p are the RBCs' diameter, density, and velocity, \vec{v} is the velocity of plasma, and Re_p is the relative Reynolds number, which is calculated by Eq. (7-8) [287]:

$$Re_p = \frac{\rho d_p |\vec{v} - \vec{v}_p|}{\mu} \quad (7-8)$$

where ρ is the density of plasma. The drag coefficient, C_d , for RBCs can be measured by equation (7-9) as:

$$C_d = a_1 + \frac{a_2}{Re_p} + \frac{a_3}{Re_p^2} \quad (7-9)$$

where a_1 , a_2 , and a_3 are constants that are used over several ranges of Re_p [288]. Virtual mass force per unit particle mass with a virtual mass factor of 0.5 and pressure gradient force per unit particle mass are assumed in the Newtons' law which are shown by Eqs. (7-10) and (7-11), respectively [289].

$$\vec{F}_{virtual\ mass} = C_{vm} \frac{\rho}{\rho_p} (\vec{v}_p \nabla \vec{v} - \frac{d\vec{v}_p}{dt}) \quad (7-10)$$

$$\vec{F}_{pressure} = \frac{\rho}{\rho_p} \vec{v}_p \nabla \vec{v} \quad (7-11)$$

where C_{vm} is the virtual mass and equals to 0.5. \vec{F}_{other} in Eq. (7-6) refers to the forces from particle collisions which are based on the deformation of particles and are calculated according to the overlap between pairs of spheres [290]. Eq. (7-6) can be written in a Lagrangian reference frame as Eq. (7-12) [291]:

$$\frac{d\vec{v}_p}{dt} = \frac{\vec{v} - \vec{v}_p}{t_p} + \vec{F} \quad (7-12)$$

where \vec{F} is representative of additional force per unit particle mass including virtual mass force and pressure gradient force, the term $\frac{\vec{v}-\vec{v}_p}{t_p}$ refers to the drag force per unit particle mass and t_p is the relaxation time which can be written in the form of Eq. (7-13) [292]:

$$t_p = \frac{\rho_p d_p^2}{18\mu} \frac{24}{C_d Re_p} \quad (7-13)$$

Eq. (7-12) is coupled by Eq. (7-14) as a set of coupled ordinary differential equations.

$$\frac{dx}{dt} = v_p \quad (7-14)$$

Eqs. (7-12) and (7-14) can be solved for constant \vec{v} and t_p by analytical integration. The particle velocity at the new location can be calculated by Eq. (7-15):

$$v_p^{n+1} = v^n + e^{-\frac{\Delta t}{t_p}}(v_p^n - v^n) - at_p \left(e^{-\frac{\Delta t}{t_p}} - 1 \right) \quad (7-15)$$

and the new location can be evaluated by Eq. (7-16) as:

$$x_p^{n+1} = x^n + \Delta(v^n + at_p) + t_p \left(1 - e^{-\frac{\Delta t}{t_p}} \right) (v_p^n - v^n - at_p) \quad (7-16)$$

where v^n and v_p^n are the fluid velocity and particle velocity at the old location [293].

7.2.3 Non-Newtonian model

blood is mainly comprised of plasma and various cell components. The cells include WBCs which occupy 0.7% of blood volume with typical size of 10-15 μm , RBCs which occupy 45% of blood and more than 99% of total blood cells, with a typical size of 6-8 μm , and platelets with typical size of 1-3 μm [294, 295]. The remaining is plasma which is an aqueous solution comprised of 95% water and other components such as circulating nucleic acids, microorganisms, proteins, and metabolites [250, 296]. Without the presence of cells in blood *i.e.* plasma, the Newtonian model can be applied; however, blood is a non-Newtonian fluid and its non-Newtonian properties are associated with the existence of such cellular components as WBCs, RBCs, and platelets. Different factors including plasma viscosity, hematocrit, RBC aggregation, and the mechanical properties of RBCs affect blood viscosity [297-300]. In order

to satisfy these conditions and get closer to the real scenario, non-Newtonian models must be considered for blood modeling. several non-Newtonian models have been reported in the literature. Here, in order to mimic the non-Newtonian behaviour of the blood to a great extent, we have used power law equation to simulate the viscosity of blood, as shown by Eq. (7-17).

$$\tau = [\eta(\dot{\gamma})]\dot{\gamma} \quad (7-17)$$

Various values for the mentioned parameters have been reported over the years [301, 302], Most of which are gained by experimental methods. The input parameters for this specific study, as reported by Sarma K and Bhat SV [303] are listed in Table 5.

Table 5: Parameters that used for non-Newtonian model

Parameters	Details	Value
k [kg.s ⁿ⁻² /m]	Consistency index	0.01691
n	Power-law index	0.7
μ_0 [kg/m-s]	Minimum viscosity limit	0.0001
μ_∞ [k/m-s]	Maximum viscosity limit	0.1

7.2.4 Separation and purity efficiencies

SE and PE, which are terms previously introduced by Fekete [278], are used to evaluate the functionality of the proposed device. SE is defined as the ratio of V_{plasma} that is collected from daughter channels to V_{total} at the main channel inlet, which is described by Eq. (7-18):

$$SE = \frac{V_{\text{plasma}}}{V_{\text{total}}} \quad (7-18)$$

PE is defined as the ratio of the total number of RBCs at the main outlet to the net amount of RBCs at the main channel inlet, described by Eq. (7-19):

$$PE_{\text{total}} = 1 - \frac{n_{\text{daughter}}}{n_{\text{inlet}}} \quad (7-19)$$

Simply put, SE indicates how much plasma is separated from bifurcations and PE shows the purity of separated plasma. The major disadvantage of the mentioned equation is that they are often inversely proportional in a same system, meaning that improving one of them deteriorates

the efficiency of the other one. Hence, a trade-off between these two parameters must be considered to optimize the design.

7.2.5 Separation principles

Zweifach [304] and Fung [305] are the first researchers who introduced and identified the bifurcation law in microvascular vessels. Based on their theory, flowing blood cells migrate to the higher flow rate regions as a result of the asymmetric applied shear forces on their surface. These shear forces produce a torque on cells. Based on Bernoulli's law, the pressure inversely changes with flow rates, meaning that regions with higher flow rates have lower pressure. Therefore, cells tend to move towards higher flow rate regions due to the center-directed torque and pressure gradient applied on them. Blood plasma skimming is another phenomenon which plays an essential role in this design [306]. It has been proven that a thin cell-free layer exists near the walls which has a considerable impact on the purity of the separated fluid, leading to the transfer of pure plasma into the daughter channels [305]. In addition to those effects, two other factors are exploited in this geometry which are diffuser shaped daughter channels and the acceleration-deceleration effect due to the constrictions in the main channel. Diffuser shaped daughter channels help the device accumulate more separated plasma, resulting in a higher SE. Constrictions in the main channel push RBCs toward the centerline and accelerate them just before each bifurcation; allowing the system to reach a higher PE. These two additional factors act together to improve the PE and SE, simultaneously.

7.2.6 Experimental Setup:

To experimentally evaluate the efficiency of the proposed channels for blood plasma separation, microchannels were first fabricated by casting PDMS on a master mold fabricated via photolithography on a silicon wafer. The channel dimensions are demonstrated in Figure 7-1. To model the non-Newtonian property of blood, polyethylene oxide (PEO, Sigma-Aldrich, $M_w = 2000$ kDa) was added to phosphate-buffered saline (PBS) running Max buffer (Sigma-Aldrich) to make a PEO solution with concentration of 1500 ppm. PEO is a biocompatible

solution which can be used for biological applications. Then, 7 μm fluorescent polystyrene particles (Magsphere-Pasadena, California), representative of RBCs, were added to the PEO solution to reach the particle concentration of 1×10^4 per ml. After connecting the fluidic tubes to the microchannel, the PEO solution was pumped into the channel by a syringe pump (Fusion 200; Chemyx Inc.) at an optimal flow rate of $48 \mu\text{l}/\text{min}$. To visualize particle trajectories inside the channel, the microchannel was mounted on an inverted fluorescence microscope (IX73, Olympus, Tokyo, Japan) equipped with a high-speed CCD (DP80, Olympus, Tokyo, Japan) and high speed (Phantom- VEO 640L) cameras. The exposure time and microscope objective were set to 100 ms and 10x for fluorescence microscopy and $50 \mu\text{s}$ and 10x for bright-field and high-speed camera imaging. The captured images were then analyzed by ImageJ software.

7.3 Results and Discussions

7.3.1 Grid study

For numerical simulation, a structured hexahedral mesh has been used. Firstly, a grid independence study has been performed based on the SE. The number of elements was progressively increased until no significant changes were observed in the SE as shown in Figure 7-2 A.

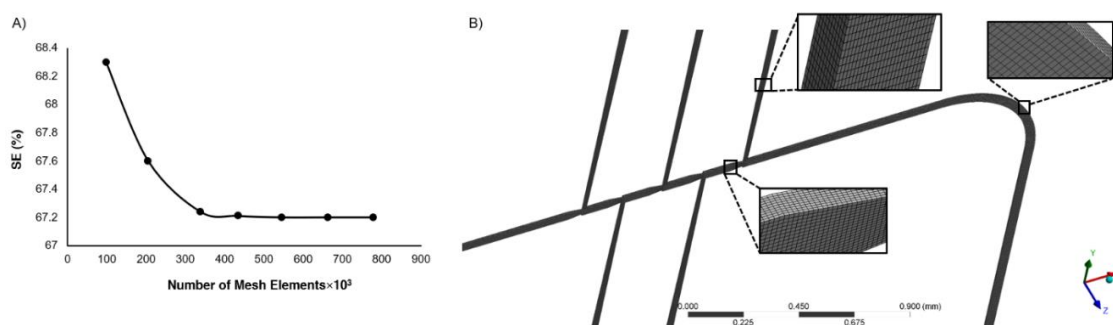


Figure 7-2: A) Grid study with different mesh element B) Mesh distribution in the different regions of the microchannel

It is observed that the error for a number of elements above 338,215 is approximately zero and the simulation becomes grid independent. Therefore, the mesh size of 338,215 has been used

for this numerical simulation. The corresponding mesh elements on the different regions of the separation device are shown in Figure 7-2 B.

7.3.2 Separation and purity efficiency

One of the most valuable aspects of this study is to use trapezoid-shaped constrictions in the main microchannel. The cross-section of the channel changes throughout the microchannel. The effects of these changes on the velocity and pressure are depicted in Figure 7-3 A and B. Due to the scale of the constrictions compared to the whole design, cropped sections of the design are displayed.

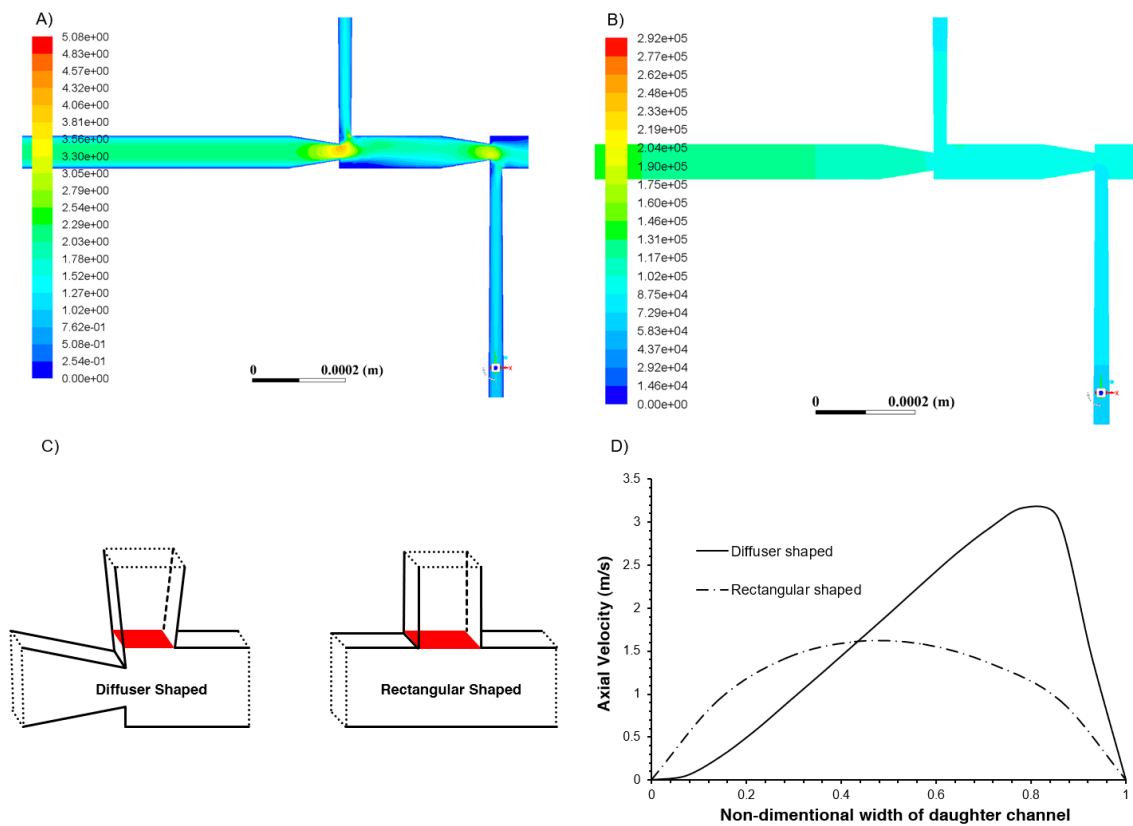


Figure 7-3: Hydrodynamic parameters throughout the channel. A) Velocity distribution (m/s) along the length of microchannel. The red regions show the acceleration part of the microchannel which is acting efficiently in the proposed geometry B) Pressure distribution (Pa) along the length of microchannel C) Two different types of bifurcation geometries used for analyzing the velocity distribution at the inlet. The mean values of velocity are reported based on the highlighted red surface exactly at the inlet of the bifurcation D) The corresponding axial velocity of the first bifurcation. The inlet velocity illustrates that more fluid is pushed through the diffuser shaped microchannel rather than a simple rectangular design so that SE is increased efficiently.

In Figure 7-3 A, high-velocity regions are shown in red, ranging from 3.81 m/s to 5.08 m/s, and light green color indicates the velocity in the range of 2 m/s to 2.8 m/s, approximately. The

average velocity of the inlet is 2 m/s, but owing to the zero boundary condition, the fully developed velocity takes a parabolic shape, indicating that the maximum velocity is more than 2 m/s. Additionally, trapezoid-shaped constrictions in the main channel accelerate the velocity; hence, a maximum velocity of 5.08 m/s in the constriction outlet is reasonable. Besides, Figure 7-3 B shows pressure contours throughout the first bifurcation which clearly indicates that in regions where flow velocity increases pressure reduces decreases. This behavior is consistent with the Bernoulli rule which states that pressure and velocity are conversely proportional.

The selected geometry for daughter channels in this study is able to collect more plasma than the rectangular one. One way to prove this fact is to compare the hydrodynamic resistances of the rectangular channel to the diffuser, which has been proven to be higher in the literature (Section 7.2.1). The other way is to compare the velocity profile at the inlet of daughter channel for both rectangular and diffuser shaped geometries, which is shown in Figure 7-3 C and D. According to Figure 7-3 D, the entrance velocity profile of the diffuser shaped daughter channel is considerably higher than the rectangular one. Therefore, the amount of plasma that is extracted from this diffuser channel is more than the rectangular one and proves that SE is efficiently increased by using this kind of bifurcations. Also, the trapezoid-shaped constrictions of the microchannel, immediately before each daughter channel, assist RBCs to accelerate, decreasing their tendency to enter the daughter channels. As a result, RBCs are encouraged to flow away from the daughter channels. Besides, RBCs intend to concentrate at the core region due to the plasma skimming effect, which consequently decreases the number of RBCs in the extracted plasma from daughter channels.

7.3.3 New conceptual design of the microchannel

Recent studies have agreed that the prevalent arrangement of channels for blood plasma separation is a main straight microchannel with five straight upward daughter channels [250, 252, 278, 282, 307, 308]. The effects of different arrangements of daughter channels, however, has not been extensively investigated. One aspect of this investigation lies in changing the

arrangement of daughter channels in an attempt to effectively improve the PE. The orientation of daughter channels alternates between upwards and downwards from the main channel as is shown in Figure 7-1. The PE of n^{th} bifurcation is defined by (7-20) as:

$$PE_{n^{\text{th}} \text{ daughter channel}} = 1 - \frac{n_{n^{\text{th}} \text{ daughter channel}}}{n_{\text{inlet of } n^{\text{th}} \text{ daughter channel}}} \quad (7-20)$$

(7-20) shows that the PE of each daughter channel can be calculated by comparing the number of RBCs just after each daughter channel, to the number of RBCs just before each daughter channel. In fact, this formula shows how many RBCs enter the daughter channel without considering other channels. Figure 7-4 illustrates the concept of the mentioned formula.

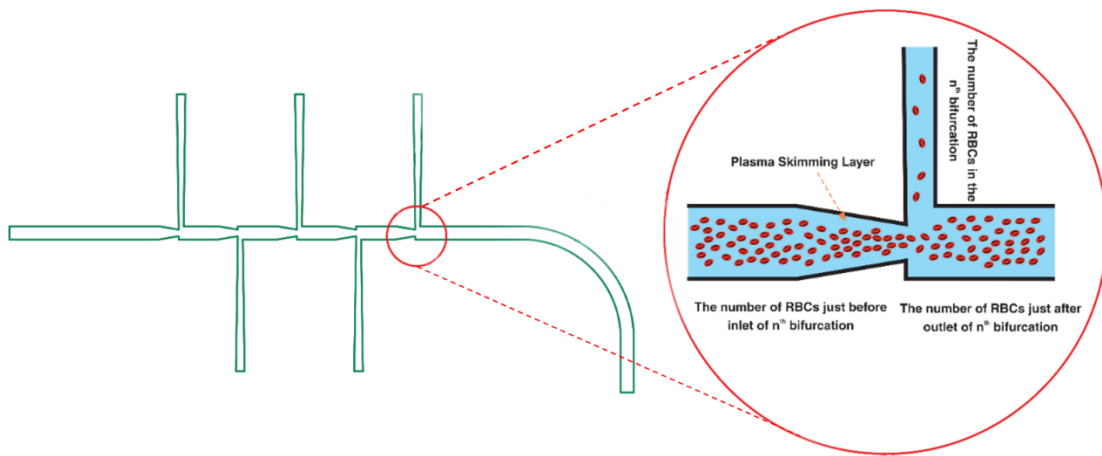


Figure 7-4: The schematic illustration of PE of n^{th} bifurcation.

Figure 7-5 shows the PE of each daughter channel, with the best configuration shown in Figure 7-1 as well as the ratio of plasma flow rate within each bifurcation to the inlet flow rate. Since a certain amount of fluid enters each daughter channel, the downstream flow rate throughout the main channel decreases after each side channel. Trapezoid-shaped zones in the main channel accelerate the flow; consequently, reduce the amount of plasma extracted from each side channel along the length of the microchannel. $Q_{\text{Plasma}}/Q_{\text{Inlet}}$ in the first daughter channel is 22.57% and decreases to approximately 13% by the final side channel. The pressure also drops throughout the main channel with a sudden drop at the entrance to each bifurcation which encourages RBCs to enter the daughter channels. However, by using trapezoid-shaped constrictions in the main channel, just before each daughter channel, RBCs quickly accelerate

and pass the inlet of the daughter channels. Therefore, the inclination of RBCs to enter the daughter channels decreases, causing a larger volume of plasma being extracted with a lower concentration of RBCs present.

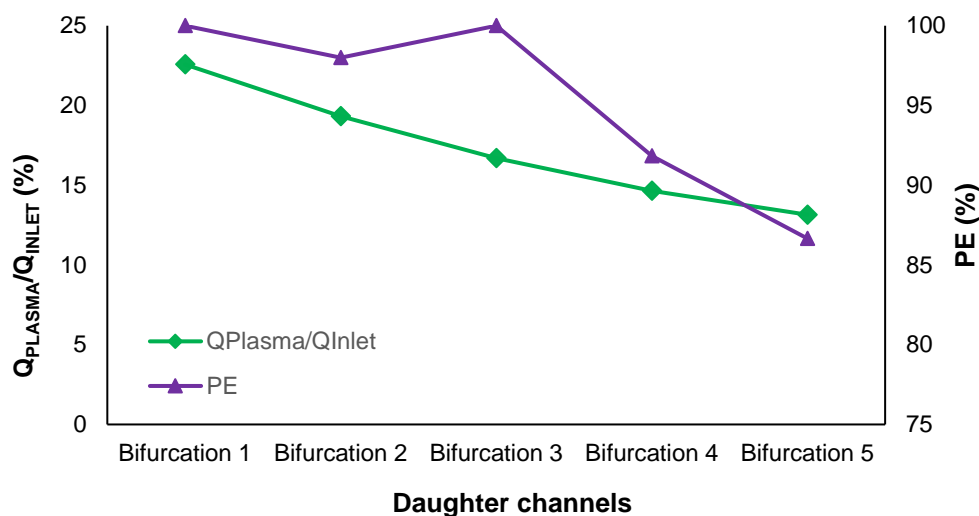


Figure 7-5: The PE of each daughter channel as well as the ratio of plasma of each bifurcation to the inlet flow rate

As shown in Figure 7-5, the percentage of PE for each bifurcation decreases along the length of the microchannel. This phenomenon is caused by the increasing concentration of the RBCs as plasma is continually skimmed from the main flow. The third bifurcation, however, does not obey this rule owing to the arrangement of the bifurcations (alternating between upwards and downwards), and this is a proof that using this arrangement positively impacts the percentage of PE achieved. The mentioned parameters of momentum and acceleration-deceleration effect directly influence the SE and PE, and with this new design of microchannel, the SE and PE reach to 86.37% and 78%, respectively. According to Figure 7-5, the lowest PE value occurs in the fourth and fifth bifurcations. Using a Lagrangian approach gives us an insight into the movement of each particle in the microchannel. Figure 7-6 A shows the Lagrangian view for a collection of particles that pass the fourth and fifth bifurcation. Although the particles passing the last constriction are accelerated, their velocity is not high enough and pressure drop along the width of the last bifurcation pushes particles into the last daughter channel. Altering the shape of the last trapezoid, as well as the daughter channel, allows us to overcome this issue. A

trenchant analysis has been carried out and shows that by changing the outward direction and design of last trapezoid, particles can be further accelerated and drawn away from the last bifurcation, leading to an increase in the PE. Figure 7-6 B shows the final generated design of corresponding geometry with the particle trajectory compared to the previous geometry.

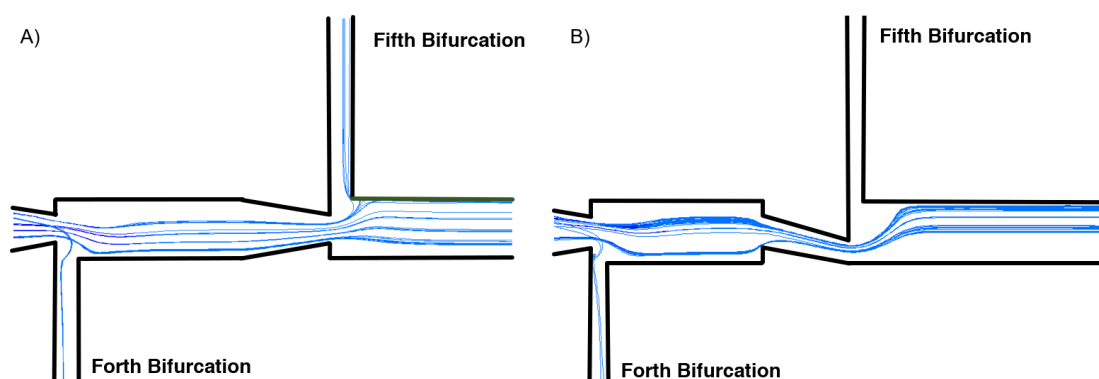


Figure 7-6: Particle trajectory along the microchannel in A) Previous designed device B) new conceptual design.

The pressure drop along the width of daughter channels is a factor that pushes the particles into the last daughter channel; however, by modifying the design of the microchannel, particles accelerate downward and the PE of last daughter channel becomes approximately 100%. It was mentioned earlier that PE and SE often negatively affect one another; therefore, by refining the geometry and creating this final generation, while the overall PE increases dramatically, the overall SE decreases very slightly. The comparison of PE for each bifurcation, as well as the comparison of overall PE and SE, between the new conceptual design and the previous one are shown in Figure 7-7. The figure has been divided into two parts by a green dash line. At the left side of the dashed line, the PE of each bifurcation in both the new conceptual design and geometry without modified constriction is compared, whilst to the right, the overall PE and SE are compared. It is worth noting that although the changes made to the fifth bifurcation increased the PE, the SE decreases as a result, but not to the same magnitude that PE increases. This larger increase in PE can compensate for the small decrease in SE, and be considered the best possible result.

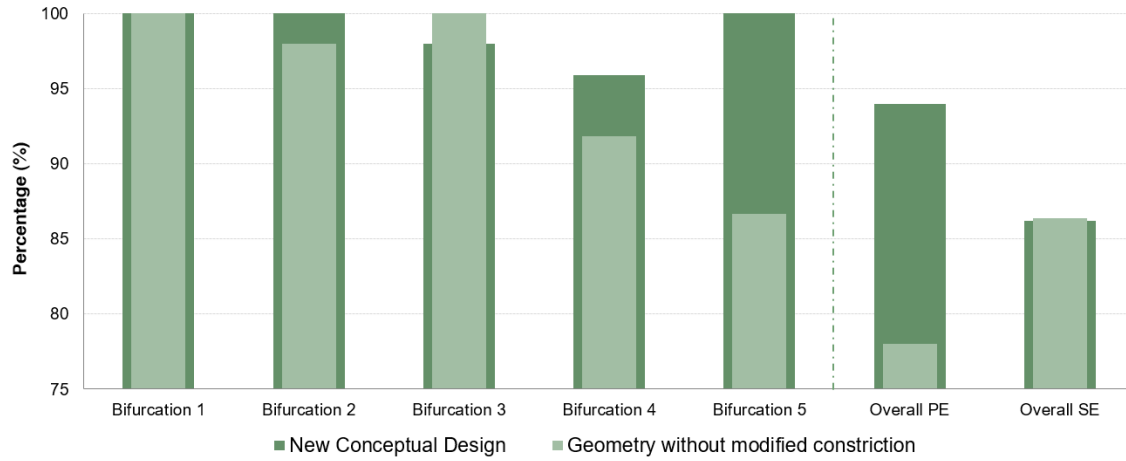


Figure 7-7: The comparison of PE of each bifurcation and the comparison of overall PE and SE between the previous geometry and the new conceptual design.

According to the right side of the dashed line in Figure 7-7, the overall PE reaches 94% and the overall SE reaches 86 %, approximately. These percentages show that a good trade-off between these two factors has occurred. High percentages of PE and SE give the conceptual design a distinct advantage over other conventional devices. A quick glance over previous studies shows that the current design can increase the PE and SE by more than 30% and 15%, respectively. Regarding the inverse relationship between PE and SE, these results clarify that an acceptable trade-off has occurred, promising more effective plasma separation for many biomedical applications.

7.3.4 Experimental results for the new conceptual design

After numerically analyzing particle trajectories throughout the conceptual design and optimizing the channel constrictions to obtain the highest efficiency, the proposed design was fabricated for further evaluation and validation by experimental approach. According to Figure 7-8, randomly dispersed particles at the channel inlet, which spatially represent the RBCs, move towards the channel center due to the plasma skimming phenomenon and Zweifach-Fung effect. Both channels with and without constriction modification were fabricated and evaluated. Particle trajectory at the last daughter branch of the non-modified design (Figure 7-8 A) shows that particles tend to exit from the last bifurcation due to the high concentration of the particles (caused by the solution exit from the previous side branches) and low hydrodynamic resistance

of this side branch. However, under the same flow condition, the conceptual design directs the particles slightly towards the non-branch side which noticeably increases the PE of the last bifurcation (Figure 7-8 B). As can be seen, particles mostly move straight towards the main outlet, while the pure solution exits from the last side branch. In addition, the magnified view (inset of Figure 7-8 B) of the particle trajectories in the last two bifurcations of the conceptual design clearly shows the effect of the proposed geometry on particle migration by further manipulation of the constrictions.

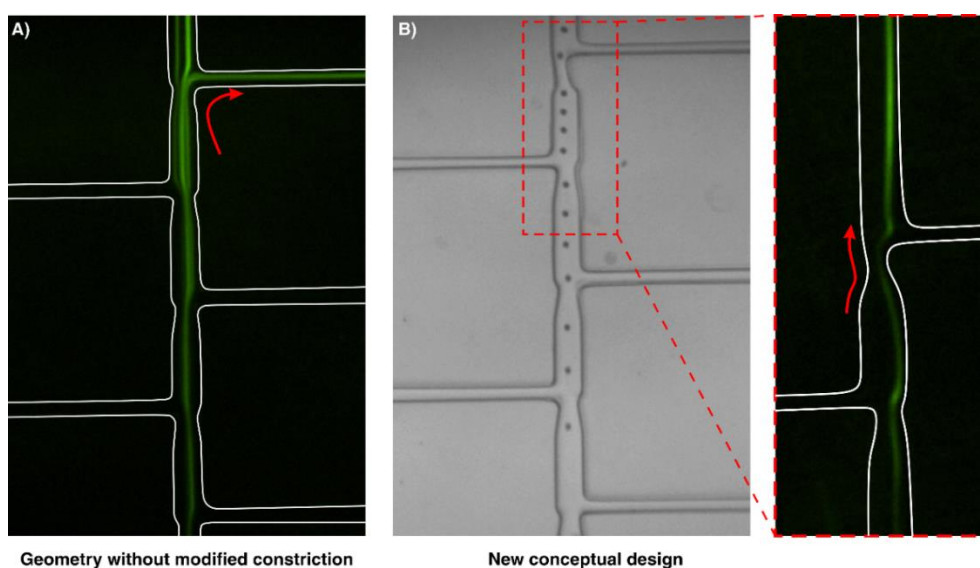


Figure 7-8: Fluorescent and bright-field images, showing the effect of channel design on the particle trajectories. A) particles exit from the last outlet of the non-modified channel. B) particle trajectory on the conceptual design, showing the efficient scenario for enhancement of PE of the extracted sample.

It should be noted that our experimental results clearly illustrate that the proposed design is highly dependent on the concentration of the cells/particles and low concentrations of particles or diluted blood samples must be run in the channel. A slight increase in concentration leads to clogging of the channel or undesired separation results. However, the beauty of these straight channels is their ability for multiplexing or parallelization to address the mentioned issues.

7.4 Conclusion

The present study involved the design of a novel microfluidic device for blood plasma separation. The design strategy has been based on three major principles including the Zweifach-Fung effect, plasma skimming phenomenon, and acceleration-deceleration effect. The

PE and SE have been introduced as two major criteria to evaluate the performance of the current device. Three-dimensional simulations were numerically performed to solve the flow field and track the particles. In order to satisfy the non-Newtonian effects of blood and approach more realistic circumstances, a non-Newtonian power-law model has been used. The RBCs were considered as rigid spherical particles with the diameter of 7 μm . First, the diffuser shaped channel was used in the daughter channels to increase the percentage of SE. Additionally, four trapezoid-shaped constrictions have been used in distinct regions of main channel, as well as a new arrangement of daughter channels, all of which have been investigated and revealed to increase the SE and PE to 86.37% and 78%, respectively. Finally, the PE of each bifurcation has been obtained, and to enhance the PE in the last bifurcation channel and overall percentage, a new kind of constriction has been introduced and applied at the entrance of the last daughter channel. Therefore, the PE of the last bifurcation increases significantly. Experimental tests concurred with the expected improvements in particle behavior through the newly developed constriction. We believe that this device can be considered as an indispensable part of microfluidic research utilizing blood-plasma separation and has the potential to be tailored for many other biological applications by optimizing the system based on the governing physics.

8

Chapter Eight: Conclusions and Future work

8.1 Conclusions

The main aim of this study is to investigate particle migration in elasto-inertial microfluidic systems within non-conventional microchannels and to propose new fabrication workflows to facilitate the fabrication of microchannels suitable for inertial microfluidic applications. Throughout this research, each chapter devotes to one aspect of elasto-inertial systems from studying the fundamentals to proposing new methods for fabrication of more complex channels. With the aim of these novel fabrication methodologies, elasto-inertial focusing in non-conventional channels was investigated and used for practical applications. Finally, a conceptual design was presented with higher separation and purity efficiency compared to its available counterparts. More detailed achievements and conclusions for each chapter are listed in the following sections.

8.1.1 Fundamentals of elasto inertial focusing in straight channels (Paper I, Chapter 4)

In this research, using a non-Newtonian (PEO) solution, particle migration in straight channels with different cross-sections were experimentally and numerically observed to understand how geometry, blockage ratio, flow rate can affect the focusing behaviors. After a comprehensive analysis, we presented a two-stage focusing model in which particles initially move to the regions with lowest viscoelastic forces (diagonal directions in square and rectangular channels), followed by a diagonal migration towards the final equilibrium positions. In addition, we studied the effects of corner angle on the focusing positions and viscoelastic force. Results showed that increasing the corner angle strengthens the center-directed elastic forces and shrinks the regions where elastic force pushes the particles towards the wall. We also investigated the influences of aspect ratio and velocity gradient on the focusing positions. Results revealed that increasing the channel width deteriorates the viscoelastic force more than the inertial force, thereby increasing one line focusing in a square channel to two lines in a rectangular channel. we realized that in order to improve focusing, the following points should be considered in non-Newtonian systems:

1. The corner angle of the cross-sections should be as large as possible. This encourages particle migration towards the center of the channel.
2. At the same hydraulic diameter, the core flow needs to be as confined as possible in all directions. This causes particles to remain focused at the center for higher flow rates.

Based on this conclusion, we developed a novel complex channel design to obtain a tighter focusing under the same conditions. We were able to use elasto-inertial forces to focus 3 μm particles in the complex channel at high flow rate of 100 $\mu\text{l/min}$. Finally, as a proof of concept, we showcased the elasto-inertial focusing of the *Saccharomyces cerevisiae* cells (3-5 μm) with high-throughput of 75 $\mu\text{l/min}$.

8.1.2 Elasto-inertial particle migration in non-conventional channels fabricated by wax 3D printing (Paper II, Chapter 5)

Sacrificial 3D printed molds have been used in fabrication of microfluidic devices, where PDMS elastomer has been cast into a wide range of dissolvable materials such as sugar alcohol isomalt [218], polyvinyl alcohol (PVA) [219], polyethylene glycol (PEG) [220], and acrylonitrile butadiene styrene (ABS) molds [221]. Although the use of these materials is a step forward in simplifying the fabrication of microfluidic chips, the resolution of microchannels obtained using these template-assisted techniques is not high enough to meet the requirement of inertial microfluidics.

In this paper, we overcome many of these limitations by employing a high-quality wax 3D printer and softlithography through a novel workflow, which eliminates the need for use of harsh chemicals, multiple cleaning steps and more importantly PDMS bonding. We have shown that by adding dummy structures to reinforce the template and dissolving the support wax on a PDMS slab to eliminate the additional handling steps, one can make various microfluidic microchannels with any arbitrary cross-section. Careful characterization of fabricated microchannels using this approach revealed that all geometries have a good surface finish with Sa of ~ 1.75 , reproducing the intended design with dimension errors of less than 3%.

In addition, focusing of 50 μm particles in Newtonian and non-Newtonian solutions, for various curved and straight channels was demonstrated to highlight the suitability of this technique for inertial microfluidics. Systematic analysis of curved microchannels using numerical simulations revealed that rectangular-shaped channels have lower helicity values compared to the circular and triangular geometries at similar flow rates. As such, for high-throughput focusing applications, a rectangular channel is preferable, as it has lower helicity values and consequently less particle mixing. As expected, experimental results revealed that the focusing positions in Newtonian and non-Newtonian solutions are quite different, due to the extra viscoelastic force applied on the particles. For the Newtonian solutions, particles find equilibrium close to the inner wall of the curved channels, while for the non-Newtonian solutions, equilibrium positions move towards the outer wall due to viscoelastic force. In straight channels, for a trapezoidal shape and Newtonian solution, increasing the flow rates resulted in a migration of the focusing line from the vertical side to the slanted side. However, for the non-Newtonian solution, particles focused at the center of the channel for all the tested flow rates. While the cross-sectional area of the complex channel is almost twice the size of the single trapezoidal channel, distinct focusing in the complex channel showed the potential of the superposition technique for high-throughput applications. Finally, as a proof of concept, we fabricated a spiral channel with a maximum cell-holding capacity able to separate microcarriers from MSCs with over 98% efficiency. We believe this new method for fabrication of complex inertial microfluidic channels will open up avenues for researchers to explore new physics and develop new applications for the promising field of microfluidics.

8.1.3 3D-Direct printing of inertial microfluidic devices (Paper III, Chapter 6)

The main aim of this study was to propose a new fabrication methodology for creating microchannels suitable for inertial microfluidic applications. The proposed method involves 3D direct printing of a channel with arbitrary geometry via a high-resolution SLA/DLP 3D printer (in this study, we use Miicraft). As the prevalent challenge of Resin microchannels is their

bonding and assembly, we have proposed a novel bonding technique based on a double adhesive tape to a transparent PMMA slab. Since the utilized PMMA is transparent, these devices are capable of bright field, phase contrast, fluorescent, or high-speed microscopy. The bonding quality was evaluated by Saffman-Taylor finger criterion and the results showed that the device is capable of withstanding pressure as high as 150 psi (nearly triple of the value reported for PDMS). Using this strategy, for the first time, we have fabricated a right-hand triangular spiral microchannel and the results reveal promising focusing behavior within the channel. Interestingly, results showed that focusing patterns in hard chips are different compared to their PDMS-made counterparts. While 10 μm particles focus at the outer wall of the PDMS-made spiral channel after 2.5 $\mu\text{l/min}$, they showed another focusing position close to the inner wall in hard chip spiral for all flow rates. We showed that previously established inertial microfluidic devices, as well as new developed channels and cross-sections, can easily be adapted into this 3D-direct-printing fabrication method with a time frame less than 3 hours.

8.1.4 Blood-plasma separation using Dean-flow coupled elasto-inertial systems (Paper IV, Chapter 7)

In this study, we designed a novel microfluidic device for blood plasma separation which has higher separation purity and efficiency compared to its conventional counterparts. The design strategy has been based on three major principles including the Zweifach-Fung effect, plasma skimming phenomenon, and acceleration-deceleration effect. Three-dimensional simulations were numerically performed to solve the flow field and track the particles. In order to satisfy the non-Newtonian effects of blood and approach more realistic circumstances, a non-Newtonian power-law model has been used. First, the diffuser shaped channel was analyzed in the daughter channels to increase the percentage of separation efficiency (SE). In addition, four trapezoid-shaped constrictions have been used in distinct regions of the main channel, as well as a new arrangement of daughter channels, all of which have been investigated and revealed to increase the separation efficiency and purity efficiency (PE) to 86.37% and 78%,

respectively. Finally, the PE of each bifurcation has been obtained, and to enhance the PE in the last bifurcation channel and overall percentage, a new kind of constriction has been introduced and applied at the entrance of the last daughter channel. Experimental tests concurred with the expected numerical improvements through the newly developed constriction, in which 7 μm particles were separated from their non-Newtonian media efficiently.

8.2 Future works

Applications of non-Newtonian fluids in inertial microfluidics are increasingly spread due to the enhanced capabilities of elasto-inertial systems for particle sorting. However, due to the lack of enough knowledge on the fundamentals of elasto-inertial systems as well as fabrication limitations, there are many potentials and issues which remain unexplored yet. In the following, some of the areas that need a systematic investigation are listed.

- 1) So far, all the numerical investigations on the fundamentals and mechanisms of particle migration in microchannels have been performed in straight channels, while experimental research have shown a great promise in the curved channels.
- 2) All the simulations performed on the particle migration as well as proposed criteria for particle focusing are based on rigid wall assumption. However, in these studies, normally, channels are deformable, which can totally change the flow dynamics and inertial forces.
- 3) In spiral channels, there are many focusing stages (confirmed by experiments) that need a comprehensive analysis to explain.
- 4) All the previous investigations in elasto-inertial systems were on rectangular and trapezoidal spiral channels. However, it is well-proven that structure and geometry can significantly affect the focusing patterns, which makes a fundamental study of particle migration in spiral and curved channels with non-rectangular geometries a crucial need.
- 5) Sheath flow elasto-inertial systems have been only used in straight channels with rectangular geometries. Therefore, there is a huge potential to enhance particle separation

in these systems by altering the channel structure and cross-sectional geometry. So far, no effort has been performed on the sheath flow elasto inertial microfluidics in spiral and serpentine channel.

- 6) Since elasto-inertial forces are strongly related to the channel geometry, proposing new fabrication workflows to readily create non-conventional channels with dimensions smaller than 100 μm is a crucial need, since the current 3D printing methodologies and the printing resolutions are not appropriate for microchannel fabrication with mentioned dimensions.
- 7) Current blood-plasma separation devices typically cannot capture platelets efficiently, and if so, they suffer from channel blockage and low throughput. Due to the importance of plasma for therapeutic and diagnostic applications, proposing new designs with high separation efficiency and purity is a crucial need.

We believe that the mentioned ideas can open new avenues for particle sorting strategies in elasto-inertial systems.

References

1. Nguyen, N.-T., S.T. Wereley, and S.A.M. Shaegh, *Fundamentals and applications of microfluidics*. 2019: Artech house.
2. Terry, S.C., J.H. Jerman, and J.B. Angell, *A gas chromatographic air analyzer fabricated on a silicon wafer*. IEEE transactions on electron devices, 1979. **26**(12): p. 1880-1886.
3. Ruzicka, J., *Flow injection analysis. From test tube to integrated microconduits*. Analytical Chemistry, 1983. **55**(11): p. 1040A-1053A.
4. Zhan, W., J. Alvarez, and R.M. Crooks, *A two-channel microfluidic sensor that uses anodic electrogenerated chemiluminescence as a photonic reporter of cathodic redox reactions*. Analytical chemistry, 2003. **75**(2): p. 313-318.
5. McDonald, J.C. and G.M. Whitesides, *Poly (dimethylsiloxane) as a material for fabricating microfluidic devices*. Accounts of chemical research, 2002. **35**(7): p. 491-499.
6. Radisic, M., R.K. Iyer, and S.K. Murthy, *Micro- and nanotechnology in cell separation*. International journal of nanomedicine, 2006. **1**(1): p. 3-14.
7. Simonnet, C. and A. Groisman, *High-Throughput and High-Resolution Flow Cytometry in Molded Microfluidic Devices*. Analytical Chemistry, 2006. **78**(16): p. 5653-5663.
8. Hur, S.C., et al., *Deformability-based cell classification and enrichment using inertial microfluidics*. Lab on a Chip, 2011. **11**(5): p. 912-920.
9. Chen, Y., et al., *Rare cell isolation and analysis in microfluidics*. Lab on a Chip, 2014. **14**(4): p. 626-645.
10. Nelson, R.J., et al., *Microfluidic apparatus and method for purification and processing*. 2003, Google Patents.
11. Zhang, J., et al., *Fundamentals and applications of inertial microfluidics: a review*. Lab on a Chip, 2016. **16**(1): p. 10-34.
12. Forbes, T.P. and S.P. Forry, *Microfluidic magnetophoretic separations of immunomagnetically labeled rare mammalian cells*. Lab on a Chip, 2012. **12**(8): p. 1471-1479.
13. Khoshmanesh, K., et al., *Dielectrophoretic platforms for bio-microfluidic systems*. Biosensors and Bioelectronics, 2011. **26**(5): p. 1800-1814.
14. Augustsson, P., et al., *Microfluidic, label-free enrichment of prostate cancer cells in blood based on acoustophoresis*. Analytical chemistry, 2012. **84**(18): p. 7954-7962.
15. Warkiani, M.E., et al., *Malaria detection using inertial microfluidics*. Lab on a Chip, 2015. **15**(4): p. 1101-1109.
16. McGrath, J., M. Jimenez, and H. Bridle, *Deterministic lateral displacement for particle separation: a review*. Lab on a Chip, 2014. **14**(21): p. 4139-4158.
17. Di Carlo, D., *Inertial microfluidics*. Lab on a Chip, 2009. **9**(21): p. 3038-3046.
18. Segre, G. and A. Silberberg, *Radial particle displacements in Poiseuille flow of suspensions*. Nature, 1961. **189**(4760): p. 209.
19. Amini, H., W. Lee, and D. Di Carlo, *Inertial microfluidic physics*. Lab on a Chip, 2014. **14**(15): p. 2739-2761.
20. Lu, X., et al., *Particle manipulations in non-Newtonian microfluidics: A review*. Journal of colloid and interface science, 2017. **500**: p. 182-201.
21. Liu, C., et al., *λ -DNA-and Aptamer-Mediated Sorting and Analysis of Extracellular Vesicles*. Journal of the American Chemical Society, 2019. **141**(9): p. 3817-3821.
22. Yuan, D., et al., *Recent progress of particle migration in viscoelastic fluids*. Lab on a Chip, 2018. **18**(4): p. 551-567.

23. Yang, S.H., et al., *Multiple-line particle focusing under viscoelastic flow in a microfluidic device*. Analytical chemistry, 2017. **89**(6): p. 3639-3647.
24. Li, D. and X. Xuan, *Fluid rheological effects on particle migration in a straight rectangular microchannel*. Microfluidics and Nanofluidics, 2018. **22**(4): p. 49.
25. Faridi, M.A., et al., *Elasto-inertial microfluidics for bacteria separation from whole blood for sepsis diagnostics*. Journal of nanobiotechnology, 2017. **15**(1): p. 3.
26. Morton, K.J., et al., *Crossing microfluidic streamlines to lyse, label and wash cells*. Lab on a Chip, 2008. **8**(9): p. 1448-1453.
27. Yang, S., A. Ündar, and J.D. Zahn, *Continuous cytometric bead processing within a microfluidic device for bead based sensing platforms*. Lab on a Chip, 2007. **7**(5): p. 588-595.
28. Cha, S., et al., *Cell stretching measurement utilizing viscoelastic particle focusing*. Analytical chemistry, 2012. **84**(23): p. 10471-10477.
29. Kim, J.Y., et al., *Lateral migration and focusing of colloidal particles and DNA molecules under viscoelastic flow*. Lab on a Chip, 2012. **12**(16): p. 2807-2814.
30. Liu, C., et al., *λ -DNA and Aptamer Mediated Sorting and Analysis of Extracellular Vesicles*. Journal of the American Chemical Society, 2019.
31. Yuan, D., et al., *On-chip microparticle and cell washing using coflow of viscoelastic fluid and newtonian fluid*. Analytical chemistry, 2017. **89**(17): p. 9574-9582.
32. Boger, D.V., *A highly elastic constant-viscosity fluid*. Journal of Non-Newtonian Fluid Mechanics, 1977. **3**(1): p. 87-91.
33. Cox, R. and H.J.C.E.S. Brenner, *The lateral migration of solid particles in Poiseuille flow—I Theory*. 1968. **23**(2): p. 147-173.
34. Anczurowski, E. and S.J.T.o.t.S.o.R. Mason, *Particle motions in sheared suspensions. XXIV. Rotation of rigid spheroids and cylinders*. 1968. **12**(2): p. 209-215.
35. Feng, J., H.H. Hu, and D.D.J.J.o.f.m. Joseph, *Direct simulation of initial value problems for the motion of solid bodies in a Newtonian fluid. Part 2. Couette and Poiseuille flows*. 1994. **277**: p. 271-301.
36. Jeffrey, R.C. and J.R.A. Pearson, *Particle motion in laminar vertical tube flow*. Journal of Fluid Mechanics, 1965. **22**(4): p. 721-735.
37. Tachibana, M.J.R.A., *On the behaviour of a sphere in the laminar tube flows*. 1973. **12**(1): p. 58-69.
38. Ho, B. and L. Leal, *Migration of rigid spheres in a two-dimensional unidirectional shear flow of a second-order fluid*. Journal of Fluid Mechanics, 1976. **76**(4): p. 783-799.
39. Feng, J., H.H. Hu, and D.D.J.J.o.F.M. Joseph, *Direct simulation of initial value problems for the motion of solid bodies in a Newtonian fluid Part 1. Sedimentation*. 1994. **261**: p. 95-134.
40. Yang, B.H., et al., *Migration of a sphere in tube flow*. 2005. **540**: p. 109-131.
41. Schonberg, J.A. and E.J.J.o.F.M. Hinch, *Inertial migration of a sphere in Poiseuille flow*. 1989. **203**: p. 517-524.
42. Asmolov, E.S., et al., *Inertial focusing of finite-size particles in microchannels*. Journal of Fluid Mechanics, 2018. **840**: p. 613-630.
43. Asmolov, E., *Dynamics of a spherical particle in a laminar boundary layer*. Fluid Dynamics, 1990. **25**(6): p. 886-890.
44. Cox, R. and S. Hsu, *The lateral migration of solid particles in a laminar flow near a plane*. International Journal of Multiphase Flow, 1977. **3**(3): p. 201-222.
45. Ho, B. and L. Leal, *Inertial migration of rigid spheres in two-dimensional unidirectional flows*. Journal of fluid mechanics, 1974. **65**(2): p. 365-400.
46. Drew, D.A., *The lift force on a small sphere in the presence of a wall*. Chemical engineering science, 1988. **43**(4): p. 769-773.

47. Karnis, A. and S. Mason, *Particle motions in sheared suspensions. XIX. Viscoelastic media*. Transactions of the Society of Rheology, 1966. **10**(2): p. 571-592.
48. Bartram, E., H. Goldsmith, and S. Mason, *Particle motions in non-Newtonian media*. Rheologica Acta, 1975. **14**(9): p. 776-782.
49. Gauthier, F., H. Goldsmith, and S. Mason, *Particle motions in non-Newtonian media. II. Poiseuille flow*. Transactions of the Society of Rheology, 1971. **15**(2): p. 297-330.
50. Tehrani, M., *An experimental study of particle migration in pipe flow of viscoelastic fluids*. Journal of Rheology, 1996. **40**(6): p. 1057-1077.
51. Leshansky, A.M., et al., *Tunable nonlinear viscoelastic "focusing" in a microfluidic device*. Physical review letters, 2007. **98**(23): p. 234501.
52. D'Avino, G., et al., *Single line particle focusing induced by viscoelasticity of the suspending liquid: theory, experiments and simulations to design a micropipe flow-focuser*. Lab on a Chip, 2012. **12**(9): p. 1638-1645.
53. Huang, P. and D. Joseph, *Effects of shear thinning on migration of neutrally buoyant particles in pressure driven flow of Newtonian and viscoelastic fluids*. Journal of non-newtonian fluid mechanics, 2000. **90**(2-3): p. 159-185.
54. Huang, P., et al., *Direct simulation of the motion of solid particles in Couette and Poiseuille flows of viscoelastic fluids*. Journal of Fluid Mechanics, 1997. **343**: p. 73-94.
55. Yang, S., et al., *Sheathless elasto-inertial particle focusing and continuous separation in a straight rectangular microchannel*. Lab on a Chip, 2011. **11**(2): p. 266-273.
56. Kang, K., et al., *DNA-based highly tunable particle focuser*. Nature communications, 2013. **4**: p. 2567.
57. Lim, E.J., et al., *Inertio-elastic focusing of bioparticles in microchannels at high throughput*. Nature communications, 2014. **5**: p. 4120.
58. Xiang, N., Q. Dai, and Z. Ni, *Multi-train elasto-inertial particle focusing in straight microfluidic channels*. Applied Physics Letters, 2016. **109**(13): p. 134101.
59. Yuan, D., et al., *Dean-flow-coupled elasto-inertial particle and cell focusing in symmetric serpentine microchannels*. Microfluidics and Nanofluidics, 2019. **23**(3): p. 41.
60. Raoufi, M.A., et al., *Experimental and numerical study of elasto-inertial focusing in straight channels*. Biomicrofluidics, 2019. **13**(3): p. 034103.
61. Bird, R.B., R.C. Armstrong, and O. Hassager, *Dynamics of polymeric liquids. Vol. 1: Fluid mechanics*. 1987.
62. Villone, M., et al., *Particle motion in square channel flow of a viscoelastic liquid: Migration vs. secondary flows*. Journal of Non-Newtonian Fluid Mechanics, 2013. **195**: p. 1-8.
63. Larson, R.G., *Constitutive equations for polymer melts and solutions*. Elsevier.
64. Asmolov, E.S., *The inertial lift on a spherical particle in a plane Poiseuille flow at large channel Reynolds number*. Journal of Fluid Mechanics, 1999. **381**: p. 63-87.
65. Matas, J.-P., J.F. Morris, and É.J.J.o.F.M. Guazzelli, *Inertial migration of rigid spherical particles in Poiseuille flow*. 2004. **515**: p. 171-195.
66. Di Carlo, D., et al., *Particle Segregation and Dynamics in Confined Flows*. Vol. 102. 2009. 094503.
67. Di Carlo, D., et al., *Continuous inertial focusing, ordering, and separation of particles in microchannels*. Proceedings of the National Academy of Sciences, 2007. **104**(48): p. 18892-18897.
68. Song, H.Y., et al., *Relationship between particle focusing and dimensionless numbers in elasto-inertial focusing*. Rheologica Acta, 2016. **55**(11-12): p. 889-900.
69. Del Giudice, F., et al., *Effect of fluid rheology on particle migration in a square-shaped microchannel*. Microfluidics and Nanofluidics, 2015. **19**(1): p. 95-104.

70. Li, G., G.H. McKinley, and A.M. Ardekani, *Dynamics of particle migration in channel flow of viscoelastic fluids*. Journal of Fluid Mechanics, 2015. **785**: p. 486-505.
71. Mach, A.J., et al., *Automated cellular sample preparation using a Centrifuge-on-a-Chip*. Lab on a Chip, 2011. **11**(17): p. 2827-2834.
72. Chan, P.C.H. and L.G. Leal, *The motion of a deformable drop in a second-order fluid*. Journal of Fluid Mechanics, 1979. **92**(1): p. 131-170.
73. Stan, C.A., et al., *The magnitude of lift forces acting on drops and bubbles in liquids flowing inside microchannels*. Lab on a Chip, 2013. **13**(3): p. 365-376.
74. Giesekus, H., *A simple constitutive equation for polymer fluids based on the concept of deformation-dependent tensorial mobility*. Journal of Non-Newtonian Fluid Mechanics, 1982. **11**(1): p. 69-109.
75. Kim, B. and J.M. Kim, *Elasto-inertial particle focusing under the viscoelastic flow of DNA solution in a square channel*. Biomicrofluidics, 2016. **10**(2): p. 024111.
76. Yang, S., et al., *Deformability-selective particle entrainment and separation in a rectangular microchannel using medium viscoelasticity*. Soft Matter, 2012. **8**(18): p. 5011-5019.
77. Seo, K.W., et al., *Particle migration and single-line particle focusing in microscale pipe flow of viscoelastic fluids*. RSC Advances, 2014. **4**(7): p. 3512-3520.
78. Seo, K.W., Y.J. Kang, and S.J.J.P.o.F. Lee, *Lateral migration and focusing of microspheres in a microchannel flow of viscoelastic fluids*. 2014. **26**(6): p. 063301.
79. Del Giudice, F., et al., *"From the Edge to the Center": Viscoelastic Migration of Particles and Cells in a Strongly Shear-Thinning Liquid Flowing in a Microchannel*. Analytical chemistry, 2017. **89**(24): p. 13146-13159.
80. Holzner, G., S. Stavrakis, and A. deMello, *Elasto-Inertial Focusing of Mammalian Cells and Bacteria Using Low Molecular, Low Viscosity PEO Solutions*. Anal Chem, 2017. **89**(21): p. 11653-11663.
81. Go, T., H. Byeon, and S.J. Lee, *Focusing and alignment of erythrocytes in a viscoelastic medium*. Scientific reports, 2017. **7**: p. 41162.
82. Xiang, N., et al., *Circular-channel particle focuser utilizing viscoelastic focusing*. Microfluidics and Nanofluidics, 2019. **23**(2): p. 16.
83. Yang, S.H., et al., *Double-line particle focusing induced by negative normal stress difference in a microfluidic channel*. Microfluidics and Nanofluidics, 2019. **23**(2): p. 21.
84. Tang, W., et al., *Elasto-inertial particle focusing in 3D-printed microchannels with unconventional cross sections*. Microfluidics and Nanofluidics, 2019. **23**(3): p. 42.
85. Ahn, S.W., et al., *Microfluidic particle separator utilizing sheathless elasto-inertial focusing*. Chemical Engineering Science, 2015. **126**: p. 237-243.
86. Liu, C., et al., *Size-based separation of particles and cells utilizing viscoelastic effects in straight microchannels*. Analytical chemistry, 2015. **87**(12): p. 6041-6048.
87. Lu, X., et al., *Continuous sheath-free separation of particles by shape in viscoelastic fluids*. Applied Physics Letters, 2015. **107**(26): p. 264102.
88. Li, D., et al., *Continuous sheath-free separation of drug-treated human fungal pathogen Cryptococcus neoformans by morphology in biocompatible polymer solutions*. Electrophoresis, 2018. **39**(18): p. 2362-2369.
89. Nam, J., et al., *Viscoelastic Separation and Concentration of Fungi from Blood for Highly Sensitive Molecular Diagnostics*. Scientific Reports, 2019. **9**(1): p. 3067.
90. Nam, J., et al., *High-throughput malaria parasite separation using a viscoelastic fluid for ultrasensitive PCR detection*. Lab on a Chip, 2016. **16**(11): p. 2086-2092.
91. Nam, J., et al., *Microfluidic device for sheathless particle focusing and separation using a viscoelastic fluid*. Journal of Chromatography A, 2015. **1406**: p. 244-250.
92. Nam, J., et al., *Hybrid capillary-inserted microfluidic device for sheathless particle focusing and separation in viscoelastic flow*. Biomicrofluidics, 2015. **9**(6): p. 064117.

93. Tan, J.K.S., et al., *Continuous Separation of White Blood Cells From Whole Blood Using Viscoelastic Effects*. IEEE Transactions on Biomedical Circuits and Systems, 2017. **11**(6): p. 1431-1437.
94. Yuan, D., et al., *Dean-flow-coupled elasto-inertial three-dimensional particle focusing under viscoelastic flow in a straight channel with asymmetrical expansion–contraction cavity arrays*. Biomicrofluidics, 2015. **9**(4): p. 044108.
95. Yuan, D., et al., *Continuous plasma extraction under viscoelastic fluid in a straight channel with asymmetrical expansion-contraction cavity arrays*. Lab Chip, 2016. **16**(20): p. 3919-3928.
96. Yuan, D., et al., *Sheathless Dean-flow-coupled elasto-inertial particle focusing and separation in viscoelastic fluid*. RSC Advances, 2017. **7**(6): p. 3461-3469.
97. Xiang, N., et al., *Fundamentals of elasto-inertial particle focusing in curved microfluidic channels*. Lab on a Chip, 2016. **16**(14): p. 2626-2635.
98. Lee, D.J., et al., *Multiplex particle focusing via hydrodynamic force in viscoelastic fluids*. Scientific reports, 2013. **3**: p. 3258.
99. Xiang, N., Z. Ni, and H. Yi, *Concentration-controlled particle focusing in spiral elasto-inertial microfluidic devices*. Electrophoresis, 2018. **39**(2): p. 417-424.
100. Yuan, D., et al., *Continuous plasma extraction under viscoelastic fluid in a straight channel with asymmetrical expansion–contraction cavity arrays*. Lab on a Chip, 2016. **16**(20): p. 3919-3928.
101. Hong, S.O., J.J. Cooper-White, and J.M. Kim, *Inertio-elastic mixing in a straight microchannel with side wells*. Applied Physics Letters, 2016. **108**(1): p. 014103.
102. Holzner, G., S. Stavrakis, and A. DeMello, *Elasto-inertial focusing of mammalian cells and bacteria using low molecular, low viscosity PEO solutions*. Analytical chemistry, 2017. **89**(21): p. 11653-11663.
103. Ha, B., et al., *Transfer of microparticles across laminar streams from non-Newtonian to Newtonian fluid*. Analytical chemistry, 2016. **88**(8): p. 4205-4210.
104. Tian, F., et al., *Microfluidic co-flow of Newtonian and viscoelastic fluids for high-resolution separation of microparticles*. Lab on a Chip, 2017. **17**(18): p. 3078-3085.
105. Nam, J., et al., *Continuous separation of microparticles in a microfluidic channel via the elasto-inertial effect of non-Newtonian fluid*. Lab on a Chip, 2012. **12**(7): p. 1347-1354.
106. Lim, H., J. Nam, and S. Shin, *Lateral migration of particles suspended in viscoelastic fluids in a microchannel flow*. Microfluidics and nanofluidics, 2014. **17**(4): p. 683-692.
107. Lu, X. and X. Xuan, *Elasto-inertial pinched flow fractionation for continuous shape-based particle separation*. Analytical chemistry, 2015. **87**(22): p. 11523-11530.
108. Andaloussi, S.E., et al., *Extracellular vesicles: biology and emerging therapeutic opportunities*. Nature reviews Drug discovery, 2013. **12**(5): p. 347.
109. Qi, H., et al., *Blood exosomes endowed with magnetic and targeting properties for cancer therapy*. ACS nano, 2016. **10**(3): p. 3323-3333.
110. Buzas, E.I., et al., *Emerging role of extracellular vesicles in inflammatory diseases*. Nature Reviews Rheumatology, 2014. **10**(6): p. 356.
111. Skog, J., et al., *Glioblastoma microvesicles transport RNA and proteins that promote tumour growth and provide diagnostic biomarkers*. Nature cell biology, 2008. **10**(12): p. 1470.
112. Liu, C., et al., *Field-free isolation of exosomes from extracellular vesicles by microfluidic viscoelastic flows*. ACS nano, 2017. **11**(7): p. 6968-6976.
113. Kim, J., et al., *Inertio-elastic flow instabilities in a 90° bent microchannel*. Soft matter, 2017. **13**(34): p. 5656-5664.
114. Wu, H., et al., *Microfluidic-based single-cell study: Current status and future perspective*. Molecules, 2018. **23**(9): p. 2347.

115. Aleklett, K., et al., *Build your own soil: exploring microfluidics to create microbial habitat structures*. The ISME journal, 2018. **12**(2): p. 312.
116. Al-Halhouli, A.a., et al., *Spiral Microchannels with Trapezoidal Cross Section Fabricated by Femtosecond Laser Ablation in Glass for the Inertial Separation of Microparticles*. Micromachines, 2018. **9**(4): p. 171.
117. Liao, Y., et al., *Three-dimensional microfluidic channel with arbitrary length and configuration fabricated inside glass by femtosecond laser direct writing*. Opt Lett, 2010. **35**(19): p. 3225-7.
118. Paiè, P., et al., *Particle focusing by 3D inertial microfluidics*. Microsystems & Nanoengineering, 2017. **3**: p. 17027.
119. Miller, B., M. Jimenez, and H. Bridle, *Cascading and Parallelising Curvilinear Inertial Focusing Systems for High Volume, Wide Size Distribution, Separation and Concentration of Particles*. Scientific Reports, 2016. **6**: p. 36386.
120. Suriano, R., et al., *Femtosecond laser ablation of polymeric substrates for the fabrication of microfluidic channels*. Applied Surface Science, 2011. **257**(14): p. 6243-6250.
121. Mukherjee, P., et al., *Single stream inertial focusing in low aspect-ratio triangular microchannels*. Lab on a Chip, 2019. **19**(1): p. 147-157.
122. Warkiani, M.E., et al., *Membrane-less microfiltration using inertial microfluidics*. Scientific Reports, 2015. **5**: p. 11018.
123. Kim, J.-A., et al., *Inertial focusing in non-rectangular cross-section microchannels and manipulation of accessible focusing positions*. Lab on a Chip, 2016. **16**(6): p. 992-1001.
124. Kim, B. and D.i.D. Cho, *Aqueous KOH etching of silicon (110) etch characteristics and compensation methods for convex corners*. Journal of the Electrochemical Society, 1998. **145**(7): p. 2499-2508.
125. Kim, J.-a., et al., *Size-dependent inertial focusing position shift and particle separations in triangular microchannels*. Analytical chemistry, 2018. **90**(3): p. 1827-1835.
126. Jia, Y., et al., *PDMS microchannel fabrication technique based on microwire-molding*. Chinese Science Bulletin, 2008. **53**(24): p. 3928-3936.
127. Kimerling, T.E., et al., *Rapid hot embossing of polymer microfeatures*. Microsystem Technologies, 2006. **12**(8): p. 730-735.
128. Lee, G.-B., et al., *Microfabricated plastic chips by hot embossing methods and their applications for DNA separation and detection*. Sensors and Actuators B: Chemical, 2001. **75**(1): p. 142-148.
129. Wang, X., et al., *A disposable, roll-to-roll hot-embossed inertial microfluidic device for size-based sorting of microbeads and cells*. Lab on a Chip, 2016. **16**(10): p. 1821-1830.
130. Hull, C.W., *Apparatus for production of three-dimensional objects by stereolithography*. 1986, Google Patents.
131. Bártolo, P.J., *Stereolithography: materials, processes and applications*. 2011: Springer Science & Business Media.
132. Melchels, F.P., J. Feijen, and D.W. Grijpma, *A review on stereolithography and its applications in biomedical engineering*. Biomaterials, 2010. **31**(24): p. 6121-6130.
133. Huang, Y.-M., S. Kuriyama, and C.-P. Jiang, *Fundamental study and theoretical analysis in a constrained-surface stereolithography system*. The International Journal of Advanced Manufacturing Technology, 2004. **24**(5-6): p. 361-369.
134. Billiet, T., et al., *A review of trends and limitations in hydrogel-rapid prototyping for tissue engineering*. Biomaterials, 2012. **33**(26): p. 6020-6041.

135. Lee, W., et al., *3D-printed microfluidic device for the detection of pathogenic bacteria using size-based separation in helical channel with trapezoid cross-section*. Scientific reports, 2015. **5**: p. 7717.
136. Au, A.K., et al., *3D-Printed Microfluidics*. Angew Chem Int Ed Engl, 2016. **55**(12): p. 3862-81.
137. Pham, D.T. and R.S. Gault, *A comparison of rapid prototyping technologies*. International Journal of machine tools and manufacture, 1998. **38**(10-11): p. 1257-1287.
138. Asghari, M., et al., *Sheathless Microflow Cytometry Using Viscoelastic Fluids*. Scientific Reports, 2017. **7**(1): p. 12342.
139. Dannhauser, D., et al., *Optical signature of erythrocytes by light scattering in microfluidic flows*. Lab on a Chip, 2015. **15**(16): p. 3278-3285.
140. Suresh, S., et al., *Connections between single-cell biomechanics and human disease states: gastrointestinal cancer and malaria*. Acta biomaterialia, 2005. **1**(1): p. 15-30.
141. Di Carlo, D., *A mechanical biomarker of cell state in medicine*. Journal of laboratory automation, 2012. **17**(1): p. 32-42.
142. Dylla-Spears, R., et al., *Single-molecule sequence detection via microfluidic planar extensional flow at a stagnation point*. Lab on a Chip, 2010. **10**(12): p. 1543-1549.
143. Kantsler, V., E. Segre, and V. Steinberg, *Critical dynamics of vesicle stretching transition in elongational flow*. Physical review letters, 2008. **101**(4): p. 048101.
144. Gossett, D.R., et al., *Hydrodynamic stretching of single cells for large population mechanical phenotyping*. Proceedings of the National Academy of Sciences, 2012. **109**(20): p. 7630-7635.
145. Wang, Z. and J. Zhe, *Recent advances in particle and droplet manipulation for lab-on-a-chip devices based on surface acoustic waves*. Lab on a Chip, 2011. **11**(7): p. 1280-1285.
146. Çetin, B. and D. Li, *Dielectrophoresis in microfluidics technology*. Electrophoresis, 2011. **32**(18): p. 2410-2427.
147. Bazaz, S.R., et al., *A hybrid micromixer with planar mixing units*. RSC Advances, 2018. **8**(58): p. 33103-33120.
148. Yamada, M., M. Nakashima, and M. Seki, *Pinched flow fractionation: continuous size separation of particles utilizing a laminar flow profile in a pinched microchannel*. Analytical chemistry, 2004. **76**(18): p. 5465-5471.
149. Hur, S.C., A.J. Mach, and D. Di Carlo, *High-throughput size-based rare cell enrichment using microscale vortices*. Biomicrofluidics, 2011. **5**(2): p. 022206.
150. Ryu, H., et al., *Patient-derived airway secretion dissociation technique to isolate and concentrate immune cells using closed-loop inertial microfluidics*. Analytical chemistry, 2017. **89**(10): p. 5549-5556.
151. Warkiani, M.E., et al., *Ultra-fast, label-free isolation of circulating tumor cells from blood using spiral microfluidics*. Nature protocols, 2016. **11**(1): p. 134.
152. Hou, H.W., et al., *Isolation and retrieval of circulating tumor cells using centrifugal forces*. Scientific reports, 2013. **3**: p. 1259.
153. Mutlu, B.R., et al., *Non-equilibrium Inertial Separation Array for High-throughput, Large-volume Blood Fractionation*. Scientific Reports, 2017. **7**(1): p. 9915.
154. Zhang, J., et al., *High-Throughput Separation of White Blood Cells From Whole Blood Using Inertial Microfluidics*. IEEE transactions on biomedical circuits and systems, 2017. **11**(6): p. 1422-1430.
155. Antfolk, M. and T. Laurell, *Continuous flow microfluidic separation and processing of rare cells and bioparticles found in blood—a review*. Analytica chimica acta, 2017. **965**: p. 9-35.
156. Syed, M.S., et al., *Selective separation of microalgae cells using inertial microfluidics*. Bioresource technology, 2018. **252**: p. 91-99.

157. Wang, X., et al., *A low-cost, plug-and-play inertial microfluidic helical capillary device for high-throughput flow cytometry*. *Biomicrofluidics*, 2017. **11**(1): p. 014107.
158. Kotz, K.T., et al., *System and method for inertial focusing cytometer with integrated optics for particle characterization*. 2018, Google Patents.
159. Moloudi, R., et al., *Inertial particle focusing dynamics in a trapezoidal straight microchannel: application to particle filtration*. *Microfluidics and Nanofluidics*, 2018. **22**(3): p. 33.
160. Zhao, Q., et al., *Flow rate-insensitive microparticle separation and filtration using a microchannel with arc-shaped groove arrays*. *Microfluidics and Nanofluidics*, 2017. **21**(3): p. 55.
161. Zhang, J., et al., *Inertial focusing in a straight channel with asymmetrical expansion-contraction cavity arrays using two secondary flows*. *Journal of Micromechanics and Microengineering*, 2013. **23**(8): p. 085023.
162. Zhang, J., et al., *Particle inertial focusing and its mechanism in a serpentine microchannel*. *Microfluidics and nanofluidics*, 2014. **17**(2): p. 305-316.
163. Mutlu, B.R., J.F. Edd, and M. Toner, *Oscillatory inertial focusing in infinite microchannels*. *Proceedings of the National Academy of Sciences*, 2018. **115**(30): p. 7682-7687.
164. Ciftlik, A.T., M. Ettori, and M.A. Gijs, *High throughput-per-footprint inertial focusing*. *Small*, 2013. **9**(16): p. 2764-2773.
165. Faridi, M.A., et al., *Elasto-inertial microfluidics for bacteria separation from whole blood for sepsis diagnostics*. *J Nanobiotechnology*, 2017. **15**(1): p. 3.
166. Patankar, N., et al., *Lift-off of a single particle in Newtonian and viscoelastic fluids by direct numerical simulation*. *Journal of Fluid Mechanics*, 2001. **438**: p. 67-100.
167. Matas, J., J. Morris, and E. Guazzelli, *Lateral forces on a sphere*. *Oil & gas science and technology*, 2004. **59**(1): p. 59-70.
168. Martel, J.M. and M. Toner, *Inertial focusing in microfluidics*. *Annual review of biomedical engineering*, 2014. **16**: p. 371-396.
169. Rubinow, S. and J.B. Keller, *The transverse force on a spinning sphere moving in a viscous fluid*. *Journal of Fluid Mechanics*, 1961. **11**(3): p. 447-459.
170. Shamloo, A. and A.J.P.o.F. Mashhadian, *Inertial particle focusing in serpentine channels on a centrifugal platform*. 2018. **30**(1): p. 012002.
171. Maxey, M.R. and J.J. Riley, *Equation of motion for a small rigid sphere in a nonuniform flow*. *The Physics of Fluids*, 1983. **26**(4): p. 883-889.
172. Warkiani, M.E., et al., *Slanted spiral microfluidics for the ultra-fast, label-free isolation of circulating tumor cells*. *Lab on a Chip*, 2014. **14**(1): p. 128-137.
173. Segre, G., *Radial Particle Displacements in Poiseuille Flow of Suspensions*. *Nature*, 1961. **189**: p. 209-210.
174. McLaughlin, J.B., *The lift on a small sphere in wall-bounded linear shear flows*. *Journal of Fluid Mechanics*, 1993. **246**: p. 249-265.
175. Joseph, D.D. and D. Ocando, *Slip velocity and lift*. *Journal of Fluid Mechanics*, 2002. **454**.
176. Jiang, D., et al., *Numerical simulation of particle focusing in a symmetrical serpentine microchannel*. *RSC Advances*, 2016. **6**(62): p. 57647-57657.
177. Volpe, A., et al., *A computational approach to the characterization of a microfluidic device for continuous size-based inertial sorting*. *Journal of Physics D: Applied Physics*, 2017. **50**(25).
178. Bhagat, A.A.S., S.S. Kuntaegowdanahalli, and I. Papautsky, *Enhanced particle filtration in straight microchannels using shear-modulated inertial migration*. *Physics of Fluids*, 2008. **20**(10).

179. LASHKARIPOUR, A., et al., *Size-controlled droplet generation in a microfluidic device for rare dna amplification by optimizing its effective parameters*. Journal of Mechanics in Medicine and Biology, 2018: p. 1850002.
180. Bhagat, A.A.S., et al., *Inertial microfluidics for sheath-less high-throughput flow cytometry*. Biomedical microdevices, 2010. **12**(2): p. 187-195.
181. Chung, A.J., et al., *Microstructure-induced helical vortices allow single-stream and long-term inertial focusing*. Lab on a Chip, 2013. **13**(15): p. 2942-2949.
182. Rafeie, M., et al., *An easily fabricated three-dimensional threaded lemniscate-shaped micromixer for a wide range of flow rates*. Biomicrofluidics, 2017. **11**(1): p. 014108.
183. Rasouli, M., et al., *Multi-criteria optimization of curved and Baffle-embedded micromixers for bio-applications*. Chemical Engineering and Processing-Process Intensification, 2018.
184. Zhou, J., et al., *Modulation of aspect ratio for complete separation in an inertial microfluidic channel*. Lab on a Chip, 2013. **13**(10): p. 1919-1929.
185. Kulasinghe, A., et al., *Enrichment of circulating head and neck tumour cells using spiral microfluidic technology*. Scientific Reports, 2017. **7**: p. 42517.
186. Amini, H., et al., *Engineering fluid flow using sequenced microstructures*. Nat Commun, 2013. **4**: p. 1826.
187. Jimenez, M., B. Miller, and H.L. Bridle, *Efficient separation of small microparticles at high flowrates using spiral channels: Application to waterborne pathogens*. Chemical Engineering Science, 2017. **157**: p. 247-254.
188. Kwon, T., et al., *Microfluidic Cell Retention Device for Perfusion of Mammalian Suspension Culture*. Scientific Reports, 2017. **7**(1): p. 6703.
189. Condina, M.R., et al., *Rapid separation and identification of beer spoilage bacteria by inertial microfluidics and MALDI-TOF mass spectrometry*. Lab on a Chip, 2019. **19**(11): p. 1961-1970.
190. Zhang, Y., et al. *Morphology control of microchannel cross-section using sacrificial spinning fiber*. in *Micro Electro Mechanical Systems (MEMS), 2017 IEEE 30th International Conference on*. 2017. IEEE.
191. Fan, L.-L., et al., *Inertial particle focusing in microchannels with gradually changing geometrical structures*. Journal of Micromechanics and Microengineering, 2016. **27**(1): p. 015027.
192. Fan, L.-L., et al., *Single particle train ordering in microchannel based on inertial and vortex effects*. Journal of Micromechanics and Microengineering, 2018. **28**(6): p. 065011.
193. Chan, H.N., et al., *Direct, one-step molding of 3D-printed structures for convenient fabrication of truly 3D PDMS microfluidic chips*. Microfluidics and Nanofluidics, 2015. **19**(1): p. 9-18.
194. Bohl, B., et al., *Multi-layer SU-8 lift-off technology for microfluidic devices*. Journal of micromechanics and microengineering, 2005. **15**(6): p. 1125.
195. Kuntaegowdanahalli, S.S., et al., *Inertial microfluidics for continuous particle separation in spiral microchannels*. Lab on a Chip, 2009. **9**(20): p. 2973-2980.
196. Lee, M.G., et al., *Label-Free Cancer Cell Separation from Human Whole Blood Using Inertial Microfluidics at Low Shear Stress*. Analytical Chemistry, 2013. **85**(13): p. 6213-6218.
197. Warkiani, M.E., et al., *An ultra-high-throughput spiral microfluidic biochip for the enrichment of circulating tumor cells*. Analyst, 2014. **139**(13): p. 3245-3255.
198. Hansson, J., et al., *Inertial microfluidics in parallel channels for high-throughput applications*. Lab on a Chip, 2012. **12**(22): p. 4644-4650.
199. Xiang, N. and Z. Ni, *High-throughput blood cell focusing and plasma isolation using spiral inertial microfluidic devices*. Biomedical Microdevices, 2015. **17**(6): p. 110.

200. Whitesides, G.M., et al., *Soft lithography in biology and biochemistry*. Annu Rev Biomed Eng, 2001. **3**: p. 335-73.
201. Abdelgawad, M., et al., *Soft lithography: masters on demand*. Lab on a Chip, 2008. **8**(8): p. 1379-1385.
202. Lee, D.-K., J.Y. Kwon, and Y.H. Cho, *Fabrication of microfluidic channels with various cross-sectional shapes using anisotropic etching of Si and self-alignment*. Applied Physics A, 2019. **125**(5): p. 291.
203. Zeinali, S., et al., *Fabrication of continuous flow microfluidics device with 3D electrode structures for high throughput DEP applications using mechanical machining*. Electrophoresis, 2015. **36**(13): p. 1432-1442.
204. Lin, Y.-C., et al., *Fabrication of microfluidic structures in quartz via micro machining technologies*. Microsystem Technologies, 2017. **23**(6): p. 1661-1669.
205. Lashkaripour, A., R. Silva, and D. Densmore, *Desktop micromilled microfluidics*. Microfluidics and Nanofluidics, 2018. **22**(3): p. 31.
206. Moloudi, R., et al., *Inertial-Based Filtration Method for Removal of Microcarriers from Mesenchymal Stem Cell Suspensions*. Scientific Reports, 2018. **8**(1): p. 12481.
207. He, Y., et al., *Micro structure fabrication with a simplified hot embossing method*. RSC Advances, 2015. **5**(49): p. 39138-39144.
208. Wang, X., et al., *A disposable, roll-to-roll hot-embossed inertial microfluidic device for size-based sorting of microbeads and cells*. Lab Chip, 2016. **16**(10): p. 1821-30.
209. He, Y., et al., *Printing 3D microfluidic chips with a 3D sugar printer*. Microfluidics and Nanofluidics, 2015. **19**(2): p. 447-456.
210. Saggiomo, V. and A.H. Velders, *Microfluidic Devices: Simple 3D Printed Scaffold-Removal Method for the Fabrication of Intricate Microfluidic Devices (Adv. Sci. 9/2015)*. Advanced Science, 2015. **2**(9): p. n/a-n/a.
211. Parekh, D.P., et al., *3D printing of liquid metals as fugitive inks for fabrication of 3D microfluidic channels*. Lab on a Chip, 2016. **16**(10): p. 1812-1820.
212. Kang, K., et al., *Fabrication of truly 3D microfluidic channel using 3D-printed soluble mold*. Biomicrofluidics, 2018. **12**(1): p. 014105.
213. Li, Z.a., et al., *Fabrication of PDMS microfluidic devices with 3D wax jetting*. RSC Advances, 2017. **7**(6): p. 3313-3320.
214. Serre, D., *Helicity and other conservation laws in perfect fluid motion*. Comptes Rendus Mécanique, 2018. **346**(3): p. 175-183.
215. Russom, A., et al., *Differential inertial focusing of particles in curved low-aspect-ratio microchannels*. New Journal of Physics, 2009. **11**(7): p. 075025.
216. Ardabili, S., et al. *Dean flow-coupled inertial focussing for ultra-highthroughput particle filtration*. in *14th International Conference on Miniaturized Systems for Chemistry and Life Sciences, Groningen, The Netherlands*. 2010.
217. Zhou, J. and I. Papautsky, *Fundamentals of inertial focusing in microchannels*. Lab on a Chip, 2013. **13**(6): p. 1121-1132.
218. Gelber, M.K. and R.J.L.o.a.C. Bhargava, *Monolithic multilayer microfluidics via sacrificial molding of 3D-printed isomalt*. 2015. **15**(7): p. 1736-1741.
219. Mohanty, S., et al., *Fabrication of scalable and structured tissue engineering scaffolds using water dissolvable sacrificial 3D printed moulds*. 2015. **55**: p. 569-578.
220. Lee, J.-S., et al., *3D printing of composite tissue with complex shape applied to ear regeneration*. 2014. **6**(2): p. 024103.
221. Saggiomo, V. and A.H. Velders, *Simple 3D Printed Scaffold-Removal Method for the Fabrication of Intricate Microfluidic Devices*. 2015. **2**(9): p. 1500125.
222. Saggiomo, V. and A.H. Velders, *Microfluidic Devices: Simple 3D Printed Scaffold-Removal Method for the Fabrication of Intricate Microfluidic Devices (Adv. Sci. 9/2015)*. Advanced Science, 2015. **2**(9).

223. Wu, L., et al., *Separation of leukocytes from blood using spiral channel with trapezoid cross-section*. Analytical chemistry, 2012. **84**(21): p. 9324-9331.
224. Park, J.Y., C.M. Hwang, and S.-H. Lee, *Ice-lithographic fabrication of concave microwells and a microfluidic network*. Biomedical Microdevices, 2009. **11**(1): p. 129-133.
225. Paiè, P., et al., *Particle focusing by 3D inertial microfluidics*. Microsystems & Nanoengineering, 2017. **3**: p. 17027.
226. Chung, C.-K., H.P. Long, and C.C. Lai *Microfluidic chip using foil-assisted CO₂ laser ablation for suspended particle separation*. Micro & Nano Letters, 2015. **10**, 500-503.
227. Verma, M.K., A. Majumder, and A. Ghatak, *Embedded template-assisted fabrication of complex microchannels in PDMS and design of a microfluidic adhesive*. Langmuir, 2006. **22**(24): p. 10291-5.
228. Song, S.-H., et al., *A rapid and simple fabrication method for 3-dimensional circular microfluidic channel using metal wire removal process*. Microfluidics and Nanofluidics, 2010. **9**(2-3): p. 533-540.
229. Sollier, E., et al., *Rapid prototyping polymers for microfluidic devices and high pressure injections*. Lab on a Chip, 2011. **11**(22): p. 3752-3765.
230. Liu, C., et al., *Inertial focusing of spherical particles in rectangular microchannels over a wide range of Reynolds numbers*. Lab on a Chip, 2015. **15**(4): p. 1168-1177.
231. Gou, Y., et al., *Progress of inertial microfluidics in principle and application*. Sensors, 2018. **18**(6): p. 1762.
232. Bhagat, A.A.S., S.S. Kuntaegowdanahalli, and I. Papautsky, *Inertial microfluidics for continuous particle filtration and extraction*. Microfluidics and Nanofluidics, 2009. **7**(2): p. 217-226.
233. Nivedita, N., P. Ligrani, and I. Papautsky, *Dean flow dynamics in low-aspect ratio spiral microchannels*. Scientific reports, 2017. **7**: p. 44072.
234. Guan, G., et al., *Spiral microchannel with rectangular and trapezoidal cross-sections for size based particle separation*. Scientific reports, 2013. **3**: p. 1475.
235. Hou, H.W., et al., *Isolation and retrieval of circulating tumor cells using centrifugal forces*. Scientific reports, 2013. **3**.
236. Winter, M., et al., *Isolation of circulating fetal trophoblasts using inertial microfluidics for noninvasive prenatal testing*. Advanced Materials Technologies, 2018. **3**(7): p. 1800066.
237. Rafeie, M., et al., *Multiplexing slanted spiral microchannels for ultra-fast blood plasma separation*. Lab on a Chip, 2016. **16**(15): p. 2791-2802.
238. Tee, C.A., et al., *Improved zonal chondrocyte production protocol integrating size-based inertial spiral microchannel separation and dynamic microcarrier culture for clinical application*. Biomaterials, 2019: p. 119409.
239. Moloudi, R., et al., *Scaled-up Inertial Microfluidics: Retention System for Microcarrier-based Suspension Cultures*. Biotechnology journal, 2019: p. 1800674.
240. Sofela, S., et al., *High-throughput sorting of eggs for synchronization of C. elegans in a microfluidic spiral chip*. Lab on a Chip, 2018. **18**(4): p. 679-687.
241. Wang, L. and D.S. Dandy, *High-Throughput Inertial Focusing of Micrometer-and Sub-Micrometer-Sized Particles Separation*. Advanced Science, 2017. **4**(10): p. 1700153.
242. Wang, L. and D.S. Dandy, *A microfluidic concentrator for cyanobacteria harvesting*. Algal research, 2017. **26**: p. 481-489.
243. Zhang, J., et al., *Fundamentals of differential particle inertial focusing in symmetric sinusoidal microchannels*. Analytical chemistry, 2019. **91**(6): p. 4077-4084.
244. Özbey, A., et al., *Inertial focusing of microparticles in curvilinear microchannels with different curvature angles*. Microfluidics and Nanofluidics, 2018. **22**(6): p. 62.

245. Ozbey, A., et al., *Inertial focusing of Cancer Cell Lines in Curvilinear Microchannels*. Micro and Nano Engineering, 2019.
246. Wu, Z., et al., *Continuous inertial microparticle and blood cell separation in straight channels with local microstructures*. Lab on a Chip, 2016. **16**(3): p. 532-542.
247. Lee, M.G., et al., *Inertial blood plasma separation in a contraction–expansion array microchannel*. Applied Physics Letters, 2011. **98**(25): p. 253702.
248. Bhagat, A.A.S., et al., *Pinched flow coupled shear-modulated inertial microfluidics for high-throughput rare blood cell separation*. Lab on a Chip, 2011. **11**(11): p. 1870-1878.
249. Jiang, D., et al., *Numerical simulation of particle migration in different contraction–expansion ratio microchannels*. Microfluidics and Nanofluidics, 2018. **23**(1): p. 7.
250. Kersaudy-Kerhoas, M. and E. Sollier, *Micro-scale blood plasma separation: from acoustophoresis to egg-beaters*. Lab on a Chip, 2013. **13**(17): p. 3323-3346.
251. Committee, A.A.o.B.B.H., *Guidelines for therapeutic hemapheresis*. Bethesda, MD: American Association of Blood Banks, 1995.
252. Yang, S., A. Ündar, and J.D. Zahn, *A microfluidic device for continuous, real time blood plasma separation*. Lab on a Chip, 2006. **6**(7): p. 871-880.
253. Al-Soud, W.A. and P. Rådström, *Purification and characterization of PCR-inhibitory components in blood cells*. Journal of clinical microbiology, 2001. **39**(2): p. 485-493.
254. BUCKNER, D., R. EISEL, and S. PERRY, *Blood cell separation in the dog by continuous flow centrifugation*. Blood, 1968. **31**(5): p. 653-672.
255. Tangen, O., H. Berman, and P. Marfey, *Gel filtration. A new technique for separation of blood platelets from plasma*. Thrombosis et diathesis haemorrhagica, 1971. **25**(2): p. 268.
256. Bruus, H., *Theoretical microfluidics*. 2008. New York: Oxford University Press.
257. Bordier, C., *Phase separation of integral membrane proteins in Triton X-114 solution*. Journal of Biological Chemistry, 1981. **256**(4): p. 1604-1607.
258. Kwon, K.W., et al., *Label-free, microfluidic separation and enrichment of human breast cancer cells by adhesion difference*. Lab on a Chip, 2007. **7**(11): p. 1461-1468.
259. Wang, Y., Y. Zhao, and S.K. Cho, *Efficient in-droplet separation of magnetic particles for digital microfluidics*. Journal of Micromechanics and Microengineering, 2007. **17**(10): p. 2148.
260. Ramsey, J.D. and G.E. Collins, *Integrated microfluidic device for solid-phase extraction coupled to micellar electrokinetic chromatography separation*. Analytical chemistry, 2005. **77**(20): p. 6664-6670.
261. Furlani, E., *Magnetophoretic separation of blood cells at the microscale*. Journal of Physics D: Applied Physics, 2007. **40**(5): p. 1313.
262. Nakashima, Y., S. Hata, and T. Yasuda, *Blood plasma separation and extraction from a minute amount of blood using dielectrophoretic and capillary forces*. Sensors and Actuators B: Chemical, 2010. **145**(1): p. 561-569.
263. Liao, S.-H., C.-Y. Chang, and H.-C. Chang, *A capillary dielectrophoretic chip for real-time blood cell separation from a drop of whole blood*. Biomicrofluidics, 2013. **7**(2): p. 024110.
264. Lenshof, A., et al., *Acoustic whole blood plasmapheresis chip for prostate specific antigen microarray diagnostics*. Analytical chemistry, 2009. **81**(15): p. 6030-6037.
265. Nam, J., et al., *Density-dependent separation of encapsulated cells in a microfluidic channel by using a standing surface acoustic wave*. Biomicrofluidics, 2012. **6**(2): p. 024120.
266. Church, C., et al., *Continuous particle separation in a serpentine microchannel via negative and positive dielectrophoretic focusing*. Journal of Micromechanics and Microengineering, 2010. **20**(6): p. 065011.
267. Fung, Y.-c., *Biomechanics: circulation*. 2013: Springer Science & Business Media.

268. Moorthy, J. and D.J. Beebe, *In situ fabricated porous filters for microsystems*. Lab on a Chip, 2003. **3**(2): p. 62-66.
269. Crowley, T.A. and V. Pizziconi, *Isolation of plasma from whole blood using planar microfilters for lab-on-a-chip applications*. Lab on a Chip, 2005. **5**(9): p. 922-929.
270. Redkar, S.G. and R.H. Davis, *Cross-flow microfiltration with high-frequency reverse filtration*. AIChE journal, 1995. **41**(3): p. 501-508.
271. Kuberkar, V., P. Czekaj, and R. Davis, *Flux enhancement for membrane filtration of bacterial suspensions using high-frequency backpulsing*. Biotechnology and bioengineering, 1998. **60**(1): p. 77-87.
272. Kiss, F., et al., *The effect of centrifugation at various g force levels on rheological properties of rat, dog, pig and human red blood cells*. Clinical hemorheology and microcirculation, 2016(Preprint): p. 1-14.
273. Nivedita, N. and I. Papautsky, *Continuous separation of blood cells in spiral microfluidic devices*. Biomicrofluidics, 2013. **7**(5): p. 054101.
274. Haerberle, S., et al., *Centrifugal extraction of plasma from whole blood on a rotating disk*. Lab on a Chip, 2006. **6**(6): p. 776-781.
275. Zhang, X.-B., et al., *Gravitational sedimentation induced blood delamination for continuous plasma separation on a microfluidics chip*. Analytical chemistry, 2012. **84**(8): p. 3780-3786.
276. Sun, M., Z.S. Khan, and S.A. Vanapalli, *Blood plasma separation in a long two-phase plug flowing through disposable tubing*. Lab on a Chip, 2012. **12**(24): p. 5225-5230.
277. Maria, M.S., et al., *Capillary flow-driven microfluidic device with wettability gradient and sedimentation effects for blood plasma separation*. Scientific reports, 2017. **7**: p. 43457.
278. Fekete, Z., et al., *Performance characterization of micromachined particle separation system based on Zweifach–Fung effect*. Sensors and Actuators B: Chemical, 2012. **162**(1): p. 89-94.
279. Prabhakar, A., et al., *A novel, compact and efficient microchannel arrangement with multiple hydrodynamic effects for blood plasma separation*. Microfluidics and Nanofluidics, 2015. **18**(5-6): p. 995-1006.
280. Kersaudy-Kerhoas, M., et al., *Hydrodynamic blood plasma separation in microfluidic channels*. Microfluidics and nanofluidics, 2010. **8**(1): p. 105-114.
281. Kersaudy-Kerhoas, M., et al., *Validation of a blood plasma separation system by biomarker detection*. Lab on a Chip, 2010. **10**(12): p. 1587-1595.
282. Shamsi, A., et al., *High throughput blood plasma separation using a passive PMMA microfluidic device*. Microsystem Technologies, 2016. **22**(10): p. 2447-2454.
283. Angelescu, D.E., *Highly Integrated Microfluidics Design*. 2011: Artech House.
284. Probstein, R.F., *Physicochemical hydrodynamics: an introduction*. 2005: John Wiley & Sons.
285. Chu, K. and A. Yu, *Numerical simulation of complex particle–fluid flows*. Powder Technology, 2008. **179**(3): p. 104-114.
286. Di Felice, R., *The voidage function for fluid-particle interaction systems*. International Journal of Multiphase Flow, 1994. **20**(1): p. 153-159.
287. White, F.M., *Fluid mechanics*, WCB. ed: McGraw-Hill, Boston, 1999.
288. Morsi, S. and A. Alexander, *An investigation of particle trajectories in two-phase flow systems*. Journal of Fluid Mechanics, 1972. **55**(02): p. 193-208.
289. Drew, D., L. Cheng, and R. Lahey, *The analysis of virtual mass effects in two-phase flow*. International Journal of Multiphase Flow, 1979. **5**(4): p. 233-242.
290. Cundall, P.A. and O.D. Strack, *A discrete numerical model for granular assemblies*. Geotechnique, 1979. **29**(1): p. 47-65.
291. Bennett, A., *Lagrangian fluid dynamics*. 2006: Cambridge University Press.

292. Gosman, A. and E. Loannides, *Aspects of computer simulation of liquid-fueled combustors*. Journal of Energy, 1983. **7**(6): p. 482-490.
293. Anderson, J.D. and J. Wendt, *Computational fluid dynamics*. Vol. 206. 1995: Springer.
294. Hou, H.W., et al., *Microfluidic devices for blood fractionation*. Micromachines, 2011. **2**(3): p. 319-343.
295. Tripathi, S., et al., *Passive blood plasma separation at the microscale: a review of design principles and microdevices*. Journal of Micromechanics and Microengineering, 2015. **25**(8): p. 083001.
296. Galdi, G.P., et al., *Hemodynamical flows*. Delhi Book Store, 2008.
297. Baskurt, O.K. and H.J. Meiselman. *Blood rheology and hemodynamics*. in *Seminars in thrombosis and hemostasis*. 2003. Copyright© 2003 by Thieme Medical Publishers, Inc., 333 Seventh Avenue, New York, NY 10001, USA. Tel.:+ 1 (212) 584-4662.
298. Chakraborty, S., *Dynamics of capillary flow of blood into a microfluidic channel*. Lab on a Chip, 2005. **5**(4): p. 421-430.
299. Kumar, N., et al., *Blood flow in non-circular microchannel under pulsating condition*. International Journal of Micro-Nano Scale Transport, 2013. **4**(1-2): p. 33-50.
300. Reinke, W., P.C. Johnson, and P. Gaetgens, *Effect of shear rate variation on apparent viscosity of human blood in tubes of 29 to 94 microns diameter*. Circulation research, 1986. **59**(2): p. 124-132.
301. Ballyk, P., D. Steinman, and C. Ethier, *Simulation of non-Newtonian blood flow in an end-to-side anastomosis*. Biorheology, 1993. **31**(5): p. 565-586.
302. Misra, J., M. Patra, and S. Misra, *A non-Newtonian fluid model for blood flow through arteries under stenotic conditions*. Journal of biomechanics, 1993. **26**(9): p. 1129-1141.
303. Sharma, K. and S. Bhat, *Non-Newtonian rheology of leukemic blood and plasma: are n and k parameters of power law model diagnostic?* Physiological chemistry and physics and medical NMR, 1991. **24**(4): p. 307-312.
304. Svanes, K. and B. Zweifach, *Variations in small blood vessel hematocrits produced in hypothermic rats by micro-occlusion*. Microvascular Research, 1968. **1**(2): p. 210-220.
305. Fung, Y.-C., *Stochastic flow in capillary blood vessels*. Microvascular research, 1973. **5**(1): p. 34-48.
306. Doyeux, V., et al., *Spheres in the vicinity of a bifurcation: elucidating the Zweifach–Fung effect*. Journal of Fluid Mechanics, 2011. **674**: p. 359-388.
307. Shamloo, A., P. Vatankeh, and M.A. Bijarchi, *Numerical optimization and inverse study of a microfluidic device for blood plasma separation*. European Journal of Mechanics-B/Fluids, 2016. **57**: p. 31-39.
308. Yang, S., A. Ündar, and J.D. Zahn, *Blood plasma separation in microfluidic channels using flow rate control*. Asaio Journal, 2005. **51**(5): p. 585-590.

Appendix

Abbreviations

a	Particle diameter
AR	channel aspect ratio
EL	Elasticity number
m	Mass of particle
D _e	Deborah number
D _H	Hydraulic diameter
Dn	Dean number
H	Channel height
N ₁	First normal stress difference
N ₂	Second normal stress difference
M _w	Molecular weight
Q	Flow rate
P	pressure
R	Channel curvature radius
Re	Reynolds number
U _m	Maximum velocity
u _p	Particle velocity
V	Velocity
w	Channel width
Wi	Weissenberg number

Symbols

λ_e	Effective relaxation time
μ	Viscosity
τ	Extra stress tensor
α	Flow rate ratio
β	Blockage ratio
η	Shear viscosity
γ	Shear rate
ρ	Density
σ	Surface tension